Spectroscopy of selected calcium and strontium containing polyatomic molecules

by

Michael J. Dick

A thesis
presented to the University of Waterloo
in fulfillment for the degree of
Doctor of Philosophy
in
Physics

Waterloo, Ontario, Canada, 2007

Author's Declaration

I hereby declare that I am the sole author of this thesis. This is a true copy of the thesis, including any required final revisions, as accepted by my examiners.

I understand that my thesis may be made electronically available to the public.

Abstract

A spectroscopic study of several calcium and strontium containing molecules has been completed. In total, seven electronic transitions from six different calcium or strontium containing species were observed and analyzed at high resolution.

Using laser excitation spectroscopy in a laser ablation source, the high-resolution spectra of the $\tilde{A}\,^2\Pi$-$\tilde{X}\,^2\Sigma^+$ transition of SrCCH, the $\tilde{B}\,^2A_1$- $\tilde{X}\,^2A_1$ transition of $CaCH_3$, the $\tilde{A}\,^2E$- $\tilde{X}\,^2A_1$ and $\tilde{B}\,^2A_1$- $\tilde{X}\,^2A_1$ transitions of $SrCH_3$, along with the $\tilde{B}\,^2E$- $\tilde{X}\,^2A_1$ transitions of $SrBH_4$ and $CaBH_4$ have been recorded and analyzed. For each molecule, a geometric structure in the ground and excited states was estimated and the fine structure constants for the excited state were investigated. A comparison of these geometries and parameters with those of other calcium and strontium containing species has yielded important information on bonding and electronic structure. For the $\tilde{A}\,^2\Pi$ state of SrCCH, the $\tilde{B}\,^2A_1$ state of $CaCH_3$, and the $\tilde{A}\,^2E$ and $\tilde{B}\,^2A_1$ states of $SrCH_3$, it was found that these states arise predominantly from $p\sigma$ or $p\pi$ atomic orbitals located on Ca^+ or Sr^+ ions, consistent with the analogous states of CaF, SrF, CaOH and SrOH. For the $\tilde{B}\,^2E$ states of $SrBH_4$ and $CaBH_4$ a similar analysis showed an increased amount of *d*-atomic orbital character in these states.

The $\tilde{D}^2\Sigma^+$ state of CaOH was investigated at high resolution using optical-optical double resonance spectroscopy in a Broida oven source. An analysis of the resulting molecular constants showed that the Ca-O bond length and spin-rotation parameter of the $\tilde{D}^2\Sigma^+$ state have the smallest values of those for all the observed $^2\Sigma^+$ states of CaOH. This evidence suggested that the $\tilde{D}^2\Sigma^+$ state arises from a Ca^+ atomic orbital of mainly $5s\sigma$ character. This atomic orbital assignment was shown to be consistent with both previous work on CaF and recent theoretical calculations on CaOH.

Acknowledgements

To begin I would like to thank my supervisor Dr. Peter Bernath. Obviously, without him none of this work would have been possible. To be a good supervisor one must be intelligent, patient and understanding, Peter has all of these characteristics and more in abundance. To the members of my committee I would like to thank you for the helpful suggestions over the past 3.5 years and for keeping me motivated to complete this degree on time.

To all the members of the Bernath group, past and present, thanks are given for making the numerous hours spent in the lab fun and enjoyable. Dejian, Shanshan, Ali, Yani, Elizabeth and Yoshi, thank you for laughing at my jokes and making me laugh. Two members of the lab require special acknowledgement. Phil Sheridan is really the one who got this investigation of calcium and strontium containing polyatomic molecules off the ground and running. Without his help and guidance I would still be floundering in the lab. He is not only a great spectroscopist but also a great friend. Finally, particular recognition is given to Jin-Guo Wang. Jin is literally one in a billion. Before coming to Waterloo I had never met anyone like him and upon leaving here I doubt I ever will again. I feel honored to have had the opportunity to meet and work with him and to now call him not only my colleague but my friend.

Next I would like to give some recognition to my family. In my last thesis, I thanked them for their unconditional support and understanding. Nothing has changed, I am still very much indebted to them.

When I departed Fredericton to pursue my PhD, I left behind a great set of friends whom I thought could never be equaled. However, as is frequently the case in science the first assumption is often wrong and this holds true in this case. The set of friends I have acquired here in Waterloo play second fiddle to no one and many thanks is owed to them. To Ray and Iouli, I thank you for all good times we had and for showing me around Waterloo. Things have truly not been the same since you left. To the members of C-Unit (Melissa, Monica, Jon and Kathleen), thank you for welcoming me into your group and for countless laughs. You have proven that the view of Upper Canadians not knowing how to have fun is clearly wrong. To Mike Earle, I thank you for being a fantastic roommate and friend. I have now lived with you longer then anyone else, except for my parents. Thank you for not driving me as crazy as they did. Also I will just say I think it is quite ironic that a kid from New Brunswick had to come all the way to Ontario to make friends with a kid from Nova Scotia. It was worth the trip.

Finally, a funny thing happened in pursuit of this degree, I not only found the answers to some interesting scientific questions, but also a great girl. To April, I thank you for being the best friend and girlfriend a guy could ask for. The amount of support and understanding you have shown me during the pursuit of this research is uncountable and to describe what it has meant to me would more then double the length of this thesis. I will just sum it up by saying: I looooooove you!

Table of Contents

List of Tables

List of Figures

Chapter 1 - Introduction and Motivation

Metal containing compounds are ubiquitous in science. The are used in chemistry, where for example, they play a significant role in catalysis and organic synthesis [1,2]. In biology, they exist in the active sites of enzymes whose functions are vital to life on earth [3]. In astrophysics, they play a critical role in understanding the composition and spectral energy distributions of cool stellar objects [4,5]. Because of their intrinsic importance, there has been a large effort to understand the properties of these molecules better. Unfortunately, due to their often increased size and complexity (a typical enzyme for example, is composed of hundreds if not thousands of atoms), direct derivation of the properties of these molecules is not simple. One method which has been employed in an attempt to understand these metal containing molecules is to approach the problem from the bottom up. That is to examine the fundamental components of such species (i.e. a metal atom bonded to a single or small number of atoms) in the hopes that once an understanding of the elementary components is reached, conclusions can be drawn about much larger metal containing species.

Gas phase spectroscopy is well suited and has been employed extensively in pursuit of these fundamental investigations [6,7]. A single gas phase spectrum can yield a wealth of information about the structure (both geometric and electronic) and bonding of a metal containing species. Amongst the most spectroscopically studied metal containing species are the alkaline earth containing molecules. These species have been of particular interest because their bonding can be described as ionic [M^+ (metal atom) L^- (ligand)], with the electronic states derived from the promotion of an unpaired electron residing in orbitals located primarily on the metal atom [8]. However, work on this group of molecules is far from complete as the majority of the high resolution spectroscopic studies of the alkaline earth containing molecules have focused on diatomic metal halides or linear hydroxides. In addition, these investigations have focused primarily on the lower lying electronic states (< 20000 cm^{-1}) of these species.

Polyatomic analogs with lower symmetry have generally only been investigated at low or medium resolution due to the increasingly complicated appearance of their molecular spectra. These complexities are a result of additional interactions not present in the linear species. However, a desire to understand these interactions actually fuels interest in the polyatomic species despite the complexity of their spectra. For example, non linear molecules may be subject to the interesting effects of Jahn-Teller coupling not present in linear molecules. These polyatomic species are of further interest due to the desire to compare the properties and structures of the alkaline earth containing molecules as the size of the ligand increases and their symmetry decreases. For example, interesting conclusions can be drawn if the spectroscopic properties of SrF, SrCCH, $SrNH_2$, $SrCH_3$, $SrBH_4$ and SrSH are compared.

A full investigation of the higher lying states (> 20000 cm^{-1}) of these alkaline earth-containing molecules is also far from complete. With the exception of an investigation of the excited states of CaF up to ~38000 cm^{-1} completed by Field and coworkers [9], the highly excited states of these molecules have been largely ignored. This is principally a reflection of the difficulty in probing the higher lying electronic states using conventional spectroscopic methods, rather than a lack of interest in these higher lying states. In fact these states are of great interest for several reasons. Firstly, as the energy of the state increases the ligand will play a more important role in the bonding resulting in an increased covalency of the metal ligand bond. This change could be of particular interest for alkaline earth containing polyatomic molecules where a change in geometry in the higher lying states as compared to the lower states could result from the alteration in bonding. For example, there is preliminary evidence [10] that suggests that CaOH, which is linear in its lower lying states, may adopt a bent geometry in some excited states. In addition, the increased covalency of the bonding may result in a decrease in the validity of the assumption that the electronic states of the alkaline earth containing molecules are derived from orbitals located primarily on the metal atom. As described above, the ligand orbitals will play a larger role in the metal-ligand bonding in the higher energy states, and will need to be accounted for. Finally, as was the case for the polyatomic molecules, it is of interest to compare the properties and structure of these higher lying states as the size and symmetry of the ligand varies. In particular, for the higher lying states, it is of interest to see if any of the states will reorder in energy as the ligand changes. Such reordering could be a reflection of a dramatic modification of the orbital character of a particular electronic state.

In an attempt to further the understanding of the alkaline earth containing molecules, the Bernath group initiated an examination of these species. The investigation occurred on two fronts, and this thesis will report on some of the results of this work.

Firstly, an examination of previously unobserved electronic transitions of several alkaline earth containing compounds using high resolution spectroscopy was conducted. This work was completed using laser induced fluorescence experiments in a laser ablation/molecular jet source. In total, the spectra of thirteen electronic transitions from nine molecules were recorded and analyzed. The results of these analyses for $CaCH_3$ (Chapter 5), $CaBH_4$ (Chapter 7), SrCCH (Chapter 4), $SrCH_3$ (Chapter 5 and 6) and $SrBH_4$ (Chapter 7) will be presented in this thesis, while the work completed on $SrNH_2$ [11], SrSH [12], CaSH [12] and BaOH [13] is presented in the associated references. For the molecules presented in this thesis, the chapters in which the results are presented will also include a more detailed explanation of the motivation behind the studies, an outline of the work previously completed, and a description of the experimental conditions employed to obtain the spectra investigated.

Secondly, an investigation of the higher lying states of the alkaline earth polyatomic molecules was completed. This work was accomplished using optical-optical double resonance spectroscopy in a Broida oven source. A total of six higher energy states from four different molecules were investigated. The results of the examination of the $\tilde{D}^2\Sigma^+$ state of CaOH will be presented in chapter 8 of this thesis. This chapter will also include an overview of previous work completed on CaOH, and the experimental setup employed in the current investigation. The work completed on the highly-excited states of SrOH [14,15], SrOD [16] and SrF [17] is described in detail in the associated references.

In addition to outlining the results of the experimental surveys completed, this thesis will also attempt to explain, in some detail, the theory and experiment used in this work. Chapter 2 includes a description of the theory relevant to the spectroscopy of alkaline earth-containing molecules, while chapter 3 is comprised of an in depth discussion of the laser ablation/molecular jet and Broida oven sources, and how they were employed in the current investigations of alkaline earth-containing molecules.

References

[1] F. A. Cotton, G. W. Wilkinson, C. A. Murillo and M. Bochmann, *Advanced Inorganic Chemistry*, Wiley, New York, 1999.

[2] R. H. Crabtree, *The Organometallic Chemistry of the Transition Metals*, Wiley-Interscience, New York, 2005.

[3] D. Voet, J. G. Voet and C. W. Pratt, *Fundamentals of Biochemistry*, Wiley, New York, 1999.

[4] L. M. Ziurys, C. Savage, J. L. Highberger, A. J. Apponi, M. Guelin and J. Cernicharo, Astrophys. J. **564**, L45 (2002).

[5] J. L. Highberger and L. M. Ziurys, Astrophys. J. **597**, 1065 (2003)

[6] P. F. Bernath, *Advances in Photochemistry*, Wiley, New York, Vol. 23, 1997.

[7] A. M. Ellis, Int. Rev. Phys. Chem. **20**, 551 (2001).

[8] S. F. Rice, H. Martin and R. W. Field, J. Chem. Phys. **82**, 5023 (1985).

[9] J. M. Berg, J. E. Murphy, N. A. Harris and R. W. Field, Phys. Rev. A. **48**, 3012 (1993).

[10] R. Pereira and D. H. Levy, J. Chem. Phys. **105**, 9733 (1996).

[11] P. M. Sheridan, M. J. Dick, J.-G. Wang and P. F. Bernath, J. Mol. Spectrosc. **233**, 278 (2005).

[12] P. M. Sheridan, M. J. Dick, J.-G. Wang and P. F. Bernath, Mol. Phys. **105** 569 (2007).

[13] S. Yu, J.-G. Wang, P. M. Sheridan, M. J. Dick and P. F. Bernath, Paper 23a, Symposium on Chemical Physics, Waterloo, ON, 3-5 November 2006.

[14] J.-G. Wang, P. M. Sheridan, M. J. Dick and P. F. Bernath, J. Mol. Spectrosc. **236**, 21 (2006).

[15] J.-G. Wang, P. M. Sheridan, M. J. Dick, S. Yu and P. F. Bernath, J. Mol. Spectrosc. (2007) (submitted).

[16] S. Yu, J.-G. Wang, P. M. Sheridan, M. J. Dick and P. F., J. Mol. Spectrosc. **240** 14 (2006).

[17] P. M. Sheridan, J.-G. Wang, M. J. Dick, S. Yu and P. F. Bernath, Paper RH03, 61st International Symposium on Molecular Spectroscopy, Columbus, OH, 19-23 June 2006.

Chapter 2 - Theory

A full understanding of molecular spectroscopy [1-5] requires an extensive knowledge of physics including, but not limited to, classical and quantum mechanics, electromagnetism and statistical thermodynamics. It is therefore not possible to cover all of molecular spectroscopy in a single chapter of a thesis. Instead this chapter will serve to outline and describe some of the theory most relevant to the spectroscopy of calcium and strontium containing polyatomic molecules. This will include an overview of the Born-Oppenheimer approximation and a discussion of the calculation of electronic energies via ligand field theory. The rotational and electronic energy level structure for both linear and symmetric top molecules will also be described, including descriptions of the spin-orbit, spin-rotation, Λ-doubling and Jahn-Teller interactions.

In this chapter, the following labeling convention will be employed; vectors are represented in bold type (e.g.. **J**) , operators have a ^ (e.g.. $\hat{\mathrm{H}}$) (vector operators are represented by only a ^), while both quantum numbers and molecular parameters are in italics (e.g. *Σ* and *B*).

2.1 The Schrödinger Equation and the Born-Oppenheimer Approximation

To fully understand any system, the total energy must be derived. To determine the energy, the Schrödinger equation must be solved,

$$\hat{\mathrm{H}}\psi = E\psi \tag{2.1}$$

in which, $\hat{H}$ is the Hamiltonian operator, ψ is the system's wavefunction, and E is the energy of the system. The Hamiltonian is an operator which describes the energy (both kinetic (T) and potential (V)) of a system in terms of the position ($\hat{x} = x$) and momentum ($\hat{p}_x = -i\hbar\frac{\partial}{\partial x}$) operators. The energy of the system can be obtained by sandwiching $\hat{H}$ between the wavefunction and its complex conjugate and integrating the resulting expression [1]:

$$E = \int \psi^* \hat{H} \psi d\tau \qquad (2.2)$$

Unfortunately, this integral is very difficult to solve for a molecular system due to the difficulty in obtaining an accurate wavefunction by solution of equation 2.1.

The non relativistic Hamiltonian is given by [1]

$$\hat{H} = \hat{T}_N + \hat{T}_e + \hat{V}_{NN} + \hat{V}_{eN} + \hat{V}_{ee} \qquad (2.3)$$

in which, $\hat{T}_N$ and $\hat{T}_e$ describe the kinetic energy of the nuclei and electrons, respectively. $\hat{V}_{NN}$ is the nuclear-nuclear repulsion energy, $\hat{V}_{eN}$ is the electron-nuclear attraction energy, and $\hat{V}_{ee}$ is the electron-electron repulsion energy. In order to solve equation 2.1, further approximations must be made.

The first approximation, known as the Born-Oppenheimer approximation, takes advantage of the fact that the electrons are much lighter than the nuclei. This, coupled with the fact that the magnitude of all the potential energy terms in the molecular Hamiltonian are approximately equal (i.e. electrons and nuclei experience similar forces), indicates that the electrons move much faster than the nuclei. As a result, the nuclei can be considered as stationary on the time scale of the electronic motion. This has two consequences which simplify the molecular Hamiltonian [1]. Firstly, the nuclear kinetic energy term ($\hat{\mathrm{T}}_{\mathrm{N}}$) in the molecular Hamiltonian becomes zero if the nuclei are "clamped". Secondly, the nuclear-nuclear repulsion ($\hat{\mathrm{V}}_{\mathrm{NN}}$) term becomes a constant if the nuclear positions are fixed. Using this approximation, the molecular Hamiltonian can then be separated into contributions from electronic and nuclear motion and gives

$$E_{total} = E_{Electronic} + E_{Nuclear} \tag{2.4}$$

In order to obtain $E_{Nuclear}$, the vibration-rotation Schrödinger equation must be solved for nuclear motion. In this equation the solution to the electronic energy ($E_{Electronic}$) appears as the potential energy function along with the nuclear kinetic energy term that was deleted from Equation 2.3 when applying the Born-Oppenheimer approximation to give the electronic Hamiltonian. In order to solve the vibration-rotation Schrödinger equation a second approximation can be invoked to further simplify the Hamiltonian by separating the rotational and vibrational motions within a molecule. If it is assumed that the vibrational motion occurs much faster then the rotational motion, then these two motions can also be separated, much as the nuclear motion was separated from the electronic motion in the Born-Oppenheimer approximation. This yields,

$$E_{total} = E_{Electronic} + E_{Nuclear} = E_{Electronic} + E_{Vibration} + E_{Rotation} \tag{2.5}$$

Having now dissected the molecular Hamiltonian into contributions from electronic, vibrational and rotational motions, calculation of the energies from each of these motions can be discussed separately. The majority of the remainder of this chapter will outline the electronic and rotational energy level patterns. As only the lowest vibrational level was observed in each of the electronic states studied in this thesis, no discussion of vibrational energies will be included.

2.2 Electronic Energy and Ligand Field Theory

Even when separated from the vibration and rotation of a molecule, an exact solution to the Schrödinger equation for the electronic energy is still very difficult to obtain. Many theoretical techniques have been applied to derive electronic energies. One approach, which has proven very effective in calculating the electronic energy of alkaline earth containing molecules, is ligand field theory. This method was first employed to describe the spectroscopic properties of gas phase molecules by Rice, Martin and Field [6] in their work on calcium monohalides and was later applied to many other systems, including the alkaline earth [7] and lanthanide monohalides [8]. Although ligand field theory is a quantitative method, only the more qualitative results will be applied to the work in this thesis.

Briefly, ligand field theory postulates that the electronic structure and properties of an alkaline earth containing molecule can be derived as a perturbation of the valence electron structure of the alkaline earth ion (Ca^+ or Sr^+ in this thesis) by a negatively charged ligand. Mathematically, this translates to the following Hamiltonian [6], which can be solved through the use of perturbation theory,

$$\hat{H} = \hat{H}^{(0)} + \hat{H}^{(1)} = \hat{H}_{M^{2+}} + \hat{H}_{LF} \tag{2.6}$$

in which $\hat{H}_{M^{2+}}$ describes the energy of the free ion and $\hat{H}_{LF}$ describes the interaction of the single valence electron on the M^{2+} ion with the negatively charged ligand treated as a point charge fixed at the internuclear separation. The electronic energy level structure predicted by this Hamiltonian can be qualitatively described by considering the three effects $\hat{H}_{LF}$ has on the free ion energy levels [6].

1) It rearranges the energy levels of the atomic ion orbitals.

2) It lifts the degeneracy of the $n\ell$ atomic orbitals by splitting them into m_ℓ components. For example a 4*p* atomic orbital will be split into 4*pσ* ($m_\ell = 0$) and 4*pπ* ($m_\ell = 1$) components.

3) It allows orbitals of the same m_ℓ to mix. For example a 3*dσ* and a 4*pσ* components can mix.

(1), (2) and (3) all play a role in determining the electronic state energy. However, the third effect has the greatest effect on the parameters for a given state, because this term gives rise to molecular electronic states that are a mixture of atomic orbitals, and hence the molecular parameters will reflect this mixing. For example if a state is comprised predominantly of very diffuse atomic orbitals, the ligand will be able to approach the M^{2+} ion closely, resulting in a small metal-ligand separation for that state. This method of interpreting the molecular parameters for an electronic state as a reflection of the atomic orbitals from which the state arises will be used throughout this thesis.

Figure 2.1 shows more specifically how $\hat{H}_{LF}$ transforms the low lying free ion energy levels of Ca^+ and Sr^+ into electronic states for molecules of $C_{\infty v}$ and C_{3v} symmetry. As can be seen in this figure, the three lowest lying electronic states of these molecules are derived primarily from atomic orbitals of *s*, *p* and *d* character (4*s*, 4*p* and 3*d* for calcium and 5*s*, 5*p* and 4*d* for strontium). The ground electronic states ($\tilde{X}^2\Sigma^+$ ($C_{\infty v}$) and $\tilde{X}^2A_1$ (C_{3v})) arise almost exclusively from the 4*sσ* and 5*sσ* atomic orbitals of calcium and strontium, respectively. In contrast, the atomic orbital character of the first excited states ($\tilde{A}^2\Pi$ ($C_{\infty v}$) and $\tilde{A}^2E$ (C_{3v})) is not quite as a simple as the ground states.

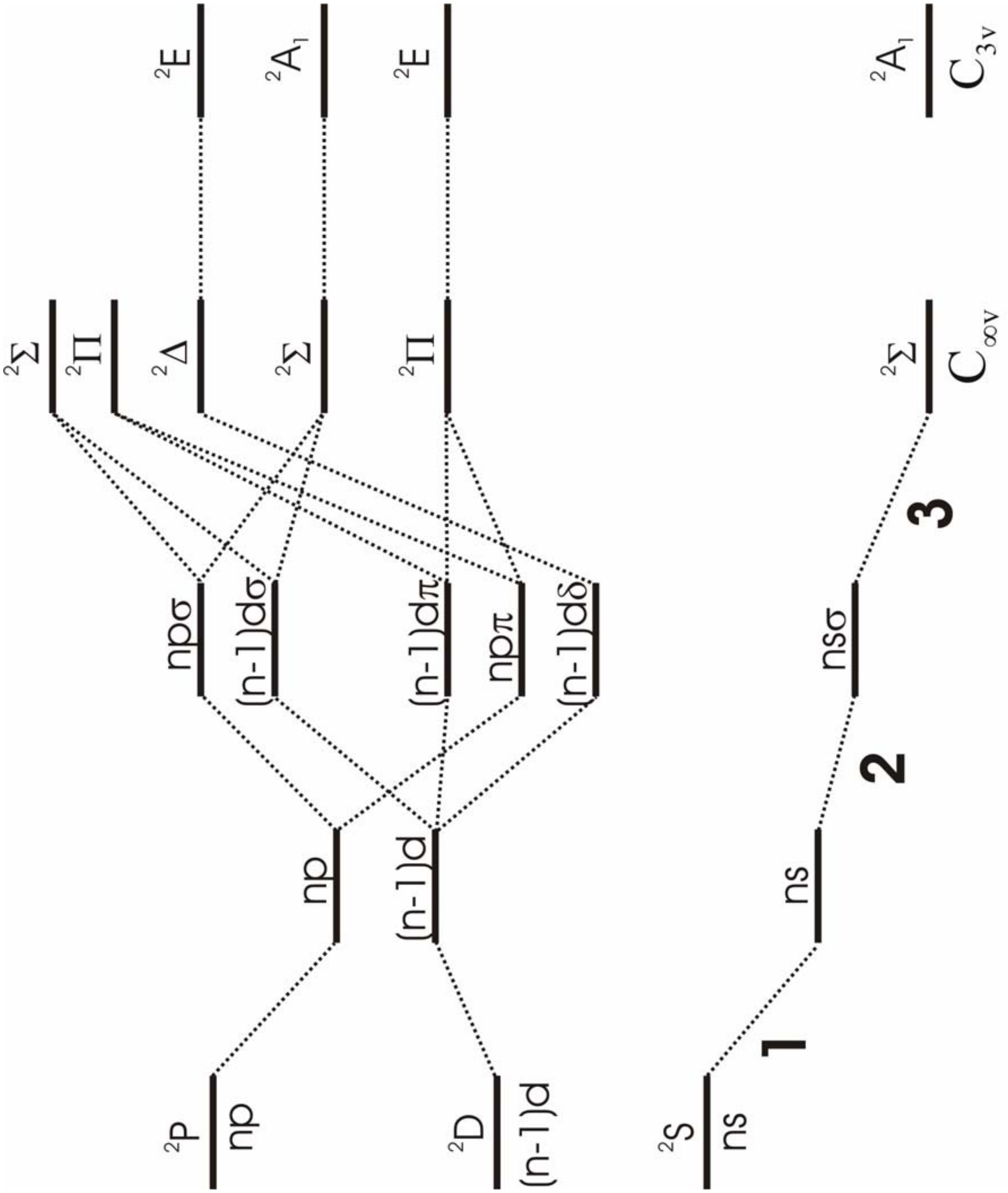

Figure 2.1 – Ligand Field Therory Predictions for Calcium and Strontium Containing Molecules.

As can be seen in figure 2.1 these states are composed of a mix of *pπ* and *dπ* atomic orbitals.

As outlined in chapter 1, the majority of the work presented in this thesis has concentrated on characterizing the low lying electronic states of calcium and strontium containing molecules. Figure 2.1 shows the identity of these low lying electronic states. For the molecules of $C_{\infty v}$ symmetry studied here (CaOH and SrCCH) the lowest lying states are of ${}^2\Pi$ and ${}^2\Sigma^+$ character, while for the molecules of C_{3v} symmetry studied here ($CaCH_3$, $SrCH_3$, $CaBH_4$ and $SrBH_4$), the lowest lying states are of ${}^2E$ and ${}^2A_1$ character. The remainder of this chapter will concentrate on describing the rotational and fine structure energy level patterns for these low lying states. The allowed transitions between these states will also be outlined.

2.3 Rotational Structure of Linear and Symmetric Top Molecules

2.3.1 Rotational Hamiltonian

Classically, the rotational kinetic energy for a rigid rotating body can be expressed as [1]

$$T = \frac{1}{2}I_x\omega_x^2 + \frac{1}{2}I_y\omega_y^2 + \frac{1}{2}I_z\omega_z^2 \tag{2.7}$$

where I_i and ω_i are the moment of inertia and angular frequency about the ith principal axis, respectively. This equation may then be simplified using the expression for total rotational angular momentum $J_i = I_i\omega_i$,

$$T = \frac{J_x^2}{2I_x} + \frac{J_y^2}{2I_y} + \frac{J_z^2}{2I_z}. \tag{2.8}$$

The rotational Hamiltonian can therefore be expressed as

$$\hat{H} = \frac{\hat{J}_x^2}{2I_x} + \frac{\hat{J}_y^2}{2I_y} + \frac{\hat{J}_z^2}{2I_z} \quad . \tag{2.9}$$

This Hamiltonian can be used to derive the rotational energy level structure for any rigid rotating body and will now be applied to linear and symmetric top molecules.

2.3.2 Rotational Energy Expression for a Linear Molecule

For a linear molecule, there is no rotational angular momentum about the *z* axis (i.e., $J_z = 0$) and the moments of inertia about the x and y axis are equal ($I_x = I_y = I$). Equation 2.9 can thus be simplified [1],

$$\hat{H} = \frac{\hat{J}_x^2}{2I} + \frac{\hat{J}_y^2}{2I} = \frac{1}{2I}(\hat{J}_x^2 + \hat{J}_y^2) = \frac{1}{2I}\hat{J}^2 . \tag{2.10}$$

When this Hamiltonian is introduced into the Schrödinger equation (equation 2.1) it can be shown that the resulting wavefunctions are the spherical harmonics and the following expression for the rotational energy levels of a linear molecule can be derived [4]:

$$E_{Rot} = \frac{h^2}{8\pi^2 I} J(J+1) = BJ(J+1) , \tag{2.11}$$

where h is Planck's constant and *J* is the rotational angular momentum quantum number.

2.3.3 Rotational Energy Expression for a Prolate Symmetric Top Molecule

For a non-linear molecule, the rotational angular momenta about all three axes (x,y,z) are non zero, and the moment of inertia associated with each of these axes can be different. To help distinguish between the three axes, the following labeling scheme was adopted. The axis with the smallest moment of inertia is termed as the *a*-axis and its moment of inertia is labeled as I_A. The axis with the largest moment of inertia is labeled as the *c*-axis and its moment of inertia is labeled as I_C. The remaining axis is therefore labeled as the *b*-axis and its moment of inertia is labeled as I_B [1]. This labeling scheme can be applied to the rotational Hamiltonian of equation 2.9 yielding,

$$\hat{H} = \frac{\hat{J}_a^2}{2I_A} + \frac{\hat{J}_b^2}{2I_B} + \frac{\hat{J}_c^2}{2I_C}. \tag{2.12}$$

For a symmetric top molecule, two of the three moments of inertia are equal and the above expression can be simplified. Specifically, for a prolate symmetric top molecule, $I_A < I_B = I_C$ and this Hamiltonian can be reduced as follows [1],

$$\hat{H} = \frac{\hat{J}_a^2}{2I_A} + \frac{\hat{J}_b^2}{2I_B} + \frac{\hat{J}_c^2}{2I_C} = \frac{\hat{J}_a^2}{2I_A} + \frac{1}{2I_B}(\hat{J}_b^2 + \hat{J}_c^2)$$

$$= \frac{\hat{J}_a^2}{2I_A} + \frac{1}{2I_B}(\hat{J}^2 - \hat{J}_a^2) = \frac{\hat{J}^2}{2I_B} + (\frac{1}{2I_A} - \frac{1}{2I_B})\hat{J}_a^2 \tag{2.13}$$

where the expressions $I_B = I_C$ and $\hat{J}^2 = \hat{J}_a^2 + \hat{J}_b^2 + \hat{J}_c^2$ where employed. All of the non-linear molecules studied in this thesis are prolate symmetric tops.

When the Schrödinger equation is solved using this Hamiltonian, the following expression for the rotational energy levels of a prolate symmetric top molecule is derived [4]:

$$E_{Rot} = \frac{h^2}{8\pi^2 I_B} J(J+1) + (\frac{h^2}{8\pi^2 I_A} - \frac{h^2}{8\pi^2 I_B}) K^2 = BJ(J+1) + (A-B)K^2, \tag{2.14}$$

where J is again the rotational angular momentum quantum number and K is the quantum number corresponding to the projection of the rotational angular momentum on the symmetry axis.

2.3.4 Centrifugal Distortion

The rotational energy expressions derived above for both the linear and prolate symmetric tops are valid as long as the rigid rotor assumption holds. Molecules are not rigid rotors, as chemical bonds are not like solid bars but are more like springs which stretch due to centrifugal distortion as the rotation of the molecule increases. To account for this distortion, other terms must be added to the above energy expressions. For example, for a linear molecule the rotational energy expression becomes [2]

$$E_J = BJ(J+1) - D[J(J+1)]^2 + \ldots \tag{2.15}$$

where D is the centrifugal distortion constant. For symmetric top molecules the effect of centrifugal distortion about each of the axes of rotation must be considered, which quickly complicates the rotational energy level expressions. Luckily, the centrifugal distortion constants, are several orders of magnitude smaller than their respective rotational constants and thus the effect of centrifugal distortion only needs to be considered for rotational levels with high values of J. As will be explained in the next chapter, the majority of the spectra recorded for this thesis included transitions only between rotational levels of low J. Therefore, the energy level pattern for the majority of the electronic states studied in this thesis could be described without the inclusion of centrifugal distortion terms so further discussion is not warranted.

2.4 Coupling of Rotational and Electronic Motion

If molecules were truly rigid rotors and rotation were the only motion that needed to be considered, the energy of linear and symmetric top molecules would be fully described by equations 2.11 and 2.14. However, as one delves deeper into the internal motion of molecules, it quickly becomes apparent that many interactions must be accounted for in order to describe fully the energy level pattern. Chief amongst these is the coupling of the rotational and electronic motions. Molecules are comprised of negatively charged electrons and positively charged nuclei. As these particles rotate, internal electric and magnetic fields are created which can play a role in determining the energy level structure of a molecule.

These interactions may be described by considering the coupling of the various angular momenta in a molecule. Angular momenta are very important in characterizing electronic states. In fact, states are often labeled based on the amount of intrinsic angular momentum the electrons within that state have.

2.4.1 Labeling of Electronic States

The various angular momenta (ignoring vibration and nuclear spin) in both linear and symmetric top molecules are listed below.

<u>Linear Molecule</u>:

L	Total electronic orbital angular momentum
$\Lambda\hbar$	Projection of **L** onto the symmetry axis
S	Total electron spin angular momentum
$\Sigma\hbar$	Projection of **S** onto the symmetry axis
R	Total nuclear rotation angular momentum
J	Total angular momentum (rotational, orbital and electron spin)
$\Omega\hbar$	Projection of **J** onto the symmetry axis

<u>Symmetric Top Molecule</u>:

L	Total electronic orbital angular momentum
$\zeta_e\hbar$	Projection of **L** onto the symmetry axis
S	Total electron spin angular momentum
$\Sigma\hbar$	Projection of **S** onto the symmetry axis
R	Total nuclear rotation angular momentum
$K_R\hbar$	Projection of **R** onto the symmetry axis

$K\hbar$	$K_R + \zeta_e$
J	Total angular momentum (rotational, orbital and electron spin)
$P\hbar$	Projection of **J** onto the symmetry axis

These angular momenta are then used to label electronic states as,

$$^{2S+1}\Lambda_{\Omega} \text{ (Linear Molecule)}$$

$$^{2S+1}A_{P} \text{ (Symmetric Top Molecule)}$$

For linear molecules ($C_{\infty v}$), it is customary to represent the values of Λ as upper case Greek letters (i.e. $\Lambda = 0, 1, 2, 3, 4$ correspond to Σ, Π, Δ, Φ and Γ states, respectively). For example, a $^2\Pi_{3/2}$ electronic state would have $S = 1/2$, $\Omega = 3/2$ and $\Lambda = 1$.

In the symmetric top case, A is the symbol for the irreducible representation that the electronic state belongs to. For molecules of C_{3v} symmetry, the electronic states are labeled as A_1, A_2 or E. For example, a $^2E_{3/2}$ electronic state would have $S = 1/2$, $P = 3/2$ and have a two-fold orbital degeneracy.

2.4.2 Hund's Coupling Cases

The way the angular momenta in a molecule couple can be used to classify electronic states. The various coupling cases were first considered by F. Hund, and are known as Hund's coupling cases.

Hund's Case (a)

In this coupling case the electronic orbital and electron spin angular momenta (**L** and **S**) couple most strongly to the symmetry axis of the molecule and precess rapidly. The projections of these angular momenta (Λ or ζ_e and Σ) then couple with the rotational angular momentum (**R**) to give **J,** the total angular momentum. This coupling scheme is summarized in Figure 2.2 for both linear [4] and symmetric top molecules [9].

The main difference between this coupling scheme for linear and symmetric top molecules is that for symmetric top molecules **R** does not necessarily point perpendicular to the symmetry axis. This is a result of the symmetric tops having three axes of rotation, and hence three vector components of **R** (R_x, R_y and R_z). When added together, the resulting angular momentum (**R**) does not necessarily point perpendicular to the symmetry axis. In contrast, the total rotational angular momentum of a linear molecule has only two components (R_x and R_y), and always points perpendicular to the symmetry axis. As a result, the nuclear rotation angular momentum of a symmetric top can have a non-zero projection onto the symmetry axis (K_R), and it must also be considered in deriving energy level expressions.

Hund's Case (b)

In this case the electronic orbital angular momentum is still coupled strongly to the symmetry axis. However, the electron spin angular momentum has decoupled from this axis and it is now more strongly coupled to the nuclear rotation angular momentum. The vector diagrams for this coupling scheme for both linear and symmetric top molecules can be found in Figure 2.3. Again, the main difference between this scheme for linear molecules as compared to symmetric tops is that **R** no longer necessarily points perpendicular to the symmetry axis for the symmetric top. Again, as in Hund's case (a), **R** has a projection onto the symmetry axis which must be considered in deriving the energy level expressions.

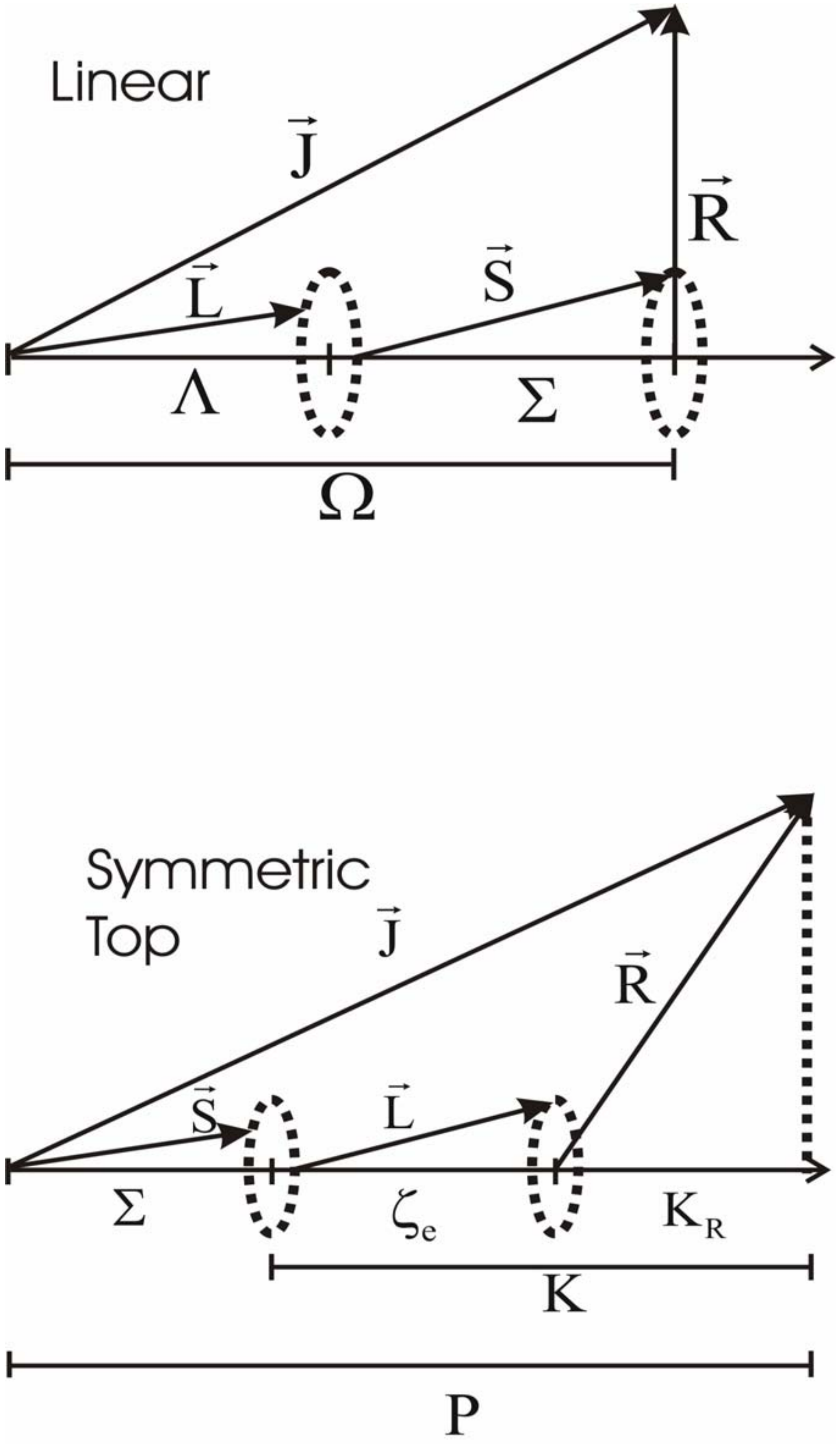

Figure 2.2 – Hund’s Case (a) Coupling Scheme for Linear and Symmetric Top Molecules

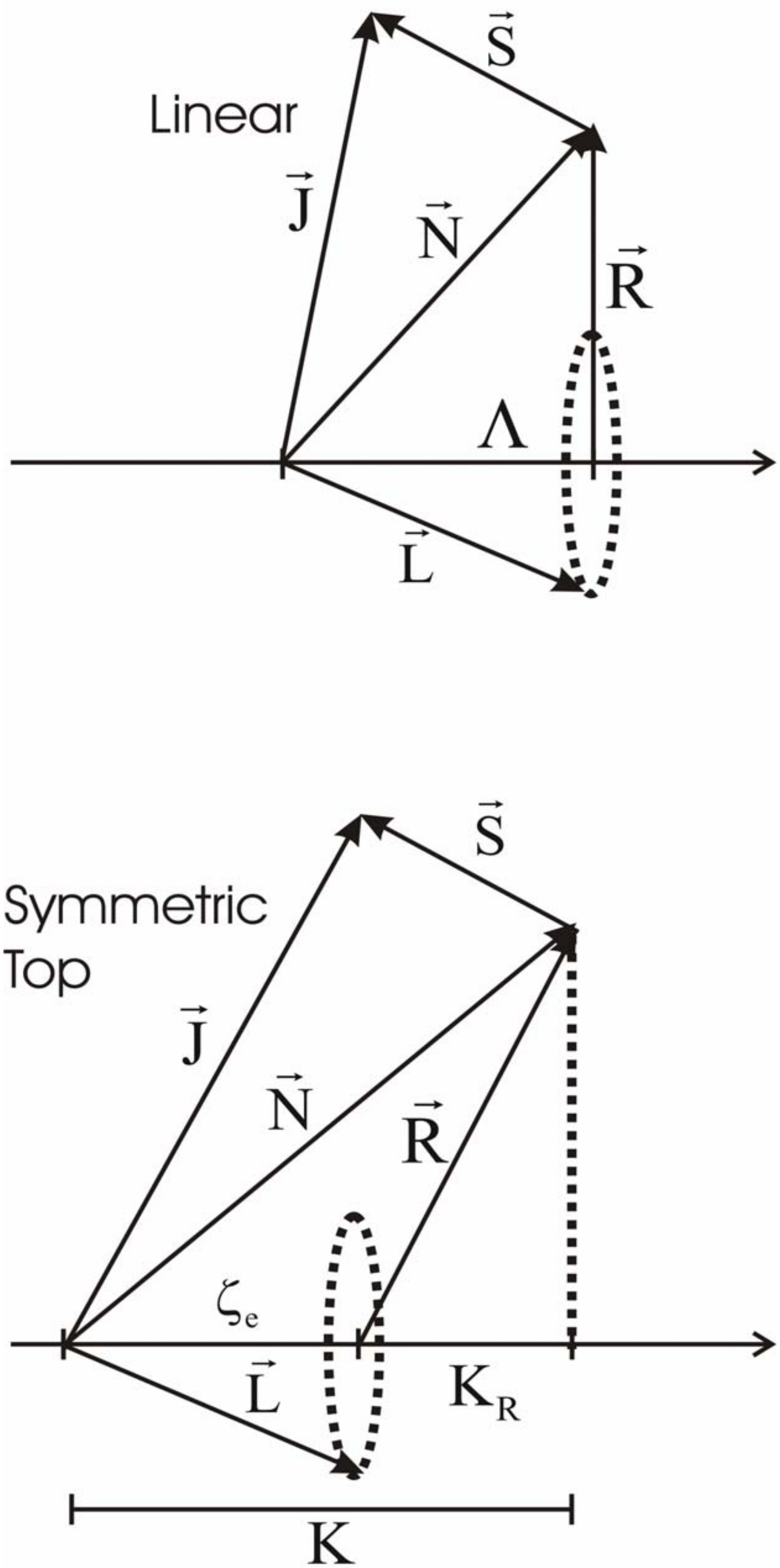

Figure 2.3 – Hund’s Case (b) Coupling Scheme for Linear and Symmetric Top Molecules

2.4.3 Modification of Rotational Energy Expressions

The previous two sections have outlined the various angular momenta in a molecule and have described the ways in which they can couple. How does the coupling of rotational and electronic motion affect the rotational energy expressions derived above (equations 2.11 and 2.14)? As was seen in the vector coupling diagrams (Figures 2.2 and 2.3), **J** is no longer the angular momentum of just nuclear rotation. **J** is now the total angular momentum and contains contributions from nuclear rotation (**R**), electronic orbital motion (**L**) and electron spin (**S**). Therefore, in order for the above rotational Hamiltonians to be valid, **J** must be replaced by **R**:

$$\hat{H} = \frac{1}{2I}(\hat{J}_x^2 + \hat{J}_y^2) \rightarrow \frac{1}{2I}(\hat{R}_x^2 + \hat{R}_y^2) = \frac{1}{2I}\hat{R}^2 \text{ (linear)} \qquad (2.16)$$

$$\hat{H} = \frac{\hat{J}^2}{2I_B} + (\frac{1}{2I_A} - \frac{1}{2I_B})\hat{J}_a^2 \rightarrow \frac{\hat{R}^2}{2I_B} + (\frac{1}{2I_A} - \frac{1}{2I_B})\hat{R}_a^2 \text{ (prolate symmetric top)}$$

(2.17)

The total angular momentum can be reintroduced into these equations by expressing **R** in terms of **J**, **L** and **S** (i.e. **R** = **J** – **L** – **S**). This reworking of the above Hamiltonians introduces new and important terms arising from the coupling of angular momenta into the rotational energy expressions. For example for a linear molecule [10],

$$\hat{H} = \frac{1}{2I}(\hat{R}_x^2 + \hat{R}_y^2) = B[(\hat{J}_x - \hat{L}_x - \hat{S}_x)^2 + (\hat{J}_y - \hat{L}_y - \hat{S}_y)^2] \qquad (2.18)$$

$$= B[(\hat{J}_x^2 + \hat{J}_y^2) + (\hat{L}_x^2 + \hat{L}_y^2) + (\hat{S}_x^2 + \hat{S}_y^2) - (\hat{J}_x\hat{L}_x + \hat{L}_x\hat{J}_x + \hat{J}_y\hat{L}_y + \hat{L}_y\hat{J}_y)]$$

$$- B[\hat{J}_x\hat{S}_x + \hat{S}_x\hat{J}_x + \hat{J}_y\hat{S}_y + \hat{S}_y\hat{J}_y) + (\hat{L}_x\hat{S}_x + \hat{S}_x\hat{L}_x + \hat{L}_y\hat{S}_y + \hat{S}_y\hat{L}_y)]$$

$$\hat{H} = B(\hat{J}^2 - \hat{J}_z^2) + B(\hat{L}^2 - \hat{L}_z^2) + B(\hat{S}^2 - \hat{S}_z^2) + B(\hat{L}_+\hat{S}_- + \hat{L}_-\hat{S}_+) \qquad (2.19)$$

$$-B(\hat{J}_+\hat{L}_- + \hat{J}_-\hat{L}_+) - B(\hat{J}_+\hat{S}_- + \hat{J}_-\hat{S}_+)$$

where $\hat{J}_x$ and $\hat{J}_y$ were written in terms of the raising and lowering operators $\hat{J}_+$ and $\hat{J}_-$,

$$\hat{J}_x = \frac{\hat{J}_+ + \hat{J}_-}{2} \tag{2.20}$$

$$\hat{J}_y = \frac{\hat{J}_+ - \hat{J}_-}{2i}. \tag{2.21}$$

Similarly, $\hat{L}_x, \hat{L}_y, \hat{S}_x$ and $\hat{S}_y$ can be expressed in terms of raising and lowering operators.

The first three terms of equation 2.19 describe the rotational motion for the state in question. The next three terms arise from cross terms introduced when the expressions for $\hat{R}_x$ and $\hat{R}_y$ were expanded. Specifically, the fourth term describes an interaction of states of the same J and Ω, but different Λ and Σ, and as will be shown plays a role in Λ-doubling. The fifth and sixth terms describe the uncoupling of the electronic and electron spin angular momenta from the symmetry axis as the rotation of the molecules increases [10].

A similar expression for the rotational Hamiltonian of a prolate symmetric top can also be derived by modifying equation 2.13 by expressing the rotational angular momentum in terms of **J**, **L** and **S**, (i.e. **R** = **J** – **L** – **S** and $R_a = J_a - L_a - S_a$) [9]

$$\hat{H} = B(\hat{J} - \hat{L} - \hat{S})^2 + (A\text{-}B)(\hat{J}_a - \hat{L}_a - \hat{S}_a)^2. \tag{2.22}$$

2.5 The Spin-Orbit and Spin-Rotation Interactions

The coupling of angular momenta and the resulting Hund's coupling cases have a physical significance which will be outlined in this section.

2.5.1 The Spin-Orbit Interaction

Due to the strong electric fields in a molecule, the electrons tend to orbit around the symmetry axis, which results in a strong interaction of **L** with this axis. This orbital precession also creates a magnetic field along the symmetry axis which interacts with the spin of the orbiting electrons. This effect is known as the spin-orbit interaction, and couples the electron spin angular momentum to the symmetry axis [4]. Electronic states with large spin-orbit interactions are classified as Hund's case (a).

The spin-orbit Hamiltonian can be expressed as the scalar product of the electronic and electron spin angular momenta [10]:

$$\hat{\mathrm{H}}_{\mathrm{SO}} = A_{SO}\,\hat{\mathbf{L}}\cdot\hat{\mathbf{S}} = A_{SO}\left(\frac{1}{2}(\hat{\mathrm{L}}_{+}\hat{\mathrm{S}}_{-} + \hat{\mathrm{L}}_{-}\hat{\mathrm{S}}_{+}) + \hat{\mathrm{L}}_{z}\hat{\mathrm{S}}_{z}\right) \text{ (linear molecule)} \tag{2.23}$$

$$\hat{\mathrm{H}}_{\mathrm{SO}} = a\,\hat{\mathbf{L}}\cdot\hat{\mathbf{S}} = a\left(\frac{1}{2}(\hat{\mathrm{L}}_{+}\hat{\mathrm{S}}_{-} + \hat{\mathrm{L}}_{-}\hat{\mathrm{S}}_{+}) + \hat{\mathrm{L}}_{z}\hat{\mathrm{S}}_{z}\right) \text{ (symmetric top molecule).} \tag{2.24}$$

A_{SO} and a are the spin-orbit coupling constants for linear and non-linear molecules, respectively. Only the $\hat{\mathrm{L}}_{z}\hat{\mathrm{S}}_{z}$ term will contribute directly to the energy of a Hund's case (a) electronic state. As mentioned in the last section, terms of the $\hat{\mathrm{L}}_{+}\hat{\mathrm{S}}_{-}$ and $\hat{\mathrm{L}}_{-}\hat{\mathrm{S}}_{+}$ type describe an interaction of rotational levels of the same J and Ω but different Λ and Σ, and play a role in Λ-doubling. However, if the case (a) state is considered to be isolated, these terms do not contribute and the following energy expressions for the spin-orbit splitting are derived from the $\hat{L}_z\hat{S}_z$ term,

$$E_{SO} = A_{SO}\,\Lambda\Sigma \text{ (linear molecule)} \tag{2.25}$$

$$E_{SO} = a\zeta_e\Sigma \text{ (symmetric top molecule).} \tag{2.26}$$

Since the projection of the electron spin onto the symmetry axis (Σ) has $2S+1$ values, these energy expressions split the electronic states into $2S+1$ spin-orbit components.

2.5.2 The Spin-Rotation Interaction

In some molecules the magnetic field along the symmetry axis created by the orbital motion of the electrons is not strong enough to couple the electron spin to it. This is most prevalent in states where the electronic angular momentum is zero (i.e. Σ states). However, in lighter molecules where the electric field along the symmetry axis is weak, this may also occur [11]. In these cases the electron spin is free to interact with another magnetic field. As shown in Figure 2.3, one possibility is for the electron spin to interact with the magnetic field created by the rotation of the nuclei. This results in the coupling of the rotational and electron spin angular momenta and is known as the spin-rotation interaction. Electronic states where the spin-rotation interaction dominates are generally Hund's case (b) states.

The spin-rotation Hamiltonians for linear and symmetric top molecules are expressed as follows [10,12]:

$$\hat{H}_{SR} = \gamma\,\hat{N}\cdot\hat{S} \text{ (linear molecules)} \tag{2.27}$$

$$\hat{H}_{SR} = \varepsilon_{aa}\hat{N}_a\hat{S}_a + \varepsilon_{bb}\hat{N}_b\hat{S}_b + \varepsilon_{cc}\hat{N}_c\hat{S}_c \text{ (symmetric top molecules).} \tag{2.28}$$

γ is the spin-rotation parameter for a linear molecule. ε_{aa}, ε_{bb} and ε_{cc} are the spin-rotation parameters for a non-linear molecule and correspond to the interaction of the electron spin with rotation about each rotational axis.

Derivation of energy expressions for the spin-rotation energy is not as simple as for the spin-orbit interaction. However, for linear molecules it can be derived if the Hamiltonian is rewritten using the Hund's case (b) coupling equation $\mathbf{J} = \mathbf{N} + \mathbf{S}$ [10] and

$$\mathbf{J}^2 = \mathbf{N}^2 + \mathbf{S}^2 + 2\mathbf{N}\cdot\mathbf{S} \text{ so that } \mathbf{N}\cdot\mathbf{S} = \frac{1}{2}(\mathbf{J}^2 - \mathbf{N}^2 - \mathbf{S}^2) \tag{2.29}$$

Applying this equation, $\hat{\mathrm{H}}_{\mathrm{SR}}$ may be written as follows,

$$\hat{\mathrm{H}}_{\mathrm{SR}} = \gamma\hat{\mathrm{N}}\cdot\hat{\mathrm{S}} = \frac{1}{2}\gamma(\hat{\mathrm{J}}^2 - \hat{\mathrm{N}}^2 - \hat{\mathrm{S}}^2)\,. \tag{2.30}$$

From this equation the following energy expression for the spin-rotation interaction in a linear molecule is derived [10],

$$E_{SR} = \frac{1}{2}\gamma[J(J+1) - N(N+1) - S(S+1)]\,. \tag{2.31}$$

At first glance it appears that this equation should shift each rotational level by the same amount. However, if the coupling of **N** and **S** is considered, it is seen that these angular momenta can couple to give multiple values of J [3] for each value of N,

$$J = (N + S), (N+S-1)\ldots\ldots|N-S|. \tag{2.32}$$

Introducing these values of J into equation 2.31 results in different spin-rotation energies for each rotational level. For example when $S = 1/2$, two spin components are produced ($J = N\pm1/2$).

Similar expressions can be derived for the spin-rotation interactions of symmetric top molecules. However, no further discussion of these expressions will be undertaken here. This is justified because the contributions to the spin-rotation parameters from the "true" spin-rotation interaction are typically small. As will be shown, they are often dominated by contributions from interactions with other electronic states.

2.6 Parity

Before any further discussions on molecular interactions are undertaken, a short explanation of parity is warranted. A parity transformation is governed by an operator that acts on the coordinates in a wavefunction. The effect of such a transformation on a molecular wavefunction is of importance because it can be used to label the wavefunction. The most commonly considered parity in molecular spectroscopy is total parity, which is governed by the inversion operator ($\hat{E}^*$) in the laboratory coordinate system. This operator inverts all the coordinates of all the particles (electrons and nuclei) in a molecule. This inversion is described in the laboratory frame and is taken through an origin at the center of mass [1],

$$\hat{E}^*\psi(X_i, Y_i, Z_i) = \psi(-X_i, -Y_i, -Z_i) = \pm\psi(X_i, Y_i, Z_i). \tag{2.33}$$

If a wavefunction transforms according to the upper sign this state is said to have positive parity, while if it transforms according to the lower sign it is said to have negative parity. Positive and negative parity states in molecules often occur in degenerate pairs. However, as will be shown, many interactions can lift this degeneracy.

General expressions for a molecular state's total parity can be derived by considering the effect of the inversion operator on the electronic, vibrational and rotational wavefunctions separately (i.e. $\hat{E}^*(\psi_{el}\psi_{vib}\psi_{rot})$).

$\hat{E}^*$ leaves the vibrational wavefunction unchanged because ψ_{vib} is a function of the internuclear separations within a molecule, which are invariant upon operation of $\hat{E}^*$,

$$\hat{E}^*\psi_{vib} = \psi_{vib}. \tag{2.34}$$

Determining the effect of the inversion operator on the electronic and rotational wavefunctions is not quite as straightforward. ψ_{rot} for linear and symmetric top molecules can be represented by the symmetric top wavefunctions. It can be shown that when the inversion operator acts on these wavefunctions, the following expressions for total parity are obtained [13],

$$\hat{E}^*\psi_{rot} = (-1)^{J-\Omega}\psi_{rot} \text{ (linear)} \tag{2.35}$$

$$\hat{E}^*\psi_{rot} = (-1)^{J-P}\psi_{rot} \text{ (symmetric top).} \tag{2.36}$$

The effect of the inversion operator on ψ_{el} is the most difficult to ascertain. ψ_{el} is defined in the molecular frame, making the effect of $\hat{E}^*$ (which acts in the laboratory frame) not obvious. However, for a linear molecule it can be shown [13] that the inversion operation is equivalent to reflection through a plane of symmetry (σ_v) in the molecular frame. Using this fact the following expression for total parity can be derived,

$$\hat{E}^*\psi_{el} = \hat{\sigma}_v\psi_{el} = (-1)^{f(S,\Sigma,\Lambda)}\psi_{el} \tag{2.37}$$

in which f(S,Σ,Λ) is a function of quantum numbers S, Σ and Λ. A similar parity dependent expression can be defined for a symmetric top molecule,

$$\hat{E}^*\psi_{el} = (-1)^{f(S,\Sigma,K)}\psi_{el}, \tag{2.38}$$

where f(S,Σ,K) is a parameter which depends on the quantum numbers S, Σ and K.

Combining the expressions for the effect of the inversion operator on the electronic, vibrational and rotational wavefunctions, the following equations for total parity can be defined for linear and symmetric top molecules,

$$\hat{E}^{*}(\psi_{el}\psi_{vib}\psi_{rot}) = (-1)^{J+f(S,\Sigma,\Lambda,\Omega)}\psi_{el}\psi_{vib}\psi_{rot} \text{ (linear)} \quad (2.39)$$

$$\hat{E}^{*}(\psi_{el}\psi_{vib}\psi_{rot}) = (-1)^{J+f(S,\Sigma,K,P)}\psi_{el}\psi_{vib}\psi_{rot} \text{(symmetric top).} (2.40)$$

For a fixed electronic state all the quantum numbers except *J* are constant and the total parity is seen to alternate from one rotational level to the next according to $(-1)^J$. In fact it is often customary to factor out this dependence on *J* and label states with the rotationally independent *e*/*f* parity [1]:

$$\hat{E}^{*}(\psi_{el}\psi_{vib}\psi_{rot}) = +(-1)^{J}\psi_{el}\psi_{vib}\psi_{rot} \text{ for } e \text{ parity} \quad (2.41)$$

$$\hat{E}^{*}(\psi_{el}\psi_{vib}\psi_{rot}) = -(-1)^{J}\psi_{el}\psi_{vib}\psi_{rot} \text{ for } f \text{ parity.} \quad (2.42)$$

This *e*/*f* parity is a reflection of the intrinsic parity of a particular rotational level due to the coupling of the various angular momenta within the molecule. In addition, *e*/*f* symmetrized basis functions may be defined as a linear combination of the $+\Lambda$ and $-\Lambda$ wavefunctions [11]. For example for linear molecule the basis functions are defined as,

$$\psi_{e} = \frac{1}{\sqrt{2}}[\psi(+\Lambda)+\psi(-\Lambda)] \quad (2.43)$$

$$\psi_{f} = \frac{1}{\sqrt{2}}[\psi(+\Lambda)-\psi(-\Lambda)]. \quad (2.44)$$

2.7 Other Important Interactions

2.7.1 Λ-Doubling Interaction

As outlined in section 2.5.1, the electrons in a molecule tend to orbit about the symmetry axis, and this motion results in the projection of the electronic angular momentum onto this axis (Λ). The electrons are free to orbit either clockwise or counter clockwise around the axis, and these two directions of motion each result in a set of degenerate rotational levels of either *e* or *f* parity. The $B(\hat{\mathrm{L}}_+\hat{\mathrm{S}}_- + \hat{\mathrm{L}}_-\hat{\mathrm{S}}_+)$ and $B(\hat{\mathrm{J}}_+\hat{\mathrm{L}}_- + \hat{\mathrm{J}}_-\hat{\mathrm{L}}_+)$ rotational terms along with the $A(\frac{1}{2}(\hat{\mathrm{L}}_+\hat{\mathrm{S}}_- + \hat{\mathrm{L}}_-\hat{\mathrm{S}}_+))$ spin-orbit term can lift this degeneracy in an effect known as Λ-doubling.

In linear molecules, Λ-doubling is most commonly observed in Π states through an interaction with neighboring Σ states. In fact, Λ-doubling is most clearly understood if the interaction of a $^1\Pi$ state with a $^1\Sigma^+$ state is considered. It can be shown that a $^1\Sigma^+$ state has only *e* parity levels [13], and as a result, only the *e* parity levels of the neighboring $^1\Pi$ state will be affected by the interaction. For example, if the $^1\Sigma^+$ state is located at a lower energy then the $^1\Pi$ state, the *e* parity levels of the Π state will be pushed up by the interaction while the *f* parity levels will remain unaffected. This effect then lifts the *e*/*f* degeneracy in the $^1\Pi$ state. Λ-doubling can also be observed in states other than Π states. For instance, the effect of Λ-doubling is also observed in Σ states. In this case it is the result of the reverse interaction where the Π state now affects the Σ state through the interaction described above. For example, in a $^2\Sigma^+$ state, Λ-doubling can split each rotational level into two *e*/*f* parity components. The effect of Λ-doubling in both $^2\Pi$ and $^2\Sigma^+$ states will be discussed in more detail in section 2.8.

Λ-doubling is also present in symmetric top molecules. For molecules of C_{3v} symmetry it is most commonly observed in E states and is a result of an interaction with neighboring A_1 states. In the E state, the Λ-doubling is not considered as a separate interaction, but instead is interpreted as a new spin-rotation parameter. Also, as was the case for Σ states, the reverse effect of Λ-doubling is seen in the A_1 states. A more detailed description of Λ-doubling in ^2E and $^2A_1$ states will be given in section 2.9.

2.7.2 The Jahn-Teller Interaction

Another important interaction that must be considered for non-linear molecules is the Jahn-Teller effect. This effect is a result of the fact that any non-linear molecule in an orbitally degenerate electronic state will structurally distort to eliminate the orbital degeneracy [1]. This distortion occurs through the coupling of the vibrational and electronic motions. This interaction has not been considered in the above discussion on the coupling of the various angular momenta in a molecule. As a result, it has not been accounted for in the energy expressions for rotation or the spin-orbit, spin-rotation and Λ-doubling interactions. In order to account for this coupling, two modifications to the derivation of the above Hamiltonians must be considered.

1) The effect of vibrational angular momentum (**G**) must be accounted for along with the other angular momenta within a non-linear molecule (i.e. $\mathbf{J} = \mathbf{R} + \mathbf{L} + \mathbf{S} + \mathbf{G}$). This will introduce a new set of operators into the above Hamiltonians, such as $\hat{J}_x\hat{G}_x + \hat{J}_y\hat{G}_y$, $\hat{G}_z$ and $\hat{G}^2$.

2) Along with the electronic and rotational wavefunctions, the vibrational wavefunction must also be considered. For example, the spin-orbit energy expression would need to be modified slightly [9] so that,

$$E_{\mathrm{SO}} = a\zeta_e \Sigma d \qquad (2.45)$$

where d ($1>|d|>0$) is known as the Jahn-Teller quenching parameter, and is representative of the size of the Jahn-Teller interaction [14].

Brown [9] and Hougen [15] have considered these two modifications and derived the amended Hamiltonians for electronic states of ^{2}E symmetry.

The Jahn-Teller effect often competes with the spin-orbit interaction to lift the orbital degeneracy in electronic states. In fact, in states where the spin-orbit splitting is large the Jahn-Teller interaction is often quenched. This is best understood by considering equation 2.45. The magnitude of d ranges from 0 when the Jahn-Teller interaction is strong to 1 when it is weak. Thus, for a weak Jahn-Teller effect ($d \approx 1$) the spin-orbit energy may be written as follows:

$$E_{\mathrm{SO}} = a\zeta_e \Sigma d \approx a\zeta_e \Sigma \,. \qquad (2.46)$$

This expression is identical to equation 2.26 which was derived by neglecting the Jahn-Teller interaction completely. As will be shown, the orbitally degenerate states of the symmetric top molecules studied in this thesis all have large spin-orbit coupling, and hence a small Jahn-Teller effect. Therefore, the energy expressions derived before the inclusion of vibrational-electronic coupling are still valid as a first approximation.

2.8 Energy Level Structure for Linear Molecules

Having outlined the majority of the pertinent interactions and labeling schemes for linear and symmetric top molecules, the resultant energy level expressions can now be applied to derive the energy level structure of the low lying electronic states of calcium and strontium containing molecules. Much attention will be focused on deriving detailed energy level structure for the $^2\Pi$ and $^2\Sigma^+$ states. This structure will then be used as the basis for deriving the energy level patterns for the more complicated ^2E and $^2A_1$ states.

2.8.1 $^2\Pi$ states

The $^2\Pi$ states studied in this thesis all belong to the Hund's case (a) coupling scheme. As a result, along with rotation, the dominant interactions in these states are spin-orbit coupling and Λ-doubling. The total energy for these states can be derived from addition of the electronic energy (T_{el}) to the solution for the appropriate rotational Hamiltonian. In this case, the appropriate Hamiltonian is derived from equations 2.19 and 2.23, where the terms that give rise to Λ-doubling, outlined in section 2.7.1, are grouped together into $\hat{H}'$.

$$\hat{H}(^2\Pi) = \hat{H}_{Rot} + \hat{H}_{SO} + \hat{H}_{\Lambda D} \tag{2.47}$$

$$\hat{H}_{Rot} = B(\hat{J}^2 - \hat{J}_z^2) + B(\hat{L}^2 - \hat{L}_z^2) + B(\hat{S}^2 - \hat{S}_z^2) - B(\hat{J}_+\hat{S}_- + \hat{J}_-\hat{S}_+)$$

$$\hat{H}_{SO} = A(\hat{L}_z\hat{S}_z)$$

$$\hat{H}' = \frac{1}{2}A(\hat{L}_+\hat{S}_- + \hat{L}_-\hat{S}_+) + B(\hat{L}_+\hat{S}_- + \hat{L}_-\hat{S}_+) - B(\hat{J}_+\hat{L}_- + \hat{J}_-\hat{L}_+)$$

Rotational Energy

The second, third and $B\hat{\mathrm{J}}_z^2$ terms of $\hat{\mathrm{H}}_{\mathrm{rot}}$ are all constant for a given spin-orbit component, and can be included in the electronic energy (T_{el}). The last term results in an interaction of the two spin orbit components of a $^2\Pi$ state, and may be neglected for molecules in the Hund's case (a) coupling scheme. Thus, the only term of $\hat{\mathrm{H}}_{\mathrm{rot}}$ which contributes directly to the rotational energy of a $^2\Pi$ state is $B\hat{\mathrm{J}}^2$, which results in the following energy expression for the rotational energy.

$$E_{\mathrm{rot}}(^2\Pi) = BJ(J+1) \tag{2.48}$$

Spin-Orbit Energy

The energy for the two spin-orbit components of a $^2\Pi$ state can be derived from equation 2.25,

$$E_{SO}(^2\Pi_{1/2}) = A\Lambda\Sigma = A(1)(-\frac{1}{2}) = -\frac{1}{2}A \tag{2.49}$$

$$E_{SO}(^2\Pi_{3/2}) = A\Lambda\Sigma = A(1)(\frac{1}{2}) = \frac{1}{2}A\,. \tag{2.50}$$

Thus, before Λ-doubling is considered a $^2\Pi$ state must be approximated as two spin-orbit components separated by the spin-orbit splitting parameter, each with a rotational structure defined by $BJ(J+1)$.

Λ-doubling

As outlined in section 2.7.1, Λ-doubling results from an interaction between states of ΔΛ = ±1. In the case of a $^2\Pi$ state, Λ-doubling arises from an interaction with a $^2\Sigma^+$ state. The first ($\frac{1}{2}A(\hat{\mathrm{L}}_+\hat{\mathrm{S}}_- + \hat{\mathrm{L}}_-\hat{\mathrm{S}}_+)$) and second ($B(\hat{\mathrm{L}}_+\hat{\mathrm{S}}_- + \hat{\mathrm{L}}_-\hat{\mathrm{S}}_+)$) terms of $\hat{\mathrm{H}}'$ result in interactions between electronic states differing in Λ and Σ by ±1 ($\Delta\Omega = 0$), and hence only affect the $^2\Pi_{1/2}$ spin-orbit component ($^2\Pi_{1/2} \leftrightarrow {}^2\Sigma^+_{1/2}$). However, the third term ($B(\hat{\mathrm{J}}_+\hat{\mathrm{L}}_- + \hat{\mathrm{J}}_-\hat{\mathrm{L}}_+)$) causes an interaction between electronic states differing in Λ and Ω by ±1 and with $\Delta\Sigma = 0$. Therefore this term affects both the $^2\Pi_{1/2}$ and $^2\Pi_{3/2}$ spin-orbit components ($^2\Pi_{3/2} \leftrightarrow {}^2\Sigma^+_{1/2}$ and $^2\Pi_{1/2} \leftrightarrow {}^2\Sigma^+_{-1/2}$). This indicates that the Λ-doubling is larger in the $^2\Pi_{1/2}$ component as compared to the $^2\Pi_{3/2}$ spin-orbit component, as all three terms in $\hat{\mathrm{H}}'$ contribute to the Λ-doubling in the $^2\Pi_{1/2}$ component while only the $B(\hat{\mathrm{J}}_+\hat{\mathrm{L}}_- + \hat{\mathrm{J}}_-\hat{\mathrm{L}}_+)$ term supplies the doubling in the $^2\Pi_{3/2}$ component. The $\frac{1}{2}A\,(\hat{\mathrm{L}}_+\hat{\mathrm{S}}_- + \hat{\mathrm{L}}_-\hat{\mathrm{S}}_+)$ term is also larger in magnitude than the other two terms, because the spin-orbit coupling parameter is much bigger than the rotational constant for electronic states belonging to the Hund's case (a) coupling scheme.

Solving for the energy expressions for Λ-doubling can be done by considering the effect of each of the terms in $\hat{\mathrm{H}}'$ on the *e*/*f* symmetrized basis functions for both the $^2\Pi$ and $^2\Sigma^+$ states [10],

$$\psi({}^2\Pi_{1/2}(\tfrac{\mathrm{e}}{\mathrm{f}})) = \frac{1}{\sqrt{2}}[\psi({}^2\Pi_{1/2}) \pm \psi({}^2\Pi_{-1/2})] \qquad (2.51)$$

$$\psi({}^2\Pi_{3/2}(\tfrac{\mathrm{e}}{\mathrm{f}})) = \frac{1}{\sqrt{2}}[\psi({}^2\Pi_{3/2}) \pm \psi({}^2\Pi_{-3/2})] \qquad (2.52)$$

$$\psi({}^2\Sigma^+(\tfrac{\mathrm{e}}{\mathrm{f}})) = \frac{1}{\sqrt{2}}[\psi({}^2\Sigma^+_{1/2}) \pm \psi({}^2\Sigma^+_{-1/2})] \qquad (2.53)$$

Following this procedure the energy expressions for the *e*/*f* parity levels of each spin-orbit component of a $^2\Pi$ state can be derived [10] as,

$$E_{\Lambda D}({}^2\Pi_{1/2}(e)) = o + \frac{q}{2}(J-1/2)^2 - \frac{p}{2}(J-1/2) \tag{2.54}$$

$$E_{\Lambda D}({}^2\Pi_{1/2}(f)) = o + \frac{q}{2}(J+3/2)^2 + \frac{p}{2}(J+3/2) \tag{2.55}$$

$$E_{\Lambda D}({}^2\Pi_{3/2}(e)) = \frac{q}{2}(J-1/2)(J+3/2) - \frac{Bq}{A_{SO}}(J+1/2)[(J+1/2)^2-1] \tag{2.56}$$

$$E_{\Lambda D}({}^2\Pi_{3/2}(f)) = \frac{q}{2}(J-1/2)(J+3/2) + \frac{Bq}{A_{SO}}(J+1/2)[(J+1/2)^2-1]. \tag{2.57}$$

The *o*, *p* and *q* parameters are defined as follows (expressed in bra/ket notation).

$$o = \sum_{\left|{}^2\Sigma^+\right\rangle} \frac{\left\langle {}^2\Pi \middle| A_{SO}\hat{L}_+ \middle| {}^2\Sigma^+ \right\rangle^2}{4(E_{{}^2\Pi} - E_{{}^2\Sigma^+})} \tag{2.58}$$

$$p = \sum_{\left|{}^2\Sigma^+\right\rangle} \frac{2B\left\langle {}^2\Pi \middle| A_{SO}\hat{L}_+ \middle| {}^2\Sigma^+ \right\rangle \left\langle {}^2\Pi \middle| \hat{L}_+ \middle| {}^2\Sigma^+ \right\rangle}{(E_{{}^2\Pi} - E_{{}^2\Sigma^+})} \tag{2.59}$$

$$q = \sum_{\left|{}^2\Sigma^+\right\rangle} \frac{2B^2\left\langle {}^2\Pi \middle| \hat{L}_+ \middle| {}^2\Sigma^+ \right\rangle^2}{(E_{{}^2\Pi} - E_{{}^2\Sigma^+})}. \tag{2.60}$$

Taking the differences between equations 2.55 and 2.54 along with equations 2.57 and 2.56, the Λ-doubling (*e*/*f*) splittings can be calculated for both the ${}^2\Pi_{1/2}$ and ${}^2\Pi_{3/2}$ spin-orbit components as

$$\Delta E_{\Lambda D}({}^2\Pi_{1/2}(f-e)) = (p+2q)(J+1/2) \tag{2.61}$$

$$\Delta E_{\Lambda D}({}^2\Pi_{3/2}(f-e)) = \frac{2Bq}{A_{SO}}(J+1/2)[(J+1/2)^2-1]. \tag{2.62}$$

Total Energy:

In summary, a Hund's case (a) $^2\Pi$ state occurs as two spin-orbit components, each with a series of rotational levels. Each rotational level is then split into two *e*/*f* parity components by Λ-doubling [10], and approximate energy level expressions are,

$$E(^2\Pi_{1/2}(e)) = T_{el} - \frac{1}{2}A_{SO} + B_{1/2}J(J+1) + \frac{q}{2}(J-1/2)^2 - \frac{p}{2}(J-1/2) \qquad (2.63)$$

$$E(^2\Pi_{1/2}(f)) = T_{el} - \frac{1}{2}A_{SO} + B_{1/2}J(J+1) + \frac{q}{2}(J+3/2)^2 - \frac{p}{2}(J+3/2) \qquad (2.64)$$

$$\begin{aligned} E(^2\Pi_{3/2}(e)) &= T_{el} + \frac{1}{2}A_{SO} + B_{3/2}J(J+1) \\ &+ \frac{q}{2}(J-1/2)(J+3/2) - \frac{B_{3/2}q}{A_{SO}}(J+1/2)[(J+1/2)^2-1] \end{aligned} \qquad (2.65)$$

$$\begin{aligned} E(^2\Pi_{3/2}(f)) &= T_{el} + \frac{1}{2}A_{SO} + B_{3/2}J(J+1) \\ &+ \frac{q}{2}(J-1/2)(J+3/2) + \frac{B_{3/2}q}{A_{SO}}(J+1/2)[(J+1/2)^2-1] \end{aligned} \qquad (2.66)$$

where *o* has been assimilated into T_{el}, and $B_{1/2}$ and $B_{3/2}$ are the rotational constants for the $^2\Pi_{1/2}$ and $^2\Pi_{3/2}$ spin-orbit components, respectively.

It should be noted that these expressions are only approximate energy level expressions for a Hund's case (a) $^2\Pi$ state derived by applying perturbation theory to the matrix which results when the Hamiltonian (equation 2.47) is evaluated with the appropriate basis functions. In order to determine the exact energies for a $^2\Pi$ state, the full matrix must be diagonalized. It should be noted however that the Hamiltonian used in the fitting of the experimental transition data measured in this thesis is slightly different then that described above. For the fitting the Hamiltonian of Brown [16] was employed. This effective Hamiltonian has been simplified by elimination of several small terms and the resulting energy level expressions differ slightly from those derived above. For instance the term yielding the *Λ*-doubling parameter, *o*, is not included in the Brown Hamiltonian rather than incorporating *o* it into T_{el} as above. Despite this difference, the approximate expressions derived above are still valid and are very useful for discussing the energy level patterns.

2.8.2 $^2\Sigma^+$ states

The $^2\Sigma^+$ states investigated in this thesis all belong to the Hund's case (b) coupling scheme. Therefore, along with rotation, the dominant interactions in these states are spin-rotation and Λ-doubling. As with $^2\Pi$ states, the total energy for $^2\Sigma^+$ states can be derived from addition of the electronic energy to the solution to the appropriate rotational Hamiltonian expressed in Hund's case (b) notation. The appropriate Hamiltonians were derived in sections 2.4.3, 2.5.2 and 2.7.1 are

$$\hat{\mathrm{H}}(^2\Sigma^+) = \hat{\mathrm{H}}_{\mathrm{Rot}} + \hat{\mathrm{H}}_{\mathrm{SR}} + \hat{\mathrm{H}}_{\Lambda\mathrm{D}} \tag{2.67}$$

$$\hat{\mathrm{H}}_{\mathrm{Rot}} = B(\hat{\mathrm{J}}^2 - \hat{\mathrm{J}}_z^2) + B(\hat{\mathrm{L}}^2 - \hat{\mathrm{L}}_z^2) - B(\hat{\mathrm{S}}^2 - \hat{\mathrm{S}}_z^2) - B(\hat{\mathrm{J}}_+\mathrm{S}_- + \hat{\mathrm{J}}_-\mathrm{S}_+)$$

$$\hat{\mathrm{H}}_{\mathrm{SR}} = \frac{1}{2}\gamma\,(\hat{\mathrm{J}}^2 - \hat{\mathrm{N}}^2 - \hat{\mathrm{S}}^2)$$

$$\hat{\mathrm{H}}' = \frac{1}{2}\,A(\hat{\mathrm{L}}_+\hat{\mathrm{S}}_- + \hat{\mathrm{L}}_-\hat{\mathrm{S}}_+) + B(\hat{\mathrm{L}}_+\hat{\mathrm{S}}_- + \hat{\mathrm{L}}_-\hat{\mathrm{S}}_+) - B(\hat{\mathrm{J}}_+\hat{\mathrm{L}}_- + \hat{\mathrm{J}}_-\hat{\mathrm{L}}_+)$$

Rotational Energy

The $B(\hat{\mathrm{L}}^2 - \hat{\mathrm{L}}_z^2)$ and $B(\hat{\mathrm{S}}^2 - \hat{\mathrm{S}}_z^2)$ terms are all small and constant for a given $^2\Sigma^+$ state and can be absorbed into the electronic energy. The rotational energy can thus be derived solely from $B(\hat{\mathrm{J}}^2 - \hat{\mathrm{J}}_z^2)$ and $B(\hat{\mathrm{J}}_+\hat{\mathrm{S}}_- + \hat{\mathrm{J}}_-\hat{\mathrm{S}}_+)$ terms and is approximately,

$$E_{Rot}({}^2\Sigma^+) = BN(N+1). \tag{2.68}$$

Spin-Rotation Energy

The spin-rotation energy for a ${}^2\Sigma^+$ state can easily be derived from equation 2.31 as

$$E_{SR}({}^2\Sigma^+) = \frac{1}{2}\gamma[J(J+1) - N(N+1) - 3/4] \tag{2.69}$$

However, the spin-rotation energy becomes complicated when the above equation is expressed using only *N*. For a ${}^2\Sigma^+$ state ($S = 1/2$) there are two values of *J* for each value of *N*, and hence the above equation gives two sets of energy levels for the state (labeled as F_1 ($J = N+1/2$) and F_2 ($J = N-1/2$)) with,

$$E_{SR}({}^2\Sigma^+(F_1)) = \frac{1}{2}\gamma[(N+1/2)(N+3/2) - N(N+1) - 3/4] = \frac{1}{2}\gamma N \tag{2.70}$$

$$E_{SR}({}^2\Sigma^+(F_2)) = \frac{1}{2}\gamma[(N-1/2)(N+1/2) - N(N+1) - 3/4] = -\frac{1}{2}\gamma(N+1). \tag{2.71}$$

The spin rotation splitting in a ${}^2\Sigma^+$ state can then be calculated by taking the difference between these two equations giving

$$\Delta E_{SR}({}^2\Sigma^+(F_2 - F_1)) = -\gamma(N+1/2). \tag{2.72}$$

Λ-doubling

The splitting caused by Λ-doubling in a ${}^2\Sigma^+$ state will be the same as the splitting in a ${}^2\Pi$ state (*e*/*f* parity lifted) except in the opposite direction. Therefore the energy expressions for the Λ-doubling energy in a $^2\Sigma^+$ state can be derived in a similar manner as that outlined in section 2.8.1 for a $^2\Pi$ state giving

$$E_{\Lambda D}(^2\Sigma^+(e)) = -o - \frac{q}{2}N^2 + \frac{p}{2}N \tag{2.73}$$

$$E_{\Lambda D}(^2\Sigma^+(f)) = -o - \frac{q}{2}(N+1)^2 - \frac{p}{2}(N+1) \tag{2.74}$$

where *o*, *p* and *q* are the same as defined for a $^2\Pi$ state (equations 2.58 – 2.60). The Λ-doubling splitting can then be calculated by taking the difference of these two equations:

$$\Delta E_{\Lambda D}(^2\Sigma^+(f-e)) = -(q+p)(N+1/2)\,. \tag{2.75}$$

Often *p* is much greater than *q*, in which the case the above equation can be simplified slightly to

$$\Delta E_{\Lambda D}(^2\Sigma^+(f-e)) \approx -p(N+1/2) = -\gamma(N+1/2)\,. \tag{2.76}$$

If this separation is compared with that caused by spin-rotation (equation 2.72), it is seen that they have the same (*N*+1/2) dependence. This similarity makes it difficult to distinguish between the Λ-doubling and spin-rotation splittings in a $^2\Sigma^+$ state. As outlined in section 2.5.2, contributions to the spin-rotation splitting from the actual spin-rotation interaction are typically small, and are dominated by an interaction with neighboring electronic states for molecules containing heavy atoms, such as those studied in this thesis. For this reason, the contribution to the separation of *e*/*f* components in a $^2\Sigma^+$ state is explained by considering only the splitting arising from Λ-doubling and ignoring any contribution from spin-rotation.

Total Energy:

In summary a $^2\Sigma^+$ state is comprised of a series of rotational levels, each split into e (F_1) and f (F_2) parity spin-components:

$$E(^2\Sigma^+(F_1(e)) = BN(N+1) + \frac{1}{2}\gamma N = B(J-1/2)(J+1/2) + \frac{1}{2}\gamma(J-1/2) \quad (2.77)$$

$$E(^2\Sigma^+(F_2(f)) = BN(N+1) - \frac{1}{2}\gamma(N+1) = B(J+1/2)(J+3/2) - \frac{1}{2}\gamma(J+3/2) \quad (2.78)$$

As with the $^2\Pi$ state, these expressions are only approximate energy level expressions. In this case, the equations were derived by applying perturbation theory to the matrix for a Hund's case (b) $^2\Sigma^+$ state, which results when the Hamiltonian (equation 2.67) is evaluated with the appropriate basis functions. In order to determine the exact energies for $^2\Sigma^+$ state the full matrix [16] must be diagonalized, which was carried out for the experimental $^2\Sigma^+$ state data fit in this thesis. However, again the approximate expressions derived above are more useful for discussing the energy level patterns.

2.8.3 $^2\Pi$ - $^2\Sigma^+$ transitions

The energy level expressions for $^2\Pi$ and $^2\Sigma^+$ states derived in the last two sections are shown pictorially in Figure 2.4. Of note in this figure is that each rotational level is identified by the quantum numbers N and J along with the parity labels e or f. Also each rotational level in the lower state is denoted by the labels F_1 or F_2, while in the upper state the $^2\Pi_{1/2}$ and $^2\Pi_{3/2}$ spin-orbit components are identified as F_1 and F_2, respectively.

Also shown in Figure 2.4 are the allowed transitions between the rotational levels of $^2\Pi$ and $^2\Sigma^+$ states. These transitions are derived from the pertinent selection rules, which themselves originate by evaluating the transition dipole moment integral [10].

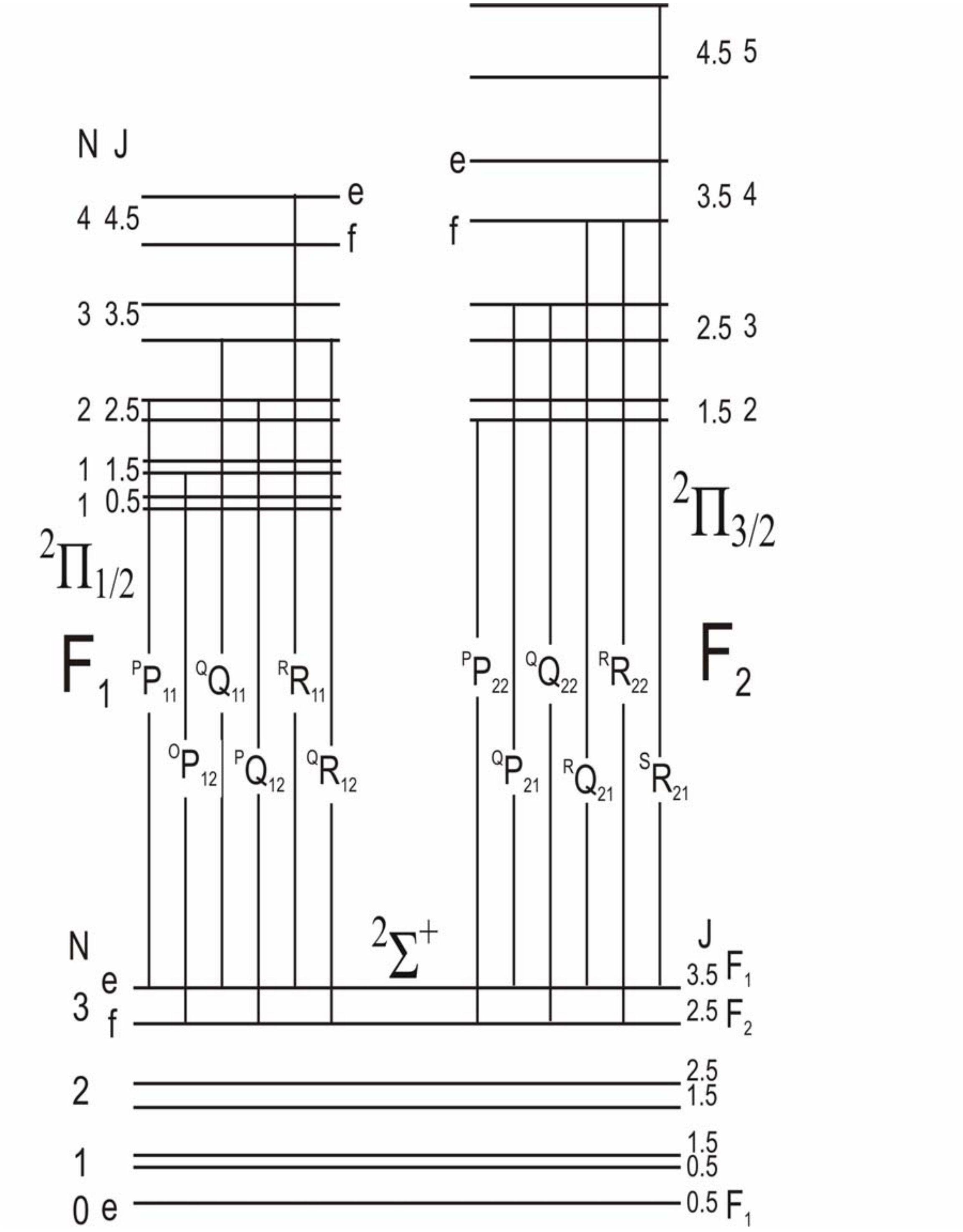

Figure 2.4 $^2\Pi$ - $^2\Sigma^+$ transition

$$\int \Psi_f(^2\Pi)^* \mu \Psi_i(^2\Sigma^+) d\tau . \tag{2.79}$$

For this integral to be non-zero and hence have transitions be allowed, the following selection rules must be obeyed: $\Delta S = 0$, $\Delta \Lambda = \pm 1$ and $\Delta J = 0, \pm 1$. Also considering parity, the following conditions must be met in order for transitions to be allowed, $e \rightarrow f$ or $f \rightarrow e$ for $\Delta J = 0$ transitions and $e \rightarrow e$ or $f \rightarrow f$ for $\Delta J = \pm 1$ transitions.

Rotational lines are grouped into branches based on their ΔJ values ($\Delta J = 0$ for Q branches, $\Delta J = +1$ for R branches, $\Delta J = -1$ for P branches). To distinguish between the two possible parity classes of branch (for example $e \rightarrow e$ or $f \rightarrow f$ for R and P branches), transitions are also labeled with their $F_i^{'}$ and $F_j^{''}$ ($i = 1,2; j = 1,2$) values and each branch is labeled by the notation $^{\Delta N}\Delta J_{F_i^{'}F_j^{''}}$. For example the $^S R_{21}$ branch has $\Delta N = +2$, $\Delta J = +1$, $F_i^{'} = 2$ (F_2 (e)) and $F_j^{''} = 1$ (F_1 (e)).

The above mentioned selection rules result in a total of 12 branches for $^2\Pi$ - $^2\Sigma^+$ transitions. Six branches occur for each spin-orbit component and are comprised of two Q branches, two P branches, and two R branches. The Q branches are always paired with a P or R branch, where the separation between the Q branch and its partner is a reflection of the spin-rotation splitting in the $^2\Sigma^+$ state.

The rotational structure for a $^2\Pi$ - $^2\Sigma^+$ spectrum is quite unique, and is comprised of branches with rotational lines spaced by ~1B and ~3B. This can be observed by considering the spacing of two consecutive rotational lines in the $^P P_{22}$ and $^R R_{22}$ branches as an example (assuming $B' = B'' = B$)

${}^{R}R_{22}(J+1) - {}^{R}R_{22}(J)$=

$$
\begin{aligned}
&= [T_{el} + E_{Rot}({}^2\Pi_{3/2}(J+2)) - E_{Rot}({}^2\Sigma^+(N+1))] - [T_{el} + E_{Rot}({}^2\Pi_{3/2}(J+1)) - E_{Rot}({}^2\Sigma^+(N))] \\
&= [T_{el} + B(J+2)(J+3) - B(N+1)(N+2)] - [T_{el} + B(J+1)(J+2) - BN(N+1)] \\
&= [T_{el} + B(J+2)(J+3) - B(J+3/2)(J+5/2)] - [T_{el} + B(J+1)(J+2) - B(J+1/2)(J+3/2)] \\
&= B(J+2)(J+3-J-1) + B(J+3/2)(J+1/2-J-5/2) = B(J+2)(2) + B(J+3/2)(-2) \\
&= 2BJ + 4B - 2BJ - 3B = B
\end{aligned}
$$

${}^{P}P_{22}(J+1) - {}^{P}P_{22}(J)$=

$$
\begin{aligned}
&= [T_{el} + E_{Rot}({}^2\Pi_{3/2}(J)) - E_{Rot}({}^2\Sigma^+(N+1))] - [T_{el} + E_{Rot}({}^2\Pi_{3/2}(J-1)) - E_{Rot}({}^2\Sigma^+(N))] \\
&= [T_{el} + B(J)(J+1) - B(N+1)(N+2)] - [T_{el} + B(J-1)(J) - BN(N+1)] \\
&= [T_{el} + B(J)(J+1) - B(J+3/2)(J+5/2)] - [T_{el} + B(J-1)(J) - B(J+1/2)(J+3/2)] \\
&= B(J)(J+1-J+1) + B(J+3/2)(J+1/2-J-5/2) = B(J)(2) + B(J+3/2)(-2) \\
&= 2BJ - 2BJ - 3B = -3B
\end{aligned}
$$

These expressions show that the unique structure of a ${}^2\Pi$ - ${}^2\Sigma^+$ transition results from transitions between electronic states that belong to two different coupling schemes, i.e. Hund's case (b) ${}^2\Sigma^+$ state to Hund's case (a) ${}^2\Pi$ state. This is in contrast to transitions within one coupling scheme in which all the branches are spaced by ~2*B*.

2.8.4 ${}^2\Sigma^+$ - ${}^2\Pi$ transitions

The allowed rotational transitions for a ${}^2\Sigma^+$ - ${}^2\Pi$ transition are shown in Figure 2.5. As can be seen in this figure, the structure is very similar to that of a ${}^2\Pi$ - ${}^2\Sigma^+$ transition. Again the pertinent selection rule, $\Delta J = 0, \pm 1$, along with the parity requirements *e*→*f* or *f*→*e* for Q branches and *e*→e or *f*→*f* for P and R branches, yields a total of twelve branches (six per spin-orbit component) for a ${}^2\Sigma^+$ - ${}^2\Pi$ transition. Also each branch is again labeled by the notation ${}^{\Delta N}\Delta J_{F_i' F_j''}$, and each Q branch is still paired with a P or R

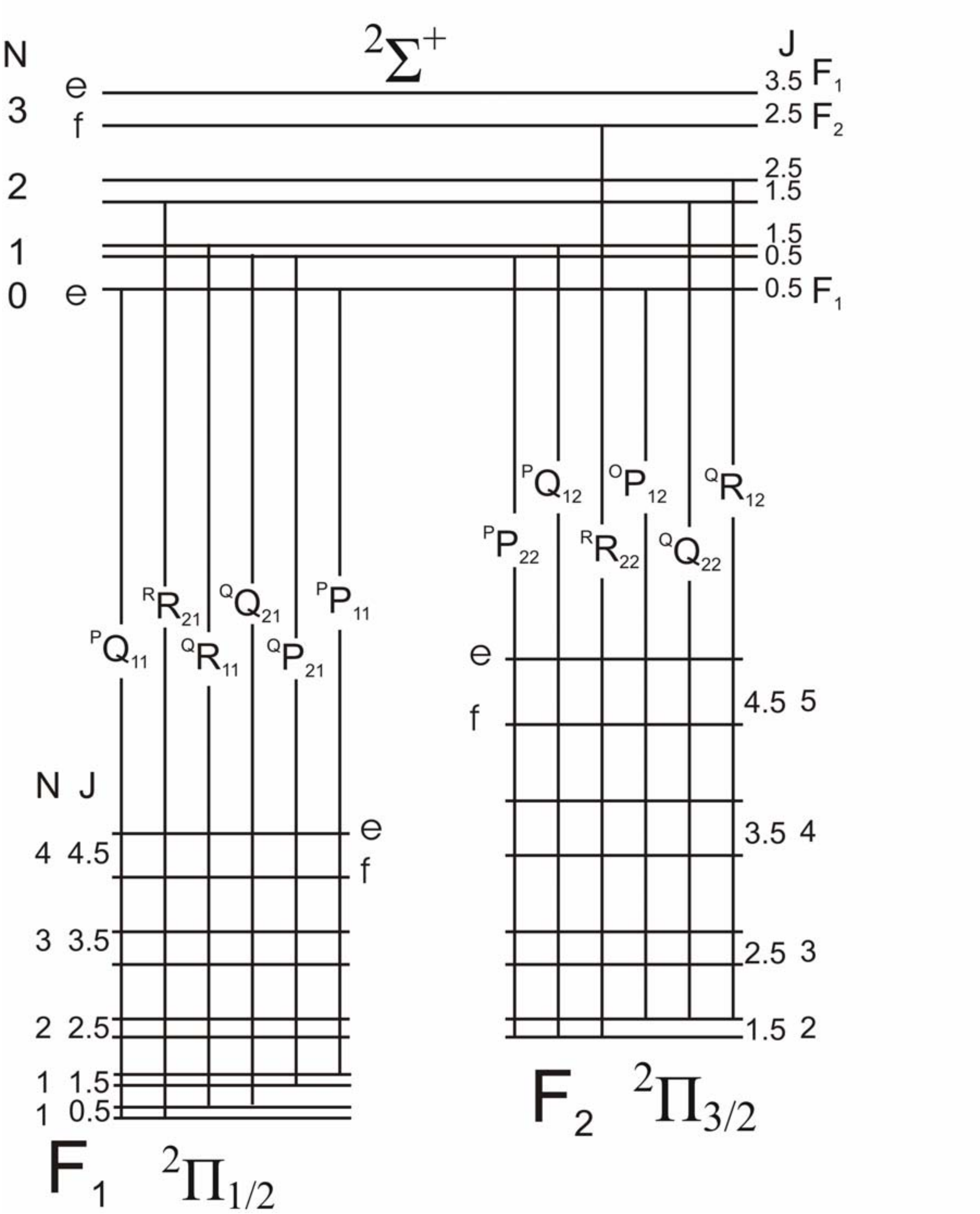

Figure 2.5 - $^2\Sigma^+$ - $^2\Pi$ transition

branch where the spacing between the branches is again a reflection of the spin-rotation splitting in the $^2\Sigma^+$ state. Finally, the spectrum for a $^2\Sigma^+$ - $^2\Pi$ transition is still composed of ~1*B* and ~3*B* spaced branches, as the transition again crosses Hund's coupling cases (Hund's case (a) $^2\Pi$ - Hund's case (b) $^2\Sigma^+$).

2.8.5 Unique Perturber and Pure Precession Approximations

Before leaving the discussion on $^2\Pi$ and $^2\Sigma^+$ states, a brief outline on how the expressions for the Λ-doubling constants *o*, *p* and *q* (equations 2.58-2.60) can be simplified using the unique perturber and pure precession approximations.

First, the unique perturber approximation removes the sum over all possible $^2\Sigma^+$ states by making the assumption that only one $^2\Sigma^+$ state is responsible for the Λ-doubling in a $^2\Pi$ state. It is assumed that the rest of the possible perturbing states are located far enough away from the $^2\Pi$ state that their effects can be neglected (i. e. $E_{^2\Pi} - E_{^2\Sigma^+}$ is large for a given $^2\Sigma^+$ state and thus its contribution to *o*, *p* and *q* is small and can be ignored).

Secondly, the pure precession relationship assumes that the perturbing $^2\Pi$ and $^2\Sigma^+$ states arise from the same (pure) atomic orbitals. For example, the 4*p* orbital of calcium from which both the first excited $^2\Pi$ (4*p*π) and $^2\Sigma^+$ (4*p*σ) state arise (Figure 2.1). Under this assumption, the effects of the operators $\hat{\mathrm{L}}_+$ and $A\,\hat{\mathrm{L}}_+$ on the $^2\Pi$ and $^2\Sigma^+$ state wavefunctions may be expressed as follows [10],

$$\left\langle {}^2\Pi \middle| \hat{L}_+ \middle| {}^2\Sigma^+ \right\rangle = \sqrt{\ell(\ell+1)} \tag{2.80}$$

$$\left\langle {}^2\Pi \middle| A\hat{L}_+ \middle| {}^2\Sigma^+ \right\rangle = A\sqrt{\ell(\ell+1)} \quad . \tag{2.81}$$

where ℓ is the atomic orbital angular momentum. Applying these assumptions, the expressions for o, p and q may be simplified to

$$o = \frac{{A_{SO}}^2 \ell(\ell+1)}{4(E_{^2\Pi} - E_{^2\Sigma^+})} \tag{2.82}$$

$$p = \frac{2BA_{SO}\ell(\ell+1)}{(E_{^2\Pi} - E_{^2\Sigma^+})} \tag{2.83}$$

$$q = \frac{2B^2\ell(\ell+1)}{(E_{^2\Pi} - E_{^2\Sigma^+})}. \tag{2.84}$$

The unique perturber and pure precession approximations can easily be applied in reverse and the expression for the spin-rotation parameter γ in a $^2\Sigma^+$ state written as follows,

$$\gamma = \sum_{|^2\Pi\rangle} \frac{2B\langle ^2\Pi | A_{SO}L_+ | ^2\Sigma^+\rangle\langle ^2\Pi | L_+ | ^2\Sigma^+\rangle}{(E_{^2\Pi} - E_{^2\Sigma^+})} = \frac{2BA_{SO}\ell(\ell+1)}{(E_{^2\Pi} - E_{^2\Sigma^+})}. \tag{2.85}$$

2.9 Energy Level Structure for Molecules of C_{3v} Symmetry

Derivation of simple energy expressions for polyatomic molecules is more difficult than for their linear counterparts. As outlined in sections 2.1 - 2.7, the Hamiltonians from which these expressions are derived are more complicated than those for their linear counterparts due to the multiple axes of rotation and the coupling of electronic and vibrational motions. Therefore, this section will be less quantitative than the last, and instead will consider each term in the pertinent Hamiltonians qualitatively and describe its effect on the energy level structure for the symmetric top molecules studied. In particular, conclusions will be drawn by comparing the C_{3v} energy level pattern with that of a linear polyatomic molecule.

2.9.1 $^2A_1$ states

A $^2A_1$ state correlates to a $^2\Sigma^+$ state in the linear limit, and like a $^2\Sigma^+$, state belongs to the Hund's case (b) coupling scheme. The total energy of a $^2A_1$ state can be derived from the solution to the appropriate rotational Hamiltonian expressed in Hund's case (b) notation (sections 2.4.3 and 2.5.2) [17] considering only the rotation and spin-rotation interactions.

$$\hat{H}(^2A_1) = \hat{H}_{Rot} + \hat{H}_{SR} \tag{2.86}$$

$$\hat{H}_{Rot} = B(\hat{N})^2 + (A\text{-}B)(\hat{N}_a)^2$$

$$\hat{H}_{SR} = \varepsilon_{aa}\hat{N}_a \cdot \hat{S}_a + \varepsilon_{bb}\hat{N}_b \cdot \hat{S}_b + \varepsilon_{cc}\hat{N}_c \cdot \hat{S}_c$$

Rotational Energy

The rotational energy for a $^2A_1$ state can be derived from the rotational Hamiltonian as

$$E_{Rot}(^2A_1) = BN(N+1) + (A-B)K^2 . \tag{2.87}$$

This expression may be further simplified by invoking the inequality in the rotational constants ($A>>B$) to give

$$E_{Rot}(^2A_1) \approx BN(N+1) + AK^2 . \tag{2.88}$$

It is this AK^2 term that is the central difference between a $^2A_1$ and a $^2\Sigma^+$ state. Without this term, the rotational energy of a $^2A_1$ state is identical to the rotational energy of a $^2\Sigma^+$ state. With this term, however, the rotational energy of a $^2A_1$ state becomes comprised of a series of $BN(N+1)$ spaced rotational levels, one series for each value of K.

These K sub-levels are spaced by $A(K+1)^2 - AK^2 = A(2K+1)$. Another way of interpreting this energy expression is to consider a ${}^2\mathrm{A}_1$ state as a series of ${}^2\Sigma^+$ states piled on top of each other, each spaced by $A(2K+1)$, with the first rotational levels in a given K-sub-level varying according to $N \geq K$. For example, for the $K = 0$ sub-level the lowest rotational levels have $N = 0$ while for the $K = 1$ sub-level $N = 1$ for the lowest rotational levels.

Spin-Rotation Energy

The spin-rotation Hamiltonian for a ${}^2\mathrm{A}_1$ state can be simplified slightly because like the rotational constants ($B = C$), the spin-rotation constants about the b and c axes are also equal ($\varepsilon_{bb} = \varepsilon_{cc}$) [12,16].

$$\hat{\mathrm{H}}_{\mathrm{SR}} = \varepsilon_{aa}\hat{\mathrm{N}}_{\mathrm{a}} \cdot \hat{\mathrm{S}}_{\mathrm{a}} + \varepsilon_{bb}(\hat{\mathrm{N}}_{\mathrm{b}} \cdot \hat{\mathrm{S}}_{\mathrm{b}} + \hat{\mathrm{N}}_{\mathrm{c}} \cdot \hat{\mathrm{S}}_{\mathrm{c}}) \tag{2.89}$$

Often, it is customary to write ε_{bc} $\left(= \dfrac{\varepsilon_{bb} + \varepsilon_{cc}}{2}\right)$ in lieu of ε_{bb}.

As with a ${}^2\Sigma^+$ state, the spin-rotation constants are primarily derived from Λ-type doubling interactions with other electronic states, rather than from the actual interaction of electron spin and molecular rotation. Using the unique perturber and pure precession approximations, ε_{bc} and ε_{aa} are defined as follows [12]:

$$\varepsilon_{bc} = \frac{2Ba\ell(\ell+1)}{(E_{{}^2E} - E_{{}^2A_1})} \tag{2.90}$$

$$\varepsilon_{aa} = \frac{2Aa\ell(\ell+1)}{(E_{{}^2A_2} - E_{{}^2A_1})}. \tag{2.91}$$

The equation for ε_{bc} is analogous to that defined for γ in a ${}^2\Sigma^+$ state, with the interaction now occurring between a ${}^2\mathrm{E}$ and a ${}^2\mathrm{A}_1$ state instead of a ${}^2\Pi$ and a ${}^2\Sigma^+$ state.

However, it should be noted that for $^2A_1$ states arising from sσ atomic orbitals ε_{bc} will equal zero as $\ell = 0$. The equation for ε_{aa} indicates that this constant arises from an interaction of the $^2A_1$ state with a neighboring $^2A_2$ state. As seen in Figure 2.1, there are no low-lying $^2A_2$ states arising from Ca^+ or Sr^+ atomic orbitals. Therefore, ε_{aa} is approximately zero in all the $^2A_1$ states studied in this thesis.

Derivation of simple energy level expressions is not as straightforward for the spin-rotation interaction in symmetric top molecules as it is for linear polyatomic molecules. However, the general effect of $\hat{H}_{SR}$ is the same for $^2A_1$ states as it is for $^2\Sigma^+$ states. This interaction splits each rotational level (N) into two spin-rotation components ($F_1(e) \rightarrow J = N+1/2$ and $F_2(f) \rightarrow J = N-1/2$). This splitting occurs in each K sub-level.

Total Energy:

In summary, the energy level structure for a $^2A_1$ state can be thought of a series of K-sub-levels, spaced by $A(2K+1)$, each with a series of rotational levels defined by the energy, $E_{Rot} = BN(N+1)$. Each rotational level is then split into two *e*/*f* parity components by the spin-rotation interaction.

2.9.2 ^2E states

A ^2E state correlates in the linear limit to a $^2\Pi$ state, and much information may be garnered by comparing these two states. Like the $^2\Pi$ states, all the ^2E states studied in this thesis belong to the Hund's case (a) coupling scheme. As a result, along with rotation, the dominant interactions in these states are spin-orbit coupling and Λ-doubling. However, as mentioned in section 2.7.1, for symmetric top molecules Λ-doubling is not given its own term in the Hamiltonian, but is instead considered as part of the spin-rotation interaction. The total energy for these states can be derived by the addition of the electronic energy (T_e) and the solution to the appropriate rotational Hamiltonian. A brief description of the derivation of this Hamiltonian has been discussed above (sections 2.4.3, 2.5.1, 2.5.2, 2.7.1 and 2.7.2). However, more detailed derivations have been given by Brown [9], Hougen [15] and Hirota [14]. These authors define the Hamiltonian for a ^{2}E state as follows

$$\hat{\mathrm{H}}(^2\mathrm{E}) = \hat{\mathrm{H}}_{\mathrm{Rot}} + \hat{\mathrm{H}}_{\mathrm{SO}} + \hat{\mathrm{H}}_{\mathrm{SR}} \tag{2.92}$$

$$\hat{\mathrm{H}} = B(\hat{\mathrm{J}} - \hat{\mathrm{L}} - \hat{\mathrm{G}} - \hat{\mathrm{S}})^2 + (A\text{-}B)(\hat{\mathrm{J}}_{\mathrm{a}} - \hat{\mathrm{L}}_{\mathrm{a}} - \hat{\mathrm{G}}_{\mathrm{a}} - \hat{\mathrm{S}}_{\mathrm{a}})^2$$

$$\mathrm{H}_{\mathrm{SO}} = a\,\hat{\mathrm{L}}_{\mathrm{z}} \cdot \hat{\mathrm{S}}_{\mathrm{z}}$$

$$\hat{\mathrm{H}}_{\mathrm{SR}} = \varepsilon_{\mathrm{aa}}\hat{\mathrm{N}}_{\mathrm{a}} \cdot \hat{\mathrm{S}}_{\mathrm{a}} + \varepsilon_{\mathrm{bb}}(\hat{\mathrm{N}}_{\mathrm{b}} \cdot \hat{\mathrm{S}}_{\mathrm{b}} + \hat{\mathrm{N}}_{\mathrm{c}} \cdot \hat{\mathrm{S}}_{\mathrm{c}}) + \varepsilon_1(\hat{\xi}_{-}^2\hat{\mathrm{N}}_{+}\hat{\mathrm{S}}_{+} - \hat{\xi}_{+}^2\hat{\mathrm{N}}_{-}\hat{\mathrm{S}}_{-})\,.$$

Rotational Energy

Derivation of a simple rotational energy expression for a ^{2}E state is not straightforward, and involves the introduction of several new terms accounting for the coupling of the electronic and vibrational angular momenta. However, to a first approximation the rotational energy may be expressed as

$$E_{Rot}\,(^2E) \approx BJ(J+1) + AK^2\ . \tag{2.93}$$

As was the case for a ^{2}A$_1$ state, it is the AK^2 term which distinguishes the ^{2}E state from its linear analog. Without this term, the rotational energy expression is identical to that of a $^2\Pi$ state (equation 2.48). However, with this term the ^{2}E state becomes a series of sub-states piled on top of each other, one state for each value of K. The spacing between two consecutive K sub-levels is given by $A(2K+1)$, and the first rotational level varies from one sub-level to the next according to $J = K-1/2$ for the F_1 component and $J = K+1/2$ for the F_2 component for sub-levels of $K > 0$ (For the $K = 0$ sublevel, $J = K+1/2$ for both spin-orbit components).

Spin-Orbit Energy

The spin-orbit interaction for a ^2E state including the effect of Jahn-Teller coupling was considered in section 2.7.2, and is

$$E_{SO} = a\zeta_e \Sigma d. \tag{2.94}$$

This equation dictates that like a $^2\Pi$ state, a ^2E state is comprised of two spin-orbit components, the energies of which are given by

$$E_{SO}(^2E_{1/2}(F_1)) = -\tfrac{1}{2}a\zeta_e d \tag{2.95}$$

$$E_{SO}(^2E_{3/2}(F_2)) = \tfrac{1}{2}a\zeta_e d. \tag{2.96}$$

Spin-Rotation Energy:

The first two terms of $\hat{H}_{SR}$ for the ^2E state are very similar those derived for a $^2A_1$ state, and again involve the spin-rotation constants ε_{aa} and ε_{bc}. ε_{bc} again arises from interaction between a $^2A_1$ and ^2E state, and is analogous to γ in the linear limit ($^2\Pi$ state). Like γ in a $^2\Pi$ state, ε_{bc} is dominated by the spin-orbit paramater in a ^2E state, and can often be neglected.

For a ^2E state, ε_{aa} now results from the interaction with another ^2E state. ε_{aa} may be defined as follows by invoking the pure precession and unique perturber approximations [18] as

$$\varepsilon_{aa} = -\frac{4a\zeta_e dA\zeta_e d}{(E_{^2E} - E_{^2E})}. \tag{2.97}$$

Figure 2.1 shows that the majority of ^{2}E states arising from the atomic orbitals of Ca$^+$ and Sr$^+$ lie quite high in energy, and as a result ε_{aa} is often very small for the states studied in this thesis.

The most important spin-rotation constant is ε_1, which accounts for the Λ-type doubling in the ^{2}E state [18], and is defined as

$$\varepsilon_1 = \frac{aB\ell(\ell+1)}{(E_{^2E} - E_{^2A_1})}. \tag{2.98}$$

This term is analogous to *p* in a $^2\Pi$ state, and accounts for the *e*/*f* parity splitting of each rotational level in the ^{2}E state. Hougen [15] has shown that the Λ-type doubling in the ^{2}E state is most prevalent in the $K = 1$ sub-level, and may be negligible in the other *K* sub-levels.

Total Energy

In summary, a Hund's case (a) ^{2}E state is comprised of two spin-orbit components, each with a series of *K* sub-levels separated by $2K+1$ times the rotational constant about the *a* axis. Each *K* sub-level contains a series of rotational levels with energies $E_{Rot} \approx BJ(J+1)$. Finally, each rotational level is split into two *e*/*f* parity components by a Λ-type doubling interaction which is accounted for in the spin-rotation Hamiltonian.

2.9.3 $^2A_1 - {}^2A_1$ transitions

The energy level structures for the $K = 0$ and $K = 1$ sub-levels of a $^2A_1$ state are shown schematically in Figures 2.6 and 2.7 respectively. In these figures, each rotational level is labeled by the quantum numbers *N*, *K* and *J*. Also, each spin-rotation component is identified with the F_1 and F_2 labels. Also shown in these figures are the allowed rotational transitions between two $^2A_1$ states, which are derived by evaluating the transition dipole moment integral,

$$\int \Psi_f(^2A_1)^* \mu \Psi_i(^2A_1) d\tau . \tag{2.99}$$

For symmetric top molecules of C_{3v} symmetry the transitions dipole moment (**μ**) points along the symmetry axis (*a*-axis) for $^2A_1 - {}^2A_1$ transitions and results in the selection rule $\Delta K_R = \Delta K = 0$ ($K = K_R$ for a $^2A_1$ state where $\zeta_e = 0$). Transitions can then be grouped into ΔK sub-bands according to which *K* values they connect, for example the $K'' = 0 \rightarrow K' = 0$ and the $K'' = 1 \rightarrow K' = 1$ sub-bands which are shown in Figures 2.6 and 2.7, respectively.

For the $K'' = 0 \rightarrow K' = 0$ sub-band, the transition dipole moment integral also yields the selection rules $\Delta N = \pm 1$ and $\Delta J = 0, \pm 1$. These selection rules result in six branches labeled by the notation ${}^{\Delta N}\Delta J_{F_i' F_j''}$ ($i = 1,2; j = 1,2$). The structure of this sub-band resembles a Hund's case (b) $^2\Sigma^+$ – Hund's case (b) $^2\Sigma^+$ transition.

For the $K'' = 1 \rightarrow K' = 1$ sub-band the transition dipole moment integral again gives the selection rule $\Delta J = 0, \pm 1$. These selection rules result in three main branches where $\Delta N = \Delta J$ (^PP, ^QQ, and ^RR) for both the F_1 and F_2 spin-rotation components. Six satellite branches are also possible, where $\Delta N \neq \Delta J$, $\Delta J = 0, \pm 1$ and $\Delta N = 0, \pm 1, \pm 2$. The $K'' = 1 \rightarrow K' = 1$ sub-band resembles a Hund's case (b) $^2\Pi$ – Hund's case (b) $^2\Pi$ transition.

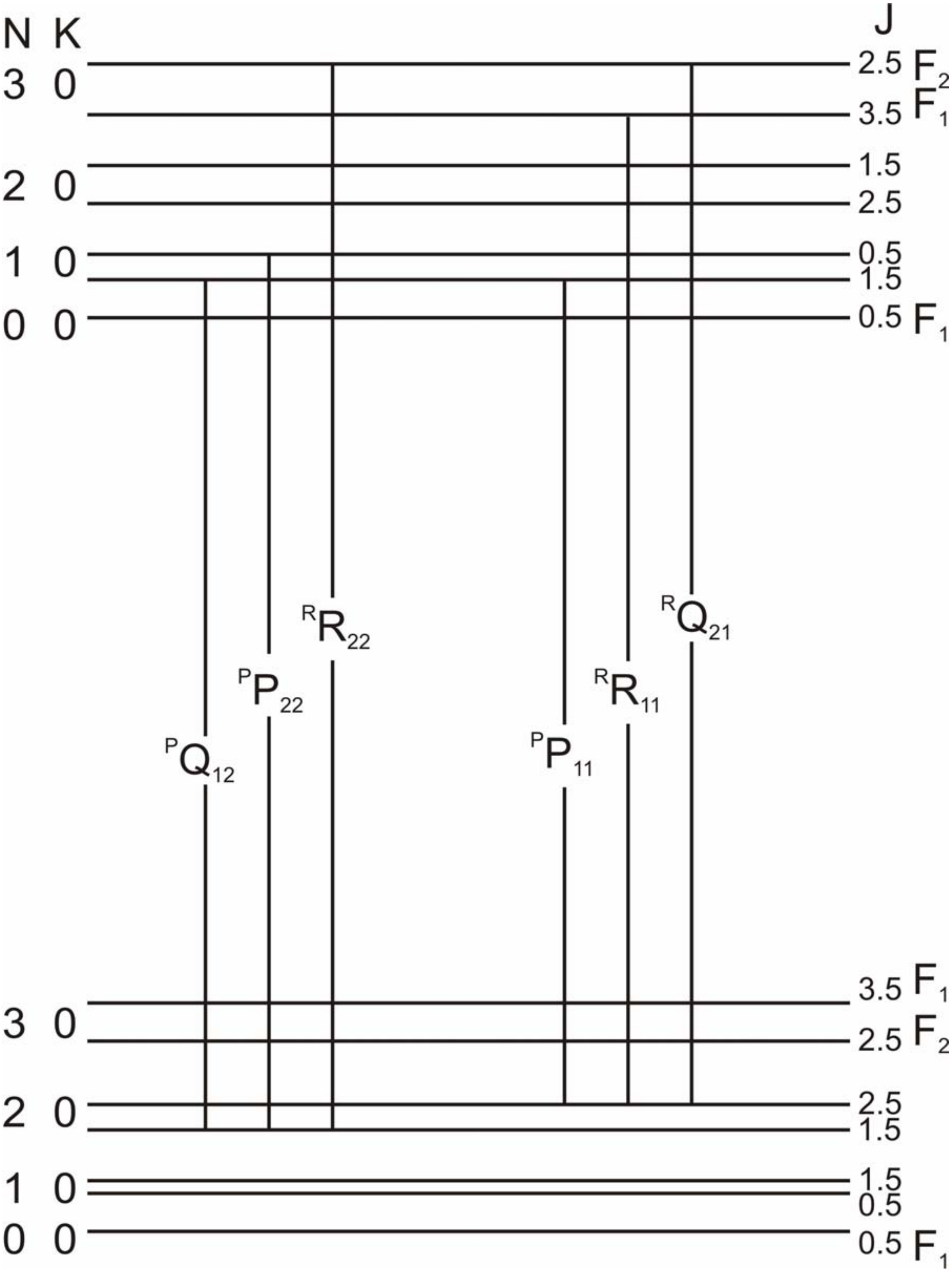

Figure 2.6 – $^2A_1$ – $^2A_1$ ($K'' = 0 \rightarrow K' = 0$) Transition

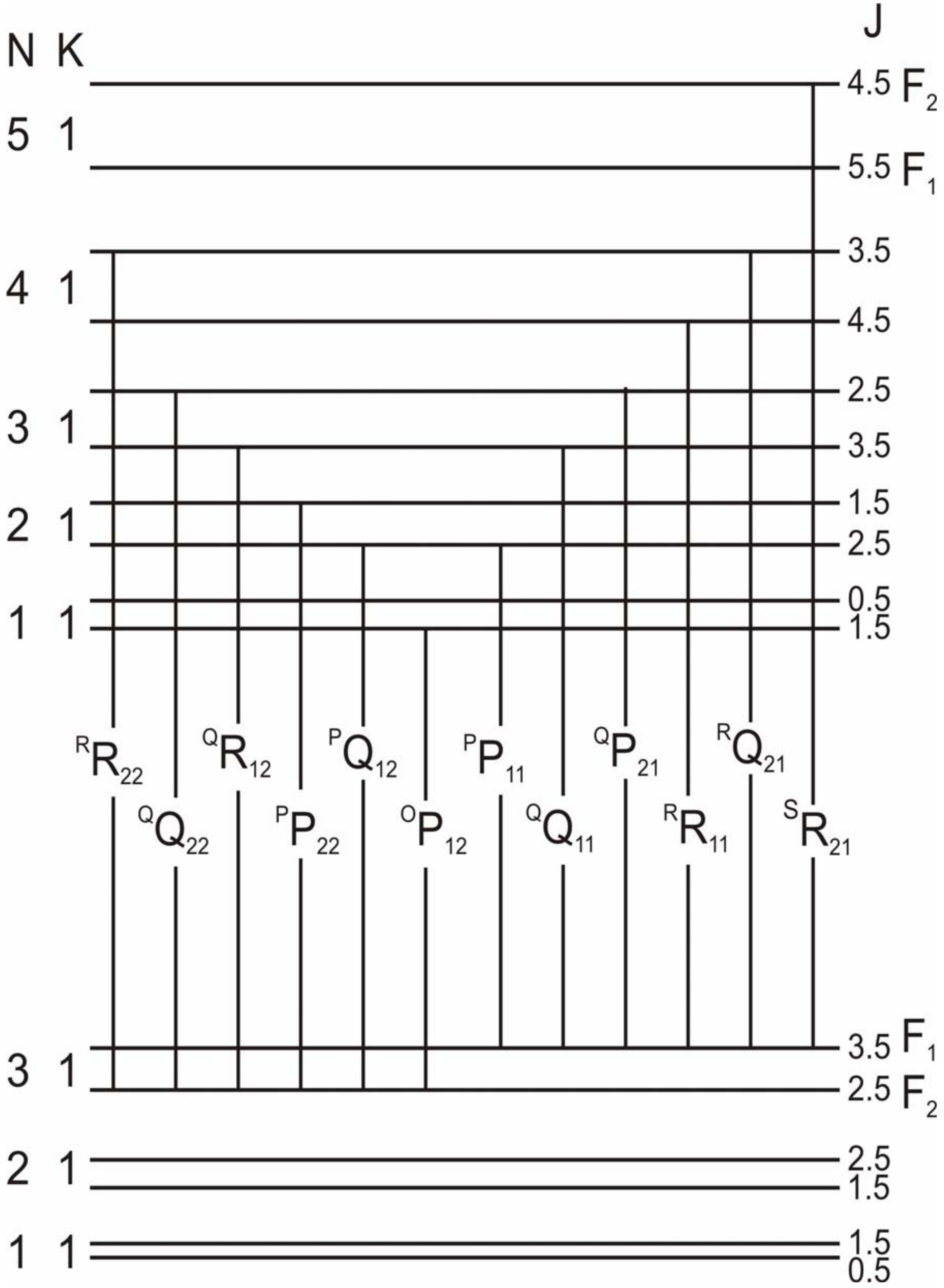

Figure 2.7 – $^2A_1$ – $^2A_1$ ($K'' = 1 \rightarrow K' = 1$) Transition

2.9.4 ^{2}E – ^{2}A$_1$ transitions

The energy level structure for the $K = 0$, $K = 1$ and $K = 2$ sub-levels of a ^{2}E state, are shown schematically in Figures 2.8, 2.9 and 2.10. As seen in these figures, each rotational level in each K sub-level is labeled by K along with the total angular momentum quantum number (J) and the parity identifiers e and f. The two spin-orbit components are also identified by the labels F$_1$ (^{2}E$_{1/2}$) and F$_2$ (^{2}E$_{3/2}$). Also shown in these figures are the allowed rotational transitions between ^{2}E and ^{2}A$_1$ states, which are again derived by evaluating the transition dipole moment integral,

$$\int \Psi_f(^2\mathrm{E})^* \mu \Psi_i(^2\mathrm{A}_1) d\tau \,. \tag{2.100}$$

The transition dipole moment lies perpendicular to the a-axis (symmetry axis) for ^{2}E - ^{2}A$_1$ transitions for prolate symmetric top molecules of C$_{3v}$ symmetry. For a ^{2}E – ^{2}A$_1$ transition, when this direction of $\boldsymbol{\mu}$ is substituted into the above integral the selection rules $\Delta K_R = 0$ and $\Delta K = \pm 1$ are derived. The difference in the selection rules for K_R and K is a reflection of the fact that $K = K_R \pm \zeta_e$ (= 1) for a ^{2}E state. As with ^{2}A$_1$ – ^{2}A$_1$ transitions, ^{2}E – ^{2}A$_1$ transitions can be grouped based into ΔK sub-bands. For example, the $K'' = 0 \rightarrow K' = 1$, $K'' = 1 \rightarrow K' = 0$ and $K'' = 1 \rightarrow K' = 2$ sub-bands are shown in Figures 2.8 – 2.10, respectively.

Each ΔK sub-band has the general appearance of a Hund's case (a) $^2\Pi$ – Hund's case (b) $^2\Sigma^+$ transition with a total of twelve branches (six branches per spin-orbit component). As for a $^2\Pi$ - $^2\Sigma^+$ transition, the selection rule is $\Delta J = 0, \pm 1$ and the parity requirements are $e \rightarrow f$ or $f \rightarrow e$ for Q branches and $e \rightarrow$e or $f \rightarrow f$ for P and R branches. Each of the branches is labeled by the notation $^{\Delta K}\Delta J_{F_i' F_j''}$ ($i = 1,2; j = 1,2$), where ΔK is indicated using a lower case r ($\Delta K = +1$) or p ($\Delta K = -1$) [19]. As with a $^2\Pi$ – $^2\Sigma^+$

transition, each of the Q branches is always paired with a P or R branch and the spacing between the Q branch and its partner is a reflection of the spin-rotation splitting in the $^2A_1$ state. Finally, as for a Hund's case (a) $^2\Pi$ – Hund's case (b) $^2\Sigma^+$ spectrum, the spacing of the rotational lines in each ΔK sub-band is quite unique, with both ~1B and ~3B spaced branches.

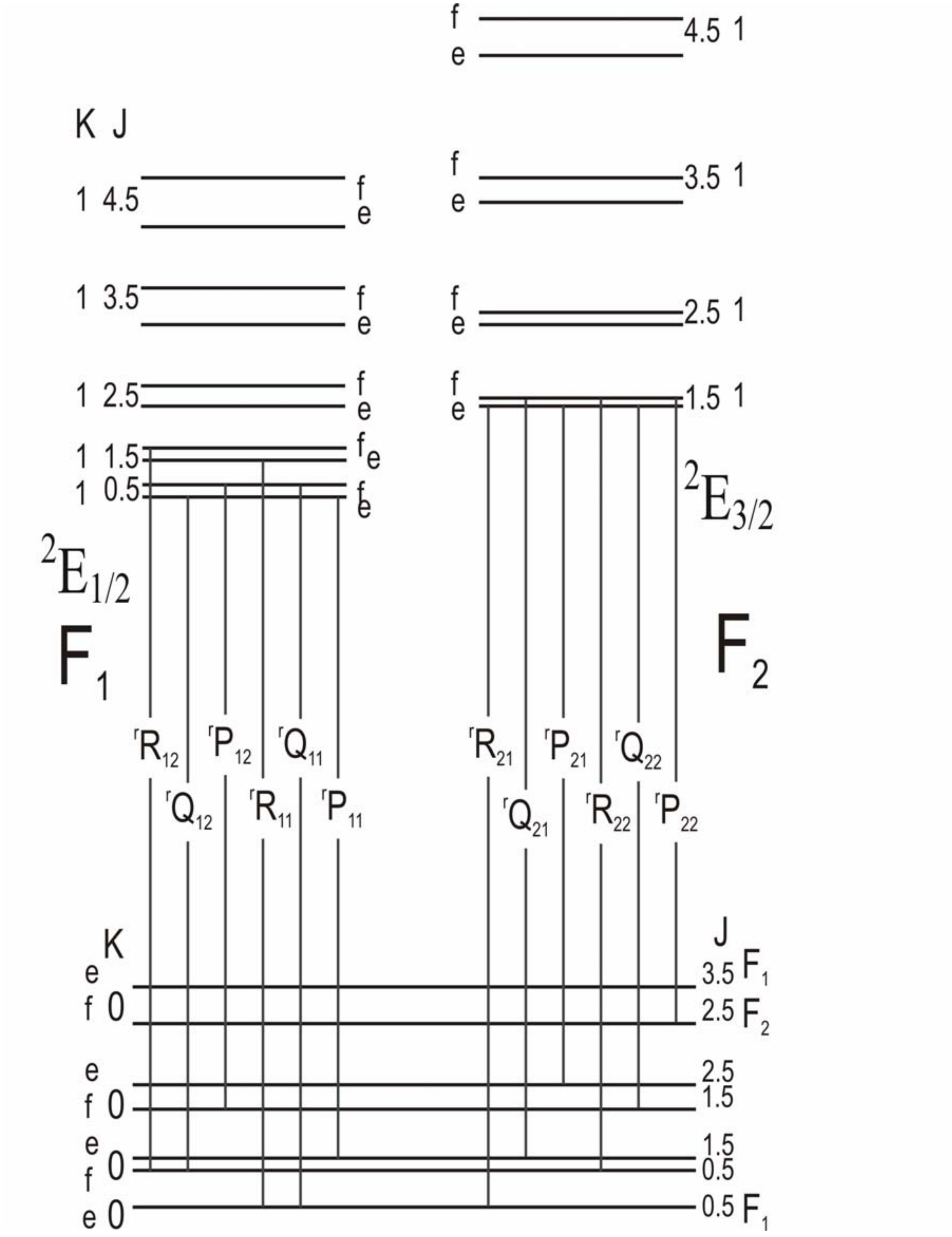

Figure 2.8 – ^{2}E – $^2A_1$ ($K'' = 0 \rightarrow K' = 1$) Transition

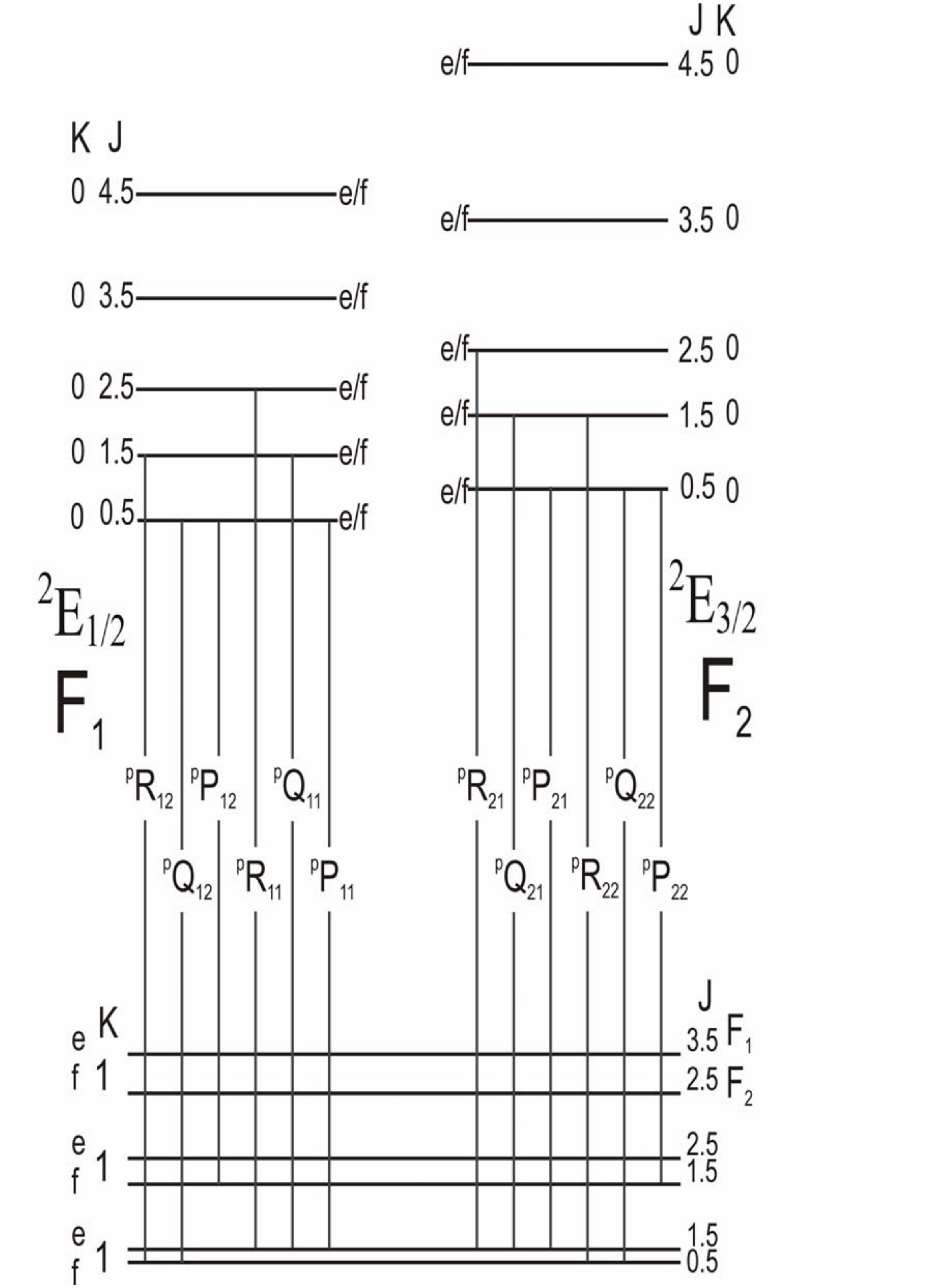

Figure 2.9 – ^{2}E – ^{2}A$_1$ ($K'' = 1 \rightarrow K' = 0$) Transition

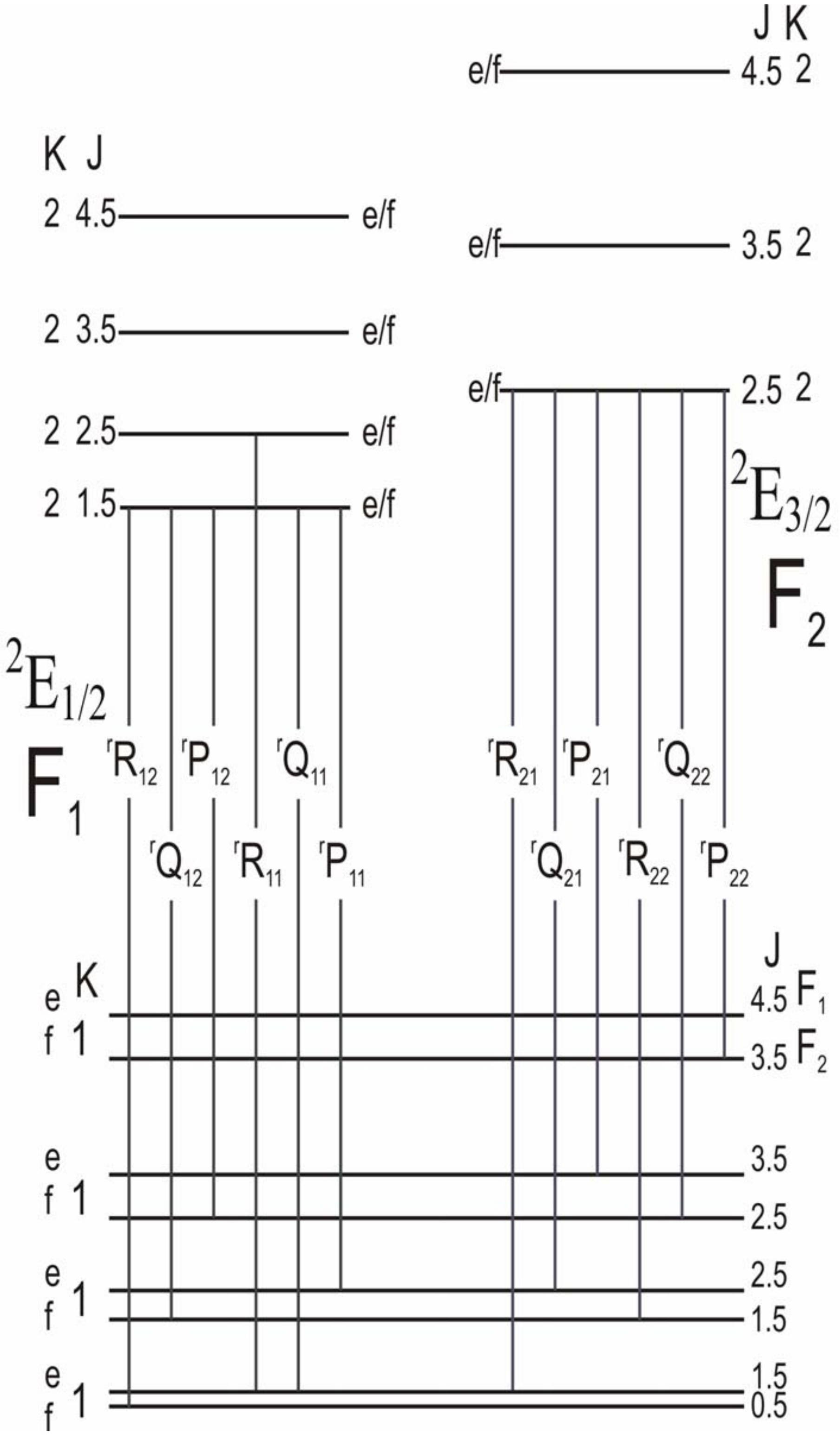

Figure 2.10 – ^2E – $^2A_1$ ($K'' = 1 \rightarrow K' = 2$) Transition

References

[1] P. F. Bernath, *Spectra of Atoms and Molecules*, Oxford University Press, New York, 2nd edition, 2005.

[2] G. Herzberg, *Molecular Spectra and Molecular Structure, Volume I – Spectra of Diatomic Molecules*, Krieger Publishing Company, Malabar, 2nd edition, 1950.

[3] G. Herzberg, *Molecular Spectra and Molecular Structure Volume III – Electronic Spectra and Electronic Structure of Polyatomic Molecules*, Krieger Publishing Company, Malabar, 1966.

[4] C. H. Townes and A. L. Schawlow, *Microwave Spectroscopy*, Dover Publications, New York, 1975.

[5] J. M. Hollas, *Modern Spectroscopy*, John Wiley and Sons, Chichester, 2nd Edition, 1996.

[6] S. F. Rice, H. Martin and R. W. Field, J. Chem. Phys. **82**, 5023 (1985).

[7] A. R. Allouche, G. Wannous and M. Aubert-Frécon, Chem. Phys. **170**, 11 (1993).

[8] A. L. Kaledin, M. C. Heaven, R. W. Field and L. A. Kaledin, J. Mol. Spectrosc. **179**, 310 (1996).

[9] J. M. Brown, Mol. Phys. **20**, 817 (1971).

[10] C. Linton, Course Notes: Physics 3152, Atomic and Molecular Physics. University of New Brunswick, 2000.

[11] S. Hopkins, *High Resolution Laser Spectroscopy of Titanium Monobromide, Hafnium Monofluoride and Strontium Monomethoxide*, PhD Thesis, University of New Brunswick, 2006.

[12] R. N. Dixon, Mol. Phys. **10**, 1 (1965).

[13] J. Brown and A. Carrington, *Rotational Spectroscopy of Diatomic Molecules*, Cambridge University Press, Cambridge, 2003.

[14] E. Hirota, *High-Resolution Spectroscopy of Transient Molecules*, Springer-Verlag, Berlin, 1985.

[15] J. T. Hougen, J. Mol. Spectrosc. **81**, 73 (1980).

[16] J. M. Brown, E. A. Colbourn, J. K. G. Watson and F. D. Wayne, J. Mol. Spectrosc. **74**, 294 (1979).

[17] C. J. Whitham, S. A. Beaton, Y. Ito and J. M. Brown, J. Mol. Spectrosc. **191**, 286 (1998).

[18] A. J. Marr, F. Grieman and T. C. Steimle, J. Chem. Phys. **105**, 3930 (1996).

[19] C. R. Brazier and P. F. Bernath, J. Chem. Phys. **91**, 4548 (1989).

Chapter 3 - Experiment

The intent of this chapter is to outline the experimental equipment and arrangements used to pursue the research presented in this thesis. This will include a discussion of the lasers employed in this work, and an explanation of the molecular sources used to make the calcium and strontium containing polyatomic species investigated. In addition, how the lasers, molecular sources and other essential equipment were combined into one overall experiment will be described. However, as the number of molecules studied in this work is quite extensive, specific experimental details such as laser dyes and gas mixtures used will be described more fully in the chapter in which the results of the work are presented.

3.1 Molecular Sources

3.1.1 Laser Ablation/Molecular Jet Source.

The heart of the laser ablation source is shown in Figure 3.1 [1]. The surface of a metal target rod is ablated by a high power pulsed laser. The resulting metal vapor is then carried into the reaction chamber by the expansion of a carrier gas. This gas is housed in an exterior mixing tank at a relatively high pressure (~100 psi), and enters the system through a pulsed solenoid valve located behind the target rod. In the case of the experiments described in this thesis, argon carrier gas seeded with a small amount of reactant gas was used. The subsequent reaction of the hot metal vapor and the reactant gas yielded the metal-containing species of interest. This reaction takes place inside a sealed vacuum chamber which is evacuated to a pressure of ~1.0×10^{-6} Torr by a

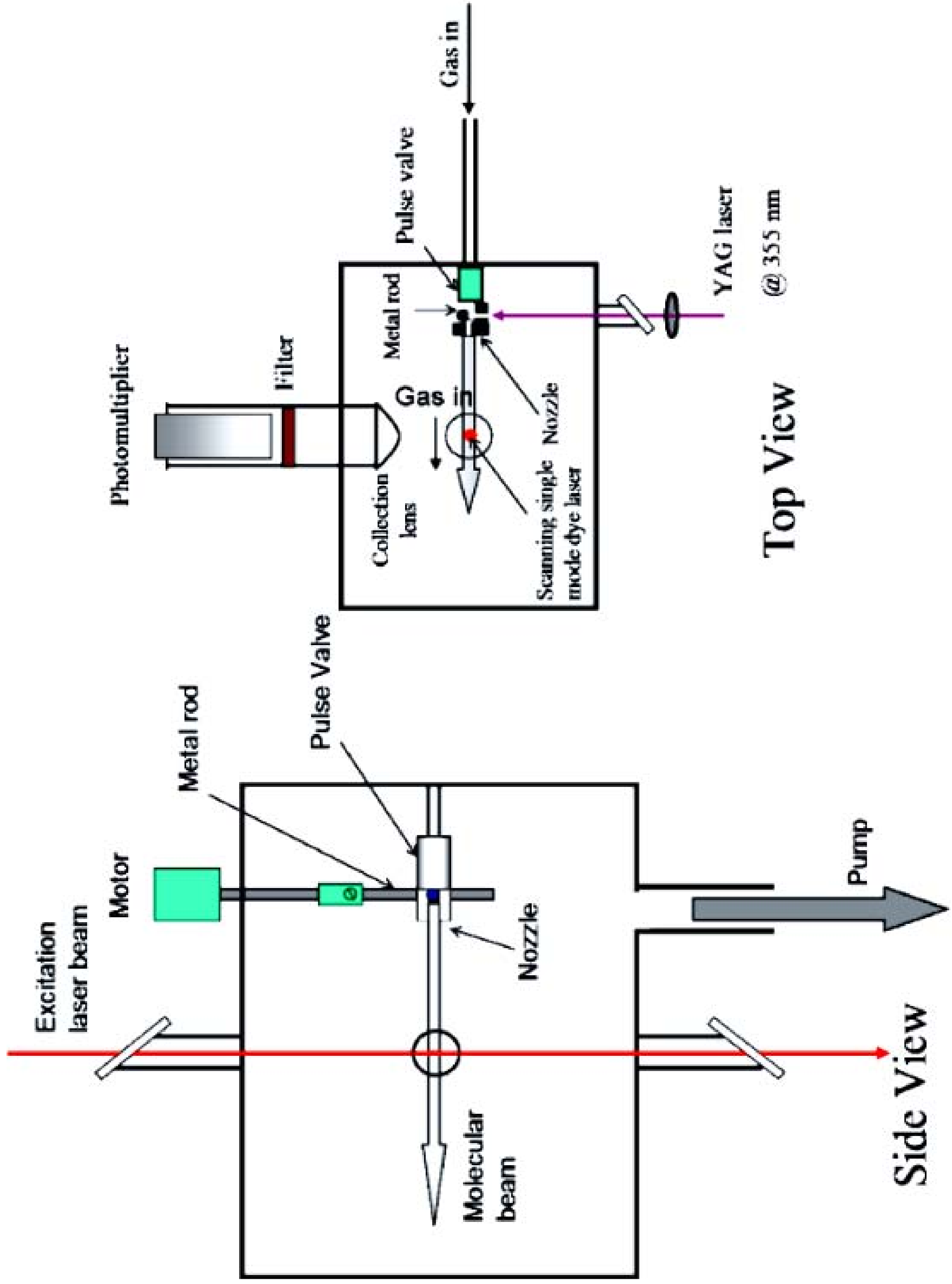

Figure 3.1 – Top and Side Views of the Laser Ablation Molecular Jet Source

diffusion pump (Edwards 250M, backed by a rotary pump). Once the experiment is running, an operating pressure of ~5.5×10^{-5} Torr is maintained.

Three factors must be considered to ensure optimum molecular production is achieved in the laser ablation/molecular jet source. First, the rod must be rotated as well as bi-directionally translated to ensure that a fresh metal surface is always exposed to the ablation laser. Without this motion, the vaporization laser will bore small holes into the rod, hampering molecule production. Secondly, the timing of the opening of the reaction gas inlet valve and the firing of the ablation laser is crucial. Ideally, the valve should open first, allowing the gas to envelop the rod before the vaporization laser is fired. In the case of the molecules studied in this thesis, the laser was fired ~300-400 μs after the opening of the valve. If the laser is fired prematurely, there will be an insufficient amount of reactant molecules surrounding the rod to produce an adequate amount of metal-containing species. A similar scenario is also possible if the laser is fired too late, after the reactant gas has already dissipated. Finally, the ratio of reactant gas to carrier gas is crucial to molecule production. Unfortunately, this ratio varies greatly from one species to another, and there is no way of determining the optimum ratio except through experimentation. However, the percentage of reactant to carrier gas is usually less then 10 percent.

The chief advantage of a laser ablation/molecular jet source is that it produces molecules with low rotational and vibrational excitation, all moving in the same direction. The resulting spectra then have relatively few spectral lines and they have reduced Doppler broadening [2]. The source achieves this advantage by utilizing the nearly 5000X difference in pressure between the reactant gas tank (~100 psi = ~5171.5 Torr) and the vacuum chamber (5.5 x 10^{-5} Torr). In the reaction region, a high pressure flow of molecules is passed through a small area, and as a result, a large number of molecular collisions occur. Through these collisions, the rotational and vibrational motions of the molecules are converted to translational energy along the axis of the molecular jet. In addition, the collisions reduce the spread of velocities in the jet [3]. For example, head on collisions will narrow the velocity profile in the jet direction. As a result, a beam of molecules is produced which, when passed into the low pressure vacuum chamber, continues to move in one direction over a long distance. This allows molecules with low rotational and vibrational energy to be probed downstream. The collection of these cold sub-Doppler spectra will be discussed later in this chapter.

3.1.2 Broida Oven

As compared to the laser ablation/molecular jet source, the Broida oven (Figure 3.2) provides a much more brute force method to produce molecules. The oven consists of a carbon crucible which is filled with the metal of interest. The crucible is then placed in a tungsten basket which is resistively heated via two electrodes until evaporation of the metal occurs. The metal vapor is then carried by a flow of argon carrier gas into the reaction region above the crucible where it reacts with a few mTorr of reactant gas creating the species of interest. The carrier and reactant gases are introduced into the system through a perforated stainless steel ring. The flow of each of these gases is controlled externally by needle valves placed between their storage tanks and the oven. To ensure that a maximum amount of heat is retained in the metal sample, the basket/crucible assembly is wrapped in zirconia insulation, and the crucible is covered by

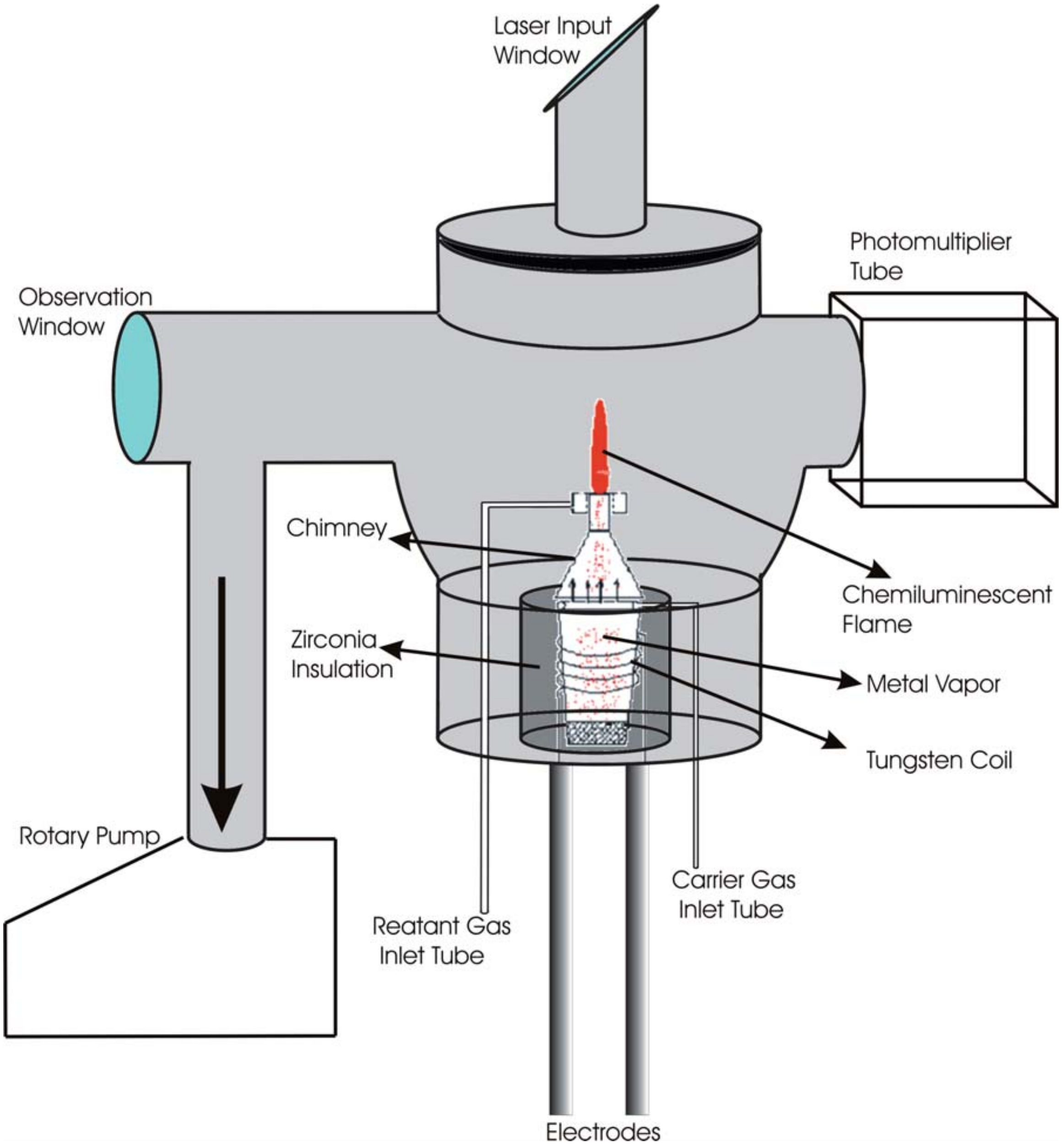

Figure 3.2 – The Broida Oven Source

a small chimney. The entire set-up is water cooled and sealed inside a vacuum chamber which is evacuated to a pressure of ~0.01 Torr using a rotary pump. Once the experiment is running, an operating pressure of ~1-2 Torr is maintained.

Two factors must be considered to ensure optimum molecule production is achieved in the Broida oven source. First, the amount of current flowing through the tungsten basket to heat the metal sample is crucial. If the current is too high and the metal is heated too fast, the lifetime of the sample will be low and the oven will need to be reloaded frequently. In contrast, if the current is too low, then the optimum reaction temperature will never be reached and no metal-containing species will be produced. Secondly, as with the laser ablation/molecular jet source, the ratio of reactant gas to carrier gas is vital to molecule production. Again, this ratio varies greatly from one species to the next, and there is no way of determining the exact value except through experimentation. However, for optimum molecule production in the Broida oven, the flow of reactant gas required is generally very small in comparison to the flow of argon carrier gas (a few mTorr of reactant gas to ~1 Torr of argon carrier gas).

The chief advantage of the Broida oven is that it produces molecules in abundance. This results in strong spectral signals, simplifying signal detection. However, unlike the laser ablation/molecular jet source, the resulting spectra are not sub-Doppler or rotationally and vibrationally cold, as the newly created molecules do not move together in a jet through a very low pressure environment. Thus, the resulting spectra are often more complicated than those obtained in the ablation source

3.2 Lasers

This section will present an overview of the lasers used in of the research presented in this thesis. This will include discussions on both the lasers used to excite the molecular transitions of interest and the laser used to vaporize the metal rod in the laser ablation/molecular jet source.

3.2.1 Continuous Wave Lasers

Three different types of continuous wave lasers (ring dye, titanium - sapphire ring and linear dye) were employed to excite the rovibronic transitions studied in this thesis. The basic operation of each of these lasers is quite similar. An argon ion laser acts as a pump source and excites the active medium (organic laser dye or titanium-sapphire crystal). This results in population inversion of the active medium and the onset of spontaneous emission in the form of fluorescence. When this fluorescence is trapped in an optical cavity, suitable positive feedback is achieved and light amplification through stimulation emission of the radiation (lasing) begins [4,5]. Where the three lasers differ is the wavelength regions they cover and the spectral linewidth of the resulting beam.

Linear Dye Laser

The arrangement of the optical cavity for the linear dye laser is shown in Figure 3.3 [4]. The fluorescence from the excited dye molecules is captured in the cavity between the high reflector, upper fold mirror and output coupler. When these mirrors are aligned correctly, laser oscillation initiates. The birefringent filter (BRF) is used to

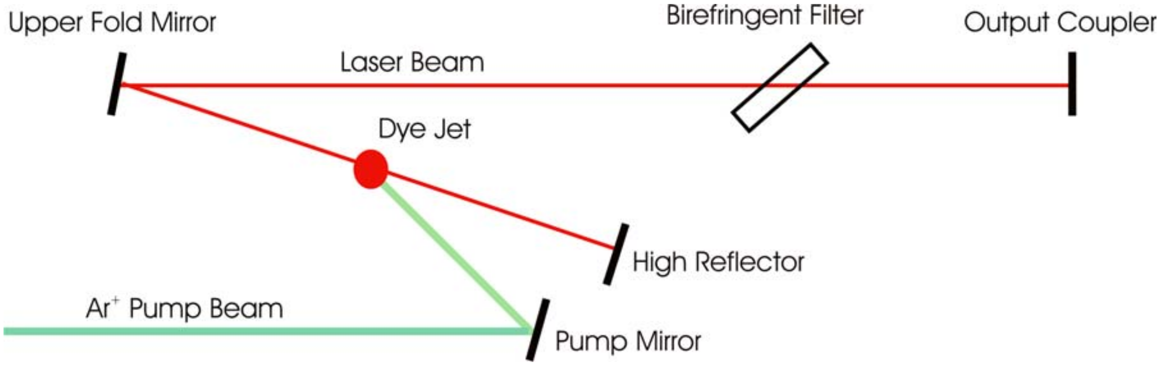

Figure 3.3 – Linear Dye laser Cavity

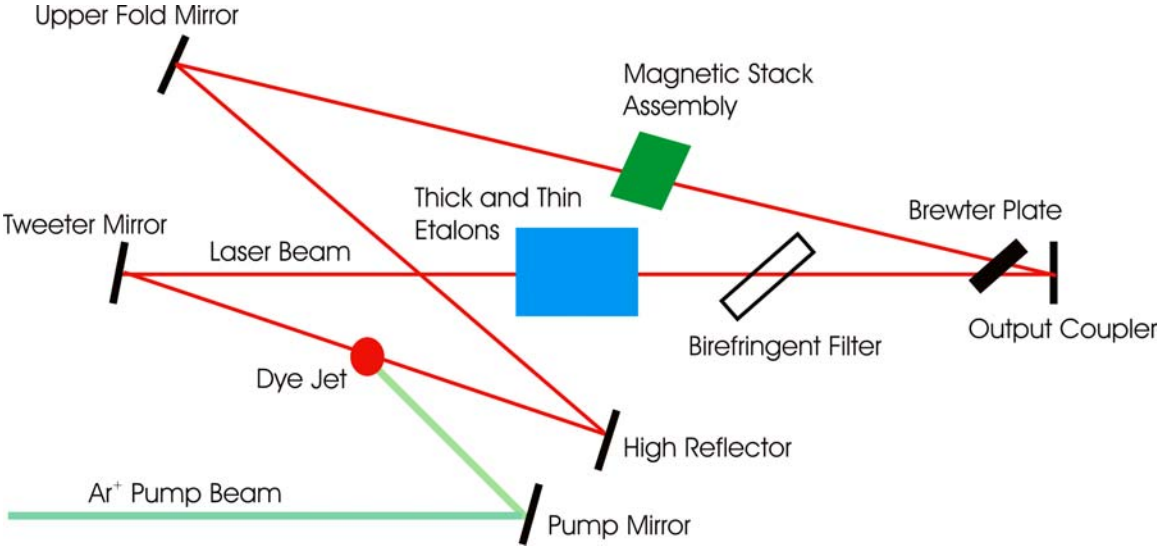

Figure 3.4 – Ring Dye Laser Cavity

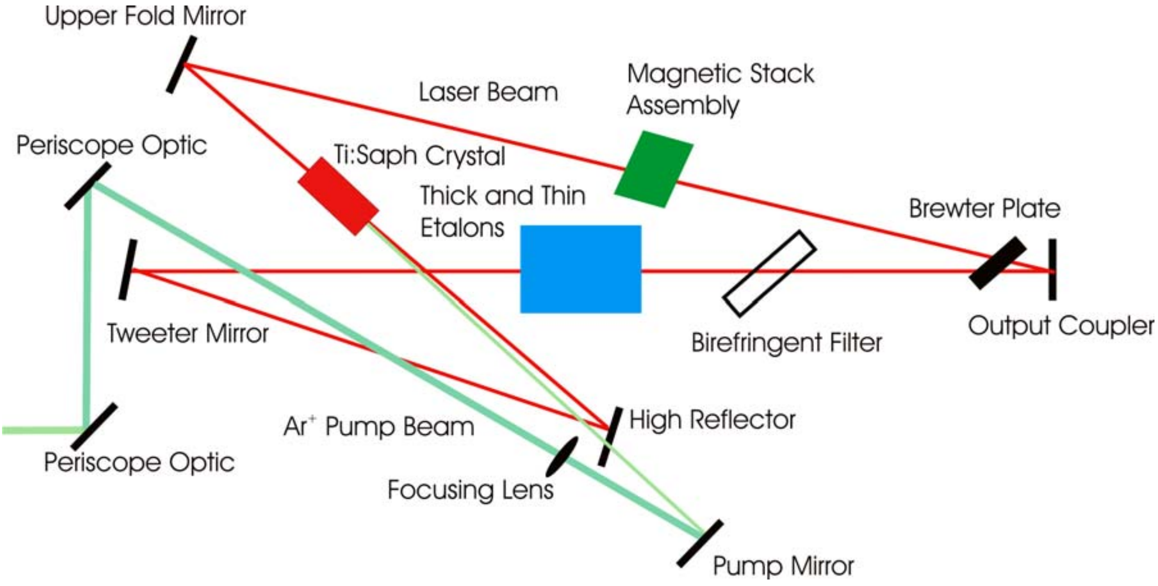

Figure 3.5 – Titanium Sapphire Laser Cavity

narrow the oscillating wavelengths which exist in the linear cavity. It does so by using the birefringent properties of a quartz crystal. Depending on the angle of rotation of the crystal, certain wavelengths of the linearly polarized laser beam will pass through the crystal unchanged, while others will be rotated and then eliminated by reflection out of the cavity [6]. Thus, by rotating the BRF the laser wavelength can be tuned over the range of fluorescence of the organic dye.

The principal advantages of the linear dye laser are the ease at which lasing can be achieved and the ability of the laser to be scanned quickly over a large spectral region. For these reasons, the linear dye laser was principally employed to conduct survey scans over large frequency regions to look for transitions of interest. The main disadvantage of this laser is the relatively large spectral linewidth (~ 1 cm^{-1}) of the output beam. This is a consequence of using only the BRF to narrow the output frequency. The resulting linewidth is too large to resolve the rotational structure of the molecules of interest. Depending on the dye and optic set used, this laser can be employed from ~ 400 to 950 nm [7]. The specific dyes employed in the linear dye laser in the work presented in this thesis can be found in each chapter.

Ring Dye Laser (Coherent 699-29)

The arrangement of the optical cavity for a ring dye laser is displayed in Figure 3.4. As was the case for the linear dye laser, the molecular fluorescence from the organic dye molecules is captured in the cavity, and when the mirrors are properly aligned laser oscillation begins. Fig. 3.4 shows that the laser beam in the ring dye cavity traces out a bowtie shape and contains many more optical elements than its linear counterpart. These elements allow only a single longitudinal mode to oscillate inside the cavity and to scan the frequency of this mode.

The function of each of these elements is best explained by taking a top down view. First, as explained above, the BRF narrows the broad fluorescence from the dye down to a linewidth of ~1 cm^{-1}. The angle of rotation of the BRF thus controls the wavelengths that can exist inside the cavity. Next, the thick and thin etalons act as interferometers and transmit combs of frequencies, because only the wavelengths that constructively interfere within the etalons continue to exist in the cavity [8]. The thin and thick etalons select a single mode within the 1 cm^{-1} bandwidth, and the single selected mode has a linewidth of ~ 10 MHz. In addition, the width of the thick etalon is variable and hence the wavelengths which can pass through the assembly can be changed [8]. Scanning of the cavity is achieved by rotating the Brewster plate. This rotation varies the effective length of the cavity, which varies the output wavelength of the laser. Finally, for proper operation of the ring dye laser to be achieved, laser oscillation around the cavity must be unidirectional (either clockwise or counter clockwise). The magnetic stack assembly helps achieve this goal. The assembly eliminates one of the directions of oscillation by rotating its polarization a few degrees while the other direction is unaffected. As a result, the rotated beam experiences extra losses by reflection from the BRF and no longer lases, while in the other direction the beam passes unchanged through the crystal [6].

The collective effect of these elements in the laser cavity ensures proper operation of the ring dye laser, and they are controlled by a Coherent Autoscan system which includes a wavemeter and a computer interface box. The wavemeter determines the frequency of the output laser beam, and then feeds this information back through the computer interface box. The box then uses this information to help control each of the optical elements and vary the laser frequency as desired. External calibration of the wavemeter is achieved by simultaneously recording the laser excitation or absorption spectra of I_2. Since the spectrum of iodine is well known, the experimental line positions can easily be compared with the atlas values [9,10]. The wavemeter parameters can then be adjusted accordingly to ensure proper calibration of the laser frequency. Depending on the dye and optic set used, the ring dye laser can operate from ~ 390 – 950 nm [7]. The specific dyes used in the ring laser can be found in the following chapters.

Titanium Sapphire Laser (Coherent 899-29)

Figure 3.5 shows the arrangement of the cavity for the titanium sapphire laser employed in the research presented in this thesis. This cavity is very similar to that of the ring dye laser, with again the BRF, thick and thin etalons, magnetic stack assembly and Brewster plate selecting a single mode and giving the laser its ability to scan [11]. Again, the laser is externally controlled by the Coherent Autoscan system which is calibrated by recording the iodine spectrum as a reference [9,10].

The main difference between the titanium sapphire and ring dye lasers is the active medium excited by the argon ion pump laser. As its name suggests, the active medium for the titanium sapphire laser is a titanium sapphire crystal. Specifically, a sapphire crystal (Al_2O_3) is doped with titanium ions, so that the Ti^{3+} ions occupy some of the Al^{3+} ion sites in the crystal lattice [4]. Like a laser dye, the crystal is excited by the argon ion pump laser and begins to fluoresce. This fluorescence is then captured in the cavity, which when aligned properly begins to lase. The crystal tends to fluoresce more in the near infrared region of the electromagnetic spectrum than do the organic dyes used in the dye laser. As a result, laser oscillation in the Ti:Saph laser occurs between 650 to 1100 nm, depending on the optics set used [11].

The chief advantage of the titanium sapphire laser over the ring dye laser is the stability of the laser induced fluorescence. The solid state crystal is a much more stable medium then the fluid dye jet, as it is not susceptible to air bubbles and other irregularities inherent the jet. One disadvantage of the titanium sapphire laser is that it is difficult to align. The fluorescence of the crystal is more difficult to see with the naked eye, making alignment more difficult than with the more visible dye fluorescence. In addition, the alignment of the pump beam is more complex than for the ring dye laser (controlled by three mirrors rather then one)

3.2.2 Nd:YAG Laser (Continuum Surelite 10)

The laser used to ablate the metal target rod in the laser ablation/molecular jet source was a pulsed Nd:YAG laser. In this laser, much as in the titanium sapphire laser, the active medium is a crystal doped with a metal ion. In this case, the crystal is $Y_3Al_5O_{12}$ (yttrium aluminum garnet or YAG) and the doping ion is Nd^{3+}, which occupies some of the Y^{3+} ion sites in the lattice [4]. Laser oscillation initiates when the neodymium ions are excited by a flash lamp (bright white light), resulting in population inversion and the eventual onset of stimulated emission. The power of the resulting laser beam can be changed by varying the brightness of the flash lamp by adjusting its input voltage. Unlike the continuous wave lasers described above, the Nd:YAG laser does not oscillate over a broad spectral range and is not tunable. Instead, lasing occurs at a single wavelength – 1064 nm. However, some variability of the output frequency can be achieved through the use of non-linear optical effects [4]. Using an appropriate crystal, the second (532 nm) or third (355 nm) harmonic of the laser wavelength can be generated.

For the experiments conducted in this thesis, the third harmonic of a Nd:YAG laser with a pulse duration of 6 ns was used. As mentioned above, the power of the Nd:YAG laser beam can be varied. This variability was essential, as the energy per pulse was crucial in creating optimum conditions for molecule production in the laser ablation/molecular jet source. If the energy per pulse was too high, then the background signal created by increased laser scatter would swamp any molecular signal of interest. However, if the energy was too low, then an insufficient amount of metal-containing molecules would be created, as an inadequate amount of metal atoms would be vaporized from the surface of the target rod. Unfortunately, the optimum energy per pulse varies dramatically from one metal-containing species to the next, and there is no way of determining the exact value except through experimental trial and error. However, for optimum production of calcium and strontium containing species, an energy per pulse of ~10 mJ (355 nm) is generally preferred. This value is slightly lower then the optimum energy employed for harder metals such as titanium (~20 mJ/pulse).

3.3 Overall Experimental Setup

3.3.1 Laser Ablation/Molecular Jet Experiment

Figure 3.6 [1] shows how the laser ablation/molecular jet source (described in section 3.1.1) is incorporated into an overall experimental setup. This arrangement

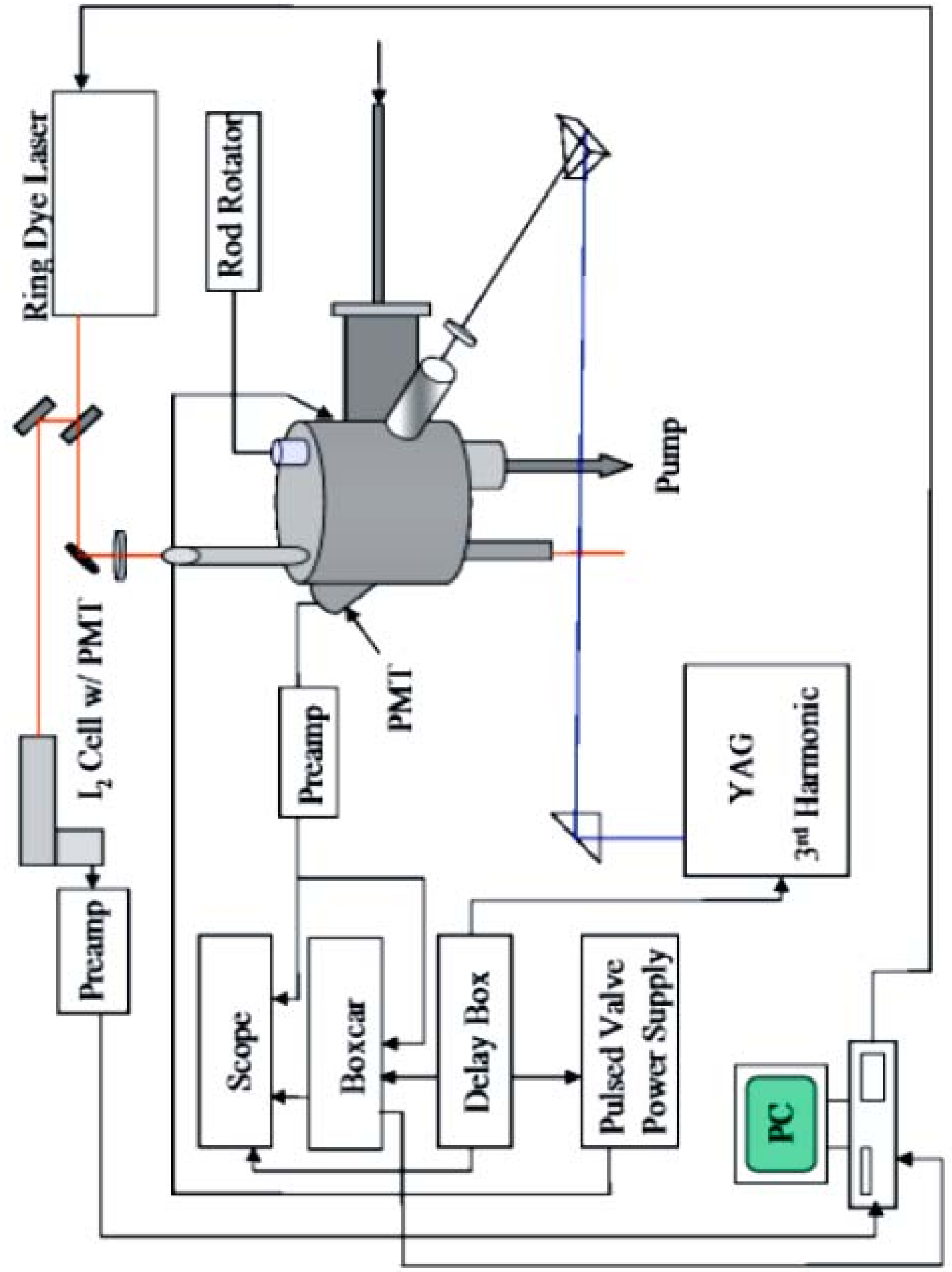

Figure 3.6 – The Laser Ablation/Molecular Jet Experimental Setup

includes the vacuum chamber in which the rod is isolated and the molecules are created, along with the lasers used for ablation (Nd:YAG) and excitation of the molecular transitions of interest (CW – Linear Dye, Ti:Saph or Ring Dye).

The best way to understand the operation of these experimental devices is to consider the timing of the components used in the experiment. As outlined in section 3.1.1, the order in which each experimental component functioned was crucial to efficient molecule production. The timing of the system is controlled by the delay generator and proceeds as follows. First, the pulse valve opens and the reactant gas envelops the target rod. This is followed by the firing of the ablation laser ~300 μs later and the subsequent reaction of gas and hot metal vapor to form the species of interest. The newly created molecules then transit the vacuum chamber as a pulse. When the pulse has traveled ~15 cm downstream, it is interrogated by the continuous wave laser which enters the source through a window located on top of the chamber. Temporal control of this is laser is unnecessary, as it is continuous rather than pulsed. The laser light promotes the newly formed molecules from their ground to excited electronic states.

Timing is also important in the detection of the spectral signal. The excited molecules quickly loose their energy by reemitting the absorbed laser light as molecular fluorescence. This fluorescence is collected by the photomultiplier tube (PMT) and sent to the boxcar integrator for processing. The boxcar is a device which serves two purposes. Firstly, since the molecules travel in a pulse and pass in front of the PMT for only a fraction of a second, it is not desirable to continuously monitor the signal from the tube. For the majority of the time there will be no signal present, and the detection system collects noise. The boxcar alleviates this sampling problem by selectively monitoring the voltage from the PMT only when the newly formed molecules are present and emitting the fluorescence of interest. When and for how long the boxcar samples the signal is dependant on the experimental conditions (size of species being created and carrier gas used), and can be varied. In the case of the experiments described in this thesis, the signal was typically sampled for a 10 μs interval, ~380 μs after the firing of the ablation laser. The second function of the boxcar is to average the signal from several pulses. Thus far, the timing described has been for one cycle of the laser ablation experiment. However, the entire sequence described above is repeated at a rate of 10 Hz, and the boxcar can average the signal from as many of these cycles as is necessary to detect the spectrum. For example, if a molecule's spectral signal is weak, the interrogation laser can be scanned slowly and the boxcar can be set to average several cycles worth of signal. For the high-resolution data collected for this thesis, a typical spectrum was collected at a CW laser scan rate of 180 s/cm^{-1}.

The timing of the experiment is monitored by an oscilloscope. Figure 3.7 [12] shows a typical oscilloscope trace. The experimental sequence is clearly evident, beginning with the gas inlet valve opening (monitored by observing the pulse sent to the valve driver) and followed by the firing of the ablation laser (results in ablation plasma seen by the PMT ~300 μs after the opening of the valve) and interrogation by the probe laser (results in fluorescence seen by the PMT ~600 μs after the opening of the valve). Also evident in the trace is that the boxcar samples only the molecular fluorescence and ignores all other PMT signals.

The final experimental spectrum is created when the signal from the boxcar is sent to the computer where it is correlated with the laser wavelength (determined by the

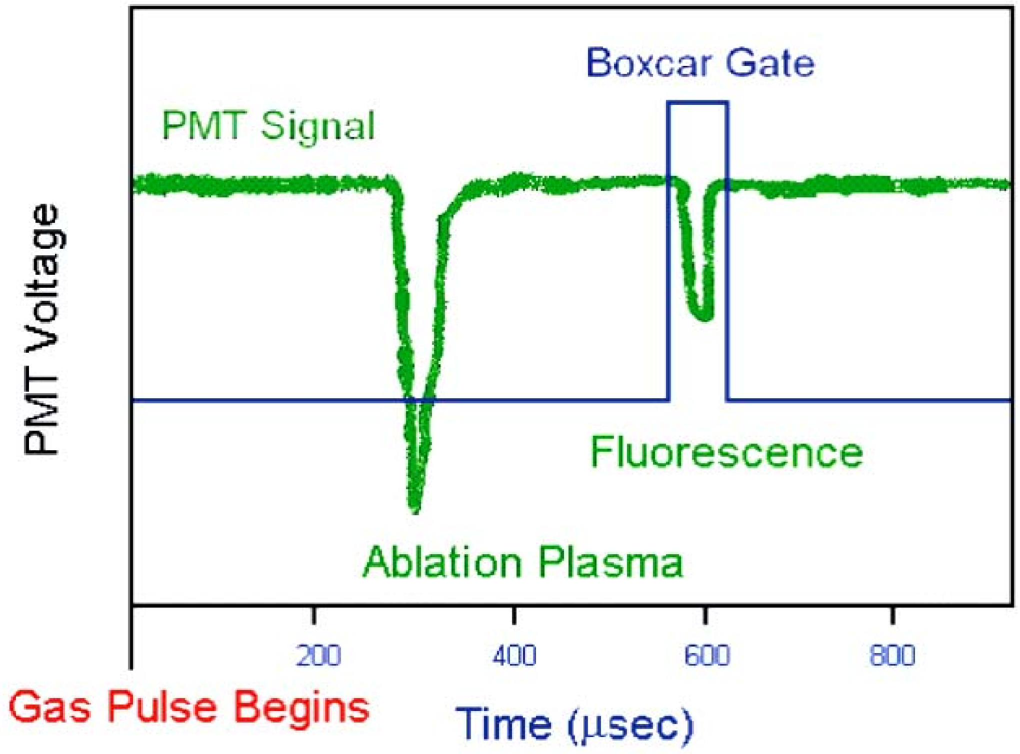

Figure 3.7 – Typical Oscilloscope Trace

laser wavemeter) as well as with the iodine calibration spectrum. Figure 3.6 [1] shows the iodine calibration setup employed for experiments in which the ring dye laser was used. For these investigations, the iodine spectrum was recorded via laser-induced fluorescence where the molecular signal is recorded by a photomultiplier tube. The experimental line positions are then compared with the atlas values [9,10], and the wavemeter parameters and experimental data are adjusted accordingly.

Two techniques were employed to help increase the signal-to-noise ratio of the final experimental spectra. Firstly, band-pass filters (± 20 nm) were placed in front of the PMT to help attenuate stray light from the ablation source. Secondly, the signal from the PMT was magnified by a preamplifier (100X Current) before being processed by the boxcar integrator.

3.3.2 Optical-Optical Double Resonance Spectroscopy in a Broida Oven Source

The higher energy states of calcium and strontium-containing polyatomic molecules were investigated using optical-optical double resonance spectroscopy (OODR) in a Broida oven source. As can be seen in Figure 3.8 [13], the overall setup employed for these OODR investigations is rather complex and the Broida oven is only one part of an intricate experiment. Also included in the experimental setup are two lasers, an optical chopper, a photomultiplier tube, and a lock-in amplifier. How these pieces of equipment work together and result in the recording of the OODR spectra recorded will be described below.

As explained in section 3.2.2, within the oven the metal-containing molecules of interest are created by heating the metal sample and reacting the resulting hot metal vapor

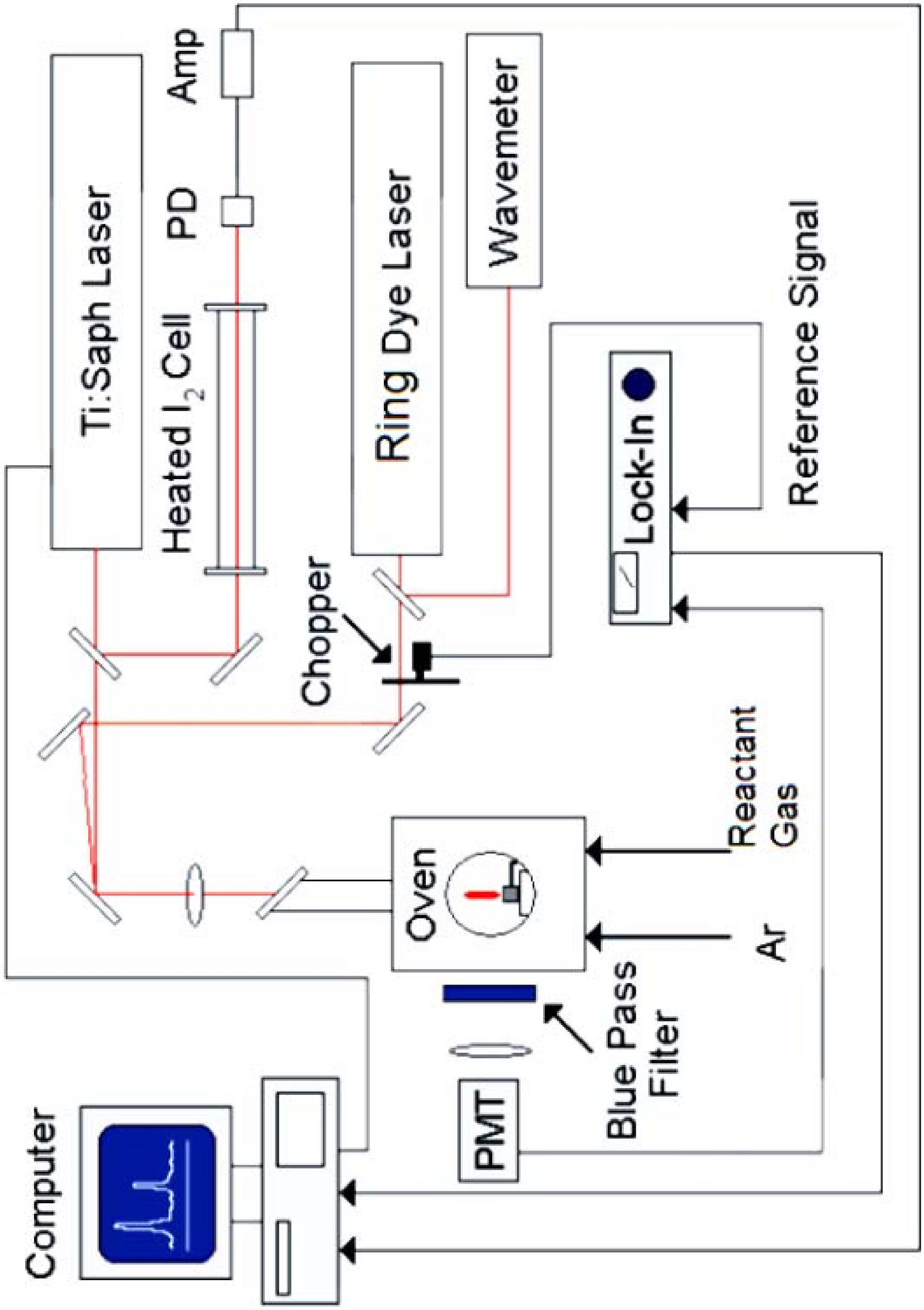

Figure 3.8 – The Overall Experimental Setup for the Optical-Optical Double Resonance Experiment

with the appropriate reactant gas. Next, the molecules are promoted from the ground to an intermediate state by a pump laser. Ideally this laser should be high in power and nearly saturate the transition. In the case of the experiments conducted in this thesis, the pump laser was a linear cavity dye laser which entered the system through a window above the oven. The frequency of this laser was monitored by an external wavemeter (Burleigh WA-2500 wavemeter junior, resolution - 0.1 cm^{-1} and update period - 0.2 seconds). Accurate pump laser wavelengths were essential so that the specific rotational levels populated in the intermediate state are known. As will be described in Chapter 8, knowing the specific rotational levels populated in the intermediate state can facilitate the assignment of the OODR spectrum.

A second laser is then introduced into the system to further excite the molecules from the intermediate level to some higher-lying state of interest. In order for the rotational levels of the higher lying state to be investigated, this probe laser should have a linewidth sufficiently narrow to scan the rotational structure of interest. In the case of the experiments presented in this thesis, the probe laser used was a titanium-sapphire ring laser.

To ensure that the maximum number of molecules are promoted to the higher lying states, both laser beams (pump and probe) must overlap in the reaction region just above the oven. To achieve this goal, the two beams are directed collinearly into the oven, and great care is taken in alignment [14]. Preliminary alignment is achieved by observing the portions of the beams reflected off the outside surface of the entrance window. This window is tilted at the Brewster angle, and hence a small fraction of each beam does not enter the reaction chamber as it is reflected away from the chamber.

When the two reflected beams are coincident, a nearly maximum overlap is also achieved in the reaction region. Final adjustments to the alignment are made following the onset of molecular production by monitoring a known OODR signal.

As the probe laser is scanned, various levels in the higher lying state are populated. The highly excited states then quickly lose this excess energy in the form of molecular fluorescence back to the ground state which, like in the laser ablation/molecular jet experiment, is collected by a photomultiplier tube. The frequency of the resulting fluorescence does not match the frequency of either the pump or probe lasers. Instead, because of the high energy of the states being probed, the photons released occur in the ultraviolet region (~355 nm).

A key difference between the OODR and laser ablation/molecular jet experiments is the lack of importance of timing in the double resonance experiment. As molecular production as well as the pump and probe lasers are all continuous, timing of the experiment is irrelevant. As a result, no boxcar is employed to selectively sample only the signal from the PMT due to molecular fluorescence. Instead the signal is sampled continuously, and unwanted signal from oven glow and scattered laser light can result in a reduction of the signal-to-noise ratio. To help remedy this problem, phase sensitive detection is used. This detection scheme is accomplished with the help of an optical chopper which modulates the pump laser beam. This in turn modulates the number of molecules promoted to the intermediate state, the number of molecules excited to the higher lying state and the resulting UV molecular fluorescence. The modulated fluorescence is then collected by the PMT and processed by a lock-in amplifier. A lock-in amplifier [15] is a device which will detect only the signal at the modulation frequency (supplied to it as a reference by the optical chopper). It then produces a DC voltage proportional to the magnitude of the modulated PMT signal. Essentially, a lock-in amplifier acts a coherent filter which eliminates all but the signal at the modulation frequency, and hence increases the signal-to-noise ratio. The phase-sensitive detection eliminates scattered light from the oven glow and probe laser, but does not eliminate the scattered light from the pump laser. As mentioned above, this laser is chopped at the modulation frequency, and therefore also contributes to the signal processed by the lock-in amplifier. To eliminate this laser scatter, a blue pass filter is placed in front of the PMT, ensuring that the signal reaching the PMT is entirely the result of the UV molecular fluorescence.

The processed signal is sent from the lock-in amplifier to the computer, where it is combined with the laser wavelength (determined by the laser wavemeter) as well as the iodine calibration spectrum, and displayed in the form of a spectrum. Figure 3.8, shows the iodine calibration setup employed for experiments in which the Ti:Saph laser was used. For these investigations, the iodine spectrum was recorded via absorption through the use of a photodiode.

References

[1] J.-G. Wang, Private Communication, 2006.

[2] G. Scoles, *Atomic and Molecular Beam Methods*, Oxford University Press, New York, 1988.

[3] J. Ross, *Advances in Chemical Physics, Volume X, Molecular Beams*, Interscience Publishers, New York, 1966.

[4] O. Svelto, *Principles of Lasers*, Plenum Publishing Corporation, New York, 4th Edition, 1998.

[5] W. Demtröder, *Laser Spectroscopy: Basic Concepts and Instrumentation*, Springer-Verlg, Berlin, 1982.

[6] S. Hopkins, *High Resolution Laser Spectroscopy of Titanium Monobromide, Hafnium Monofluoride and Strontium Monomethoxide*, PhD Thesis, University of New Brunswick, 2006.

[7] http://www.exciton.com/wavelength_chart.html.

[8] *CR699-29 Autoscan Operating Manual*, Coherent Laser Products Division, Paolo Alto, 1987.

[9] S. Gerstenkorn and P. Luc *Atlas du Spectre d'Absorption de la Molecule d'Iode* Laboratoire Aimé-Cotton, CNRS II, 91405, Orsay, 1978.

[10] S. Gerstenkorn, J. Vergès and J. Chevillard, *Atlas du Spectre d'Absorption de la Molecule d'Iode* Laboratoire Aimé-Cotton, CNRS II 91405, Orsay, 1982.

[11] *CR899-29 Autoscan Operating Manual*, Coherent Laser Products Division, Palo Alto, 1987.

[12] P. Sheridan, M. J. Dick and S. Yu, *Manual for Laser Ablation/Molecular Jet Chamber*, Waterloo, 2006.

[13] J.-G. Wang, P. M. Sheridan, M. J. Dick, S. Yu and P. F. Bernath, Paper RH04, 61st International Symposium on Molecular Spectroscopy, Columbus, OH, 19-23 June 2006.

[14] J.-G. Wang, P. M. Sheridan, M. J. Dick and P. F. Bernath, J. Mol. Spectrosc. **236**, 21 (2006).

[15] J. H. Scofield, Amer. J. Phys. **62** 129 (1994).

Chapter 4 - The $\tilde{A}\,^2\Pi$-$\tilde{X}\,^2\Sigma^+$ Transition of SrCCH

4.1 Introduction

Work on the metal monoacetylides has progressed steadily over the past 20 years. These investigations, which include both theory and experiment, have focused mainly on the alkali and alkaline-earth metals, with the notable exceptions of Cr and Yb [1,2]. A brief summary of this work follows.

Experimentally, the alkali metal monoacetylides have been studied in their ground states by millimeter wave spectroscopy. From the pure rotational spectra of LiCCH, NaCCH and KCCH [3-6], each species has been shown to be linear in its $^1\Sigma^+$ ground state. This work is in agreement with Scalmani et al. [7], who have investigated the electronic properties of these molecules using *ab initio* methods. Unfortunately, no information is available for the excited electronic states of these species, perhaps because these excited states are not expected to be bound.

The alkaline earth monoacetylides have been the subject of more extensive investigations than their alkali counterparts. The ground electronic states of MgCCH, CaCCH and SrCCH ($^2\Sigma^+$) have been studied by several experimental techniques [5,8-11], as well as by *ab initio* calculations [12-14]. In addition, experimental data exist for the excited states of these molecules. For CaCCH, the $\tilde{A}\,^2\Pi$-$\tilde{X}\,^2\Sigma^+$ transition has been observed experimentally at both low [15,16] and high resolution [17-21], including a determination of the dipole moments for the $\tilde{A}$ and $\tilde{X}$ states of CaCCH using Stark spectroscopy [22]. In addition, the $\tilde{B}\,^2\Sigma^+$ - $\tilde{X}\,^2\Sigma^+$ [23] and $\tilde{C}\,^2\Delta$ - $\tilde{X}\,^2\Sigma^+$ transitions [24] of CaCCH have been observed at low resolution using cavity ring down and laser excitation spectroscopy, respectively. The $\tilde{A}\,^2\Pi$-$\tilde{X}\,^2\Sigma^+$ transition of MgCCH has also been examined at both low [25,26] and at high resolution [27]. The $\tilde{A}$ - $\tilde{X}$ transition of SrCCH was first observed by Bernath and coworkers [15] at low resolution, while Ellis and coworkers have reported measurements of the $\tilde{B}\,'^2\Delta$ - $\tilde{X}\,^2\Sigma^+$ transition at low resolution [28].

In this chapter, the first high resolution spectroscopic analysis of the $\tilde{A}\,^2\Pi$-$\tilde{X}\,^2\Sigma^+$ transition of SrCCH is reported. For the $\tilde{A}\,^2\Pi$ state, rotational and fine structure constants have been determined. Trends in the geometries and Λ-doubling constants for the alkaline-earth monoacetylides will be discussed.

4.2 Experimental

The $\tilde{A}$ - $\tilde{X}$ transition of SrCCH was observed using the laser ablation source described in detail in Chapter 3; therefore, only the minor modifications made for this study will be discussed. In our work, the third harmonic (355 nm) of a pulsed (10 Hz) Nd/YAG laser (10 mJ/pulse) was used to vaporize a strontium target rod. (The first and second harmonics were found to produce a weaker SrCCH signal). The molecular beam was formed by the expansion of a 7% gas mixture of HCCH in Ar at a backing pressure of 100 psi, resulting in a rotational temperature of only 4 - 6 K. Following the work on MgCCH [27], a 10% mixture of CH_4 in Ar was tested as the reactant gas mixture, but HCCH was found to yield stronger SrCCH signals. Band pass filters (± 20 nm) were used to attenuate most of the plasma radiation from the ablation source.

Low resolution spectra were obtained using an Ar^+-pumped linear dye laser operating with DCM laser dye (maximum power of 800 mW when the pump power is 5

W). A typical scan rate of ~1000 cm^{-1} in 20 minutes was employed. Signals from the boxcar integrator and frequency readings from a wavemeter (Burleigh WA – 2500 Wavemeter Jr) were processed using a data acquisition program written in Labview (National Instruments).

High resolution spectra were obtained using a Coherent Autoscan 699-29 ring dye laser system (described in Chapter 3) with a line width of 10 MHz. The spectra were calibrated using I_2 lines [29] which were recorded at the same time as the experimental data. A typical spectrum was taken in 5 cm^{-1} segments at a scan speed of 60 seconds per wavenumber with a spectral sampling of 10 MHz per step. Several of these scans (4 to 6) were then averaged together to further increase the signal-to-noise ratio. Typical experimental line widths were 350 MHz, as a result of residual Doppler broadening of the molecular jet as it passes through the detection region.

4.3 Results and Analysis

Initially, a broadband survey spectrum was measured for SrCCH over the range 14000 – 16000 cm^{-1}. A portion of this spectrum is shown in Figure 4.1. The spin-orbit components of the $\tilde{A} - \tilde{X}\ (0_0^0)$ transition of SrCCH are clearly visible on the red side of the spectrum. The location of these features at 14182 cm^{-1} ($^2\Pi_{1/2}$ - $^2\Sigma^+$) and 14454 cm^{-1} ($^2\Pi_{3/2}$ - $^2\Sigma^+$) is consistent with previous observations [15]. Also visible is the $\tilde{A}\,^2\Pi$ - $\tilde{X}\,^2\Sigma^+\ (0_0^0)$ transition of SrOH, which is present as a result of impurities in the system, and the $^3P_1 - {}^1S_0$ atomic transition of Sr. Two additional small features can be attributed to the (υ_3) Sr-C stretching mode of SrCCH; the $^2\Pi_{1/2}$ - $^2\Sigma^+\ (3_0^1)$ transition is located at

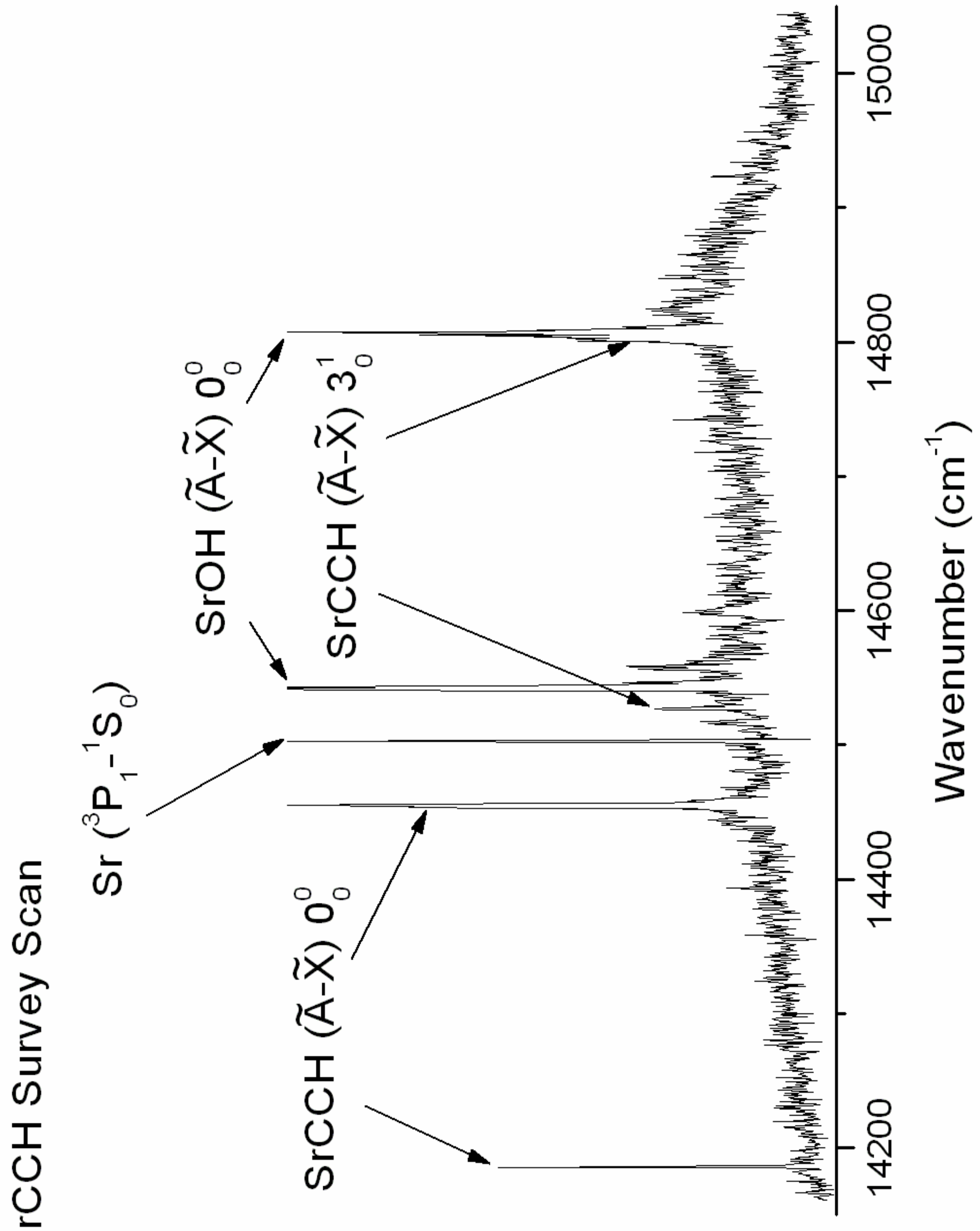

Figure 4.1 – Low resolution survey scan taken looking for SrCCH.

14527 cm^{-1} and the $^2\Pi_{3/2}$- $^2\Sigma^+$ (3^1_0) transition is found at 14800 cm^{-1}. Unfortunately, the $^2\Pi_{3/2}$- $^2\Sigma^+$ (3^1_0) transition is overlapped with the $\tilde{A}\,^2\Pi_{3/2}$ - $\tilde{X}\,^2\Sigma^+$ (0^0_0) transition of SrOH.

Using the wavemeter positions determined from the low-resolution study, high resolution spectra of the $^2\Pi_{1/2}$ - $^2\Sigma^+$ and $^2\Pi_{3/2}$ - $^2\Sigma^+$ (0^0_0) bands of SrCCH were obtained. In Figure 4.2, spectra of these two spin-orbit components are shown, one above the other for comparison. These spectra exhibit a typical Hund's case (a) $^2\Pi$ - Hund's case (b) $^2\Sigma^+$ structure for a linear molecule with, as explained in Chapter 2, ~1*B* and ~3*B* spaced branches are present. The structure for the $^2\Pi_{1/2}$ - $^2\Sigma^+$ and $^2\Pi_{3/2}$ - $^2\Sigma^+$ spin components differ, as expected, with the $^2\Pi_{3/2}$ - $^2\Sigma^+$ transition exhibiting a larger origin gap, as well as the ~1*B* spaced branches of the $^2\Pi_{1/2}$ - $^2\Sigma^+$ sub-band being more compressed.

High resolution spectra were also obtained for the (3^1_0) bands of the $^2\Pi_{1/2}$ - $^2\Sigma^+$ and $^2\Pi_{3/2}$ - $^2\Sigma^+$ transitions. Figure 4.3 shows a high resolution spectrum of the $^2\Pi_{1/2}$ - $^2\Sigma^+$ (3^1_0) band in the top panel, with the corresponding (0^0_0) band below for comparison. Unfortunately, the signal-to-noise ratio has significantly decreased in comparison to that of the (0^0_0) band; however, similar structure is still visible between the two. Even at high resolution, the $^2\Pi_{3/2}$ - $^2\Sigma^+$ (3^1_0) transition proved to be too heavily overlapped with the SrOH $\tilde{A}\,^2\Pi_{3/2}$ - $\tilde{X}\,^2\Sigma^+$ (0^0_0) band to obtain a clear spectrum.

Identification of the general branch structure for the $\tilde{A}\,^2\Pi$ - $\tilde{X}\,^2\Sigma^+$ transition of SrCCH was accomplished using the $\tilde{A}\,^2\Pi$ - $\tilde{X}\,^2\Sigma^+$ transition of SrOH [30,31] as a guide. Initial *J* assignments were made using combination differences, as described by Herzberg [32]. In Figure 4.4 a subsection of the $^2\Pi_{3/2}$ - $^2\Sigma^+$ transition is shown with these *J* assignments. The data were analyzed using a Hund's case (a) $^2\Pi$ - Hund's case (b) $^2\Sigma^+$

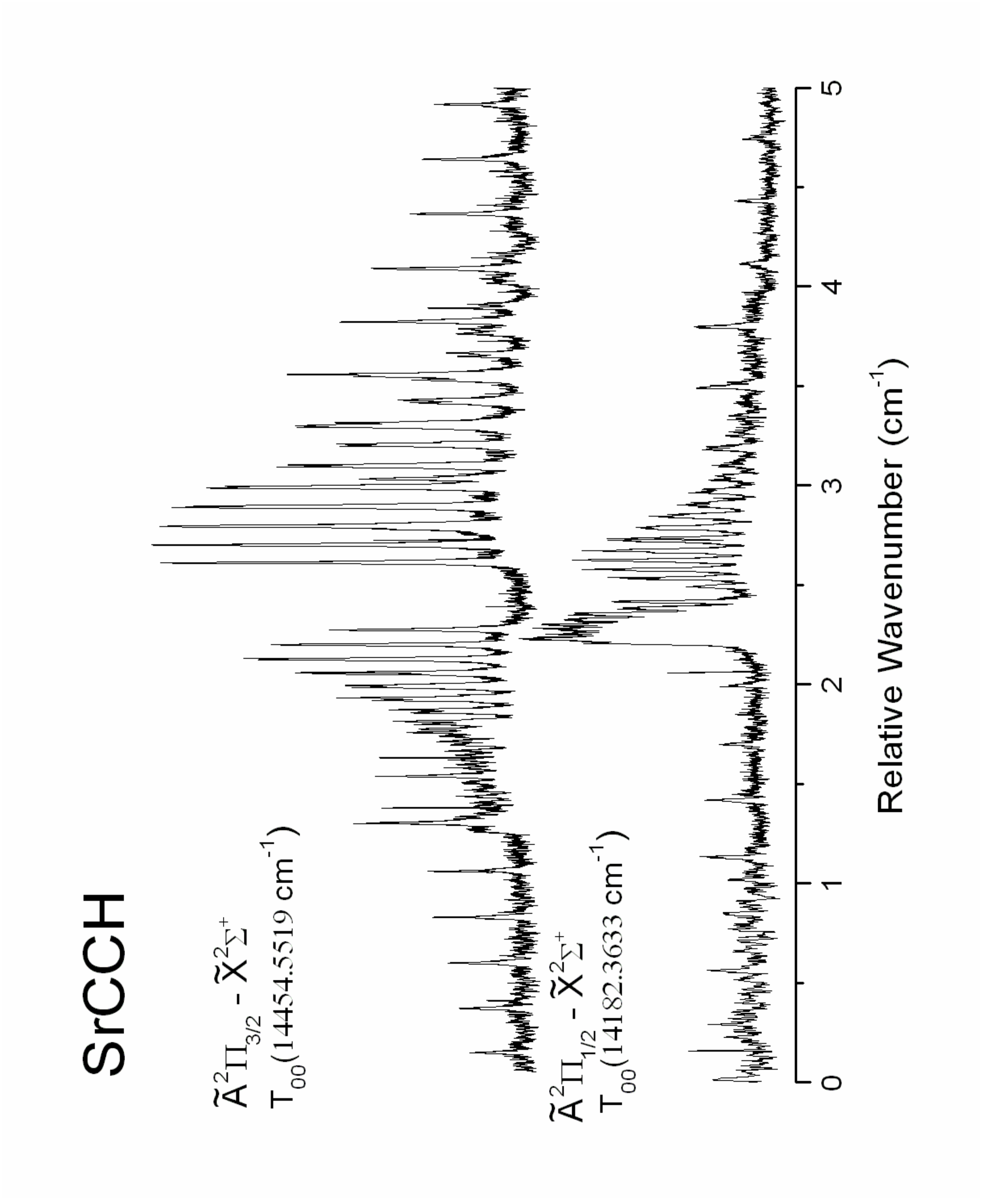

Figure 4.2 - High resolution spectra of the two spin-orbit components of the $\tilde{A}$ - $\tilde{X}$ transition of SrCCH.

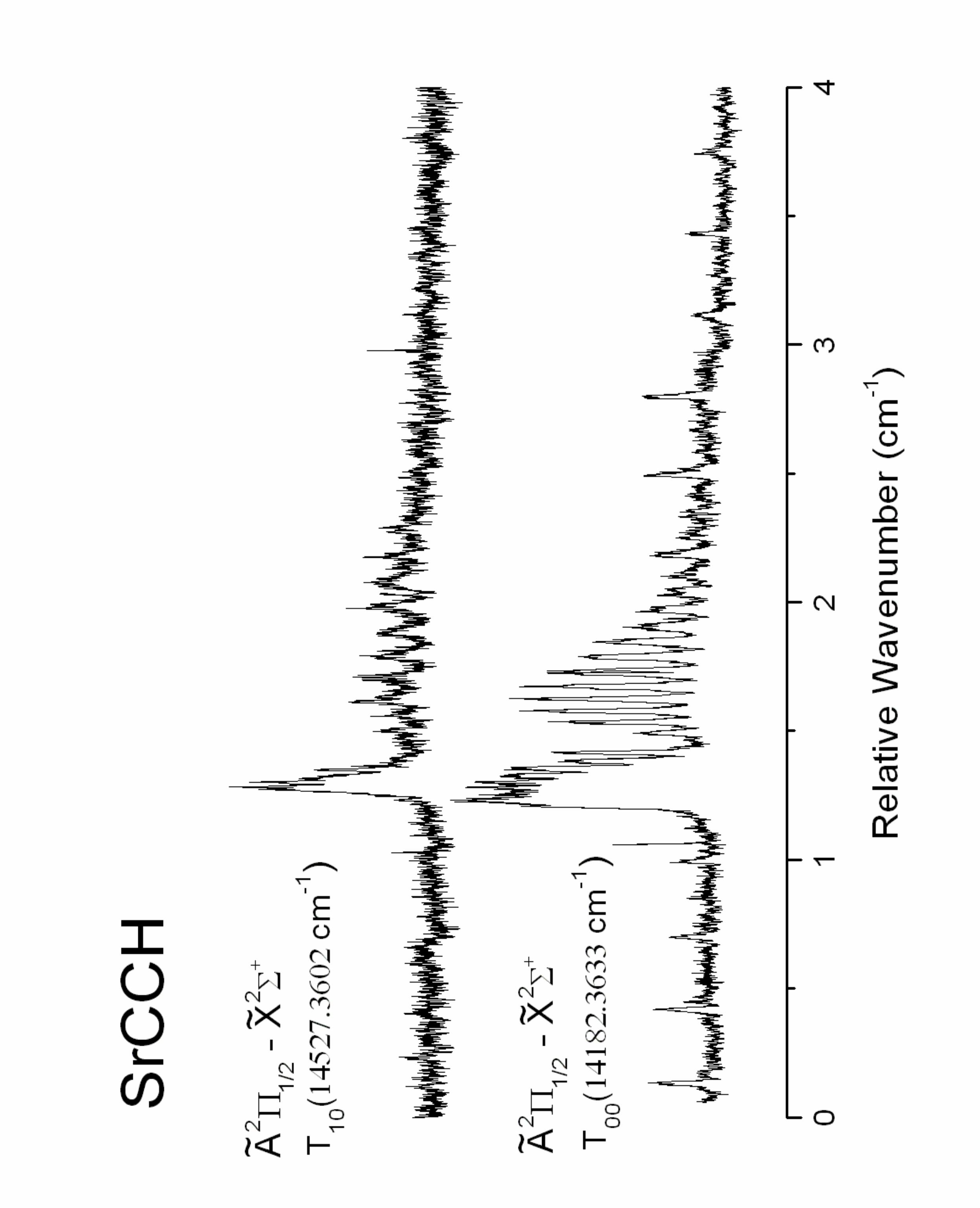

Figure 4.3 - High resolution spectra of the lower spin-orbit component of SrCCH in the (0_0^0) and (3_0^1 Sr-C stretch) bands of the $\tilde{A}$ - $\tilde{X}$ transition.

rotational Hamiltonian in a non-linear least squares fitting program. The usual $\hat{N}^2$ Hamiltonian of Brown et. al. [33] was used. For the (0_0^0) band of the $\tilde{A}$ - $\tilde{X}$ transition, the 118 lines listed in Table 4.1 were included in the fit, as well as the microwave data [11] previously measured for SrCCH. Rotational and fine structure parameters determined for both the $\tilde{X}\,(0_0)$ and $\tilde{A}\,(0^0)$ states are listed in Table 4.2. Because of the low J values accessed in this study, centrifugal distortion terms, such as D and A_D, were not well determined for the $\tilde{A}$ state.

For the (3_0^1) band, only a portion of the $^2\Pi_{1/2}$- $^2\Sigma^+$ spin component was analyzable. A total of 23 lines from the P_1, Q_{12}, Q_1, and R_{12} branches were fit separately while holding the $\tilde{X}\,^2\Sigma^+(0_0)$ constants fixed at the values determined in the (0_0^0) analysis. Additionally, the spin-orbit constant of the (3^1) state was fixed to the (0_0^0) value. As a result, only T, B, and p (Table 4.2) values were determined for the (3^1) vibrational level of the $\tilde{A}$ state.

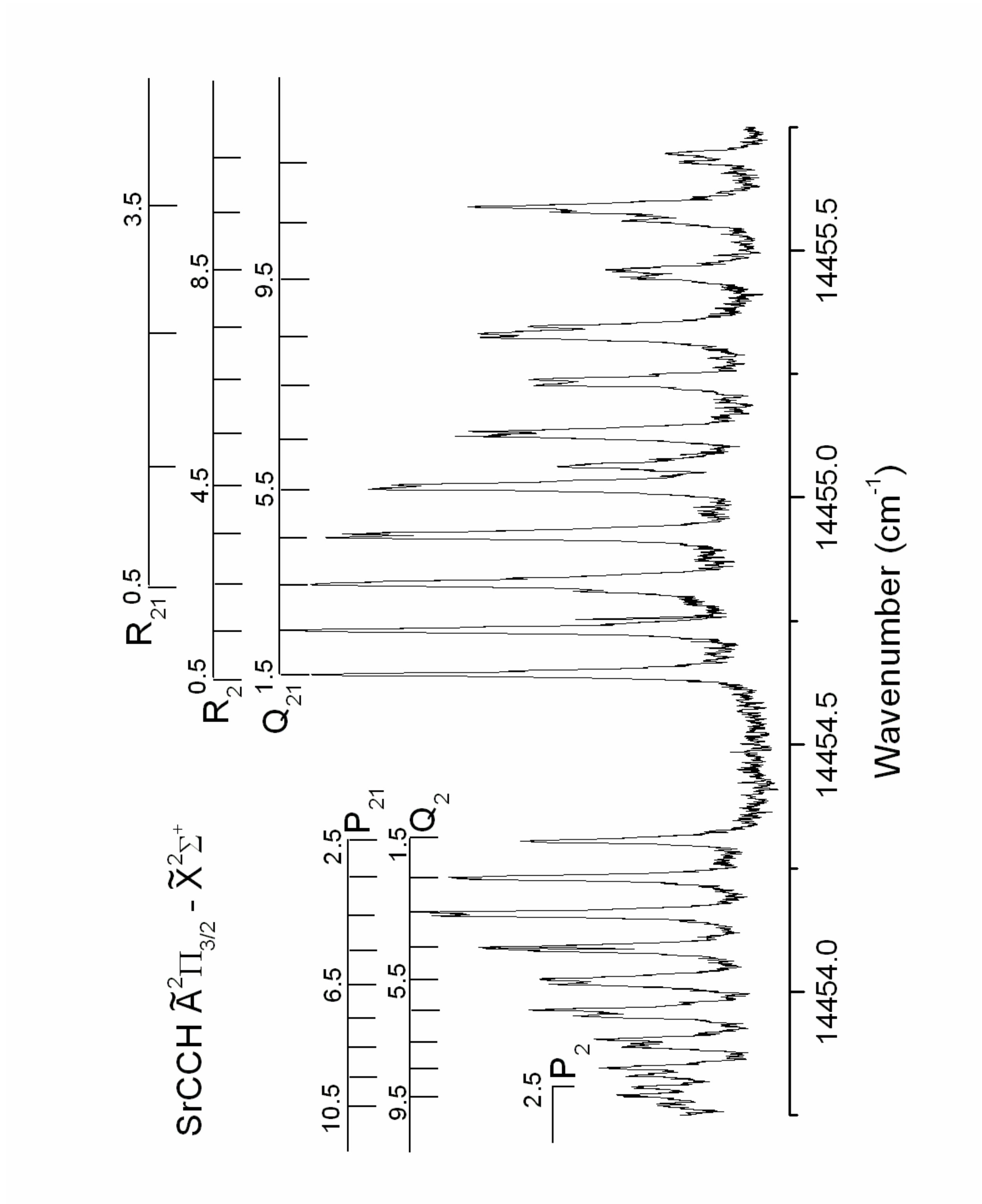

Figure 4.4 - A subsection of the high-resolution spectrum of the $\tilde{A}\,^2\Pi_{3/2}$- $\tilde{X}\,^2\Sigma^+$ spin component of SrCCH.

Table 4.1 Measured Line Positions (in cm^{-1}) for the $\widetilde{A}\,^2\Pi - \widetilde{X}\,^2\Sigma^+$ (0_0^0) Transition of SrCCH

$^2\Pi_{1/2}$ - $^2\Sigma^+$

J″	$P_1(J)$	OMC	$R_1(J)$	OMC	$Q_1(J)$	OMC	$P_{12}(J)$	OMC	$R_{12}(J)$	OMC	$Q_{12}(J)$	OMC
0.5			14182.8560	-0.0239	14182.4924	0.0048			14182.5371	0.0053	14182.4184	0.0043
1.5	14182.4184	0.0069	14183.1856	0.0026	14182.5379	0.0086	14181.9888	-0.0011	14182.5788	0.0005	14182.3794	-0.0028
2.5	14182.3794	0.0015	14183.4958	0.0064	14182.5788	0.0048	14181.6976	-0.0021	14182.6255	-0.0023	14182.3503	-0.0032
3.5	14182.3503	0.0027	14183.7943	-0.0045	14182.6255	0.0036	14181.4187	0.0060	14182.6719	-0.0084	14182.3212	-0.0068
4.5	14182.3212	0.0008	14184.1136	0.0024	14182.6815	0.0088	14181.1348	0.0061	14182.7332	-0.0025	14182.3006	-0.0050
5.5	14182.3006	0.0043	14184.4318	0.0053	14182.7253	-0.0011			14182.7893	-0.0044	14182.2813	-0.0049
6.5	14182.2813	0.0061	14184.7407	-0.0038	14182.7804	-0.0023			14182.8540	-0.0002	14182.2739	0.0042
7.5	14182.2519	-0.0051	14185.0676	0.0026	14182.8378	-0.0036			14182.9147	-0.0022	14182.2518	-0.0042
8.5	14182.2319	-0.0096	14185.3848	-0.0031	14182.9027	0.0002			14182.9804	-0.0013		
9.5			14185.7164	0.0036	14182.9634	-0.0022			14183.0468	-0.0014		
10.5			14186.0467	0.0071	14183.0261	-0.0043			14183.1138	-0.0024		
11.5									14183.1945	0.0092		

$^2\Pi_{3/2}$ - $^2\Sigma^+$

J″	$P_2(J)$	OMC	$R_2(J)$	OMC	$Q_2(J)$	OMC	$P_{21}(J)$	OMC	$R_{21}(J)$	OMC	$Q_{21}(J)$	OMC
1.5			14454.6422	0.0005	14454.3053	-0.0037			14454.8100	0.0033	14454.6422	0.0030
2.5	14453.8027	-0.0070	14454.7322	-0.0016	14454.2319	-0.0023	14454.3053	0.0005	14455.0631	-0.0007	14454.7322	0.0027
3.5	14453.5684	0.0002	14454.8239	-0.0050	14454.1605	-0.0019	14454.2319	0.0036	14455.3317	0.0080	14454.8240	0.0010
4.5	14453.3309	0.0011	14454.9257	-0.0014	14454.0903	-0.0032	14454.1540	-0.0008	14455.5885	0.0019	14454.9187	-0.0007
5.5	14453.0901	-0.0044	14455.0255	-0.0027	14454.0264	-0.0009	14454.0825	-0.0016	14455.8527	0.0005	14455.0171	-0.0017
6.5	14452.8602	-0.0019	14455.1339	0.0018	14453.9645	0.0008	14454.0165	0.0002	14456.1212	0.0007	14455.1239	0.0028
7.5	14452.6304	-0.0022	14455.2376	-0.0011	14453.9037	0.0011	14453.9514	0.0004	14456.3951	0.0039	14455.2263	0.0003
8.5	14452.4016	-0.0041	14455.3474	-0.0005	14453.8453	0.0015	14453.8891	0.0009	14456.6709	0.0068	14455.3237	-0.0098
9.5	14452.1798	-0.0016	14455.4610	0.0016	14453.7913	0.0042	14453.8290	0.0013	14456.9464	0.0073	14455.4445	0.0012
10.5			14455.5781	0.0050	14453.7309	-0.0013	14453.7696	0.0003			14455.5595	0.0042
11.5			14455.6949	0.0061	14453.6774	-0.0015	14453.7030	-0.0097			14455.6769	0.0076
12.5			14455.7983	-0.0079	14453.6274	0.0006	14453.6615	0.0039				
13.5			14455.9227	-0.0023			14453.6053	0.0014				
14.5							14453.5449	-0.0063				
15.5							14453.4970	-0.0022				

Table 4.2 Molecular Parameters (in cm^{-1}) Determined for SrCCH

Parameter	$\tilde{X}\ ^2\Sigma^+\ 0_0$	$\tilde{A}\ ^2\Pi\ 0^0$	$\tilde{A}\ ^2\Pi\ 3^1$
T	0.0	14318.45764(78)	14663.4912(15)
B	0.08337782(16)^a	0.084975(25)	0.086362(61)
$D \times 10^7$	0.26805(38)	10.5(1.4)	
$H \times 10^{14}$	6.48(29)		
$\gamma \times 10^3$	1.69664(94)		
A		272.1886(13)	272.1886
$A_D \times 10^4$		-1.13(20)	
p		-0.1101(34)	-0.05623(97)
$q \times 10^3$		9.3(1.7)	

^{a} Values in parentheses are 1σ standard deviations, in units of the last significant digits.

4.4 Discussion

As a result of the rotational analysis of the $\tilde{A}\ ^2\Pi$ - $\tilde{X}\ ^2\Sigma^+$ transition of SrCCH a molecular structure can be calculated for the $\tilde{A}$ state. Unfortunately, data for other isotopologues were not obtained, so some bond lengths must be assumed. Following the structure determination for the $\tilde{X}\ ^2\Sigma^+$ state of SrCCH, the C-H and C-C bond lengths were fixed to the experimental values for acetylene, 1.056 Å and 1.204 Å respectively [34]. Using the rotational constant obtained for the $\tilde{A}$ state, the Sr – C bond length was calculated to be 2.43 Å. It is difficult to exactly determine the uncertainty in the Sr-C separation. However if the errors in the C-C and C-H bond lengths are taken as ±0.002 Å and ±0.003 Å [34] respectively then a rough of estimate of the uncertainty (±0.012 Å) in the Sr-C separation can be obtained.

The Sr-C bond length is slightly smaller than that observed for the ground state [11], 2.46 Å. MgCCH [27] and CaCCH [18] have also shown a similar decrease in the metal-carbon bond length in the first excited state relative to the ground state. This effect has also been observed in other linear Sr containing molecules such as SrOH [30,31], and may likely be due to the increase in the distance of the unpaired electron from the ligand in the $\tilde{\mathrm{A}}$ state as compared to the $\tilde{\mathrm{X}}$ state. This allows the CCH$^-$ ligand to get closer to the Sr$^+$ metal center.

The vibrational frequency of the Sr-C stretch (υ_3) in the $\tilde{\mathrm{A}}$ state was also determined for SrCCH. This value, 345.0335 cm^{-1}, is slightly smaller than the previously reported value of 354 cm^{-1} [15], which was obtained using low resolution techniques. Unfortunately, the vibrational frequency of the Sr-C stretch for the $\tilde{\mathrm{X}}$ state of SrCCH was not determined in the current work. However, a value of 343 cm^{-1} was determined in the previous low resolution work [15]. If the vibrational frequencies of the Sr – C stretch for the ground and first excited states are compared, a small increase of only ~2 cm^{-1} is found. This suggests that the Sr – C bond strength is similar in both states. This change is much smaller than the ~55 cm^{-1} increase recently observed for MgCCH [27].

Additionally, in this analysis the Λ-doubling parameter *p* of the $\tilde{\mathrm{A}}\ ^2\Pi$ state of SrCCH was determined for the first time. As a result this constant can be compared to those of the other alkaline-earth monoacetylides, MgCCH and CaCCH. This comparison is useful for examining the validity of the pure precession relationships. Table 4.3 lists the Λ-doubling constants of the $\tilde{\mathrm{A}}$ state for the alkaline-earth monoacetylides. As shown in Chapter 2, according to the pure precession and unique perturber relationships the *p* constant should be proportional to $A_{SO}/\Delta E(\tilde{\mathrm{A}} - \tilde{\mathrm{B}})$, and hence should become increasingly negative as long as the $\tilde{\mathrm{B}}$ state is the main perturber and is higher in energy then the $\tilde{\mathrm{A}}$ state. As mentioned in the recent work on MgCCH [27], small Mg containing molecules often do not follow this trend due to an interaction between the $\tilde{\mathrm{A}}$ state and a repulsive $^2\Pi_i$ state and/or a spin polarization of the outer most two electrons on the ligand. However for CaCCH and SrCCH, *p* is negative and larger in magnitude for

SrCCH. This follows the expected trend (i.e., $p(\text{SrCCH}) < p(\text{CaCCH})$) as the $\tilde{B}\,^2\Sigma^+$ is expected to be closer in energy for SrCCH than for CaCCH. More work on the other alkaline-earth monoacetylides will be needed to see if this trend holds beyond SrCCH and CaCCH.

Table 4.3 Lambda Doubling Parameters[a] for MCCH Species

State	Parameter	MgCCH[b]	CaCCH[c]	SrCCH[d]
$\tilde{A}\,^2\Pi$	p	$4.22(22)\text{x}10^{-4}$	-0.03016(1)	-0.1101(33)
	q	$2.99(28)\text{x}10^{-5}$	$-6.947(55)\text{x}10^{-5}$	$9.3(1.7)\text{x}10^{-3}$

[a] In cm^{-1}; values in parenthesis are 1σ standard deviations, in units of the last significant digits.

[b] From Ref [26].

[c] From Ref [18].

[d] This work.

In both the current investigation of SrCCH and the previous work on CaCCH a search for the $\tilde{B}\,^2\Sigma^+$ state resulted in no observation of them by fluorescence excitation spectroscopy, and suggested that these states are predissociative. However, assuming the pure precession and unique perturber relationships are valid for the alkaline earth monoacetylides, the location of the $\tilde{B}\,^2\Sigma^+$ states can be estimated using the expression,

$$p = \frac{2A_{SO}B\ell(\ell+1)}{E(\tilde{A}^2\Pi) - E(\tilde{B}^2\Sigma^+)} \tag{4.1}$$

Recently, the validity of this equation was confirmed for CaCCH [23]. Using cavity ringdown laser spectroscopy, Tokaryk et al. located the $\tilde{B}\,^2\Sigma^+$ state ~1065 cm^{-1} above the $\tilde{A}\,^2\Pi$. This spacing is in excellent agreement with the spacing predicted by equation 4.1 (~1080 cm^{-1}, using a value of $\ell=1$ for a p atomic orbital) [18]. In addition, the fact that the $\tilde{B}\,^2\Sigma^+$ state was observed using an absorption experiment, but not in emission, is consistent with the assumption that this state is predissociative. Applying equation 4.1 to SrCCH, the $\tilde{B}\,^2\Sigma^+$ state should be located ~840 cm^{-1} above the $\tilde{A}$ state or at ~15160 cm^{-1}. As mentioned before, low resolution survey scans obtained up to 16000 cm^{-1} resulted in no observation of this state. A cavity ringdown laser spectroscopic experiment might be able to locate the $\tilde{B}\,^2\Sigma^+$ state of SrCCH.

References

[1] H-P. Loock, A. Bérces and B. Simard, J. Chem. Phys. **107**, 2720 (1997).

[2] D.J. Brugh, R.S. DaBell and M.D. Morse, J. Chem. Phys. **121**, 12379 (2004).

[3] A.J. Apponi, M.A. Brewester and L.M. Ziurys, Chem. Phys. Lett. **298**, 161 (1998).

[4] D.B. Grotjahn, A.J. Apponi, M.A. Brewster, J. Xin and L.M. Ziurys, Angew. Chemie. Int. Ed. **37**, 2678 (1998).

[5] M.A. Brewster, A.J. Apponi, J. Xin and L.M. Ziurys, Chem. Phys. Lett. **310**, 411 (1999).

[6] J. Xin and L.M. Ziurys, Astrophys. J. **501**, L151 (1998).

[7] G. Scalmani, J.L. Brédas and V. Barone, J. Chem. Phys. **112**, 1178 (2000).

[8] M. A. Anderson and L. M. Ziurys, Astrophys J. **439**, L25 (1995).

[9] M. A. Anderson and L. M. Ziurys, Astrophys. J. **444**, L57 (1995).

[10] M. Li and J. Coxon, J. Mol. Spectrosc. **184**, 395 (1997).

[11] B.P. Nuccio, A.J. Apponi and L.M. Ziurys, Chem. Phys. Lett. **247**, 283 (1995).

[12] D.E. Woon, Astrophys. J. **456**, 602 (1996).

[13] D.E. Woon, Chem. Phys. Lett. **274**, 299 (1997).

[14] W.-T. Chan and I.P. Hamilton, Chem. Phys Lett. **297**, 217 (1998).

[15] A.M.R.P. Bopegedra, C.R. Brazier and P.F. Bernath, Chem. Phys. Lett. **136**, 97 (1987).

[16] C.J. Whitham, B. Soep, J-P. Visticot and A. Keller, J. Chem Phys. **93**, 991 (1990).

[17] A.M.R.P. Bopegedra, C.R. Brazier and P.F. Bernath, J. Mol. Spectrosc. **129**, 268 (1988).

[18] M. Li and J. Coxon, J. Mol. Spectrosc. **176**, 206 (1996).

[19] M. Li and J. Coxon, J. Mol. Spectrosc. **180**, 287 (1996).

[20] M. Li and J. Coxon, J. Mol. Spectrosc. **183**, 250 (1997).

[21] M. Li and J. Coxon, J. Mol. Spectrosc. **196**, 14 (1999).

[22] A.J. Marr, J. Perry and T.C. Steimle, J. Chem. Phys. **103**, 3861 (1995).

[23] D. W. Tokaryk, A. G. Adam and M. E. Slaney, Chem. Phys. Lett. **433**, 264 (2007).

[24] M. Elhanine, R. Lawruszczuk and B. Soep, Chem. Phys. Lett. **288**, 785 (1998).

[25] G.K. Corlett, M.S. Beardah and A.M. Ellis, J. Mol. Spectrosc. **185**, 202 (1997).

[26] G.K. Corlett, A.M. Little and A.M. Ellis, Chem. Phys. Lett. **249**, 53 (1996).

[27] D.W. Tokaryk, A.G. Adam and W.S. Hopkins, J. Mol. Spectrosc. **230**, 54 (2005).

[28] G.M. Greetham and A.M. Ellis, J. Mol. Spectrosc. **206**, 198 (2001).

[29] S. Gerstenkorn and P. Luc *Atlas du Spectre d'Absorption de la Molecule d'Iode* Laboratoire Aimé-Cotton, CNRS II, 91405, Orsay, 1978.

[30] C.R. Brazier and P.F. Bernath, J. Mol. Spectrosc. **114**, 163 (1985).

[31] P.I. Presunka and J.A. Coxon, Chem. Phys. Lett. **190**, 97 (1995).

[32] G. Herzberg, *Molecular Spectra and Molecular Structure, Vol. I – Spectra of Diatomic Molecules*, 2nd edition, Krieger Publishing Company, Malabar, 1950.

[33] J. M. Brown, E. A. Colbourn, J. K. G. Watson and F. D. Wayne, J. Mol. Spectrosc. **74**, 294 (1979).

[34] *Handbook of Chemistry and Physics*, 63rd edition, CRC Press, Boca Raton, 1982.

Chapter 5 – The $\tilde{B}^2A_1$- $\tilde{X}^2A_1$ Transitions of $CaCH_3$ and $SrCH_3$

5.1 Introduction

The metal monomethyls (MCH_3), have been the subject of much research. In particular, the alkali, alkaline-earth, group 13 and transition metal monomethyls have been studied quite extensively using both experimental and theoretical methods.

A variety of theoretical methods have been used to examine the electronic structure, chemical reactivity, and spectroscopic parameters of many MCH_3 molecules. The monomethyls of the alkali and alkaline-earth metals, $LiCH_3$ [1-4], $NaCH_3$ [1,2,4], KCH_3 [2], $BeCH_3$ [5], $MgCH_3$ [5-8], $CaCH_3$ [5,9-11], and $SrCH_3$ [9], and of the group 13 metals $AlCH_3$ [12], $GaCH_3$ [13] have received the greatest attention. For most of the transition metals, theoretical investigations have been limited to the comprehensive work of Bauschlicher and co-workers [14] in which metal-carbon bond dissociation energies as well as geometries for all the first and second-row transition metal monomethyls and their positive ions were calculated. Only a few theoretical studies exist for individual transition metal species, for example $ZnCH_3$ [15-17], $NiCH_3$ [18], and $FeCH_3$ [19].

The metal monomethyls have also been studied by a wide array of experimental techniques. Mass spectrometric studies have been used to detect alkyl aluminum fragments such as $AlCH_3$ [20,21]. The electronic and vibrational structure of $CrCH_3$ and $NiCH_3$ [22] have been probed using resonant two-photon ionization spectroscopy. Ion beam studies have been used to measure the dissociation energies of the reaction products of transition metals with alkanes, such as $CoCH_3^+$ [23] and $MnCH_3^+$ [24]. A variety of laser excitation experiments, including fluorescence depletion (FDS), zero electron kinetic energy (ZEKE) photoelectron, and resonance-enhanced multiphoton ionization

(REMPI) spectroscopies, have been used to characterize $ZnCH_3$ and $CdCH_3$ [25-32]. In addition, Ziurys and co-workers have measured pure rotational spectra of many of these species using millimeter-wave spectroscopy. Their studies have included the monomethyls of Li, Na, K, Al and Cu [33-37]. They also determined the first r_o structures for Li, K and Cu monomethyls [35,37] by recording the spectra of several isotopologues.

The main focus of the work presented in this chapter has centered on further investigations of the alkaline earth monomethyls. The first of these species to be observed were $CaCH_3$ and $SrCH_3$ [38]. In that work, the low-resolution spectra of the $\tilde{A}\,^2E$- $\tilde{X}\,^2A_1$ and $\tilde{B}\,^2A_1$- $\tilde{X}\,^2A_1$ transitions were recorded and a vibrational analysis by laser spectroscopy was performed. Subsequently, high-resolution spectra of the $\tilde{A}\,^2E$ - $\tilde{X}\,^2A_1$ transition of $CaCH_3$ [39,40] were measured from which rotational and fine structure parameters were determined. This study was followed by the detection of $MgCH_3$ via high-resolution laser excitation spectroscopy of the $\tilde{A}\,^2E$ - $\tilde{X}\,^2A_1$ transition [41], and additional investigations of the rovibronic structure and bonding in this molecule were carried out [26,42]. The pure rotational spectra of the main isotopologues $MgCH_3$, $CaCH_3$ and $SrCH_3$ as well as of $BaCH_3$, have been measured using millimeter-wave spectroscopy [43-46]. Also, hyperfine structure in $CaCH_3$ has been observed by the pump/probe microwave-optical double resonance (PPMODR) technique [47].

Despite these numerous studies, the $\tilde{B}\,^2A_1$ state has not yet been examined at high-resolution for any of the alkaline-earth monomethyls. In order to further investigate the low-lying states of the alkaline-earth metal monomethyls, a high-resolution study of the $\tilde{B}\,^2A_1$- $\tilde{X}\,^2A_1$ electronic transitions of $CaCH_3$ and $SrCH_3$ was initiated. From this analysis of the high-resolution spectra, rotational and fine structure parameters have been determined for the $\tilde{B}\,^2A_1$ state for the first time. A comparison of the structure of these alkaline-earth monomethyls in their low-lying electronic states and of the fine structure constants in the $\tilde{B}\,^2A_1$ state in terms of the pure precession approximation will be presented.

5.2 Experimental

SrCH$_3$ and CaCH$_3$ were synthesized using the laser ablation/molecular beam apparatus described more fully in Chapter 3. Only a brief discussion of the experimental parameters used in the investigation of the $\tilde{B}\,^2A_1$- $\tilde{X}\,^2A_1$ transitions of CaCH$_3$ and SrCH$_3$ will be presented here. The third harmonic (355 nm) of a pulsed (10 Hz) Nd/YAG laser (10 mJ/pulse) was used to vaporize either a calcium or strontium metal target rod. Using a gas mixture of 1% tetramethyltin in Ar at a backing pressure of 100 psi, a free jet expansion was formed following the reaction of the hot metal atoms with the gas mixture. Rotationally cooled (4 – 6 K) CaCH$_3$ and SrCH$_3$ molecules were interrogated by a probe laser ~15 cm downstream. The resulting laser induced fluorescence was collected using a photomultiplier tube, with the plasma radiation from the ablation source being attenuated using band pass filters (± 20 nm). The signal was sent through a preamplifier (100X current) and then processed by a boxcar integrator.

A Coherent 699-29 ring dye laser system (described in Chapter 3) was used to obtain high-resolution spectra of the $\tilde{B}\,^2A_1$- $\tilde{X}\,^2A_1$ transitions of CaCH$_3$ and SrCH$_3$ (line width ~10 MHz). The I$_2$ spectrum, recorded simultaneously with the experimental data, was used to calibrate the line positions [48]. Spectra were typically obtained in 5 cm^{-1}

segments at a scan speed of 180 seconds per cm^{-1} with a spectral data sampling of 10 MHz per step. For $CaCH_3$, up to four 5 cm^{-1} scan segments (obtained on the same day) were averaged together in order to increase the signal-to-noise ratio. Experimental line widths were ~350 MHz, a result of residual Doppler broadening in the molecular jet.

5.3 Results

Using the previous low-resolution investigation [38] as a guide, high resolution spectra of the $\tilde{B}\,^2A_1$- $\tilde{X}\,^2A_1$ transitions of $CaCH_3$ and $SrCH_3$ were recorded. The overall spectrum for each molecule is plotted in Figure 5.1 ($SrCH_3$ on top; $CaCH_3$ on bottom) on a relative wavenumber axis for comparison. As described in Chapter 2, each of these spectra exhibits a pattern typical for a Hund's case (b) $^2\Sigma$ – Hund's case (b) $^2\Sigma$ parallel type transition with well defined P and R branches and rotational line spacings of ~ 2B [49]. Where the spectra of each molecule differ is in the area of the origin. A larger gap is observed in $CaCH_3$, suggesting the Q branch transitions have been shifted.

As described in chapter 2, $SrCH_3$ and $CaCH_3$ are prolate symmetric top molecules and belong to the C_{3v} point group. The transition dipole moment lies along the *a* molecular axis (metal-carbon bond), and for $^2A_1 - {}^2A_1$ transitions, the selection rule $\Delta K = 0$ results and transitions can be grouped into sub-bands labeled by K. Not mentioned in Chapter 2 is the effect of nuclear spin statistics on the observed spectra. These statistics group rotational levels into two nuclear spin states: *ortho* (K = 3N, where N is an integer) and *para* ($K \neq$ 3N) [50]. The primary effect of these nuclear spin states is to enhance the intensity of the $K'' = 1$ levels beyond what is expected for normal collisional

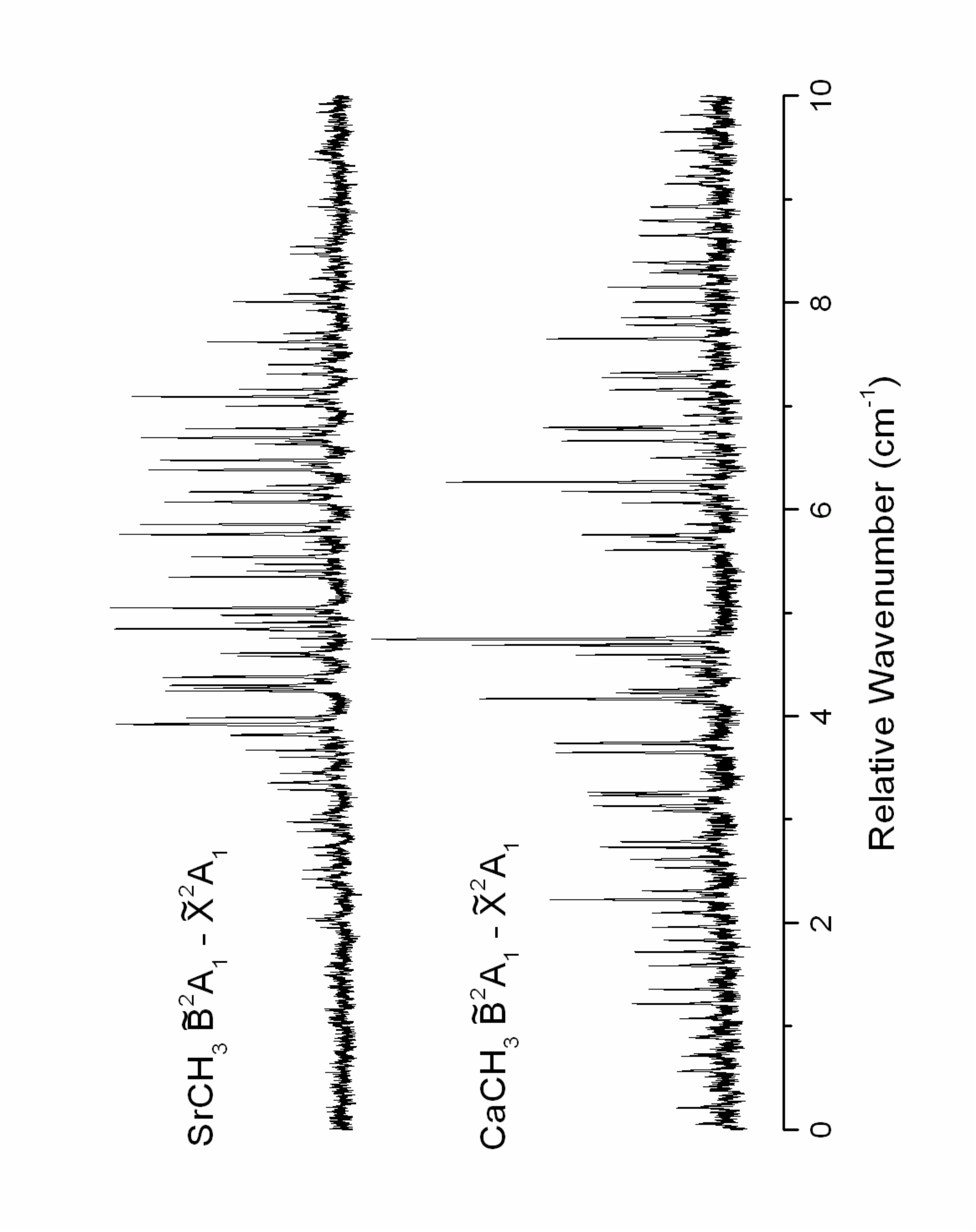

Figure 5.1 - Overall high-resolution spectra of the $\tilde{B}\,^2A_1$- $\tilde{X}\,^2A_1$ transition of $SrCH_3$ (top panel) and $CaCH_3$ (bottom panel).

cooling because *para* states cannot cool to *ortho* states or vice versa in the free jet expansion. As a result, both $K'' = 0$ (*ortho*) and $K'' = 1$ (*para*) levels of the $\tilde{X}\,^2A_1$ state are populated in our molecular jet, and transitions originating from both levels are expected to be readily observed in our spectra. Energy level diagrams and rotational transition structure for the $K = 0$ and 1 sub-bands of the $\tilde{B}\,^2A_1$- $\tilde{X}\,^2A_1$ transitions are presented Chapter 2.

For $SrCH_3$, individual P and R branches were identified in the spectrum of the $\tilde{B}\,^2A_1$- $\tilde{X}\,^2A_1$ transition with little difficulty. Each branch was then assigned as arising from either the F_1 or F_2 spin component, based on their relative line spacings, which differed due to the spin-rotation interaction being larger in the $\tilde{B}\,^2A_1$ state than in the $\tilde{X}\,^2A_1$ state. Ground-state combination differences, available from the millimeter-wave work [45], were used to match the corresponding P and R branches across the origin and confirm the J assignments. Initially, the P and R branches of the $K = 0$ sub-band were added to the fitting program, followed by those of the $K = 1$ sub-band. The remaining satellite and ^QQ branches were then predicted, identified, and added to the fit. For the $\tilde{B}\,^2A_1$- $\tilde{X}\,^2A_1$ transition, 108 lines were measured and are listed in Appendix A1. Figure 5.2 shows a short section of the high-resolution spectrum of the $\tilde{B}\,^2A_1$- $\tilde{X}\,^2A_1$ transition of $SrCH_3$ with these branch assignments. Transitions arising from the $K = 0$ sub-band are labeled on top in italics, while those from the $K = 1$ sub-band are labeled below. The effect of the larger spin rotation interaction in the $\tilde{B}\,^2A_1$ state is apparent in the line spacings observed; for example, the $^PP_{11}$ and $^RR_{22}$ branches possess a greater spacing than the $^PP_{22}$ and $^RR_{11}$ branches. The $^QR_{12}$, $^QP_{12}$, $^QQ_{22}$ and $^QP_{21}$ branches of the K

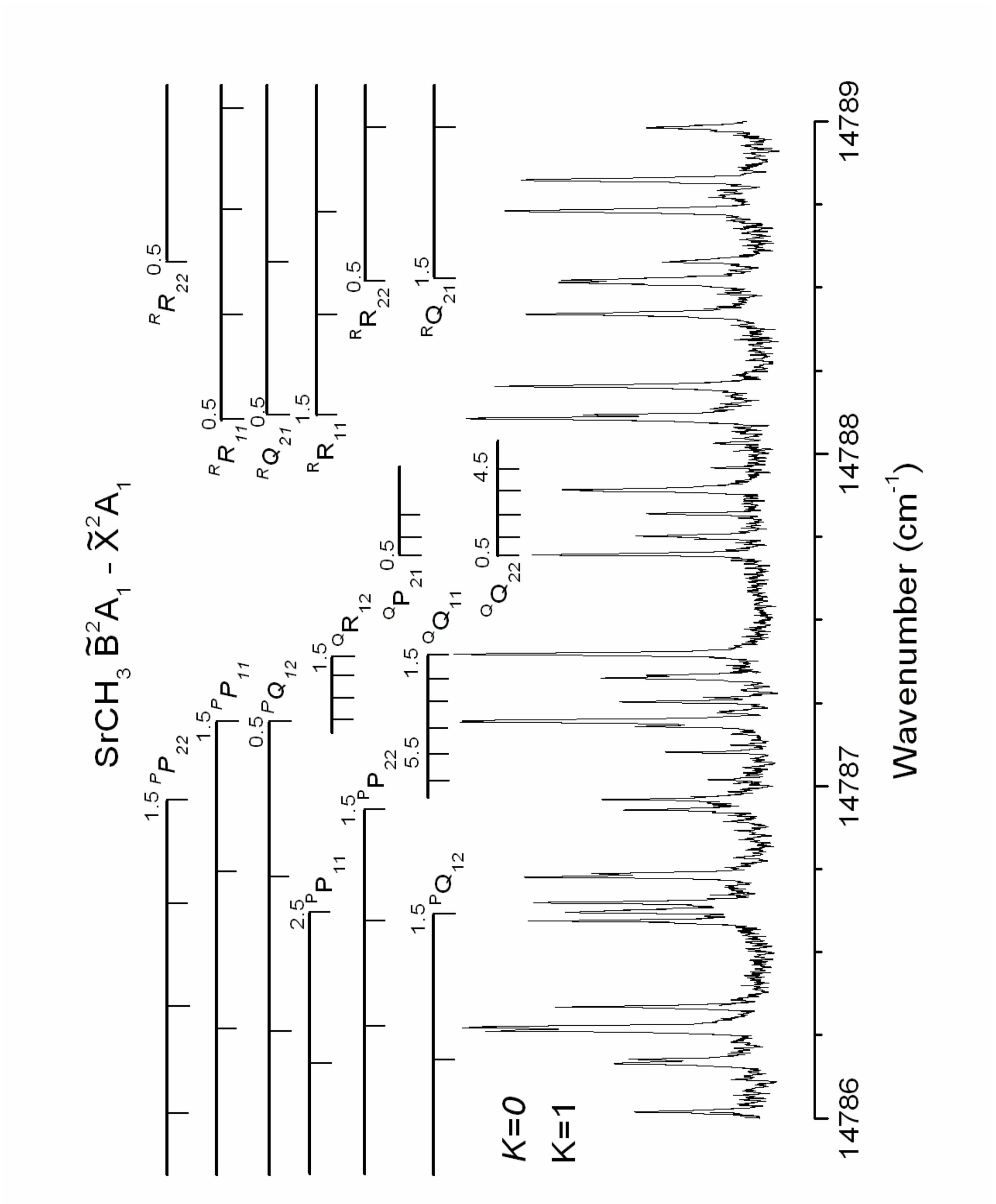

Figure 5.2 - A sub-section of the $\tilde{B}\,^2A_1$- $\tilde{X}\,^2A_1$ spectrum of $SrCH_3$ near the origin is shown with branch assignments.

= 1 sub-band are found near the origin, each exhibiting an evenly spaced pattern of lines with J values increasing in the direction away from the origin.

Initially, line assignments of the of the $\tilde{B}\,^2A_1$- $\tilde{X}\,^2A_1$ transition of $CaCH_3$ were made following the method outlined for $SrCH_3$. Main and satellite branch transitions of the $K = 0$ sub-band were first identified and added to the fit. However, the remaining unassigned features did not exhibit a similar spectral pattern, as was observed for the $K = 1$ sub-band of $SrCH_3$. Although these lines could be grouped into branches, their relative spacings did not resemble those observed in the $K = 0$ sub-band, making assignment of the F_1 and F_2 spin components difficult. Also, as mentioned previously, no clear $\Delta N = 0$ transitions (${}^QQ_{11}$, ${}^QQ_{22}$, ${}^QR_{12}$, ${}^QP_{21}$ branches) were found in the origin region, although a condensed area of lines was observed to lower wavenumbers. Despite these differences, quantum numbers were finally assigned to the remaining features using lower state combination differences [44]. For the $\tilde{B}\,^2A_1$- $\tilde{X}\,^2A_1$ transition, 132 lines were measured and are listed in Appendix A2. Figure 5.3 shows a subsection of the $\tilde{B}\,^2A_1$- $\tilde{X}\,^2A_1$ spectrum of $CaCH_3$. As mentioned before, the structure of the $K = 0$ sub-band (labeled on top in italics) appears similar to that observed for $SrCH_3$. For the $K = 1$ sub-band (labeled on bottom) each branch appears shifted to lower wavenumbers relative to the $K = 0$ sub-band. All $\Delta N = 0$ branches appear condensed, with the ${}^QQ_{22}$ and ${}^QP_{21}$ branches exhibiting an uneven spacing. The red shift of the $K = 1$ sub-band suggests a perturbation in the $K' = 1$ levels of the $\tilde{B}\,^2A_1$ state as the $K'' = 1$ levels of the $\tilde{X}\,^2A_1$ state [44,47] appear to be unperturbed.

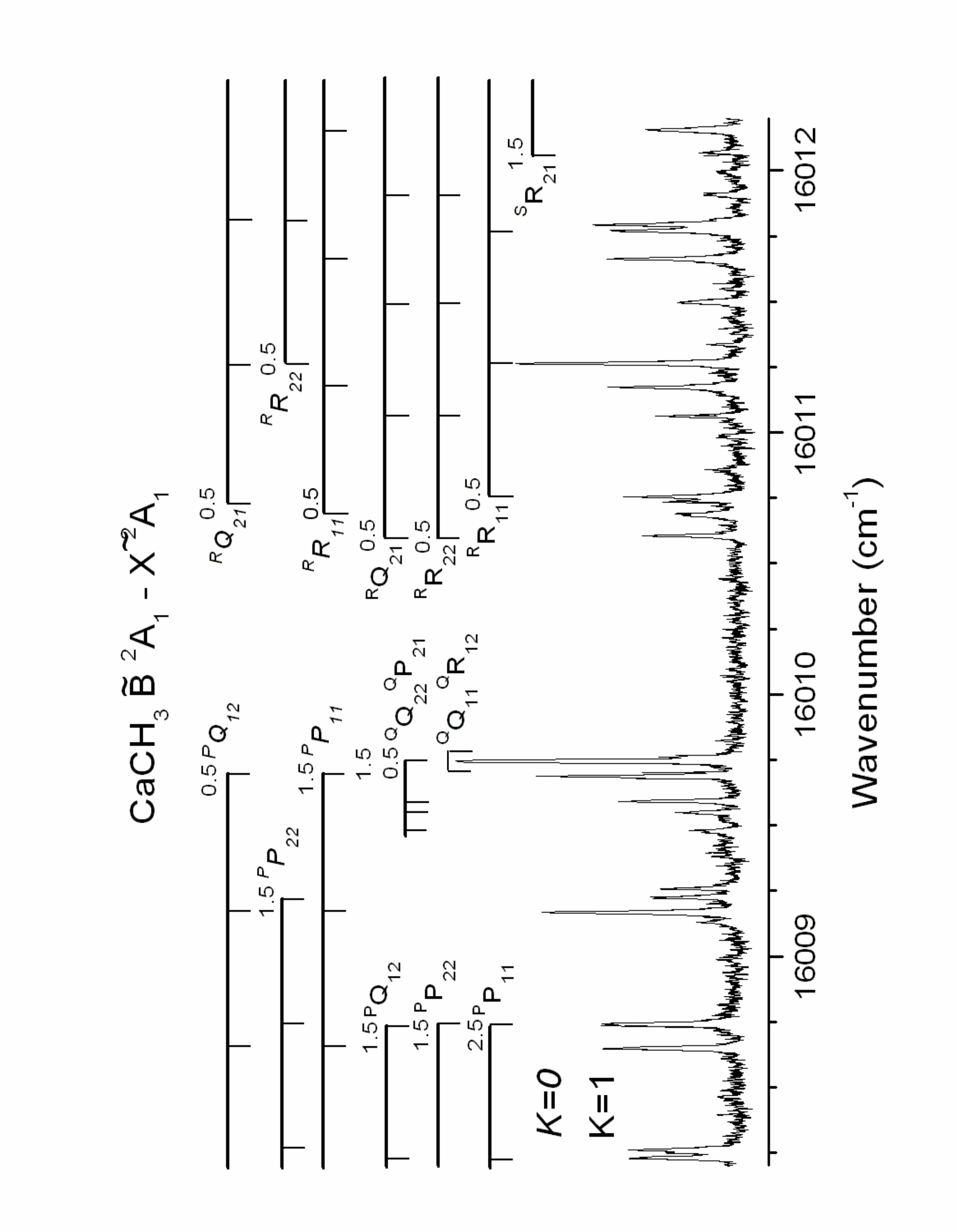

Figure 5.3 - A sub-section of the $\tilde{B}\,^2A_1$- $\tilde{X}\,^2A_1$ spectrum of $CaCH_3$ near the origin is shown with branch assignments.

5.4 Analysis

The data recorded for the $\tilde{B}\,^2A_1$- $\tilde{X}\,^2A_1$ transitions of $CaCH_3$ and $SrCH_3$ were fit using an appropriate effective Hamiltonian to model each $^2A_1$ state of the form [41,45,51]

$$\hat{H}_{Eff} = \hat{H}_{Rot} + \hat{H}_{CD} + \hat{H}_{SR} \tag{5.1}$$

As described in Chapter 2, $\hat{H}_{Rot}$ describes the rotational motion and $\hat{H}_{SR}$ accounts for the spin-rotation fine structure interaction. The other term ($\hat{H}_{CD}$) contains centrifugal distortion terms not elaborated on in Chapter 2.

Using the fitting program developed by Pickett [52], a least squares fit of the experimental data to the Hamiltonian in equation 5.1 was performed. For $SrCH_3$, the data set included all lines arising from the $K = 0$ and $K = 1$ sub-bands ($J \leq 10.5$) and the pure rotational data [45], which was included to obtain proper experimental errors. The two data sets were weighted according to their experimental uncertainties (optical transitions - 0.003 cm^{-1}; pure rotational data - 60 kHz). Values of the spectroscopic constants determined in the final fit for the $\tilde{B}\,^2A_1$ and $\tilde{X}\,^2A_1$ states of $SrCH_3$ are listed in Table 5.1. The ground state $\tilde{X}\,^2A_1$ parameters in the fit differ slightly from the millimeter-wave work because ε_{aa} was fit and the centrifugal distortion constant D_K and the spin-rotation centrifugal distortion constants D_{NKS} and D_{NS} were fixed to zero. These changes produced residuals smaller than those previously reported [45] and are similar to the changes made in the refit of the millimeter-wave data of $CaCH_3$ in the subsequent PPMODR study [47] of this molecule. In addition, the A rotational constant in the ground state was fixed to the theoretical value [9]. For the $\tilde{B}\,^2A_1$ state, the values of the B rotational constant, the centrifugal distortion constant D_{NK} and the spin rotation constant ε_{bc} were determined. Because transitions from the $K = 1$ sub-band were included in the fit, the A rotational constant (actually ΔA) as well as ε_{aa} could be ascertained.

For $CaCH_3$, transitions arising from only the $K = 0$ sub-band were included in the final fit using the same weighting factors as for $SrCH_3$. All attempts to include data from the $K = 1$ sub-band failed because of the perturbation. The pure rotational transitions of $CaCH_3$ [44] were included in the final fit. The spectroscopic parameters derived from the fit of the data for the $\tilde{B}\,^2A_1$ and $\tilde{X}\,^2A_1$ states of $CaCH_3$ are also listed in Table 5.1. The ground state constants are in good agreement with those reported in the PPMODR work [47]. The A rotational constant was fixed at the value determined experimentally in the analysis of the $\tilde{A}\,^2E$ - $\tilde{X}\,^2A_1$ transition [39]. For the $\tilde{B}\,^2A_1$ state, only B and ε_{bc} could be determined from the limited data set.

Table 5.1 Spectroscopic Constants (in cm^{-1}) for the $\tilde{B}\,^2A_1$ and $\tilde{X}\,^2A_1$ States of $CaCH_3$ and $SrCH_3$

Constant [a]	$CaCH_3$		$SrCH_3$	
	$\tilde{X}\,^2A_1$	$\tilde{B}\,^2A_1$	$\tilde{X}\,^2A_1$	$\tilde{B}\,^2A_1$
T	0.0	16010.19525(60)	0.0	14787.58134(64)
A	5.44831 [b]		5.390 [c]	5.30929(84)
B	0.252384873(17)	0.2532542(98)	0.193833336(16)	0.193603(14)
D_N	3.54482(19) x 10^{-7}		2.14893(11) x 10^{-7}	
D_{NK}	1.99555(21) x 10^{-5}		1.61349(51) x 10^{-5}	5.3(1.8) x 10^{-5}
H_{NK}	4.044(23) x 10^{-10}		2.920(22) x 10^{-10}	
H_{KN}	3.520(21) x 10^{-9}		3.19(43) x 10^{-9}	
ε_{aa}	0.0002187(73)		0.000884(35)	-0.2522(21)
ε_{bc}	0.00185214(37)	-0.03577(12)	0.00412853(44)	-0.14878(11)

[a] Values in parenthesis are 1σ standard deviations, in units of the last significant digits.

[b] Fixed to experimental value [39]

[c] Fixed to theoretical value [9].

5.5 Discussion

The structures of $CaCH_3$ and $SrCH_3$ in the $\tilde{B}\,^2A_1$ states can be estimated using the rotational constants derived in this study. Table 5.2 contains the known geometric parameters for the $\tilde{X}\,^2A_1$, $\tilde{A}\,^2E$, and $\tilde{B}\,^2A_1$ states of these molecules. Unfortunately, no relevant isotopologue data is available for these species; therefore, at least one structural parameter was assumed in each state. Because the C-H bond length should exhibit the smallest change on electronic excitation, as in $CaOCH_3$ [53], this parameter was fixed to the ground-state theoretical value in each state for each molecule. For $SrCH_3$, an additional assumption was made by using the theoretical value of the *A* rotational constant in the $\tilde{X}\,^2A_1$ state. For $CaCH_3$, no additional assumptions regarding the $\tilde{A}\,^2E$ and $\tilde{X}\,^2A_1$ states were necessary, as *A* was determined experimentally in the previous optical analysis. In the $\tilde{B}\,^2A_1$ state, the metal-carbon bond length was fixed to the ground-state value, since *A* could not be determined.

Table 5.2 Structural Parameters for Alkaline-Earth Monomethyls

State	Parameter	$CaCH_3$	$SrCH_3$ [a]
$\tilde{X}\,^2A_1$	$r_{M\text{-}C}$ (Å)	2.348	2.487
	$r_{C\text{-}H}$ (Å)[b]	1.102	1.104
	$\theta_{H\text{-}C\text{-}H}$ (°)	105.3	105.8
$\tilde{A}\,^2E$	$r_{M\text{-}C}$ (Å)	2.342	
	$r_{C\text{-}H}$ (Å)[b]	1.102	
	$\theta_{H\text{-}C\text{-}H}$ (°)	106.2	
$\tilde{B}\,^2A_1$	$r_{M\text{-}C}$ (Å)	2.348[c]	2.492
	$r_{C\text{-}H}$ (Å)[b]	1.102	1.104
	$\theta_{H\text{-}C\text{-}H}$ (°)	106.6	107.0

a Value of *A* in the ground state fixed to the theoretical value [14].
b Fixed to theoretical value [9].
c Fixed to ground state value.

Before structural information from the rotational constants in the excited states of calcium and strontium monomethyl is extracted, the second order spin-orbit contributions to these parameters need to be considered. For the *A* rotational constant of the $\tilde{A}\,^2E$ state of $CaCH_3$, second-order contributions were found to comprise only ~0.35% of its total value [40]. Similarly, for the *A* and *B* rotational constants of the $\tilde{B}\,^2A_1$ states of $CaCH_3$ and $SrCH_3$, the effect was calculated to be less than 0.1% of these parameters. Therefore, differences observed between the rotational constants in the excited states of $CaCH_3$ and $SrCH_3$ are due to structural changes, and the geometries derived in Table 5.2 can be considered without modification.

Although the geometric parameters for $CaCH_3$ and $SrCH_3$ listed in Table 5.2 are based on several assumptions, they provide a reasonable estimate of the metal-carbon bond length in these low-lying electronic states. For $CaCH_3$ the metal-carbon bond length decreases ~0.006 Å from the $\tilde{X}\,^2A_1$ state ($s\sigma$ orbital) to the $\tilde{A}\,^2E$ state ($p\pi$ orbital), while in $SrCH_3$, the metal-carbon bond length exhibits a small increase (0.005 Å) between the $\tilde{X}\,^2A_1$ and $\tilde{B}\,^2A_1$ ($p\sigma$ orbital) electronic states. For calcium and strontium polyatomic radicals (MOH, MCCH, MNH_2 and $MOCH_3$), the metal-ligand bond length has typically been observed to decrease by > 0.01 Å on excitation from the ground state to similar low-lying electronic states (Chapter 4 and Refs. 51,53-56). As described in the last chapter, this bond length shortening has been rationalized by the effect of the unpaired electron ($p\sigma$ or $p\pi$) being polarized away from the ligand in these states, allowing for a greater electrostatic interaction between the metal cation and the anionic ligand. This occurs regardless of the ligand, as the unpaired electron is located on the metal center. Using simple molecular orbital theory, the bond length behavior of these calcium and strontium polyatomics can be explained. The energy overlap of the metal and ligand orbitals that form the σ bond decreases as one goes from CH_3 to CCH to NH_2 to OH. Therefore, among these ligands, the metal-carbon bond in MCH_3 can be considered the most covalent in character and the metal-oxygen bond in MOH the least. In the highly ionic hydroxides, an increase in the metal-ligand electrostatic interaction on excitation is expected to have a greater effect in shortening the bond length than in the more covalent monomethyls.

As explained in Chapter 2, the spin-rotation fine structure interaction is composed of two main contributions: a first-order direct interaction of the electron spin with molecular rotation and a second-order part due to spin-orbit coupling [57]. For molecules containing heavy atoms, the second-order term generally dominates. An expression for the second-order spin-orbit coupling contribution has been given by Dixon [58] for a non-linear molecule. Also, as previously described, this equation can be simplified using the pure precession and unique perturber approximations. Under these approximations, it is assumed that there are only two interacting electronic states arising from the same atomic orbital (for example $p\sigma$ and $p\pi$). For the $\tilde{B}\,^2A_1$ state of $CaCH_3$ and $SrCH_3$, these approximations result in the following expression for the ε_{bc} spin rotation constant [51]:

$$\varepsilon_{bc} = \frac{4BA_{SO}}{E_{\tilde{A}} - E_{\tilde{B}}} \tag{5.2}$$

where B is the rotational constant ($\tilde{B}$ state), A_{so} is the spin-orbit constant for a linear analog, and $E_{\tilde{A}}$ and $E_{\tilde{B}}$ are the energies of the $\tilde{A}\,^2E$ and $\tilde{B}\,^2A_1$ states respectively. Using the A_{so} values for the corresponding hydroxides (CaOH [59]: 66.2 cm^{-1}; SrOH [60]: 263.5 cm^{-1}) and the corresponding electronic excitation energies ($E_{\tilde{A}}$ $CaCH_3$ [41]:

14743.4 cm^{-1}; $E_{\tilde{A}}$ SrCH$_3$ (chapter 6): 13800.4 cm^{-1}), ε_{bc} is calculated to be -0.0529 cm^{-1} and -0.2068 cm^{-1} for CaCH$_3$ and SrCH$_3$, respectively. The experimental values are approximately 45% smaller in magnitude than the calculated values, and in both cases the signs are in agreement with the calculation. Deviations between the experimental and calculated values most likely arise from the simple assumptions involved in obtaining Equation 5.2. For example, the unpaired electron in the $\tilde{B}\,^2A_1$ state is most likely not completely *p* in character; some metal *d* character is very likely present.

As shown in chapter 2, the pure precession and unique perturber approximations can also be used to derive a similar expression for the ε_{aa} spin rotation parameter [51]:

$$\varepsilon_{aa} = \frac{-4AA^{so}}{E_{^2A_2} - E_{\tilde{B}}} \tag{5.3}$$

where A is the rotational constant ($\tilde{B}$ state). Using the experimental value of ε_{aa} for SrCH$_3$, a $^2A_2$ state is predicted to lie at ~37000 cm^{-1}. Theoretical calculations would be useful in confirming the existence of such a state and in predicting its properties. Unfortunately, because a value of ε_{aa} could not be obtained in the $\tilde{B}\,^2A_1$ state of CaCH$_3$, a comparison can not be made with SrCH$_3$.

As mentioned previously, the $K' = 1$ levels of the $\tilde{B}\,^2A_1$ state are perturbed and could not be fitted using the $^2A_1$ symmetric top Hamiltonian of Equation 5.1. However, the lines of the $K = 1$ sub-band could be assigned quantum numbers using lower state combination differences [44] and term values obtained for the $K' = 1$ levels. In order to investigate the nature of the perturbation, the excited-state term values for the $K = 1$ sub-band are plotted in Figure 5.4 on a relative energy scale along side those of the $K = 0$ sub-band. The $K' = 0$ energy levels follow the expected ordering for a state with a negative value of the ε_{bc} spin rotation parameter (as predicted by pure precession) in which the F_1 levels lie lower in energy than the F_2 levels and their separation increases with increasing N. The $K' = 1$ levels should exhibit a similar pattern, but this is not the case. The relative energies of the F_1 levels do not change greatly between the $K' = 0$ and $K' = 1$ levels; however, the F_2 levels are clearly pushed down in energy, so much so that they are now below the F_1 levels. This effect is observed in all of the rotational levels observed in this study, which suggests that the perturbation is global in nature and affects primarily the F_2 levels of the $\tilde{B}\,^2A_1$ state of $CaCH_3$.

Considering the limited information available on the energy levels of $CaCH_3$, it is hard to identify the perturbing state with confidence. However, one possibility is that a vibrational level of the $\tilde{A}\,^2E$ state could be interacting with the $\tilde{B}\,^2A_1$ state ($\Delta E(\tilde{B} - \tilde{A}) = 1267$ cm^{-1}). The vibrational frequency for the Ca-C stretch (υ_3) in the $\tilde{A}\,^2E$ state of $CaCH_3$ is ~ 413 cm^{-1} [38]. The energy of three quanta of this vibration in the $\tilde{A}\,^2E_{3/2}$ (14779 cm^{-1}) F_2 spin component lies very close in energy to the $K' = 1$ level (~3 cm^{-1}) of the $\tilde{B}\,^2A_1$ state, while $3\upsilon_3$ in the $\tilde{A}\,^2E_{1/2}$(14700 cm^{-1}) F_1 spin component lies ~75 cm^{-1} below the $K' = 1$ level of the $\tilde{B}\,^2A_1$ state. The location of these levels matches the observation that the F_2 levels are more perturbed. More work will be necessary to confirm the identity of the perturbing state. It would be very interesting to examine the $\tilde{B}\,^2A_1$- $\tilde{X}\,^2A_1$ transition of the $CaCD_3$ isotopologue to see if the perturbation changes as both the location of the electronic states and vibrational frequencies shift.

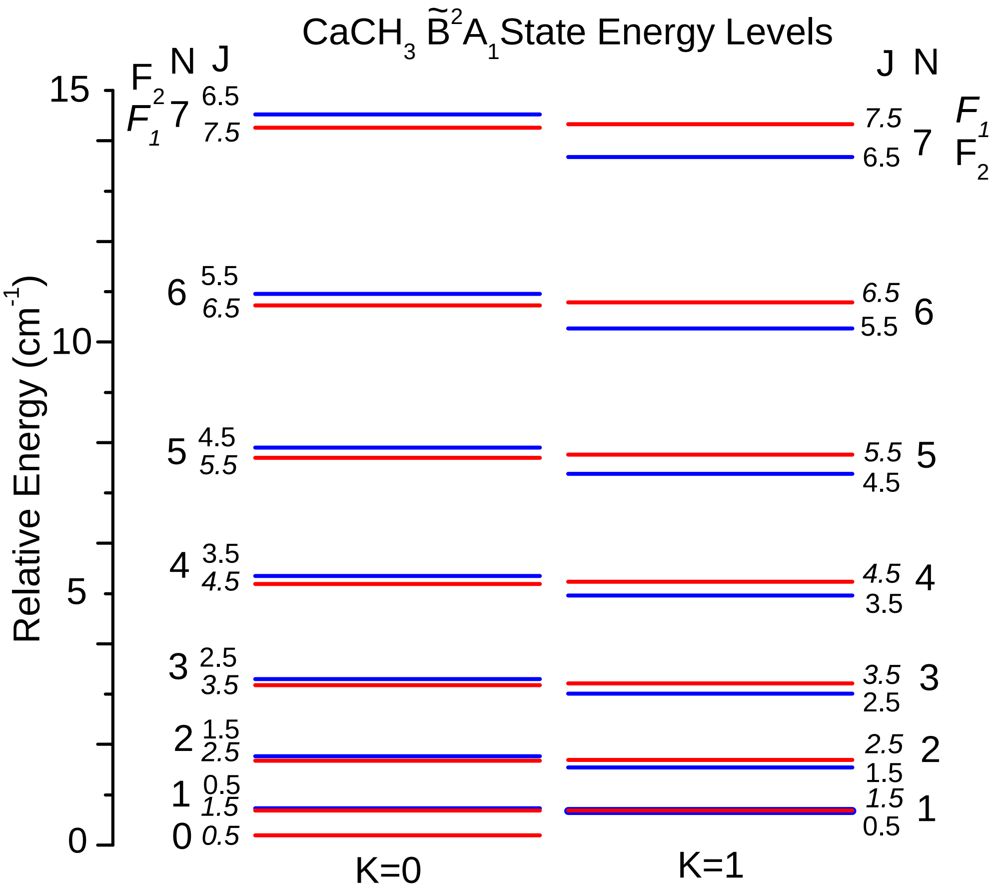

Figure 5.4 - Term values of the rotational energy levels of the K′ = 0 and 1 levels of the $\tilde{B}\,^2A_1$ state of $CaCH_3$ plotted on a relative energy scale.

References

[1] C. Lambert, M Kaupp and P. v. R. Schleyer, Organometalics **12**, 853 (1993)**.**

[2] S. C. Tyerman, G. K. Corlett, A. M. Ellis and T. A. Claxton, J Mol. Struct. **364**, 107 (1996).

[3] J. Breidung and W. Thiel, J. Mol. Struct, **599**, 239 (2001).

[4] G. Scalmani, J. L. Brédas and V. Barone, J. Chem. Phys. **112**, 1178 (2000).

[5] A. F. Jalbout, Chem. Phys. Lett. **340**, 571 (2001).

[6] A. J. McKinley and E. Karakyriakos, J. Phys. Chem. A, **104**, 8872 (2000).

[7] R. Drissi El Bouzaidi, A. El Hammadi, M. El Mouhtadi, H. Cardy and A Dargelos, J. Mol. Struct. **497**, 165 (2000).

[8] D. E. Woon, J. Chem. Phys. **104**, 9495 (1996).

[9] W.-T. Chan and I. P. Hamilton, Chem Phys. Lett. **297**, 217 (1998).

[10] J. V. Ortiz, J. Chem. Phys. **92**, 6728 (1990).

[11] A. El Hammadi, M. El Mouhtadi, H. Cardy and A. Dargelos, J. Mol. Struct. **624**, 1 (2003).

[12] S. Q. Jin, Y. Xie and H. F. Schaefer III, Chem. Phys. Lett. **170**, 301 (1990).

[13] B. C. Hoffman, C. D. Sherrill and H. F. Schaefer III, J. Mol. Struct. **370**, 93 (1996).

[14] C. W. Bauschlicher Jr., S. R. Langhoff, H. Partridge and L. A. Barnes, J. Chem. Phys. **91**, 2399 (1989).

[15] V. B. Zakrzewski and J. V. Ortiz, J. Chem. Phys. **100**, 6508 (1994).

[16] A. J. McKinley, E. Karakyriakos, L. B. Knight Jr., R. Babb and A. Williams, J. Phys. Chem. A. **104**, 3528 (2000).

[17] Ch. Jamorski, A. Dargelos, Ch. Teichteil and J. P. Daudey, Chem. Phys. **178**, 39 (1993).

[18] A. K. Rappe and W. A. Goddard III, J. Am. Chem. Soc. **99,** 3966 (1977).

[19] A. Veldkamp and G. Frenking, J. Comp. Chem. **13**, 1184 (1992).

[20] Y. Zhang and M. Stuke, J. Phys. Chem. **93**, 4503 (1989).

[21] R. Srinivas, D. Sülzle and H. Schwarz, J. Am. Chem Soc. **112**, 8334 (1990).

[22] D. J. Brugh, R. S. Dabell and M. D. Morse, J. Chem. Phys. **121**, 12379 (2004).

[23] P. B. Armentrout and J. L. Beauchamp, J. Am. Chem. Soc. **103**, 784 (1981).

[24] L. S. Sunderlin and P. B. Armentrout, J. Phys. Chem. **94**, 3589 (1990).

[25] M. B. Pushkarsky, T. A. Barckholtz and T. A. Miller, J. Chem. Phys. **110**, 2016 (1999).

[26] T. A. Barckholtz, D. E. Powers, T. A. Miller and B. E. Bursten, J. Am. Chem. Soc. **121**, 2576 (1999).

[27] S. I. Panov, D. E. Power and T. A. Miller, J. Chem. Phys. **108**, 1335 (1998).

[28] A. Penner and A. Amirav, Chem. Phys. Lett. **176,** 147 (1991).

[29] E. S. J. Robles, A. M. Ellis and T. A. Miller, Chem. Phys. Lett. **178**, 185 (1991).

[30] R. L. Jackson, Chem. Phys. Lett. **174**, 53 (1990).

[31] T. M. Cerny, X. Q. Tan, J. M. Williamson, E. S. J. Robles, A. M. Ellis, and T. A. Miller, J. Chem. Phys. **99**, 9376 (1993).

[32] A. M. Ellis, E. S. J. Robles and T. A. Miller, Chem. Phys. Lett. **190**, 599 (1992).

[33] M. D. Allen, T. C. Pesch, J. S. Robinson, A. J. Apponi, D. B. Grotjahn and L. M. Ziurys, Chem. Phys. Lett. **293**, 397 (1998).

[34] B. Z. Li, J. Xin and L. M. Ziurys, Chem. Phys. Lett. **280**, 513 (1997).

[35] D. B. Grotjahn, T. C. Pesch, M. A. Brewster and L. M. Ziurys, J. Am. Chem. Soc. **122**, 4735 (2000).

[36] J. S. Robinson and L. M. Ziurys, Astrophys. J. **472**, L131 (1996).

[37] D. B. Grotjahn, D. T. Halfen, L. M. Ziurys and A. L. Cooksy, J. Am. Chem. Soc. **126**, 12621 (2004).

[38] C. R. Brazier and P. F. Bernath, J. Chem. Phys. **86**, 5918 (1987).

[39] C. R. Brazier and P. F. Bernath, J. Chem. Phys. **91**, 4548 (1989).

[40] A. J. Marr, F. Grieman and T. C. Steimle, J. Chem. Phys. **105**, 3930 (1996).

[41] R. Rubino, J. M. Williamson, and T. A. Miller, J. Chem. Phys. **103**, 5964 (1995).

[42] A. P. Salzberg, B. E. Applegate and T. A. Miller, J. Mol. Spectrosc. **193**, 434 (1999).

[43] M. A. Anderson and L. M. Ziurys, Astrophys. J. **452**, L157 (1995).

[44] M. A. Anderson and L. M. Ziurys, Astrophys. J. **460**, L77 (1996).

[45] M. A. Anderson, J. S. Robinson and L. M. Ziurys, Chem. Phys. Lett. **257**, 471 (1996).

[46] J. Xin, J. S. Robinson, A. J. Apponi and L. M. Ziurys, J. Chem. Phys. **108**, 2703 (1998).

[47] K. C. Namiki, and T. C. Steimle, J. Chem. Phys. **110**, 11309 (1999).

[48] S. Gerstenkorn and P. Luc *Atlas du Spectre d'Absorption de la Molecule d'Iode* Laboratoire Aimé-Cotton, CNRS II, 91405, Orsay, 1978.

[49] P. F. Bernath, Spectroscopy and Photochemistry of Polyatomic Alkaline Earth Containing Molecules, Advances in Photochemistry **23**, 1 (1997).

[50] C. H. Townes and A. L. Schawlow, *Microwave Spectroscopy*, Dover, New York (1975).

[51] C. J. Whitham, S. A. Beaton, Y. Ito and J. M. Brown, J. Mol. Spectrosc. **191**, 286 (1998).

[52] H. M. Pickett, J. Mol. Spectrosc. **148,** 371 (1991).

[53] P. Crozet, A. J. Ross, C. Linton, A. G. Adam, W. S. Hopkins, and R. J. Le Roy, J. Mol. Spectrosc. **229,** 224 (2005).

[54] J. Nakagawa, R. F. Wormsbecher and D. O Harris, J. Mol. Spectrosc. **97**, 37 (1983).

[55] P. M. Sheridan, M. J. Dick, J.-G. Wang, and P. F. Bernath, J. Mol. Spectrosc. **233**, 278 (2005).

[56] A. J. Marr, M. Tanimoto, D. Goodridge and T. C. Steimle, J. Chem. Phys. **103**, 4466 (1995).

[57] H. Lefebvre-Brion and R. W. Field, *The Spectra and Dynamics of Diatomic Molecules*, Elesevier, Amsterdam (2004).

[58] R. N. Dixon, Mol. Phys. **10**, 1 (1965).

[59] R. C. Hilborn, Z. Qingshi and D. O. Harris, J. Mol. Spectrosc. **97**, 73 (1983).

[60] C. R. Brazier and P. F. Bernath, J. Mol. Spectrosc. **114**, 163 (1985).

Chapter 6 - The $\tilde{A}\,^2E - \tilde{X}\,^2A_1$ Transition of $SrCH_3$

6.1 Introduction

Symmetric top molecules in orbitally degenerate states (E symmetry) are of particular interest because they may be subject to distortions due to the Jahn-Teller interaction, in which the molecule deforms to a non-symmetric geometry to remove the orbital degeneracy [1]. This effect may compete with spin-orbit coupling in these states to lift the orbital degeneracy, and will in turn alter the energies of the vibrational and rotational levels of the molecule.

The rotational energy level pattern of molecules in ^2E states was first explored by Brown [2] and later by Hougen [3] and Watson [4]. Brown derived the first effective Hamiltonian, while Hougen added terms to account for the Jahn-Teller effect. In addition, Hougen showed that the Jahn-Teller interaction can contribute to the values of the various rotational parameters of a ^2E state.

The first high-resolution experimental observation of a molecule in a ^2E state was performed by King and Warren in 1969 on FSO_3 [5]. This investigation was followed by the landmark study of the $\tilde{X}\,^2E$ state of CH_3O by Endo, Saito and Hirota [6] using microwave spectroscopy. In their analysis, they successfully applied the effective Hamiltonians of Brown and Hougen to the ground state of the methoxy radical. This work has been followed by high-resolution studies of CH_3O [7-10], CH_3S [11] and C_5H_5 [12], all of which have ^2E electronic ground states.

Another group of molecules in which ^2E electronic states are present are the metal monomethyls and monomethoxides. To date, the $\tilde{A}\,^2E$ states of $MgCH_3$ [13], $CaCH_3$

[14,15], $CaOCH_3$ [16,17], $SrOCH_3$ [18], $ZnCH_3$ [19] and $CdCH_3$ [19,20] have been investigated at high resolution. For these molecules, spin-orbit coupling has been found to dominate over the Jahn-Teller interaction in the lowest vibrational level of the $\tilde{A}\ ^2E$ state. In addition, the contribution of the Jahn-Teller effect to the rotational parameters of the $\tilde{A}\ ^2E$ states of these molecules has been shown to be far outweighed by interactions with other nearby excited states. Spectroscopic results concerning molecules with ^2E states have been reviewed by Barckholtz and Miller [21].

In order to further investigate molecules in ^2E states, high resolution spectra of the $\tilde{A}\ ^2E$ - $\tilde{X}\ ^2A_1$ transition of $SrCH_3$ was recorded and analysed. The fine structure and geometric parameters along with the Jahn-Teller interaction in the $\tilde{A}\ ^2E$ state of $SrCH_3$ will be discussed in this chapter.

6.2 Experimental

$SrCH_3$ was produced in the gas phase using the laser ablation/molecular jet source described in Chapter 3. Only the specific experimental details related to this investigation of the $\tilde{A}\ ^2E$ - $\tilde{X}\ ^2A_1$ transition of $SrCH_3$ will be presented here. For this experiment, a gas mixture of 1% tetramethyl tin in Ar, at a backing pressure of 100 psi, is introduced into a reaction nozzle assembly via a pulsed valve. As the gas mixture passes in front of a strontium target rod, the third harmonic (355 nm) of a pulsed (10 Hz) Nd/YAG laser (10 mJ/pulse) strikes the metal surface to produce strontium vapor. In the resulting high energy plasma, $SrCH_3$ forms and exits the nozzle assembly into a low pressure chamber (~1×10^{-7} Torr) to form a molecular jet (T_{Rot} ~4 – 6 K). The molecules are probed perpendicular to the jet ~15 cm downstream with a visible laser. A photomultiplier tube (PMT), located perpendicular to the jet, is used to collect any resulting fluorescence. Band pass filters (± 20 nm), centered on the probe laser frequency, are used to attenuate radiation from the plasma emission. The collected fluorescence signal is sent from the PMT, through a preamplifier (100X current), to a boxcar integrator. The laser excitation spectrum is then plotted as total fluorescence signal versus probe laser wavenumber.

In this study, two high-resolution ring laser systems (described in Chapter 3) were used to obtain the rotationally resolved spectra of the two spin-orbit components of the $\tilde{A}\,^2E$ - $\tilde{X}\,^2A_1$ transition of $SrCH_3$, based on the previous low-resolution work [22]. For the $\tilde{A}\,^2E_{1/2}$ - $\tilde{X}\,^2A_1$ spin-orbit component (~13655 cm^{-1}), a Coherent 899-29 titanium sapphire ring laser system (line width ~10 MHz) was utilized. Spectra were recorded in 5 cm^{-1} segments at a scan speed of 60 s/cm^{-1} with a data sampling interval of 10 MHz. The I_2 spectrum was recorded simultaneously in absorption to calibrate the line positions [23]. For the $\tilde{A}\,^2E_{3/2}$ - $\tilde{X}\,^2A_1$ spin-orbit component (~13935 cm^{-1}), a Coherent 699-29 ring dye laser system (line width ~10 MHz) operating with DCM laser dye was employed. Spectra were acquired by averaging together several (2 to 4) 5 cm^{-1} segments obtained at a scan speed of 180 s/cm^{-1} with a data sampling interval of 10 MHz. The laser excitation spectrum of I_2 was measured simultaneously to calibrate the line positions [24]. The slower scan speed and segment averaging used to record spectra of this spin-orbit component were necessary to achieve an adequate signal-to-noise ratio. The decrease in signal strength observed for the $\tilde{A}\,^2E_{3/2}$ - $\tilde{X}\,^2A_1$ transition can be attributed to several factors, including lower output power of the dye laser in this spectral region and the degradation of the Sr rod during the experiment. For both spin-orbit components experimental line widths of ~350 MHz were observed due to residual Doppler broadening of the molecular jet as it interacts with the probe laser.

6.3 Results

As described in Chapter 2, $SrCH_3$ is a prolate symmetric top molecule belonging to the C_{3v} point group. The $\tilde{A}\,^2E$ - $\tilde{X}\,^2A_1$ transition of this molecule corresponds to a $p\pi \leftarrow s\sigma$ type promotion of the unpaired electron located on the strontium atom. Figure 6.1 shows the overall spectrum obtained for the two spin-orbit components of the $\tilde{A}\,^2E$ - $\tilde{X}\,^2A_1$ transition of $SrCH_3$. The appearance of this transition is similar to that for a $^2\Pi$ - $^2\Sigma^+$ perpendicular type transition of a linear molecule such as SrCCH (Chapter 4) with ~1B and ~3B spaced branches present. The lower molecular symmetry of $SrCH_3$, however, results in a more complicated spectral pattern.

The energy levels of the $\tilde{A}\,^2E$ state can be labeled according to a Hund's case (a) coupling scheme. This coupling scheme and all the angular momenta associated with it were described in Chapter 2.

As was the case for the $\tilde{B}\,^2A_1$ - $\tilde{X}\,^2A_1$ transition of $SrCH_3$ (Chapter 5), nuclear spin statistics group rotational levels into two nuclear spin states: *ortho* (K = 3N, where N is an integer) and *para* ($K \neq$ 3N) [25]. The existence of two nuclear spin states affects the rotational cooling of the molecules in the free jet expansion because *ortho* and *para* molecules behave like separate species and cannot cool into one another. As a result of this phenomenon, both the K'' = 0 and K'' = 1 levels are populated in the jet. Transitions arising from three sub-bands (K' = 1 ← K'' = 0, K' = 0 ← K'' = 1 and K'= 2 ← K''= 1) are therefore expected to be the most intense in our spectra. The energy level structure and

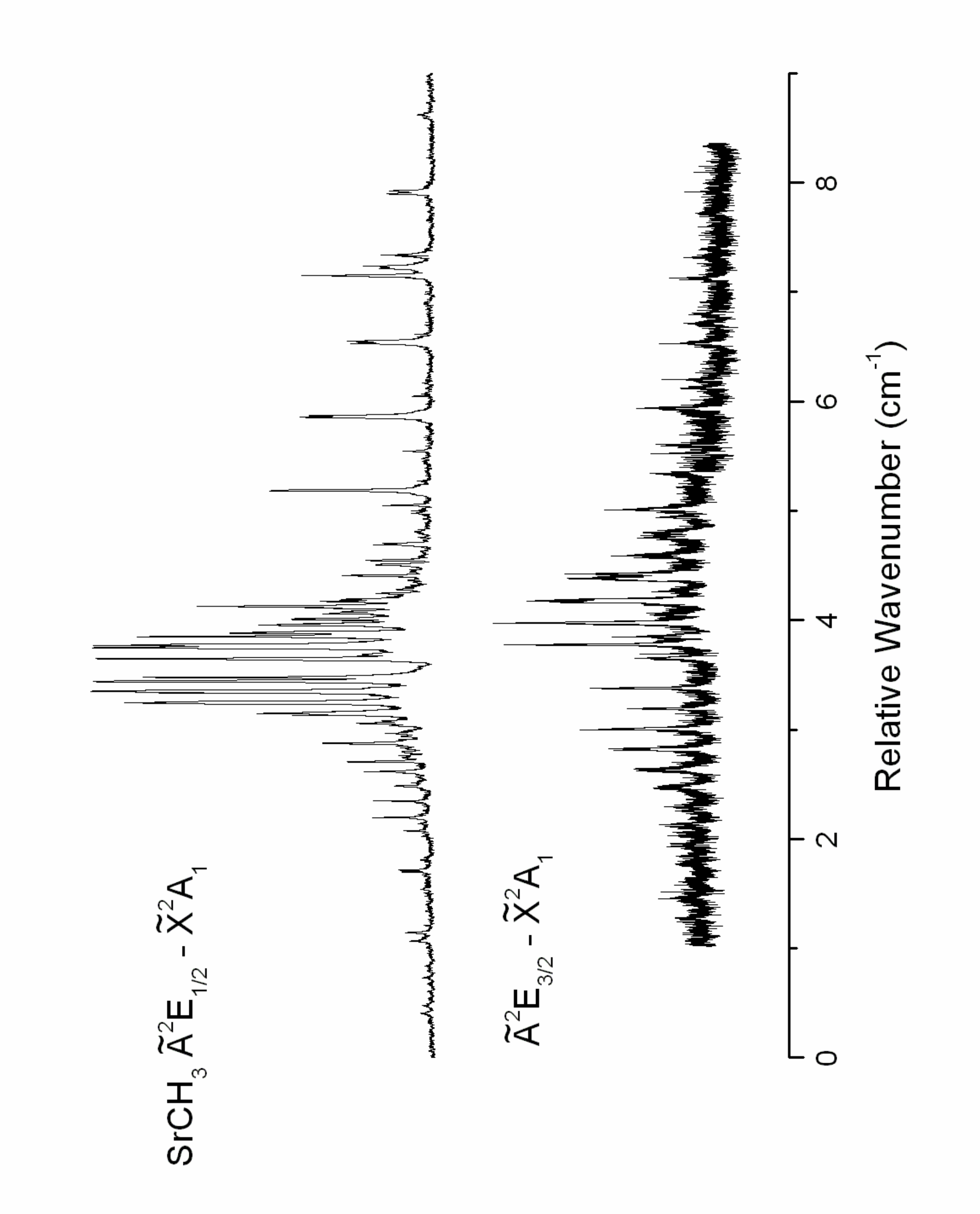

Figure 6.1 - Overall high-resolution spectra of the $\tilde{A}\ ^2E_{1/2}$ - $\tilde{X}\ ^2A_1$ (top panel) and $\tilde{A}\ ^2E_{3/2}$ - $\tilde{X}\ ^2A_1$ (bottom panel) spin-orbit components of $SrCH_3$.

the associated transition diagrams for each of these ΔK sub-bands were described in Chapter 2 (Figures 2.8 – 2.10).

Line assignments of the $\tilde{A}\,^2E$ - $\tilde{X}\,^2A_1$ transition were made by initially identifying series of branches in the $\tilde{A}\,^2E_{1/2}$ - $\tilde{X}\,^2A_1$ spin-orbit component. Branch identifications were aided by using the $\tilde{A}\,^2E_{1/2}$ - $\tilde{X}\,^2A_1$ transition of $CaCH_3$ as a guide [15]. Lower state combination differences [26] were then used to assign J and K values to each of the 18 possible branches of this spin-orbit component. Branch assignments in the $K' = 0 \leftarrow K'' = 1$ and $K' = 2 \leftarrow K'' = 1$ sub-bands were facilitated by the unresolved parity doubling in the $K' = 0$ and $K' = 2$ levels of the $\tilde{A}\,^2E$ state [3]. This proved helpful because, for example, in the $K' = 2 \leftarrow K'' = 1$ sub-band, the position of the $^rR_{12}$ branch can only be predicted from the $^rP_{12}$ branch if the parity doubling is not negligible. However, if the parity splitting is unresolved, then any of the 5 remaining branches of this sub-band can be used to predict the location of this branch. The observation of first lines aided in the unambiguous assignment of K' values [15]. For the $\tilde{A}\,^2E_{3/2}$ - $\tilde{X}\,^2A_1$ spin-orbit component, identification of the branches proceeded by the same method as for the $\tilde{A}\,^2E_{1/2}$ - $\tilde{X}\,^2A_1$ component. In addition, line assignments in this component were aided by the almost negligible parity splitting in the $K' = 1$ state. As a result, all the branches in the $K' = 1 \leftarrow K'' = 0$ sub-band could be related in a similar manner as the $K' = 0 \leftarrow K'' = 1$ and $K' = 2 \leftarrow K'' = 1$ sub-bands, in which the parity splitting is unresolved.

A total of 186 lines in 35 of the 36 possible branches from the three ΔK sub-bands of the two spin-orbit components were identified and assigned for the $\tilde{A}\,^2E$ - $\tilde{X}\,^2A_1$ transition of $SrCH_3$. These data can be found in Appendix A3. A portion of the $\tilde{A}\,^2E_{1/2}$ - $\tilde{X}\,^2A_1$ spectrum, with line assignments, is shown in Figure 6.2. Fifteen of the eighteen

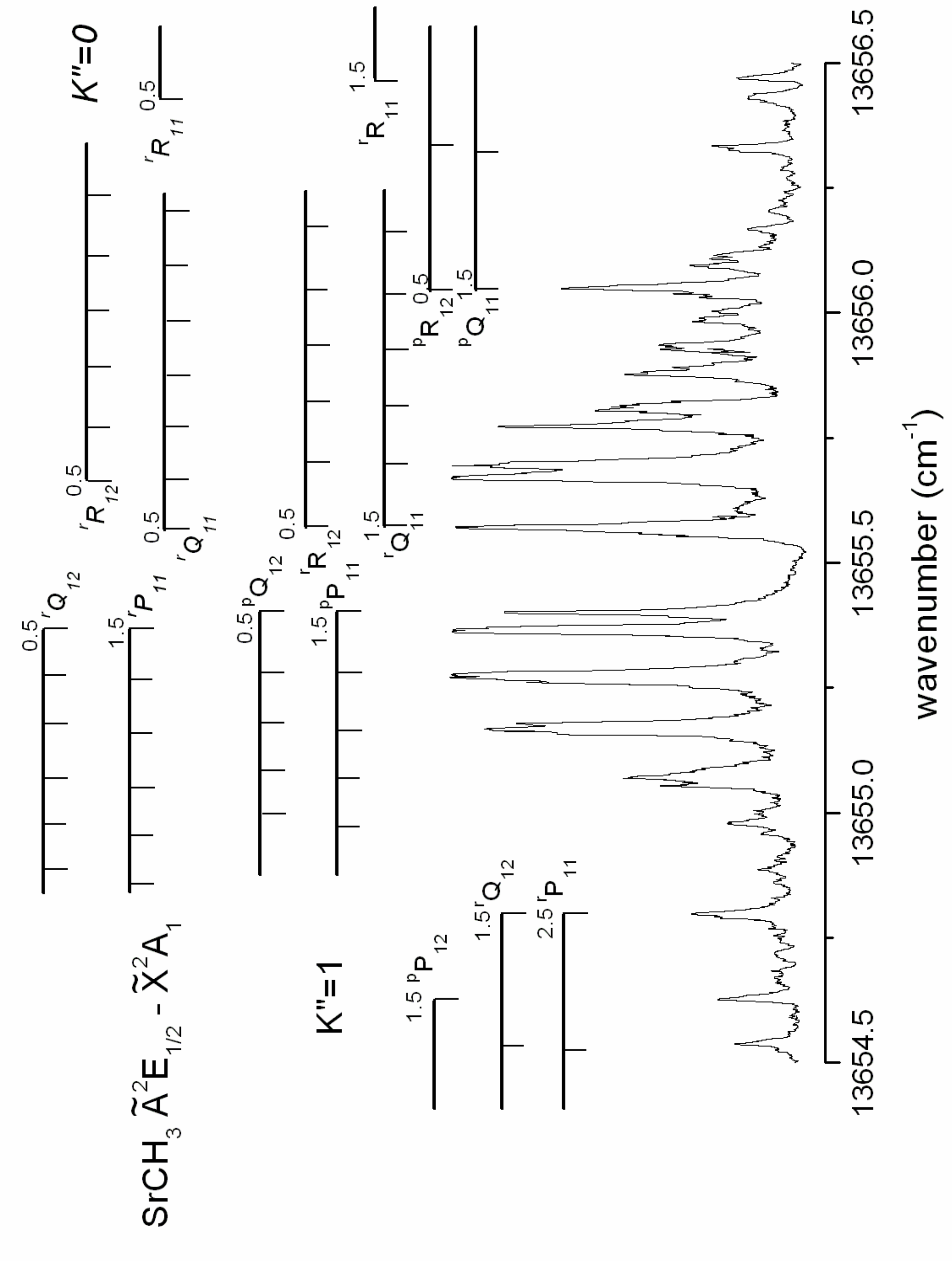

Figure 6.2 - A portion of the high-resolution spectrum (with assignments) of the $\tilde{A}\,^2E_{1/2}$ - $\tilde{X}\,^2A_1$ spin-orbit component of SrCH$_3$.

possible branches in the three ΔK sub-bands of this spin orbit component are shown here, identified by the branch notation ${}^{\Delta K}\Delta J_{F_i' F_j''}$ (i = 1, 2; j = 1, 2). Transitions arising from the $K' = 1 \leftarrow K'' = 0$ sub-band are labeled on top in italics, while those from the $K' = 0 \leftarrow K'' = 1$ and $K' = 2 \leftarrow K'' = 1$ sub-bands are shown below. Each individual rotational line is labeled by its J value. The similar band origin of each of the ΔK sub-bands causes the spectrum to appear congested.

6.4 Analysis

The $\tilde{A}\,{}^2E$ - $\tilde{X}\,{}^2A_1$ transition data of $SrCH_3$ were modeled using the effective Hamiltonian [2,3,6,13],

$$\hat{H}_{Eff} = \hat{H}_{Rot} + \hat{H}_{CD} + \hat{H}_{SR} + \hat{H}_{SO} + \hat{H}_{Cor} + \hat{H}_{JT} \qquad (6.1)$$

in which the individual terms describe the rotational motion of the molecule ($\hat{H}_{Rot}$), the centrifugal distortion to the rotation ($\hat{H}_{CD}$), the spin-rotation interaction ($\hat{H}_{SR}$), the spin-orbit coupling ($\hat{H}_{SO}$), the Coriolis effect ($\hat{H}_{Cor}$) and the Jahn-Teller interactions ($\hat{H}_{JT}$). The final three terms in Equation 6.1 were set to zero to model the $\tilde{X}\,{}^2A_1$ state, and the entire expression was used to describe the $\tilde{A}\,{}^2E$ state. This Hamiltonian is slightly different than the one ${}^2E$ states described in chapter 2. Firstly, the Jahn-Teller term was not included in the Hamiltonian described in Chapter 2 because, as will shown, its effect was negligible in the $\tilde{A}\,{}^2E$ state of $SrCH_3$. Secondly, the Coriolis coupling term, which arises from a coupling of the rotational and vibrational motions, was incorporated into the

$\hat{\mathrm{H}}_{\mathrm{Rot}}$ of Chapter 2. It was not treated separately as in equation 6.1. The above Hamiltonian was incorporated into a least squares fitting program using the matrix elements of Endo in a Hund's case (a) basis [6].

Initially, the optical data were fit using the rotation (A, B), spin-orbit ($a\zeta_e d$, $a_D\zeta_e d$), spin-rotation (ε_{aa}, $\varepsilon_{bc} = (\varepsilon_{bb}+\varepsilon_{cc})/2$, ε_1), Coriolis ($A\zeta_t$), and Jahn-Teller (h_1) terms in the $\tilde{\mathrm{A}}\,^2\mathrm{E}$ state. The ground state constants were fixed to previously determined values (Chapter 5). In this initial fitting, the constants h_1 and ε_{bc} could not be ascertained reliably from our data set. Interestingly, these parameters were determined in the analysis of the high resolution spectrum of the $\tilde{\mathrm{A}}\,^2\mathrm{E}$ - $\tilde{\mathrm{X}}\,^2\mathrm{A}_1$ transition of $\mathrm{CaOCH_3}$ [16,17]. As a result, we performed a fit of the $\mathrm{CaOCH_3}$ data using our least-squares fitting program, and found our program reproduced the previous values. However, when the more extensive $\mathrm{CaOCH_3}$ data set was reduced to include only the same J values from the same ΔK sub-bands observed in our current study of $\mathrm{SrCH_3}$, h_1 and ε_{bc} could not be obtained reliably. In order to determine h_1 and ε_{bc} from the $\mathrm{CaOCH_3}$ data set, we found that lines with $J' > 9.5$ had to be included in the fit. As a result, h_1 and ε_{bc} were both fixed to zero in subsequent fits of the $\tilde{\mathrm{A}}\,^2\mathrm{E}$ - $\tilde{\mathrm{X}}\,^2\mathrm{A}_1$ transition data of $\mathrm{SrCH_3}$. In addition, because of the low J values ($J' \leq 8.5$) observed in our spectra, the centrifugal distortion terms (D_N, D_{NK} and D_K) in the $\tilde{\mathrm{A}}\,^2\mathrm{E}$ state were also fixed to zero. All 186 assigned rotational lines from the three ΔK sub-bands of the $\tilde{\mathrm{A}}\,^2\mathrm{E}$ - $\tilde{\mathrm{X}}\,^2\mathrm{A}_1$ transition and the 137 pure rotational lines of the $\tilde{\mathrm{X}}\,^2\mathrm{A}_1$ state [26] were included in the final fit, in which all of the ground-state constants except A were allowed to vary. The A rotational constant in the ground state was fixed to the theoretical value [27], because no previous experimental value was available and no transitions where $\Delta K_R \neq 0$ were observed in this work. The two data sets were weighted according to their experimental uncertainties: 0.005 cm^{-1} for the optical data and 60 kHz for the pure rotational data. The spectroscopic constants for the $\tilde{A}\,^2E$ and $\tilde{X}\,^2A_1$ states derived from this final fit are listed in Table 6.1.

Table 6.1. Spectroscopic Constants (in cm^{-1}) for the $\tilde{A}\,^2E$ and $\tilde{X}\,^2A_1$ States of $SrCH_3$

Constant [a]	$\tilde{X}\,^2A_1$	$\tilde{A}\,^2E$
T	0.0	13800.3762(9)
$a\zeta_e d$		279.1651(17)
$a_D\zeta_e d$		-0.0297(15)
$A\zeta_t$		5.24833(83)
A	5.390 [b]	5.33494(75)
B	0.193833336(16)	0.195068(21)
D_N	$2.14893(11) \times 10^{-7}$	
D_{NK}	$1.61349(51) \times 10^{-5}$	
H_{NK}	$2.920(21) \times 10^{-10}$	
H_{KN}	$3.18(43) \times 10^{-9}$	
ε_{aa}	0.000883(34)	0.3692(33)
ε_{bc}	0.00412853(43)	
ε_1		-0.09415(12)

[a] Values in parenthesis are 1σ standard deviations, in units of the last significant digits.
[b] Fixed to theoretical value [27].

6.5 Discussion

The energy separation of the two spin-orbit components of the $\tilde{A}\,^2E$ state is given by the constant $a\zeta_e d$. Within this parameter, a describes the magnitude of the spin-orbit coupling, ζ_e is the projection of the electronic angular momentum, **L**, onto the symmetry axis and d is the Jahn-Teller quenching parameter ($1 > |d| > 0$). The magnitude of these terms can be estimated by comparing $a\zeta_e d$ with the spin-orbit constant, A_{SO}, of other linear strontium-containing molecules such as SrOH ($A_{SO} = 263.5878$ cm^{-1}) [28] and SrCCH ($A_{SO} = 272.1886$ cm^{-1}) (Chapter 4) in their $\tilde{A}\,^2\Pi$ states. These values of A_{SO} are quite similar to $a\zeta_e d$ (279.1651 cm^{-1}) in the $\tilde{A}\,^2E$ state of $SrCH_3$. Therefore, we can conclude that the quantity $\zeta_e d$ must be close to 1. As mentioned in Chapter 2, for a ^{2}E state derived predominantly from a *p* orbital, as is the case for the $\tilde{A}\,^2$E state of SrCH$_3$ (5*p*) (chapter 2 – Figure 2.1), ζ_e is expected to be close to 1. In this scenario, *d* must also be approximately 1, which indicates that the Jahn-Teller distortion is small in the lowest vibrational level of the $\tilde{A}\,^2$E state. If the Jahn-Teller interaction is neglected and hence $d = 1$, then a value of ζ_e can be estimated using the following equation [13]

$$\zeta_t = \zeta_e d + \frac{1-d}{2}\zeta_2 \tag{6.2}$$

in which ζ_t is the projection of the vibronic angular momentum onto the symmetry axis (Sr-C bond) and ζ_2 is the vibrational Coriolis coupling coefficient for the Jahn-Teller active degenerate vibrational mode. From this equation, if $d = 1$ then ζ_t must equal ζ_e. Using the values of *A* (rotational constant) and $A\zeta_t$ for the ground vibrational level of the $\tilde{A}\,^2$E state found in Table 1, $\zeta_t = \zeta_e$ is calculated to be 0.9838. The value of ζ_e (0.9838) for the $\tilde{A}\,^2$E state is in very good agreement with the expected value of 1. Finally, assuming $d = 1$ and using $\zeta_e = 0.9838$ and $a\zeta_e d = 279.1651$ cm^{-1}, the magnitude of the spin-orbit coupling constant in the $\tilde{A}\,^2$E state is estimated to be $a = 283.772$ cm^{-1}.

As described in Chapter 2, the spin rotation parameter ε_{aa} for the $\tilde{A}\,^2$E state of SrCH$_3$ can be estimated by considering the second-order contribution to this parameter arising from spin-orbit coupling. For molecules containing heavy atoms, the first-order contribution to the spin-rotation parameter is typically much smaller than the second-order portion, and may be neglected [10]. The second-order spin-orbit contribution to ε_{aa}

is composed of two factors, electronic ($\varepsilon_{aa}^{(2e)}$) and vibrational ($\varepsilon_{aa}^{(2v)}$) [10,29]. The vibrational term is dominated by the Jahn-Teller interaction, which was previously shown to be small in the $\tilde{A}\,^2E$ state of SrCH$_3$, and will be ignored. The electronic contribution can be approximated using second-order perturbation theory, and has the following form for a non-linear molecule [30],

$$\varepsilon_{aa}^{(2)} = -\sum_{\alpha\neq\alpha'} \frac{4\langle\alpha|a\mathrm{L}_z|\alpha'\rangle\langle\alpha'|A\mathrm{L}_z|\alpha\rangle}{\mathrm{E}_{\alpha} - \mathrm{E}_{\alpha'}} \tag{6.3}$$

where α' is the electronic state of interest, α are other perturbing electronic states, and E is the state energy. Equation 6.3 can be simplified by invoking the unique perturber approximation. For SrCH$_3$, the closest possible perturbing state is the $\tilde{E}\,^2E$ state (the $\tilde{C}\,^2E$ state arises from metal $d\delta$ orbitals, corresponding to a $^2\Delta$ state in the linear limit, and cannot connect to the $\tilde{A}\,^2E$ state). If we approximate $\langle\tilde{A}\,^2E|\mathrm{L}_z|\tilde{E}\,^2E\rangle$ as $\zeta_e d$, then the expression for $\varepsilon_{aa}^{(2)}$ is reduced to

$$\varepsilon_{aa}^{(2)} = -\frac{4\langle\tilde{A}\,^2E|a\mathrm{L}_z|\tilde{E}\,^2E\rangle\langle\tilde{A}\,^2E|A\mathrm{L}_z|\tilde{E}\,^2E\rangle}{\mathrm{E}_{\tilde{A}^2E} - \mathrm{E}_{\tilde{E}^2E}} = -\frac{4a\zeta_e dA\zeta_e d}{\mathrm{E}_{\tilde{A}^2E} - \mathrm{E}_{\tilde{E}^2E}} = -\frac{4a\zeta_e dA\zeta_t}{\mathrm{E}_{\tilde{A}^2E} - \mathrm{E}_{\tilde{E}^2E}} \tag{6.4}.$$

Unfortunately, the energy separation between the $\tilde{A}\,^2E$ and $\tilde{E}\,^2E$ states in SrCH$_3$ is not known. For CaCH$_3$, Ortiz [31] has calculated the energy of the $\tilde{E}\,^2E$ state resulting in a $\tilde{A}\,^2E$ - $\tilde{E}\,^2E$ splitting of ~13930 cm^{-1}. Using this energy separation as an estimate for SrCH$_3$ and the values of $a\zeta_e d$ (279.1651 cm^{-1}) and $A\zeta_t$ (5.24833 cm^{-1}), $\varepsilon_{aa}^{(2)}$ is calculated to be 0.4207 cm^{-1}. This value is in very reasonable agreement with the experimentally determined constant (0.3692 cm^{-1}), considering the assumptions made in deriving Equation 6.4 and estimating the $\tilde{\mathrm{A}}\,^2\mathrm{E}$ - $\tilde{\mathrm{E}}\,^2\mathrm{E}$ energy splitting.

The spin-rotation parameter, ε_1, can also be calculated by considering second-order contributions arising from spin-orbit coupling. Using the pure precession relationship and the unique perturber approximation, the following expression for ε_1 has been derived (Chapter 2)

$$\varepsilon_1 = \frac{aB\ell(\ell+1)}{\mathrm{E}_{\tilde{\mathrm{A}}^2\mathrm{E}} - \mathrm{E}_{\tilde{\mathrm{B}}^2\mathrm{A}_1}} \qquad (6.5),$$

where ℓ is the atomic orbital angular momentum. Using the values a = 283.772 cm^{-1}, B = 0.195068 cm^{-1}, E($\tilde{\mathrm{A}}\,^2\mathrm{E}$) = 13800.3762 cm^{-1}, E($\tilde{\mathrm{B}}\,^2\mathrm{A}_1$) = 14787.58134 cm^{-1} (Chapter 5) and assuming that the $\tilde{\mathrm{A}}\,^2\mathrm{E}$ state arises solely from a p atomic orbital (ℓ=1), ε_1 is estimated to be - 0.1121 cm^{-1}. This value has the same sign but is approximately 20% larger in magnitude than the experimentally determined parameter (-0.09415 cm^{-1}). Aside from the assumptions made in the derivation of this expression, this difference may indicate that the $\tilde{\mathrm{A}}\,^2\mathrm{E}$ state is not composed entirely of p orbital character; d orbitals may be mixing in.

It has also been shown that ε_1 is analogous to the Λ-doubling constant p in $^2\Pi$ states. The two parameters are related by the expression $\varepsilon_1 = p/2$ [3]. If we compare $2\varepsilon_1$ = -0.1883 cm^{-1} in the $\tilde{\mathrm{A}}\,^2\mathrm{E}$ state of $SrCH_3$ with the p values in the $\tilde{\mathrm{A}}\,^2\Pi$ state of other linear strontium-containing molecules such as SrOH (-0.143289 cm^{-1}) [28] and SrCCH (-

0.1101 cm^{-1}) (Chapter 4) we find that they are quite similar. This is not unexpected, as the electronic structure of these molecules is mostly derived from the Sr^+ ion and is not expected to change dramatically with different ligands.

From the rotational constants shown in Table 6.1, the structure of $SrCH_3$ in the $\tilde{A}\,^2E$ state can be estimated. Because no isotopologue data exists for the $\tilde{A}\,^2E$ state, the C-H bond length was held fixed to the ground state theoretical value [27]. This assumption is reasonable, because the C-H bond length should exhibit the smallest change upon electronic excitation [16]. In addition, the *A* rotational constant in the ground state was fixed to the theoretical value [27]; therefore, the *A* value determined in the $\tilde{A}\,^2E$ state is a measure of the change in *A* from the ground state. In order to ensure that differences in the rotational constants between the ground and excited electronic states are due only to changes in geometry, second-order spin-orbit contributions must be considered. For the $\tilde{A}\,^2E$ state of $CaCH_3$ the second -order contributions were found to comprise only ~0.35% of the value of the *A* rotational constant [15]. A similar calculation for the $\tilde{A}\,^2E$ state of $SrCH_3$ shows that the second-order contributions to the rotational parameters, *A* and *B,* are less then 0.25% of the total value, and may be safely ignored. The estimated structural parameters of the $\tilde{X}\,^2A_1$ and $\tilde{A}\,^2E$ states of $SrCH_3$ are shown in Table 6.2, along with those of the $\tilde{B}\,^2A_1$ state. The Sr-C bond length was found to decrease slightly (~0.006 Å) upon promotion of the unpaired electron from the $\tilde{X}\,^2A_1$ state to the $\tilde{A}\,^2E$ state. A decrease in the metal-ligand bond length between the $\tilde{A}\,^2\Pi$ and $\tilde{X}\,^2\Sigma^+$ states has also been observed in other strontium polyatomic molecules such as SrOH (~0.02 Å) [28] and SrCCH (~0.03 Å) (Chapter 4) . This bond length shortening has been attributed to the polarization of the unpaired electron away from the ligand in the *pπ* orbital ($\tilde{A}\,^2E$ state) as compared to the *sσ* orbital ($\tilde{X}\,^2A_1$ state). As a result, the electrostatic interaction between the strontium cation and anionic ligand increases, and the metal-ligand bond length shortens. In addition, the polarization of the unpaired electron away from the ligand allows more room for the CH_3 umbrella to open. In Table 6.2, the H-C-H bond angle is found to increase by ~0.8° between the $\tilde{X}\,^2A_1$ and $\tilde{A}\,^2E$ states of $SrCH_3$. This behavior is similar to the ~0.9° increase observed in the $\tilde{A}\,^2E$ state of $CaCH_3$ as compared to the ground state [15]. In $SrCH_3$ (as in $CaCH_3$) these structural differences are very small, and the metal-ligand bond length change is less than observed for the corresponding transitions in SrOH and SrCCH.

Table 6.2. Structural Parameters for $SrCH_3$

State	Parameter	$SrCH_3$ [a]
$\tilde{X}\,^2A_1$	$r_{M\text{-}C}$ (Å)	2.487
	$r_{C\text{-}H}$ (Å)[b]	1.104
	$\theta_{H\text{-}C\text{-}H}$ (°)	105.8
$\tilde{A}\,^2E$	$r_{M\text{-}C}$ (Å)	2.481
	$r_{C\text{-}H}$ (Å)[b]	1.104
	$\theta_{H\text{-}C\text{-}H}$ (°)	106.6
$\tilde{B}\,^2A_1$	$r_{M\text{-}C}$ (Å)	2.492
	$r_{C\text{-}H}$ (Å)[b]	1.104
	$\theta_{H\text{-}C\text{-}H}$ (°)	107.0

a Value of A in ground state fixed to theoretical value [27].
b Fixed to theoretical value [27].

References

[1] H. A. Jahn and E. Teller, Proc. R. Soc. Lond. A **161**, 220 (1937).

[2] J. M. Brown, Mol. Phys. **20**, 817 (1971).

[3] J. T. Hougen, J. Mol. Spectrosc. **81**, 73 (1980).

[4] J. K. G. Watson, J. Mol. Spectrosc. **103**, 125 (1984).

[5] G. W. King and C. H. Warren, J. Mol. Spectrosc. **32**, 138 (1969).

[6] Y. Endo, S. Saito and E. Hirota, J. Chem. Phys. **81**, 122 (1984).

[7] T. Momose, Y. Endo, E. Hirota and T. Shida, J. Chem. Phys. **88**, 5338 (1988).

[8] S. C. Foster, P. Misra, T.-Y. D. Lin, C. P. Damo, C. C. Carter and T. A. Miller, J. Phys. Chem. **92**, 5914 (1988).

[9] X. Liu, C. P. Damo, T.-Y. D. Lin, S. C. Foster, P. Misra , L. Yu and T. A. Miller, J. Phys. Chem. **93**, 2266 (1989).

[10] X. Liu, S. C. Foster, J. M. Williamson, L. Yu and T. A. Miller, Mol. Phys. **69**, 357 (1990).

[11] Y.-C. Hsu, X. Liu and T. A. Miller, J. Chem. Phys. **90**, 6852 (1989).

[12] L. Yu, S. C. Foster, J. M. Williamson, M. C. Heaven and T. A. Miller, J. Phys. Chem. **92**, 4263 (1988).

[13] R. Rubino, J. M. Williamson and T. A. Miller, J. Chem. Phys. **103**, 5964 (1995).

[14] C. R. Brazier and P. F. Bernath, J. Chem. Phys. **91**, 4548 (1989).

[15] A. J. Marr, F. Grieman and T. C. Steimle, J. Chem. Phys. **105**, 3930 (1996).

[16] P. Crozet, F. Martin, A. J. Ross, C. Linton, M. J. Dick and A. G. Adam, J. Mol. Spectrosc. **213**, 28 (2002).

[17] P. Crozet, A. J. Ross, C. Linton, A. G. Adam, W. S. Hopkins and R. J. LeRoy, J. Mol. Spectrosc. **229**, 224 (2005).

[18] L. C. O'Brien, C. R. Brazier and P. F. Bernath, J. Mol. Spectrosc. **130**, 33 (1988).

[19] T. M. Cerny, X. Q. Tan, J. M. Williamson, E. S. J. Robles, A. M. Ellis and T. A. Miller, J. Chem. Phys. **99**, 9376 (1993).

[20] M. B. Pushkarsky, T. A. Barckholtz and T. A. Miller, J. Chem. Phys. **110**, 2016 (1999).

[21] T. A. Barckholtz and T. A. Miller, Int. Rev. Phys. Chem. **17**, 435 (1998).

[22] C. R. Brazier and P. F. Bernath, J. Chem. Phys. **86**, 5918 (1987).

[23] S. Gerstenkorn, J. Verges and J. Chevillard, *Atlas du Spectre d'Absorption de la Molécule d'Iode* Laboratoire Aimé-Cotton, CNRS 91405, Orsay, 1982.

[24] S. Gerstenkorn and P. Luc, *Atlas du Spectre d'Absorption de la Molécule d'Iode* Laboratoire Aimé-Cotton, CNRS 91405, Orsay, 1978.

[25] C. H. Townes and A. L. Schawlow, *Microwave Spectroscopy*, Dover, New York 1975.

[26] M. A. Anderson, J. S. Robinson and L. M. Ziurys, Chem. Phys. Lett. **257**, 471 (1996).

[27] W.-T. Chan and I. P. Hamilton, Chem. Phys. Lett. **297**, 217 (1998).

[28] J.-G. Wang, P. M. Sheridan, M. J. Dick and P. F. Bernath, J. Mol. Spectrosc. **235**, 283 (2006).

[29] X. Liu, L. Yu and T. A. Miller, J. Mol. Spectrosc. **140**, 112 (1990).

[30] R. N. Dixon, Mol. Phys. **10,** 1 (1965).

[31] J. V. Ortiz, J. Chem. Phys. **92**, 6728 (1990).

Chapter 7 - The $\tilde{B}^2E-\tilde{X}^2A_1$ Transitions of $CaBH_4$ and $SrBH_4$

7.1 Introduction

$CaBH_4$ and $SrBH_4$ are the only members of the isoelectronic 2*p* ligand family of molecules (CaF/SrF, CaOH/SrOH, $CaNH_2$/$SrNH_2$, and $CaCH_3$/$SrCH_3$) (Refs. 1-4 and Chapters 5 and 6) that have not yet been observed using high resolution spectroscopy. From the previous investigations of the molecules in this series, the metal-ligand bonding has been found to be largely ionic, and to occur between the metal cation and the heaviest atom of the negatively charged ligand. In contrast, the borohydride anion (BH_4^-), which possesses a tetrahedral structure, cannot form a bond directly between the central boron and metal atoms [5,6]. In this case, the metal-ligand bonding in the alkaline-earth borohydrides must occur through bridging hydrogens. As a result, three structures are possible, monodentate (one bridging hydrogen – C_{3v} symmetry), bidentate (two bridging hydrogens – C_{2v} symmetry) and tridentate (three bridging hydrogens - C_{3v} symmetry) [7].

The electronic structure of the molecules in the 2*p* ligand series has been well described in terms of a perturbation of the metal atomic orbitals by the ligand. The unique geometric configurations possible for the alkaline-earth borohydrides may disrupt this perturbation description, and may have an affect on the excited state electronic structure, which makes them of particular interest for spectroscopic investigation.

One group of metal borohydrides that has been the subject of several studies, both theoretical and experimental, is the alkali metal borodydrides. The experimental work [7-16] has consisted primarily of microwave spectroscopic investigations in the gas phase. In those studies, the rotational and hyperfine parameters have been determined for the ground electronic states of $NaBH_4$ [7-10], $NaBD_4$ [8,11], $LiBH_4$ [8,12,13], $LiBD_4$ [11]

and KBH_4 [9,11]. Based on isotopic data, lithium and sodium borohydrides were found to possess the tridentate structure in the ground state. Theoretical studies [17-26] have also predicted this geometric configuration for the ground state. Additionally, several of these studies have calculated a low-energy barrier to internal rotation of the ligand [17,20-23,25,26], in which the BH_4^- cycles from one tridentate minimum to another through a bidentate intermediate structure. This phenomenon will manifest itself in the observed rotational spectra as a doubling of spectral lines [27]. In the rotational spectroscopic studies of the alkali metal borohydrides, this doubling of spectral lines was not resolved, indicating that the barrier to the internal motion of the BH_4^- group is larger than calculated.

Studies involving the alkaline-earth borohydrides have been far less extensive. Pianalto et al. [28] have used laser excitation and dispersed fluorescence experiments in a Broida oven to examine the $\tilde{A}^2A_1 - \tilde{X}^2A_1$ and $\tilde{B}^2E - \tilde{X}^2A_1$ electronic transitions of $CaBH_4$ and $SrBH_4$ at low resolution. From their spectra, they suggested that these molecules possessed C_{3v} symmetry and a tridentate structure similar to the structure found later for the alkali borohydrides. Most interestingly, they found that the first excited ${}^2A_1$ and ${}^2E$ states appeared to be reversed in energy relative to the corresponding states in the metal monomethyls, $SrCH_3$ (Chapters 5 and 6) and $CaCH_3$ (Chapter 6 and Refs. 29,30). Subsequently, Ortiz [31] used electron propagator methods to calculate the energy, vibrational frequencies, geometric structure and orbital character of several electronic states of $CaBH_4$. From this work, a tridentate structure was predicted for $CaBH_4$; however, the first excited ${}^2E$ and ${}^2A_1$ electronic states were found to be ordered in energy the same as in $CaCH_3$, contrary to the experimental work. In addition, Chan and Hamilton [32] have used density functional theory to calculate ground-state geometries and vibrational frequencies for the monoborohydrides of calcium and strontium. They also found that the tridentate structure was the lowest in energy in the ground electronic state.

In an attempt to further understand the geometric and excited state electronic properties of $CaBH_4$ and $SrBH_4$, and to reconcile the discrepancy between theory and experiment for $CaBH_4$, the high-resolution laser excitation spectra of the $\tilde{B}^2E - \tilde{X}^2A_1$ transitions of both calcium and strontium monoborohydrides were recorded. For each molecule, the rotational and fine-structure parameters have been determined for the ground and excited electronic states. These constants have conclusively established that the first two excited electronic states are reversed in energy order relative to their MCH_3 analogues. A discussion of the geometry, energy ordering and orbital character for the observed states will be presented. In addition, a comparison of the observed spectroscopic parameters with those of $SrCH_3$ and $CaCH_3$ will be described.

7.2 Experimental

The laser ablation/molecular jet source described in Chapter 3 was used to produce the borohydrides of calcium and strontium in the gas phase. First, a gas mixture was introduced into a reaction nozzle via a pulsed valve. For this synthesis a mixture of 5% diborane in argon (Praxair), at a backing pressure of 100 psi, was used as the reactant gas. Next, the third harmonic (355 nm) of a pulsed (10 Hz) Nd/YAG laser (10 mJ/pulse) was used to vaporize a metal target rod (calcium or strontium) located in the nozzle. Inside the reaction region, a high energy plasma was formed in which the diborane reacted with the metal vapor producing the metal borohydrides. The molecules then exited into the low pressure chamber (~1 x 10^{-7} Torr), forming a molecular jet with a low rotational temperature (T_{rot} ~4 - 6 K). A probe laser was then sent perpendicularly through the expansion ~15 cm downstream. The resulting molecular fluorescence was collected by a photomultiplier tube, sent through a preamplifier (100X current) and processed by a boxcar integrator. Band-pass filters (± 20 nm) were used to help attenuate stray radiation from the ablation laser and plasma emission.

Initially, low resolution survey scans were obtained using an argon-ion pumped linear dye laser (linewidth ~30 GHz) scanned at a speed of ~50 cm^{-1} per minute. DCM and pyridine-2 laser dyes were used to observe the spectral region of interest (~13500 cm^{-1} to 15500 cm^{-1}) with a typical maximum output power of ~1 W (pump power ~5 W). A Labview data acquisition program was used to plot the output signals from the boxcar integrator versus the wavenumber of the laser, which was obtained using a wavemeter (Burleigh WA-2500 Wavemeter Jr.) interfaced with the program.

For the $\tilde{B}^2E - \tilde{X}^2A_1$ transitions of both $CaBH_4$ and $SrBH_4$, a Coherent Autoscan 699-29 ring dye laser system, operating with DCM laser dye, was used to obtain high resolution spectra (linewidth ~10 MHz, output power of ~1 W (pump power ~8 W)). Generally, spectra were obtained in 5 cm^{-1} portions at a scan rate of 180 s/cm^{-1} and a data sampling rate of 10 MHz. To achieve an adequate signal-to-noise ratio, several (2 - 4) portions were usually averaged together. The final spectra were then calibrated using the line positions of I_2 obtained from simultaneously recording its laser excitation spectra [33].

7.3 Results

Figure 7.1 shows low resolution survey spectra of the $\tilde{A}^2A_1$-$\tilde{X}^2A_1$ and $\tilde{B}^2E$-$\tilde{X}^2A_1$ transitions of $CaBH_4$ and $SrBH_4$. In each spectrum, three peaks are clearly present. For $CaBH_4$, the separation between the first and second peaks is ~600 cm^{-1}, while the second and third peaks are spaced by ~70 cm^{-1}. The 70 cm^{-1} separation is in the range of the spin-orbit splitting previously measured for the $\tilde{A}$ states of CaF, CaOH and $CaCH_3$ [1,2,29,30]. This suggests that the second and third peaks are two spin-orbit components of an orbitally degenerate electronic state. This scenario is only possible if the molecule possess a geometric configuration with C_{3v} symmetry. For a molecule having C_{2v} symmetry, such as $CaNH_2$ [34], no two of the first three excited states should be spaced by this ~70 cm^{-1} separation exhibited by calcium-containing molecules (C_{2v} symmetry eliminates first order spin-orbit coupling). Therefore, the wavenumber separations exhibited by the first three peaks for $CaBH_4$ suggests that C_{2v} symmetry is unlikely.

A similar conclusion can be arrived at for $SrBH_4$, where the second and third peaks are spaced by ~200 cm^{-1}. This separation is consistent with the previously observed spin-orbit splitting in the $\tilde{A}$ states of SrF, SrOH and $SrCH_3$ (refs. 1-3 and Chapter 6). As a result, for the borohydrides the first excited $^2A_1$ state was found to lie lower in energy then the first excited ^2E state, consistent with the previous observations of the metal borohydrides [28]. It is also of interest to note the decreased intensity of the $\tilde{A}^2A_1$-$\tilde{X}^2A_1$ transitions as compared to the $\tilde{B}^2E$-$\tilde{X}^2A_1$ transitions in the spectra in Figure 7.1. For each molecule the decreased signal strength was observed previously [28] and does not seem to be simply an effect due to lower laser power. The decrease in

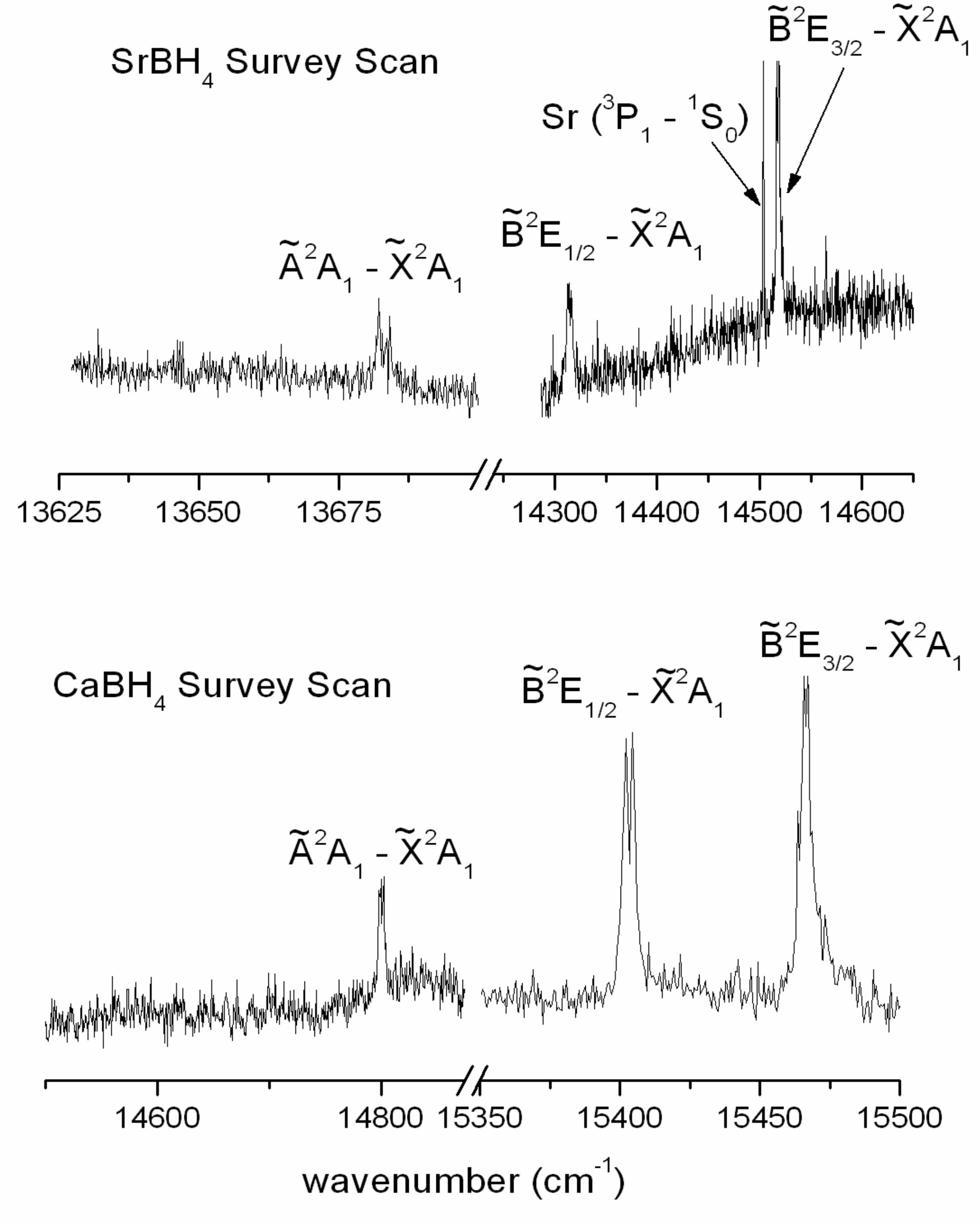

Figure 7.1 - Low resolution spectra recorded for the $\tilde{A}^2A_1 - \tilde{X}^2A_1$ and $\tilde{B}^2E - \tilde{X}^2A_1$ transitions of $SrBH_4$ (upper panel) and $CaBH_4$ (lower panel).

intensity of the $\tilde{A}^2A_1-\tilde{X}^2A_1$ transitions impeded the measurement of their high resolution spectra.

Figure 7.2 shows the overall high resolution spectra obtained for both spin-orbit components of the $\tilde{B}^2E-\tilde{X}^2A_1$ transitions of $CaBH_4$ and $SrBH_4$. As described in Chapter 2, the $\tilde{B}^2E-\tilde{X}^2A_1$ transitions correspond to a $p\pi \leftarrow s\sigma$ promotion on the calcium or strontium ion. Transitions of this type should have the general appearance of a Hund's case (a) $^2\Pi$ – Hund's case (b) $^2\Sigma^+$ perpendicular transition of a corresponding linear molecule such as CaCCH [35,36] or SrCCH (Chapter 4). In this case, two spin-orbit components are present, each with a well defined origin and ~1*B* and ~3*B* spaced branches. For $SrBH_4$, the $\tilde{B}^2E_{3/2}-\tilde{X}^2A_1$ component (lower left panel) indeed exhibits the appearance of a perpendicular transition with ~1*B* and ~3*B* spaced branches. The $\tilde{B}^2E_{1/2}-\tilde{X}^2A_1$ component (upper left panel), on the other hand, exhibits a pattern that closely resembles a parallel transition with only ~2*B* spaced branches present. For the $\tilde{B}^2E-\tilde{X}^2A_1$ transition of $CaBH_4$, neither spin-orbit component (top and bottom right panels) has the anticipated perpendicular-like appearance, nor a clear origin.

The energy level structure of both the $\tilde{B}^2E$ and $\tilde{X}^2A_1$ states of the metal monoborohydrides closely resembles that of the corresponding monomethyls (Chapter 6 and Refs. 29,30) and was described in Chapter 2.

As was the case for $SrCH_3$, and $CaCH_3$ (Chapters 5 and 6), the effect of nuclear spin statistics must be considered for the borohydrides and gives rise to two nuclear spin states: *ortho* ($K = 3N$, where N is an integer) and *para* ($K \neq 3N$) [37] which,

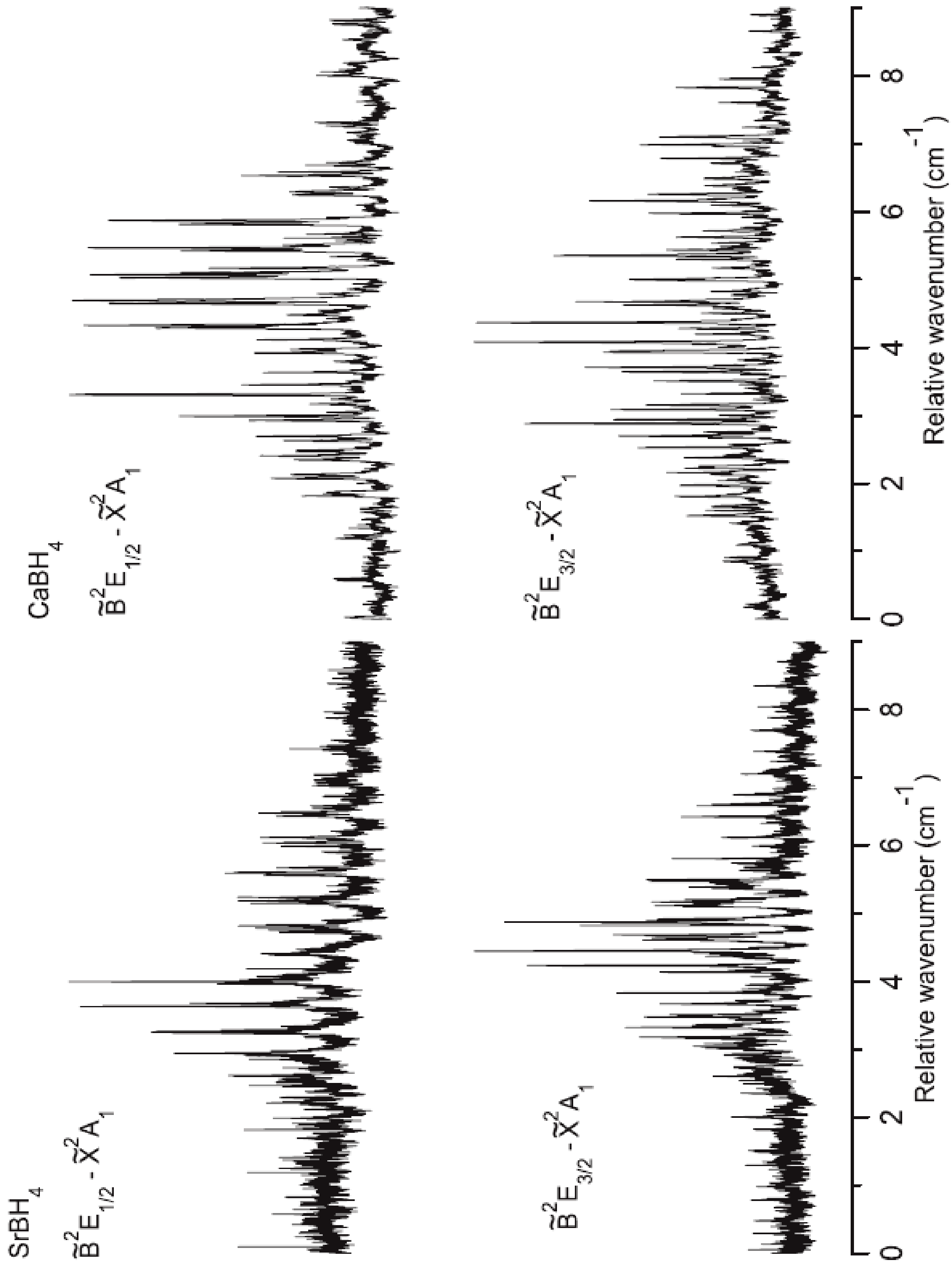

Figure 7.2 - High resolution spectra of the two spin-orbit components of the $\tilde{B}^2E - \tilde{X}^2A_1$ transition of SrBH$_4$ and CaBH$_4$.

cannot rotationally cool to one another in the free jet expansion. As a result both $K'' = 0$ and $K'' = 1$ levels are populated in the jet. Therefore, according to the selection rule $\Delta K = \pm1$, three ΔK sub-bands should be predominantly observed in our spectra, $K' = 1 \leftarrow K'' = 0$, $K' = 0 \leftarrow K'' = 1$, and $K' = 2 \leftarrow K'' = 1$.

Rotational assignments of the $\tilde{B}^2E - \tilde{X}^2A_1$ transition of $SrBH_4$ were completed by first examining the $\tilde{B}^2E_{3/2} - \tilde{X}^2A_1$ spin-orbit component. The similar appearance of this component with the $\tilde{A}^2E_{3/2} - \tilde{X}^2A_1$ transition of $SrCH_3$ (Chapter 6) facilitated branch assignments. Because no previous ground state combination differences were available, rotational assignments were made within each ΔK sub-band using first lines and newly generated combination differences. Subsequently, this set of lower state combination differences was used to make rotational assignments in the $\tilde{B}^2E_{1/2} - \tilde{X}^2A_1$ component, which lacked any similarity with the corresponding component of $SrCH_3$. In this case, a series of branches on each side of the origin were first identified and then grouped together utilizing the combination differences. Using this method, 17 of the 18 possible branches from all three observed ΔK sub-bands were identified in this spin-orbit component. Figure 7.3 shows a portion of the spectra with line assignments ($^{\Delta K}\Delta J_{F_i' F_j''}$ (i = 1, 2; j = 1, 2)) for each spin-orbit component of the $\tilde{B}^2E - \tilde{X}^2A_1$ transition of $SrBH_4$. The unusual structure of the $\tilde{B}^2E_{1/2} - \tilde{X}^2A_1$ component, as compared to the $\tilde{B}^2E_{3/2} - \tilde{X}^2A_1$ spin-orbit component, can clearly be observed in the four branches ($^rP_{11}$, $^rQ_{12}$, $^pR_{12}$, $^pQ_{11}$) that have converged near the origin and have adopted an appearance similar to a strong Q branch.

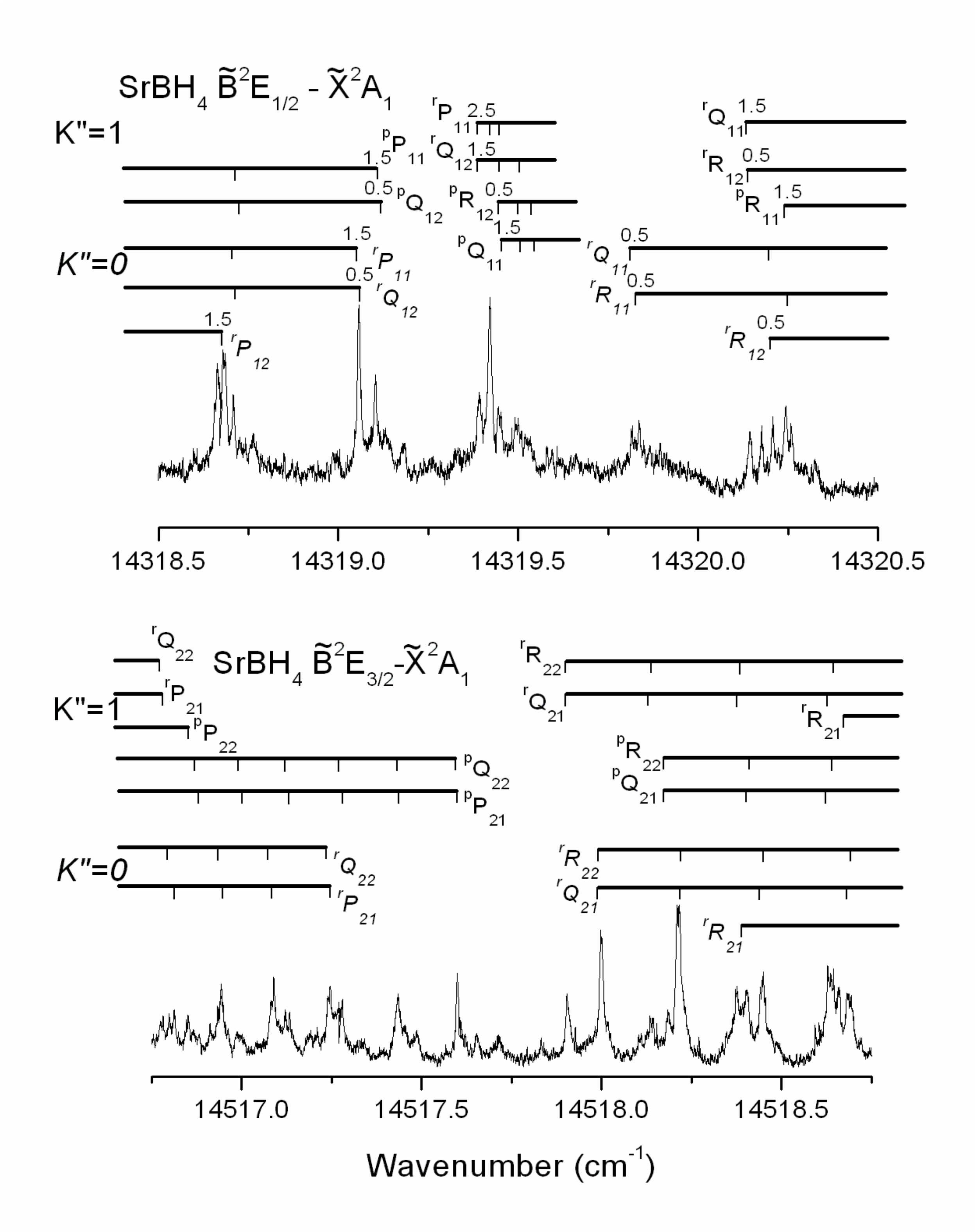

Figure 7.3 - Subsections of the high resolution spectra of the $\tilde{B}^2E_{1/2}$ - $\tilde{X}^2A_1$ (top panel) and the $\tilde{B}^2E_{3/2}$ - $\tilde{X}^2A_1$ (bottom panel) spin-orbit components of $SrBH_4$.

Assignment of the $\widetilde{B}^2E - \widetilde{X}^2A_1$ transition of $CaBH_4$ was not as straightforward. Unfortunately, the spin-orbit components did not exhibit the appearance of perpendicular transitions, and both were exceptionally congested. In addition, each component lacked a clear origin, making it difficult to identify the starting position of any branch. As a result, a different approach was utilized in order to make the rotational assignments. Again, as with $SrBH_4$, a set of lower-state combination differences was not available from previous spectroscopic work. However, in the analysis of the $\widetilde{B}^2E - \widetilde{X}^2A_1$ transition of $SrBH_4$, the lower-state combination differences were found to be consistently ~1.02 times smaller then the analogous combination differences for $SrCH_3$ [38]. Therefore, initially this factor was applied to the lower-state combination differences of $CaCH_3$ [39] in order to generate a new set of combination differences for $CaBH_4$, which were then used to make rotational assignments for all of the possible R and P branches in the $\widetilde{B}^2E_{3/2} - \widetilde{X}^2A_1$ spin-orbit component. As was the case for $SrBH_4$, the lower-state combination differences from this component were then applied to the $\widetilde{B}^2E_{1/2} - \widetilde{X}^2A_1$ spin-orbit component of $CaBH_4$. Using this method 10 of the 12 possible R and P branches for this spin-orbit component were identified. The two branches that were not observed (${}^{r}P_{12}$ and ${}^{p}R_{11}$) form combination difference pairs with the ${}^{r}R_{12}$ and ${}^{p}P_{11}$ branches, respectively. As a result, the J assignments of the ${}^{r}R_{12}$ and ${}^{p}P_{11}$ branches were made by identifying their first lines. All 12 possible Q branches, from both spin-orbit components, were also assigned. However, the majority of these branches were not completely resolved from their associated P or R branch, suggesting that the ground state spin-rotation interaction is quite small. Figure 7.4 shows a portion of the high resolution spectra with rotational

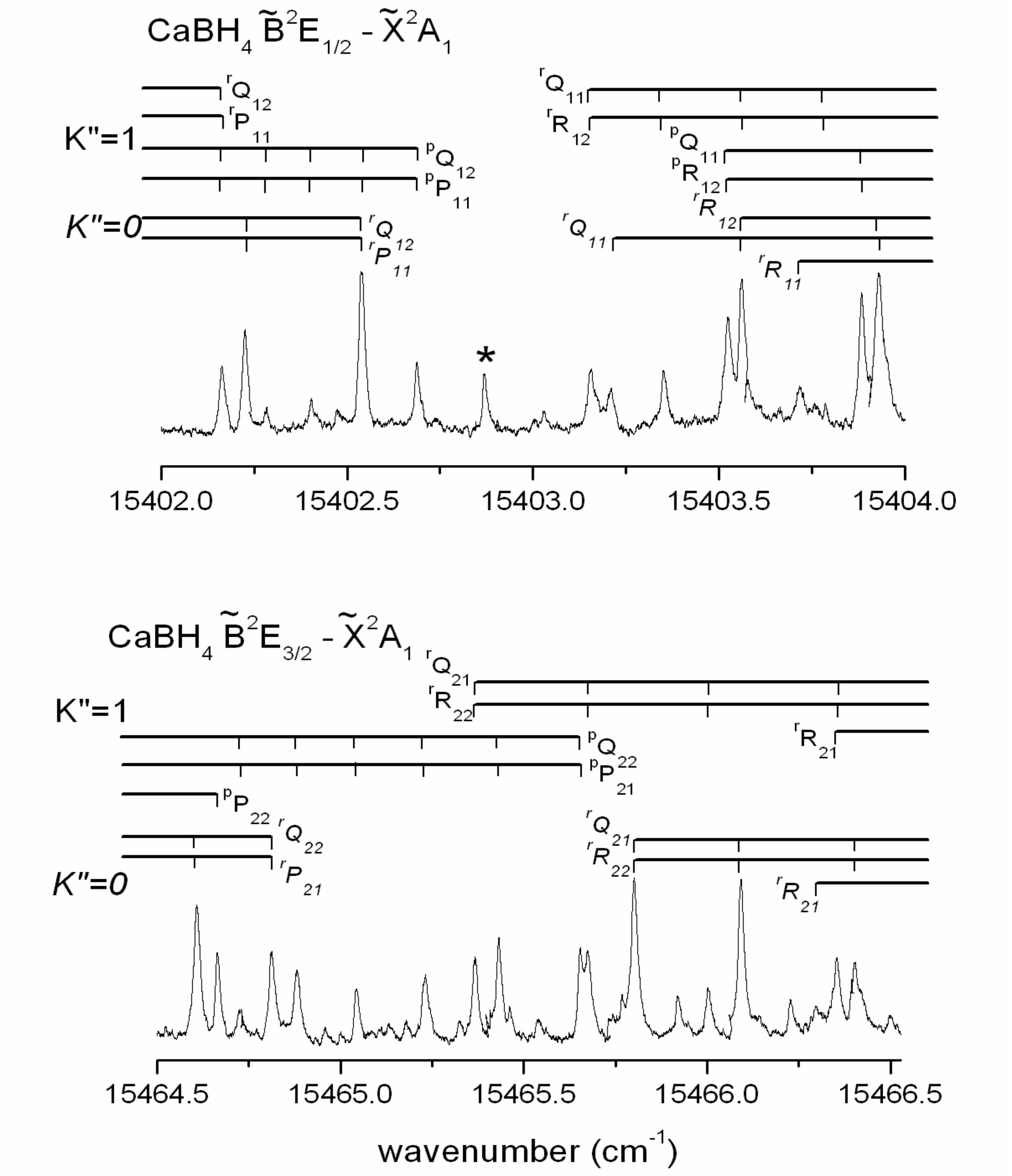

Figure 7.4 - A portion of the high resolution spectra, including rotational assignments, for each spin-orbit component of the $\tilde{B}^2E - \tilde{X}^2A_1$ transition of $CaBH_4$.

assignments ($^{\Delta K}\Delta J_{F_i' F_j''}$ (i = 1, 2; j = 1, 2)) for each spin-orbit component of this electronic transition. In the top spectrum, the starting positions of the branches of the $\tilde{B}^2E_{3/2}$-$\tilde{X}^2A_1$ component can be observed to vary greatly from those of $SrBH_4$. For example, the $^pP_{21}$ branch begins to the blue of the $^rR_{22}$ branch, which obscures the origin of the $\tilde{B}^2E_{3/2}$-$\tilde{X}^2A_1$ spin-orbit component. This irregular pattern contributed to the difficulty in identifying the starting positions for each series of lines.

7.4 Analysis

The $\tilde{B}^2E$-$\tilde{X}^2A_1$ transitions of $SrBH_4$ and $CaBH_4$ were modeled using a symmetric top effective Hamiltonian [40,41,42] that incorporated the rotation of the molecule, along with centrifugal distortion corrections, and the spin-rotation, spin-orbit, Jahn-Teller, and Coriolis interactions. Using the matrix elements of Endo et al. [41] in a Hund's case (a) basis, this Hamiltonian was incorporated into a computer program and a least squares fit of the measured data was performed.

For $SrBH_4$, 181 lines from 35 of the 36 possible branches from all three observed ΔK sub-bands were included in the fit. Clearly resolved lines were weighted according to the experimental uncertainty (0.004 cm^{-1}), while overlapped lines were deweighted slightly (0.008 cm^{-1}). The measured lines can be found in Appendix A4. In the ground state, only one rotation (B) and one spin-rotation ($\varepsilon_{bc} = (\varepsilon_{bb} + \varepsilon_{cc})/2$) constant were allowed to vary. The A rotational constant in the ground state could not be determined from the current data set, because no $\Delta K = 0$ transitions were observed. As a result it was fixed to the theoretical value given by Chan and Hamilton [32]. Additionally, no centrifugal distortion terms were found to be necessary, due to the low J values ($J'' < 9.5$) observed in the spectra. For the excited state, a set of molecular constants similar to those used to describe the $\tilde{A}^2E$ state of $SrCH_3$ (Chapter 6) were employed. These included rotation (A, B), spin-orbit ($a\zeta_e d$, $a_D\zeta_e d$), Coriolis ($A\zeta_t$), and spin-rotation (ε_{aa}, ε_1) terms. The spectroscopic parameters for the $\tilde{B}^2E$ and $\tilde{X}^2A_1$ states of $SrBH_4$ derived from the final fit are listed in Table 7.1, along with those of the $\tilde{A}^2E$ and $\tilde{X}^2A_1$ states of $SrCH_3$ for comparison.

Table 7.1. Spectroscopic Constants (in cm^{-1}) for the $\tilde{A}\,^2E$ and $\tilde{X}\,^2A_1$ States of $SrCH_3$ and the $\tilde{B}\,^2E$ and $\tilde{X}\,^2A_1$ States of $SrBH_4$.

	$SrCH_3$[b]		$SrBH_4$	
Constant[a]	$\tilde{X}\,^2A_1$	$\tilde{A}\,^2E$	$\tilde{X}\,^2A_1$	$\tilde{B}\,^2E$
T	0.0	13800.3762(9)	0.0	14422.5566(18)
$a\zeta_e d$		279.1651(17)		198.4994(36)
$a_D\zeta_e d$		-0.0297(15)		-0.0337(15)
$A\zeta_t$		5.24833(83)		4.0123(11)
A	5.390[c]	5.33494(75)	4.213[c]	4.17708(76)
B	0.193833336(16)	0.195068(21)	0.188367(50)	0.194290(44)
D_N	2.14893(11) x 10^{-7}			
D_{NK}	1.61349(51) x 10^{-5}			
H_{NK}	2.920(21) x 10^{-10}			
H_{KN}	3.18(43) x 10^{-9}			
ε_{aa}	0.000883(34)	0.3692(33)		0.0792(44)
ε_{bc}	0.00412852(43)		0.002619(39)	
ε_1		-0.09415(12)		0.18509(16)

[a] Values in parenthesis are 1σ standard deviations, in units of the last significant digits.
[b] From Chapter 6
[c] Fixed to theoretical value [32].

The fitting of the $\tilde{B}^2E - \tilde{X}^2A_1$ transition data of $CaBH_4$ was not as straightforward as it was for $SrBH_4$. In the first attempt at fitting the rotational transitions of the three observed ΔK sub-bands, residuals for the $^PP_{11}$ branch were found to be unusually large.

As a result, a second fit was conducted without this branch. A subsequent prediction, using the parameters of this fit, indicated that the *J* values of the $^{P}P_{11}$ branch should be decreased by one from the original assignment. Initially, this result was not surprising as this branch was originally assigned by identification of a supposed first line. However, these new *J* assignments of the $^{P}P_{11}$ branch resulted in one line (identified with an * in Figure 7.4) being unassigned. Subsequent attempts to ascertain the identity of this line in the context of this fit were unsuccessful. The iodine calibration spectrum and etalon trace signal were examined closely to ensure that this line was a real feature, and not the result of a laser mode hop. In addition, attempts at reassigning the observed branches of all three ΔK sub-bands in the $\tilde{B}^2E_{1/2} - \tilde{X}^2A_1$ spin-orbit component to include this line were unsuccessful. The line positions of the $^{P}P_{11}$ branch were also calculated using the lower-state combination differences from the 2 – 1 sub-band to determine the $K'' = 1$ rotational level energies, and the upper-state ($K' = 0$) rotational level energies were calculated from upper-state combination differences of the $^{P}R_{12}$ and $^{P}P_{12}$ branches (assuming that the *e* and *f* parity splitting in the $K' = 0$ levels was negligible, as it was for $CaCH_3$ [29,30], $SrCH_3$ (Chapter 6) and $SrBH_4$. This calculation showed that the new *J* assignments for the $^{P}P_{11}$ branch with one line left unassigned were plausible.

Using these rotational line assignments, 169 lines from 34 of the 36 possible branches were included in the fit, and are listed in Appendix A5. As with $SrBH_4$, clearly resolved (0.004 cm^{-1}) and overlapped lines (0.008 cm^{-1}) were weighted differently. In the ground state, only the rotational constant, *B*, was allowed to vary. As with $SrBH_4$, no $\Delta K = 0$ transitions were observed, therefore the *A* rotational constant in the ground state could not be determined, and was fixed to the theoretical value [32]. As mentioned previously, the spin-rotation splitting in the $\tilde{X}^2A_1$ state appeared unresolved, so ε_{bc} was fixed to zero. In the upper state, the rotation (A, B), spin-orbit ($a\zeta_e d$), Coriolis ($A\zeta_t$), and spin-rotation ($\varepsilon_{aa}, \varepsilon_1$) terms were included in the fit. Unlike for $SrBH_4$, it was found that the $a_D\zeta_e d$ term could not be determined for $CaBH_4$. The spectroscopic parameters for the $\tilde{B}^2E$ and $\tilde{X}^2A_1$ states of $CaBH_4$ determined from this fit are listed in Table 7.2 along with those of the $\tilde{A}^2E$ and $\tilde{X}^2A_1$ states of $CaCH_3$ for comparison.

One likely explanation for the identity of the unassigned line in the $\tilde{B}^2E_{1/2}$ - $\tilde{X}^2A_1$ spin-orbit component is that it is indeed the first line of the $^PP_{11}$ branch. This would suggest that the rotational energy levels of the $K' = 0$ state of the $\tilde{B}^2E_{1/2}$ spin-orbit component are being perturbed by some nearby electronic state. As mentioned in Chapter 5, for $CaCH_3$, the $K' = 1$ level of the $\tilde{B}^2A_1$ state was found to be perturbed by a vibrational level of the $\tilde{A}^2E$ state. A similar scenario is possible for $CaBH_4$, in which a vibronic level of the $\tilde{A}^2A_1$ state interacts with the $K' = 0$ state of the $\tilde{B}^2E_{1/2}$ spin-orbit component. As a result an alternative fit of the $\tilde{B}^2E - \tilde{X}^2A_1$ transition data of $CaBH_4$, in which the data from the 0-1 subband of the $\tilde{B}^2E_{1/2} - \tilde{X}^2A_1$ spin-orbit component was removed, was performed. This alternative fit included both spin-orbit components of the 1-0 and 2-1 subbands and only the 0-1 subband of the the $\tilde{B}^2E_{3/2} - \tilde{X}^2A_1$ component. In this fit, the rotation (A, B), spin-orbit ($a\zeta_e d$), Coriolis ($A\zeta_t$), and spin-rotation ($\varepsilon_1, \varepsilon_{aa}$) parameters were determined, and are also included in Table 7.2 for comparison.

Table 7.2. Spectroscopic Constants (in cm^{-1}) for the $\tilde{A}\,^2E$ and $\tilde{X}\,^2A_1$ States of $CaCH_3$ and the $\tilde{B}\,^2E$ and $\tilde{X}\,^2A_1$ States of $CaBH_4$.

	$CaCH_3$[b]		$CaBH_4$[d]		$CaBH_4$[e]	
Constant[a]	$\tilde{X}\,^2A_1$	$\tilde{A}\,^2E$	$\tilde{X}\,^2A_1$	$\tilde{B}\,^2E$	$\tilde{X}\,^2A_1$	$\tilde{B}\,^2E$
T	0.0	14743.3882(11)	0.0	15438.3932 (62)	0.0	15438.3936(19)
$a\zeta_e d$		72.7092(18)		62.9654(11)		62.9646(34)
$a_D\zeta_e d$		-8.86×10^{-4}				
$A\zeta_t$		5.3600(3)		4.12669(49)		4.1272(12)
A	5.44831	5.3855(6)	4.230[c]	4.18596(44)	4.230[c]	4.18637(65)
B	0.2523847	0.254270(7)	0.247357(30)	0.255106(26)	0.24734(31)	0.255127(30)
D_K	7.03×10^{-5}	6.437×10^{-5}				
D_N	3.544852×10^{-7}	3.6203×10^{-7}				
D_{NK}	1.995314×10^{-5}	1.2980×10^{-5}				
$\eta_e\zeta_t$		3.522×10^{-5}				
ε_{aa}		0.0129(17)		-0.0480(11)		-0.0477(30)
ε_{bc}	0.00185105	0.0196(17)				
ε_1		-0.0251(1)		0.086045(81)		0.08618(10)

[a] Values in parenthesis are 1σ standard deviations, in units of the last significant digits.

[b] From reference [30]

[c] Fixed to theoretical value [32].

[d] Fit included 34 of the 36 possible branches for the $\tilde{B}\,^2E$ - $\tilde{X}\,^2A_1$ transition. The $^PP_{11}$ branch is labeled such that one line remains unassigned.

[e] Fit included all of the possible branches for the $\tilde{B}\,^2E_{3/2}$ - $\tilde{X}\,^2A_1$ spin-orbit component and all of the observed branches for the 1-0 and 2-1 subbands of the $\tilde{B}\,^2E_{1/2}$ - $\tilde{X}\,^2A_1$ spin-orbit component. No lines from the 0-1 subband of the $\tilde{B}\,^2E_{1/2}$ - $\tilde{X}\,^2A_1$ spin-orbit component were included.

7.5 Discussion

Because rotational constants for only one isotopologue of both $CaBH_4$ and $SrBH_4$ were determined in this study, it is difficult to ascertain the structural parameters of these molecules. One approach that can be employed to extract structural information from the observed rotational constants is to fix the geometry of the BH_4^- ligand to that calculated for the ground state by Chan and Hamilton [32], and assume that the ligand structure is invariant upon promotion from the $\tilde{X}^2A_1$ to $\tilde{B}^2E$ state. Using this method, the rotational constant *B* can be used to derive the metal-boron separation. The calculated distances are listed in Table 7.3, along with the theoretical values [31,32] for comparison. For the ground states there is very good agreement (less than a 1% difference) between the metal-boron separations obtained in this work and those calculated by Chan and Hamilton [32]. The agreement is slightly worse for the calculations of Ortiz [31]. For the excited states, no theoretical predictions of the rotational constants exist; therefore, no direct comparison of the experimental metal-boron separations to the theoretical values can be made.

Table 7.3. Metal – ligand separations for the borohydrides and monomethyls of calcium and strontium

State	M-L Separation	$CaBH_4$[a]	$CaBH_4$	$CaCH_3$[d]
$\tilde{X}^2A_1$	$r_{Ca\text{-}L}$ (Å)	2.416	2.414[b], 2.430[c]	2.348
^2E	$r_{Ca\text{-}L}$ (Å)	2.376		2.342
		$SrBH_4$[a]	$SrBH_4$	$SrCH_3$[e]
$\tilde{X}^2A_1$	$r_{Sr\text{-}L}$ (Å)	2.574	2.596[b]	2.487
^2E	$r_{Sr\text{-}L}$ (Å)	2.532		2.481

[a] Calculated from the rotational constant, *B*, from the current investigation and fixing BH_4^- ligand geometry to that of ref. [32].
[b] Theoretical from ref. [32], [c] Theoretical from ref. [31].
[d] Experimental from Chapter 5, [e] Experimental from Chapter 6.

Using these experimental values of the metal-ligand separation, the change in this separation from the $\tilde{X}^2A_1$ to $\tilde{B}^2E$ state can be examined. For $CaBH_4$ and $SrBH_4$, the metal-ligand separations decrease by factors of 0.9834 (0.040 Å) and 0.9837 (0.042 Å), respectively. This is in contrast to the metal-ligand separation in $CaCH_3$ and $SrCH_3$, where from the $\tilde{X}^2A_1$ to $\tilde{A}^2E$ states the metal-carbon distances (Table 7.3) decreased by factors of only 0.9963 (0.006 Å) and 0.9968 (0.006 Å), respectively. The larger decrease in the metal-ligand separation for the metal borohydrides, as compared to the metal monomethyls, is consistent with the theoretical calculations of Ortiz [31] for $CaBH_4$. In this work, the metal-boron separation in the first excited ^2E state was found to decrease by a factor of 0.9794 (0.05 Å) from that for the ground state. This larger change in the metal-ligand separation was attributed to an increased amount of *d* atomic orbital character in the first excited ^2E state of $CaBH_4$ as compared to $CaCH_3$. It was suggested that this increase in the *d* orbital character would result in the unpaired electron residing in a more diffuse orbital, which in turn allows the BH_4^- ligand to more closely approach the Ca^+ cation. Similar calculations for $SrBH_4$ do not exist, but as mentioned previously, a similar change between the ground and excited-state rotational constants was observed. This may imply that an increased amount of *d* character is also present in the $\tilde{B}^2E$ state of $SrBH_4$ as compared to $SrCH_3$.

Finally, fluxional behavior, in which the BH_4^- ligand undergoes internal rotation, was predicted to have a low energy barrier in the alkali metal borohydrides. However, a splitting of rotational lines inherent with the internal rotation of the BH_4^- ligand [27] was not resolved in the $\tilde{B}^2E - \tilde{X}^2A_1$ transitions of $CaBH_4$ and $SrBH_4$. This indicates that the barrier to this internal motion is high in the borohydrides of calcium and strontium, as it is in $NaBH_4$ [7] and $LiBH_4$ [12].

For both $CaBH_4$ and $SrBH_4$, the orbitally degenerate $\tilde{B}^2E$ state may be subject to Jahn-Teller coupling. However, electronic states that exhibit a large spin-orbit interaction are expected to exhibit a small Jahn-Teller splitting [43]. Additionally, electronic states arising predominantly from atomic orbitals located on the metal atom, such as the $\tilde{B}^2E$ states of the metal borohydrides, should have reduced Jahn-Teller coupling. This is a result of the hydrogen atoms of the ligand being located far from the metal atom, which causes the coupling of degenerate vibrational and electronic wave functions to be small [44].

Assuming that the Jahn-Teller coupling is small in the $\tilde{B}^2E$ states of $CaBH_4$ and $SrBH_4$, the projections of the electronic (ζ_e) and vibronic (ζ_t) angular momenta on the symmetry axis can be calculated for these states. First, ζ_t can be calculated from the ratio of $A\zeta_t$ to A for the $\tilde{B}^2E$ state of each molecule ($CaBH_4$ $\zeta_t = 0.9859$, $SrBH_4$ $\zeta_t = 0.9606$). Next, these values of ζ_t can be used to calculate ζ_e via the following equation [45]

$$\zeta_t = \zeta_e d + \frac{1-d}{2}\zeta_2 \tag{7.1}$$

in which d is the Jahn-Teller quenching parameter ($1>|d|>0$) and ζ_2 is the vibrational Coriolis coupling coefficient for the Jahn-Teller active degenerate vibrational mode. If the Jahn-Teller effect is neglected ($d = 1$), then according to Equation 7.1 $\zeta_e = \zeta_t$, and hence $\zeta_e = 0.9859$ and 0.9606 for $CaBH_4$ and $SrBH_4$, respectively. For an electronic state derived primarily from a *p* atomic orbital ζ_e should be close to 1. Any reduction in this value can be attributed to an increase in the amount of atomic orbital character other then

p. Although these values of ζ_e indicate that the $\tilde{B}^2E$ states of $CaBH_4$ and $SrBH_4$ arise predominantly from p orbitals located on the metal, a comparison with the ζ_e values of $CaCH_3$ (0.9953) [29] and $SrCH_3$ (0.9838) (Chapter 6) shows that they are reduced slightly for the borohydrides. This suggests that the $\tilde{B}^2E$ states of $CaBH_4$ and $SrBH_4$ contain less p orbital character than the $\tilde{A}^2E$ states of the corresponding monomethyls.

A final indication of the reduction of the amount of p orbital character in $\tilde{B}^2E$ states of $CaBH_4$ and $SrBH_4$ as compared to the $\tilde{A}^2E$ states of $CaCH_3$ and $SrCH_3$ can be found by examining the spin-orbit interaction. The energy separation of the two spin-orbit components of the $\tilde{B}^2E$ states is given by $a\zeta_e d$, where a describes the magnitude of the spin-orbit splitting. A value of a may be calculated using the expression $a\zeta_e d = a\zeta_t$, assuming that the Jahn-Teller interaction may be neglected. For $SrBH_4$ ($a\zeta_e d$ = 198.4994 cm^{-1}), the magnitude of the spin-orbit coupling constant is estimated to be a = 206.6411 cm^{-1}. This value is 27 percent smaller than the value for $SrCH_3$ (a = 283.772 cm^{-1} Chapter 6). This reduction may be rationalized by considering the atomic orbital contributions to the spin-orbit splitting parameter for the first excited ^2E states of either $SrCH_3$ or $SrBH_4$, which are given by the equation

$$a = c_{5p\pi}^2 \zeta_{5p} + c_{4d\pi}^2 \zeta_{4d} + c_{n\ell}^2 \zeta_{n\ell} \tag{7.2}$$

where $c_{5p\pi}$, $c_{4d\pi}$ and $c_{n\ell}$ are expansion coefficients and ζ_{5p}, ζ_{4d} and $\zeta_{n\ell}$ are the atomic spin-orbit coupling parameters [46]. This equation can be further simplified by removing the contributions from atomic orbitals other then $5p\pi$ and $4d\pi$ to give,

$$a = c_{5p\pi}^2 \zeta_{5p} + c_{4d\pi}^2 \zeta_{4d} \tag{7.3}$$

This is a relatively safe assumption because, for example, in the case of SrOH [47] the $5p\pi$ and $4d\pi$ orbitals comprise 92 percent of the orbital character of the $\tilde{\mathrm{A}}\,^2\Pi$ state. For strontium, the atomic spin-orbit coupling parameter is larger for the *5p* orbital (ζ_{5p} = 534 cm^{-1}) than it is for the *4d* orbital (ζ_{4d} = 112 cm^{-1}) [48]. Thus, if the amount of *5p* character decreases and the amount of *4d* character, increases the molecular spin-orbit coupling constant is reduced. This change in the amount of *d* character most likely accounts for the majority of the 27 percent reduction in the magnitude of the molecular spin-orbit coupling constant in $SrBH_4$ compared to that for $SrCH_3$.

A similar reduction in the molecular spin-orbit coupling parameter, *a*, in the first excited $^2\mathrm{E}$ state is observed for $CaBH_4$ (a = 63.87 cm^{-1}) as compared to $CaCH_3$ (a = 72.7092 cm^{-1}) [30]. In this case the spin-orbit coupling constant may be calculated according to the equation

$$a = c_{4p\pi}^2 \zeta_{4p} + c_{3d\pi}^2 \zeta_{3d} \tag{7.4}$$

For calcium, the atomic spin orbit coupling parameter is again larger for the *p* orbital (ζ_{4p} = 148 cm^{-1}) than for the *d* orbital (ζ_{3d} = 24 cm^{-1}) [49], but the difference in magnitude is not as great as for strontium. The reduction in *a* can again most likely be largely attributed to an increase in the amount of *d* character in the $\tilde{\mathrm{B}}\,^2\mathrm{E}$ state of $CaBH_4$ as compared to the $\tilde{\mathrm{A}}\,^2\mathrm{E}$ state of $CaCH_3$.

Another interesting comparison that can be made between the monomethyls and borohydrides of strontium and calcium involves the spin-rotation constant ε_1. As described in Chapter 2, the pure precession relationship and unique perturber approximation can be used to derive the following expression for ε_1

$$\varepsilon_1 = \frac{aB\ell(\ell+1)}{E_{^2E} - E_{^2A_1}} \tag{7.5}$$

where ℓ is the atomic orbital angular momentum and E is the state energy. This equation shows that ε_1 arises from an interaction of a $^2\mathrm{E}$ state with a neighboring $^2\mathrm{A}_1$ state. This is analogous to the Λ-doubling constant, p, in a $^2\Pi$ state, which accounts for its interaction with a neighboring $^2\Sigma^+$ state. According to Equation 7.5, the sign of ε_1 should be dependant on the relative energy positioning of the $^2\mathrm{E}$ and $^2\mathrm{A}_1$ states. For example, if the $^2\mathrm{E}$ state lies higher in energy then the $^2\mathrm{A}_1$ state, then ε_1 will have a positive sign. For both $\mathrm{CaBH_4}$ (0.08618 cm^{-1}) and $\mathrm{SrBH_4}$ (0.18509 cm^{-1}) the sign of ε_1 has changed in comparison with $\mathrm{CaCH_3}$ (-0.0251 cm^{-1}) [30] and $\mathrm{SrCH_3}$ (-0.09415 cm^{-1} Chapter 6). This is further evidence that the first excited $^2\mathrm{E}$ and $^2\mathrm{A}_1$ states in the borohydrides are reordered in energy compared to the monomethyls [23].

For both $\mathrm{CaBH_4}$ and $\mathrm{SrBH_4}$, the magnitude of ε_1 has increased in comparison with the monomethyls. As both a and B have decreased for $\mathrm{CaBH_4}$ and $\mathrm{SrBH_4}$, this increase in magnitude is a reflection of the first excited $^2\mathrm{E}$ and $^2\mathrm{A}_1$ states lying closer in energy for the borohydrides. In the $\tilde{\mathrm{B}}^2\mathrm{E}$ state of $\mathrm{SrBH_4}$, the magnitude of ε_1 is nearly equal to the rotational constant, B (0.194290 cm^{-1}). As mentioned previously, ε_1 is analogous to the Λ-doubling constant, p, and the two parameters can be related by the expression $\varepsilon_1 = p/2$ [41]. Kopp and Hougen [50] have shown that if p equals approximately twice the B value in a $^2\Pi_{1/2}$ state, the energy level structure of this state becomes very similar to that of a $^2\Sigma^+$ state. Applying these arguments to a $^2\mathrm{E}_{1/2}$ state, if ε_1 equals approximately B, then the energy level structure of this state will appear like a $^2\mathrm{A}_1$ state. This is precisely what has been observed in the $\tilde{B}^2E_{1/2}$ spin-orbit component of $SrBH_4$, and it explains the unique structure of this component, in which each branch is spaced by ~2*B*. A similar structure is not seen in the $\tilde{B}^2E_{1/2}-\tilde{X}^2A_1$ spin-orbit component of $CaBH_4$, as ε_1 has increased, but is not quite equal in magnitude to *B*. Therefore, ~1*B* and ~3*B* spaced branches are still observed in this spin-orbit component.

Finally, it is of interest to compare the experimentally determined values of ε_1 with those derived from Equation 7.5. For $SrBH_4$ the values $a = 206.6411$ cm^{-1}, $B = 0.194290$ cm^{-1}, $E(\tilde{B}\,^2E) = 14422.5566$ cm^{-1} and $E(\tilde{A}\,^2A_1) = 13685$ cm^{-1} were used. Assuming that the $\tilde{B}\,^2E$ state arises solely from a *p* atomic orbital ($\ell=1$), ε_1 was estimated to be 0.1089 cm^{-1}. For $CaBH_4$ ($a = 63.87$ cm^{-1}, $B = 0.255127$ cm^{-1}, $E(\tilde{B}\,^2E) = 15438.3936$ cm^{-1}, $E(\tilde{A}\,^2A_1) = 14800$ cm^{-1} and $\ell=1$), a similar calculation estimated ε_1 to be 0.051 cm^{-1}. For each molecule the calculated value is approximately 40% smaller than the experimentally determined parameter, consistent with $\ell>1$ and additional *d* orbital character. However, some of these differences may be attributed to the approximations made in deriving Equation 7.5. Similar calculations of ε_1 in the $\tilde{A}^2E$ state of $CaCH_3$ and $SrCH_3$ (Ref. 29 and Chapter 6) found differences between the calculated and experimentally determined parameters of only about 20%. This better agreement for the monomethyls as compared to the borohydrides is consistent with more *p* atomic orbital character (ℓ closer to 1) in the $\tilde{A}^2E$ state of the monomethyls as compared to the $\tilde{B}^2E$ state of the borohydrides.

The remaining experimentally determined spin-rotation constant (ε_{aa}) also can be estimated using the unique perturber approximation and pure precession relationship (Chapter 2).

$$\varepsilon_{aa} = -\frac{4a\zeta_e dA\zeta_t}{E_{\tilde{B}^2E} - E_{Higherlying\,^2E}} \qquad (7.6)$$

According to the above equation, ε_{aa} should be positive for the $\tilde{\mathrm{B}}^2\mathrm{E}$ states of $SrBH_4$ and $CaBH_4$. A value of 0.0792 cm^{-1} was determined for ε_{aa} in the $\tilde{\mathrm{B}}^2\mathrm{E}$ state of $SrBH_4$. Unfortunately, this parameter cannot be quantitatively estimated using Equation 7.6, as no information exists for any of the other excited ^2E states of $SrBH_4$. However, qualitatively this equation does indicate that ε_{aa} should be small and positive, as the neighboring ^2E states should be higher in energy than the $\tilde{\mathrm{B}}^2\mathrm{E}$ state of $SrBH_4$. Interestingly, a similar qualitative agreement was not found for ε_{aa} in the $\tilde{\mathrm{B}}^2\mathrm{E}$ state of $CaBH_4$, where this constant (ε_{aa} = -0.0477 cm^{-1}) was found to be small and negative, in disagreement with Equation 7.6. However, ε_{aa} was only marginally determined in both fits of $CaBH_4$, making its true physical significance somewhat dubious.

One possible explanation for the negative value of ε_{aa} for $CaBH_4$ is that it is a result of a perturbation to the $\tilde{\mathrm{B}}^2\mathrm{E}_{1/2}$ spin-orbit component. For $CaCH_3$ (Chapter 5), the $\tilde{\mathrm{B}}^2\mathrm{A}_1$ state was found to be perturbed. In this case, the K' = 1 energy levels were affected by an interaction with an excited $\tilde{\mathrm{A}}^2\mathrm{E}$ vibrational state. This perturbation caused the energy levels of the F_1 spin-rotation component to be higher in energy than those of the F_2 component, contrary to the K' = 0 energy level. As a result, the K' = 1 sublevel data could not be included in the final fit. A similar interaction is possible, in reverse, in $CaBH_4$ where the $\tilde{\mathrm{B}}^2\mathrm{E}$ state interacts with an excited vibrational level of the

$\tilde{A}^2A_1$ state. The unambiguous assignment of the ${}^{P}P_{11}$ branch in the 0-1 sub-band of the $\tilde{B}^2E_{1/2}$ - $\tilde{X}^2A_1$ spin-orbit component suggests that the K' = 0 rotational levels of this spin-orbit component are perturbed. More specifically, the ${}^{P}P_{11}$ branch terminates in levels with *e* parity, which suggests that these levels are the most affected by the perturbation. This is further supported since the assignment of the ${}^{P}P_{12}$ and ${}^{P}R_{12}$ branches without complication suggests that the *f* levels of the K' = 0 state of the $\tilde{B}^2E_{1/2}$ spin-orbit component are relatively unaffected by the perturbation. This scenario where the *e* and *f* parity levels are affected differently by the perturbation is possible as long as the parity splitting in the perturbing state is large and the *e* level interaction is more in resonance than the *f* level interaction. From the pure precession and unique perturber approximations [46], it is known that the parity splitting in the $\tilde{A}^2A_1$ should be similar to that of the $\tilde{B}^2E_{1/2}$ spin-orbit component. In this component the splitting is described by ε_1, and as outlined previously, the magnitude of this parameter has increased significantly in comparison with $CaCH_3$ [29,30]. This increase in magnitude could result in the perturbation dominating the *e* levels of the K' = 0 sublevel of the $\tilde{B}^2E_{1/2}$ spin-orbit component. However, when the K' = 0 data was removed from the fit, a negative value of ε_{aa} was still found, further suggesting that the K' = 1 and 2 levels may also be affected, although less severely. Unfortunately, it is difficult to determine which of the vibrational levels of the $\tilde{A}^2A_1$ state is causing the perturbation, as little information exists on the excited states of $CaBH_4$. Ortiz [31] has calculated vibrational frequencies for the ground electronic state of $CaBH_4$. In his work, the frequency of the lateral motion of the borohydride ligand relative to the symmetry axis was predicted to be 528 cm^{-1}. This is within 20 percent of $\widetilde{A}^2A_1$ - $\widetilde{B}^2E_{1/2}$ separation (~ 638 cm^{-1}), making the first level of this vibration a possible candidate for the perturbing state.

References

[1] P. F. Bernath, *Advances in Photochemistry*. (Wiley, New York, 1997), Vol. 23, p.1.

[2] A. M. Ellis, Int. Rev. Phys. Chem. **20,** 551 (2001).

[3] C. M. Gittins, N. A. Harris, R. W. Field, J. Vergès, C. Effantin, A. Bernard, J. D'Incan, W. E. Ernst, P. Bündgen and B. Engels, J. Mol. Spectrosc. **161**, 303 (1993).

[4] P. M. Sheridan, M. J. Dick, J.-G. Wang and P. F. Bernath, J. Mol. Spectrosc. **233**, 269 (2005).

[5] B. D. James and M. G. H. Wallbridge, Prog. Inorg. Chem. **11**, 99 (1970).

[6] T. J. Marks and J. R. Kolb, Chem. Rev. **77**, 263 (1977).

[7] Y. Kawashima, C. Yamada and E. Hirota, J. Chem. Phys. **94**, 7707 (1991).

[8] Y. Kawashima and E. Hirota, J. Mol. Spectrosc. **153**, 466 (1992).

[9] Y. Kawashima, Y. Ohshima, Y. Endo and E. Hirota, J. Mol. Spectrosc. **174**, 279 (1995).

[10] Y. Kawashima, O. N. Ulenikov and E. Hirota, Mol. Phys. **101**, 623 (2003).

[11] Y. Kawashima and E. Hirota, J. Chem. Phys. **102**, 6961 (1995)

[12] Y. Kawashima and E. Hirota, J. Chem. Phys. **96**, 2460 (1992).

[13] E. Hirota and Y. Kawashima, J. Mol. Spectrosc. **181**, 352 (1997).

[14] W. C. Price, H. C. Longuet-Higgins, B. Rice and T. F. Young, J. Chem. Phys. **17**, 217 (1949).

[15] W. C. Price, J. Chem. Phys. **17**, 1044 (1949).

[16] E. H. Coker and D. E. Hofer, J. Chem. Phys. **48**, 2713 (1968).

[17] A. I. Boldyrev, O. P. Charkin, N. G. Rambidi and V. I. Avdeev, Chem. Phys. Lett. **44**, 20 (1976).

[18] J. D. Dill, P. v. R. Schleyer, J. S. Binkley and J. A. Pople, J. Am. Chem. Soc. **99**, 6159 (1977).

[19] R. Bonaccorsi, E. Scrocco and J. Tomasi, Theoret. Chimi. Acta. **52**, 113 (1979).

[20] V. Barone, G. Dolcetti, F. Lelj and N. Russo, Inorg. Chem. **20**, 1687 (1981).

[21] L. Y. Baranov and A. I. Boldyrev, Chem. Phys. Lett. **96**, 218 (1983).

[22] V. Kellö, M. Urban and A. I. Boldyrev, Chem. Phys. Lett. **106**, 455 (1984).

[23] D. J. DeFrees, K. Raghavachari, H. B. Schlegel, J. A. Pople and P. v. R. Schleyer, J. Phys. Chem. **91**, 1857 (1987).

[24] R. Bonaccorsi, O. P. Charkin and J. Tomasi, Inorg. Chem. **30**, 2964 (1991).

[25] J. S. Francisco and I. H. Williams, J. Phys. Chem. **96**, 7567 (1992).

[26] V. V. Nefedova, A. I. Boldyrev and J. Simons, J. Chem. Phys. **98**, 8801 (1993).

[27] E. Hirota, J. Mol. Spectrosc. **153**, 447 (1992).

[28] F. S. Pianalto, A. M. R. P. Bopegedera, W. T. M. L. Fernando, R. Hailey, L. C. O'Brien, C. R. Brazier, P. C. Keller and P. F. Bernath, J. Am. Chem. Soc. **112**, 7900 (1990).

[29] C. R. Brazier and P. F. Bernath, J. Chem. Phys. **91**, 4548 (1989).

[30] A. J. Marr, F. Grieman and T. C. Steimle, J. Chem. Phys. **105**, 3930 (1996).

[31] J. V. Ortiz, J. Am. Chem. Soc. **113**, 1102 (1991).

[32] W.-T. Chan and I. P. Hamilton, Chem. Phys. Lett. **316**, 171 (2000).

[33] S. Gerstenkorn and P. Luc, *Atlas du Spectre d'Absorption de la Molécule d'Iode* (Laboratoire Aimé-Cotton, CNRS 91405, Orsay, France, 1978).

[34] A. M. R. P. Bopegedra, C. R. Brazier and P. F. Bernath, J. Phys. Chem. **91**, 2779 (1987).

[35] A.M.R.P. Bopegedera, C.R. Brazier and P.F. Bernath, J. Mol. Spectrosc. **129**, 268 (1988).

[36] M. Li and J.A. Coxon, J. Mol. Spectrosc. **176**, 206 (1996).

[37] C. H. Townes and A. L. Schawlow, *Microwave Spectroscopy* (Dover, New York 1975).

[38] M. A. Anderson, J. S. Robinson and L. M. Ziurys, Chem. Phys. Lett. **257**, 471 (1996).

[39] M. A. Anderson and L. M. Ziurys, Astrophys. J. **460**, L77 (1996).

[40] Y. Endo, S. Saito and E. Hirota, J. Chem. Phys. **81**, 122 (1984).

[41] J. T. Hougen, J. Mol. Spectrosc. **81**, 73 (1980).

[42] J. M. Brown, Mol. Phys. **20**, 817 (1971).

[43] G. Herzberg, *Molecular Spectra and Molecular Structure, Vol. III – Electronic Spectra and Electronic Structure of Polyatomic Molecules*. (Krieger, Malabar, 1991).

[44] T. M. Cerny, X. Q. Tan, J. M. Williamson, E. S. J. Robles, A. M. Ellis and T. A. Miller, J. Chem. Phys. **99**, 9376 (1993).

[45] R. Rubino, J. M. Williamson and T. A. Miller, J. Chem. Phys. **103**, 5964 (1995).

[46] H. Lefebvre-Brion and R. W. Field, *The Spectra and Dynamics of Diatomic Molecules*. (Elsevier, Amsterdam, 2004).

[47] J.-G. Wang, P. M. Sheridan, M. J. Dick and P. F. Bernath, J. Mol. Spectrosc. **236**, 21 (2006).

[48] C. E. Moore, Atomic Energy Levels, NSRDS Natl. Bur. Stand. No. 35, U.S. GPO, Washington, DC, 1971, p. 192. (strontium)

[49] C. E. Moore, Atomic Energy Levels, NSRDS Natl. Bur. Stand. No. 35, U.S. GPO, Washington, DC, 1971, p. 246. (calcium).

[50] I. Kopp and J. T. Hougen, Can. J. Phys. **45**, 2581 (1967).

Chapter 8 - The $\tilde{D}^2\Sigma^+ - \tilde{A}^2\Pi$ transition of CaOH

8.1 Introduction

The previous four chapters have discussed investigations of the spectra and structure of the lower lying states of some strontium and calcium-containing polyatomic molecules. The higher-lying states of these polyatomic molecules are also of interest because the molecular structure may vary as the energy of the state increases and the metal-ligand bond becomes more covalent. Also the ordering and atomic orbital character of the electronic states may change with respect to their diatomic counterparts. One experimental method which can be used to study these higher energy states is optical-optical double resonance spectroscopy (OODR) [1,2].

A prime candidate for a study of the higher energy states is CaOH. As CaF has already been extensively studied [e.g., 3], comparisons of the electronic state ordering between these two isoelectronic calcium-containing molecules can easily be made. In addition, preliminary evidence indicates that some of the higher states of CaOH may adopt a nonlinear geometry, in contrast to the lower states in which CaOH has been found to be linear.

The first high resolution spectroscopic investigation of CaOH was completed by Hilborn and coworkers [4]. In that study, the $\tilde{A}^2\Pi - \tilde{X}^2\Sigma^+$ transition was observed and preliminary rotational constants were determined for each state. That work was followed by a more extensive investigation of this transition by Bernath and Brazier [5], in which the molecular parameters were refined. Subsequent studies of the $\tilde{A}^2\Pi - \tilde{X}^2\Sigma^+$ transition have probed the vibrational structure of each state using laser-induced fluorescence spectroscopy [6-11]. In addition, the $\tilde{A}^2\Pi - \tilde{X}^2\Sigma^+$ transition for the isotopologue CaOD has also been studied [12]. The $\tilde{B}^2\Sigma^+ - \tilde{X}^2\Sigma^+$ transition has also been observed both at low [13] and high [5,14] resolution, while, the $\tilde{C}^2\Delta - \tilde{X}^2\Sigma^+$ transitions of both CaOH and CaOD have been recorded at high resolution using the technique of laser excitation spectroscopy [15,16]. Pure rotational transitions in the ground state have been recorded by millimeter wave spectroscopy [17-20], and hyperfine constants arising from the hydrogen nucleus have been determined in the $\tilde{X}^2\Sigma^+$ state using the pump/probe microwave-optical double resonance technique [21]. Finally, the dipole moment of CaOH in the $\tilde{X}^2\Sigma^+$, $\tilde{A}^2\Pi$ and $\tilde{B}^2\Sigma^+$ states has been determined using Stark spectroscopy [22].

The higher energy states of CaOH (> 23000 cm^{-1}) have not been as thoroughly investigated as the lower states. Pereira and Levy [23] have used resonance-enhanced multiphoton ionization and laser-induced fluorescence spectroscopic techniques in a molecular beam source to observe the $\tilde{D}^2\Sigma^+ - \tilde{X}^2\Sigma^+$, $\tilde{E}^2\Sigma^+ - \tilde{X}^2\Sigma^+$ and $\tilde{F}^2\Pi - \tilde{X}^2\Sigma^+$ transitions of CaOH. From their moderate resolution spectra, they were able to determine preliminary rotational constants for the $\tilde{D}^2\Sigma^+$ state. In addition, they observed several vibrational bands for each electronic transition and found extensive activity in the bending mode of the $\tilde{F}^2\Pi$ state, indicating that CaOH could possess a nonlinear configuration in this state. Finally, the $\tilde{G}^2\Pi - \tilde{B}^2\Sigma^+$ transitions of both CaOH and CaOD has been recorded at moderate resolution using OODR spectroscopy [24]. Several vibrational bands were observed, and preliminary rotational and vibrational constants were determined for the $\tilde{G}^2\Pi$ state.

In this chapter, the results of a high-resolution study of the $\tilde{D}^2\Sigma^+ - \tilde{A}^2\Pi$ transition of CaOH using OODR spectroscopy will be presented. For the $\tilde{D}^2\Sigma^+$ state, rotational and fine structure constants have been determined. Using these parameters, the molecular structure and the orbital character for the $\tilde{D}^2\Sigma^+$ state have been derived. In addition, a comparison of the energy state ordering between CaOH and CaF will be presented.

8.2 Experimental

Gas phase CaOH was produced in a Broida-type oven (Chapter 3) by resistively heating calcium metal in a graphite crucible until sublimation occurred. The metal vapor was then carried into the reaction region above the crucible by a flow of argon carrier gas (~1-2 Torr). The calcium atoms were reacted with a few mTorr of concentrated hydrogen peroxide, which was introduced through a perforated stainless steel ring located above the crucible. This reaction produced a chemiluminescent flame of CaOH molecules.

The $\tilde{D}^2\Sigma^+ - \tilde{A}^2\Pi$ transition of CaOH was studied using OODR spectroscopy. A linear cavity dye laser (Kiton red laser dye, output power ~ 1 W, bandwidth ~1 cm^{-1}) was used to excite the $\tilde{A}^2\Pi - \tilde{X}^2\Sigma^+$ transition. The excitation wavelength was systematically varied in order to populate specific groups of rotational levels in the intermediate $\tilde{A}^2\Pi$ state. For example, in order to populate the maximum number of rotational levels, the pump laser was tuned to the band heads of each spin-orbit component of the $\tilde{A}^2\Pi - \tilde{X}^2\Sigma^+$ transition (~15957 cm^{-1} for the P_{11} and Q_{12} heads and ~16027 cm^{-1} for the P_{21} and Q_{22} heads). A single mode titanium-sapphire ring laser (probe laser, bandwidth ~10 MHz) operating in the 750 to 870 nm range was used to promote the CaOH molecules from the intermediate $\tilde{A}^2\Pi$ state to the $\tilde{D}^2\Sigma^+$ state.

As described in Chapter 3, the pump and probe laser beams were directed collinearly into the Broida oven chamber and overlapped in the chemiluminescent flame where the concentration of CaOH was greatest. Care was taken to ensure that the two beams were precisely overlapped to ensure that a maximum number of molecules were excited to the $\tilde{D}^2\Sigma^+$ state. As the probe laser wavelength was scanned, UV fluorescence from the $\tilde{D}^2\Sigma^+$ state was detected using a photomultiplier tube (PMT) with a 500 nm blue pass filter. Phase sensitive detection was utilized by amplitude modulating the pump beam with a mechanical chopper and processing the output signal of the PMT with a lock-in amplifier. The combination of the blue pass filter and phase sensitive detection ensured that the fluorescence signals observed arose only from the OODR experiment.

Typically spectra were recorded in 5 cm^{-1} segments at a scan speed of 30 seconds per wavenumber and a data sampling interval of 20 MHz. Absorption spectra of heated I_2 were recorded simultaneously to calibrate the spectra of the $\tilde{D}^2\Sigma^+ - \tilde{A}^2\Pi$ transition [25].

8.3 Results and Analysis

From the previous work of Pereira and Levy [23], approximate probe laser frequencies for this investigation of the $\tilde{D}^2\Sigma^+ - \tilde{A}^2\Pi$ transition of CaOH were determined. In Figure 8.1, high-resolution spectra for the $\tilde{D}^2\Sigma^+ - \tilde{A}^2\Pi_{3/2}$ spin-orbit component using two different pump laser wavenumbers are shown. In the upper panel

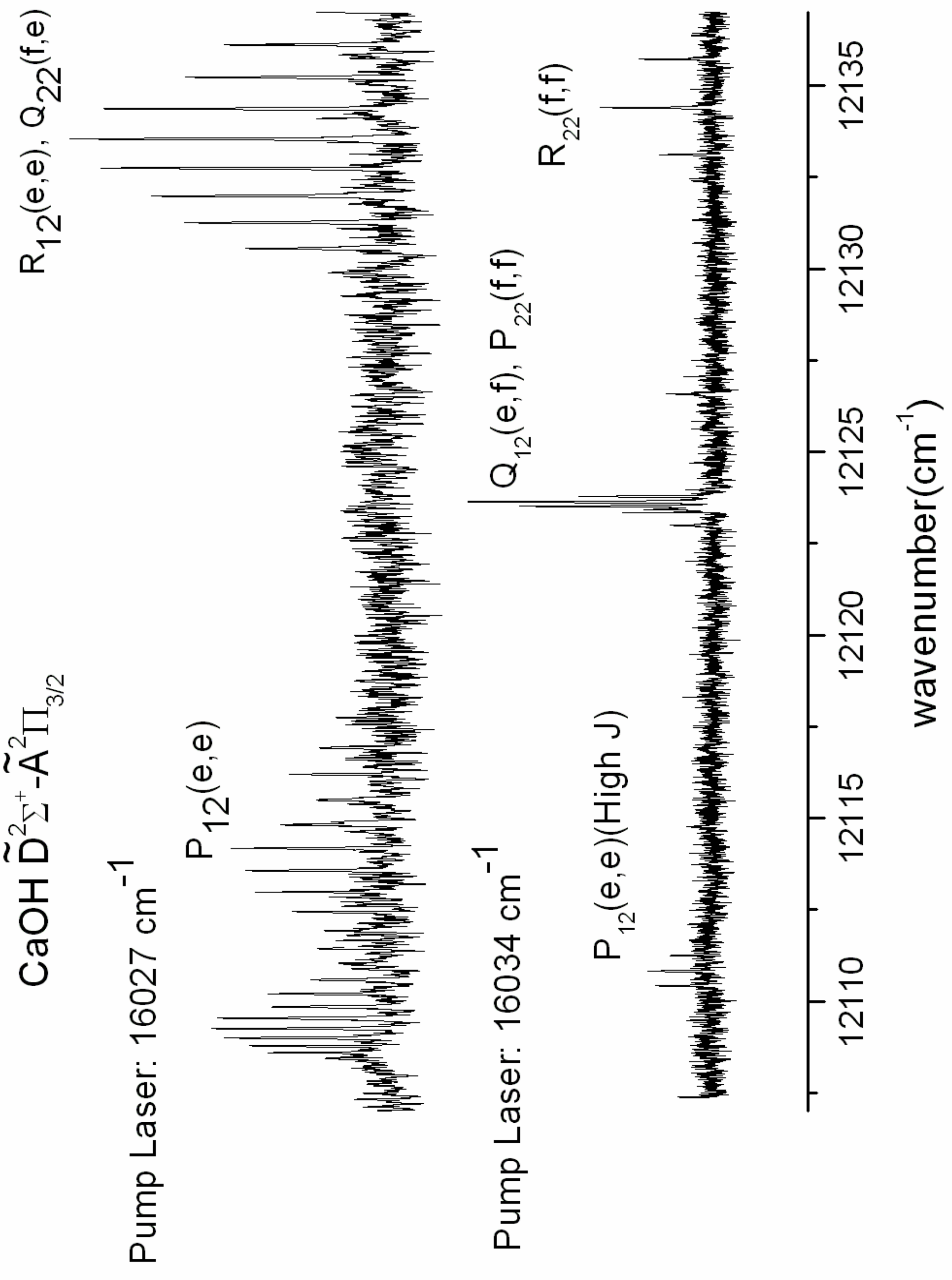

Figure 8.1 - Optical-optical double resonance spectra of the $\tilde{D}^2\Sigma^+ - \tilde{A}^2\Pi_{3/2}$ transition of CaOH taken with two different pump laser frequencies.

the pump laser wavenumber (16027 cm^{-1}) corresponds to the $Q_{22}(e,f)$ and $P_{21}(e,e)$ heads in the $\tilde{A}^2\Pi_{3/2}-\tilde{X}^2\Sigma^+$ transition, which results in *e* parity levels in the intermediate state being predominantly populated. As a result, the observed branches in the upper panel are $P_{12}(e,e)$, $R_{12}(e,e)$ and $Q_{22}(f,e)$. The pattern of two intense regions of lines for the $P_{12}(e,e)$ branch is a result of the distribution of *J* levels populated by the pump laser. In the lower panel, the pump laser wavenumber (16034 cm^{-1}) corresponds to the $R_{22}(f,f)$ branch in the $\tilde{A}^2\Pi_{3/2}-\tilde{X}^2\Sigma^+$ transition. The change in pump laser frequency results in fewer lines being observed because the pump laser is no longer tuned to a band head. In addition, because the *f* parity levels in the $\tilde{A}^2\Pi_{3/2}$ state are now being predominantly populated, the observed features in the $\tilde{D}^2\Sigma^+-\tilde{A}^2\Pi_{3/2}$ transition are the $Q_{12}(e,f)$, $P_{22}(f,f)$ and $R_{22}(f,f)$ branches. Finally, the lines located at ~12110 cm^{-1} belong to high *J* values of the $P_{12}(e,e)$ branch, which are present as a result of the pump laser additionally exciting high *J* lines in the $Q_{22}(e,f)$ and $P_{21}(e,e)$ branches of the $\tilde{A}^2\Pi-\tilde{X}^2\Sigma^+$ transition.

Figure 8.2 contains a collection of spectra recorded for the $\tilde{D}^2\Sigma^+-\tilde{A}^2\Pi_{3/2}$ transition by systematically varying the pump laser wavenumber. By increasing the laser by one wavenumber at a time and scanning the probe laser over the same spectral region, the $Q_{12}(e,f)$ and $P_{22}(f,f)$ branches could be tracked from low *J* to high *J*, in and out of the band head. The resulting spectra facilitated the rotational assignment of these branches. In addition, at high *J* values a splitting between the $Q_{12}(e,f)$ and $P_{22}(f,f)$ branches was resolved, which is a result of the spin-rotation splitting in the $\tilde{D}^2\Sigma^+$ state.

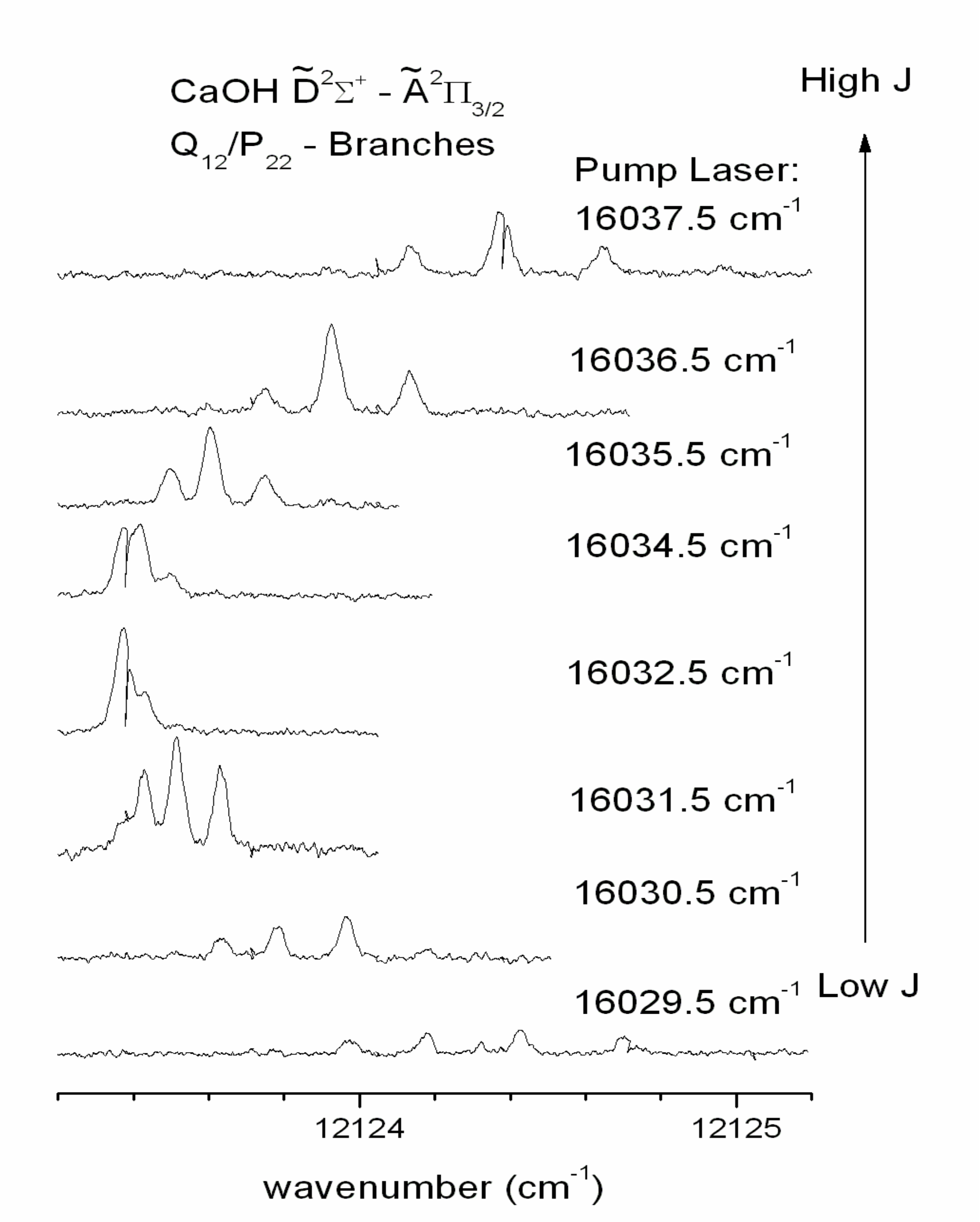

Figure 8.2 – Systematic pumping of the Q_{12} and P_{22} branches of the $\tilde{D}^2\Sigma^+ - \tilde{A}^2\Pi_{3/2}$ transition of CaOH.

Rotational assignments for $\tilde{D}^2\Sigma^+ - \tilde{A}^2\Pi_{3/2}$ transition were made using lower state combination differences in the $\tilde{A}^2\Pi$ state [4,5]. A total of 205 rotational lines from 9 of the 12 branches from both spin orbit components of the $\tilde{D}^2\Sigma^+ - \tilde{A}^2\Pi$ transition of CaOH were assigned. The measured lines are available in Appendix A6. A least-squares fit of the measured data to a Hunds's case (b) $^2\Sigma^+$ - Hund's case (a) $^2\Pi$ ($\hat{N}^2$) Hamiltonian of Brown [26] was performed. To minimize the uncertainties and determine the molecular parameters of the $\tilde{D}^2\Sigma^+$ state more precisely, the pure rotational [17] and $\tilde{A}^2\Pi - \tilde{X}^2\Sigma^+$ (0_0^0) transition data [4,5] were included in the fit. Each data set was weighted according to its experimental uncertainty. The estimated uncertainty for the pure rotational data was 1.7 x 10^{-6} cm^{-1}. For the $\tilde{D}^2\Sigma^+ - \tilde{A}^2\Pi$ and $\tilde{A}^2\Pi - \tilde{X}^2\Sigma^+$ (0_0^0) [5] transitions, the uncertainties were estimated as 0.005 cm^{-1} for clean lines and 0.02 cm^{-1} for overlapped lines. The $\tilde{A}^2\Pi - \tilde{X}^2\Sigma^+$ (0_0^0) transition data of Hilborn et al. [4] were weighted by uncertainties of 0.02 cm^{-1}. The spectroscopic parameters determined in the fit are listed in Table 8.1. The standard deviation of the fit was ~0.004 cm^{-1} which is consistent with the experimental uncertainty. For the $\tilde{D}^2\Sigma^+$ state, the band origin, T_{00}, (28156.2006 cm^{-1}) and rotational constant, B, (0.3590134 cm^{-1}) are similar in value, but more precisely determined, than they were in the previous work (T_{00} = 28153 cm^{-1}, B = 0.36445 cm^{-1}) [23]. In addition, the centrifugal distortion constant, D, and the spin-rotation parameter, γ, were determined for the first time.

Table 8.1 Spectroscopic constants (in cm^{-1}) for CaOH[a,b]

Constant	$\tilde{X}^2\Sigma^+$ (000)	$\tilde{A}^2\Pi$ (000)	$\tilde{D}^2\Sigma^+$ (000)
T	0.0	15997.77579(64)	28156.20008(99)
B	0.334334107(32)	0.3412272(15)	0.3590164(26)
D	3.86000(86)x10^{-7}	3.8960(65)x10^{-7}	3.995(14)x10^{-7}
γ	1.15957(51)x10^{-3}		8.47(35)x10^{-4}
A		66.81480(89)	
A_D		-1.741(10)x10^{-4}	
p		-4.3064(71)x10^{-2}	
q		-3.447(24)x10^{-6}	

[a] Values in parenthesis are 1σ standard deviations, in units of the last significant digits.

[b] Combined fit of the $\tilde{D}^2\Sigma^+$ - $\tilde{A}^2\Pi$ transition data, $\tilde{X}^2\Sigma^+$ state millimeter-wave data [18], and the $\tilde{A}^2\Pi$ - $\tilde{X}^2\Sigma^+$ transition data [10,11].

8.4 Discussion

The spin-rotation constant in the $\tilde{D}^2\Sigma^+$ state of CaOH was found to be positive and very small (γ = 8.47 x 10^{-4} cm^{-1}). As described in Chapter 2, the value of γ in the $\tilde{D}^2\Sigma^+$ state can be rationalized by considering the second-order contributions to this parameter arising from spin-orbit coupling. By invoking the unique perturber and pure precession relationships, the following expression for γ can be derived [27]:

$$\gamma = \frac{2A_{SO}B\ell(\ell+1)}{E(^2\Pi) - E(\tilde{D}^2\Sigma^+)}, \tag{1}$$

where B, is the rotational constant, A_{SO}, is the spin-orbit constant, ℓ, is the atomic orbital angular momentum of the $^2\Pi$ state, and E is the state energy. Using the value of γ in the $\tilde{D}^2\Sigma^+$ state, the location of the perturbing $^2\Pi$ state can be estimated. Assuming the perturbing state has molecular parameters similar to those for the $\tilde{A}^2\Pi$ state (A_{SO} ~ 67 cm^{-1}, B ~0.34 cm^{-1} and $\ell = 1$) [5], the perturbing $^2\Pi$ state would lie approximately 100000 cm^{-1} above the $\tilde{D}^2\Sigma^+$ state. This separation is unreasonable, as two $^2\Pi$ states have already been identified within 10000 cm^{-1} of the $\tilde{\mathrm{D}}^2\Sigma^+$ state ($\tilde{\mathrm{F}}^2\Pi$ (30215 cm^{-1}) [23] and $\tilde{\mathrm{G}}^2\Pi$ (36230.2 cm^{-1}) [24]).

A more plausible explanation for the small magnitude of the spin-rotation parameter in $\tilde{\mathrm{D}}^2\Sigma^+$ state is that like the $\tilde{\mathrm{X}}^2\Sigma^+$ ($4s\sigma$) state, it arises from a Ca^+ atomic orbital of predominantly $s\sigma$ character ($5s\sigma$). Electronic states arising from atomic orbitals of $s\sigma$ character do not form a pure precession pair with neighboring $^2\Pi$ states. This explains the similarity in the γ values of the $\tilde{\mathrm{X}}^2\Sigma^+$ (1.159647×10^{-3} cm^{-1}) and $\tilde{\mathrm{D}}^2\Sigma^+$ (8.47×10^{-4} cm^{-1}) [5] states. In contrast, the $\tilde{\mathrm{B}}^2\Sigma^+$ state, which arises from an atomic orbital of mainly $4p\sigma$ character and forms a unique perturber pair with the $\tilde{\mathrm{A}}^2\Pi$ state, has a γ value (-4.3615×10^{-2} cm^{-1}) that is over an order of magnitude larger than those for the other $^2\Sigma^+$ states.

The rotational data for the $\tilde{\mathrm{D}}^2\Sigma^+$ state was successfully modeled using a $^2\Sigma^+$ Hamiltonian, confirming a linear structure for CaOH in this state. Table 8.2 shows a comparison of the Ca-O and O-H bond lengths for the first vibrational levels of the electronic states of CaOH which have been studied at high resolution. For the $\tilde{\mathrm{B}}^2\Sigma^+$, $\tilde{\mathrm{C}}^2\Delta$ and $\tilde{\mathrm{D}}^2\Sigma^+$ states, rotational constants exist for only one isotopologue, so the O-H bond lengths were fixed to the value obtained for the ground state. The r_0 (Ca-O) value in the $\tilde{\mathrm{D}}^2\Sigma^+$ state is 3 – 6% smaller than in any other observed state. This is consistent with the assignment of $5s\sigma$ atomic orbital character for the $\tilde{\mathrm{D}}^2\Sigma^+$ state, as this orbital should be diffuse, allowing the OH^- ligand to approach more closely to the Ca^+ cation, resulting in a shorter Ca-O bond. It should be noted that the assumption that the O-H bond length does not change upon excitation to the $\tilde{\mathrm{D}}^2\Sigma^+$ state ignores the possibility of large amplitude bending motion. This motion would effectively reduce the O-H bond length and increase the observed B value for the $\tilde{D}^2\Sigma^+$ state. In order to derive a more reliable molecular structure, data for CaOD is needed.

Table 8.2 Bond Lengths (Å) for CaOH

	$\tilde{X}^2\Sigma^{+\,a}$	$\tilde{A}^2\Pi^{\,b}$	$\tilde{B}^2\Sigma^{+\,c}$	$\tilde{C}^2\Delta^{\,d}$	$\tilde{D}^2\Sigma^{+\,e}$
r_0(CaO)	1.985	1.964	1.969	2.019	1.912
r_0(OH)	0.921	0.920	0.921	0.921	0.921

[a] Determined from the millimeter-wave data of CaOH [18] and CaOD [20]
[b] Determined from the optical data of CaOH [10,11] and CaOD [24]
[c] Determined from the optical data of CaOH [11] and a fixed r_0 (OH) of 0.921 Å
[d] Determined from the optical data of CaOD [27] and a fixed r_0 (OH) of 0.921 Å
[e] Determined from the optical data of CaOH [this work] and a fixed r_0 (OH) of 0.921 Å

In a recent publication, Taylor et al. [28] used the effective valence shell Hamiltonian method to examine the ground and excited states of CaOH. For the $\tilde{D}^2\Sigma^+$ state, they determined values for the band origin (28027 cm^{-1}) and Ca-O bond length (1.926 Å). Our experimental observations (T_{00} = 28156.20007 cm^{-1}, r_0 (Ca-O) = 1.912 Å) agree well and confirm these theoretical predictions. Taylor et al. have also suggested that the $\tilde{D}^2\Sigma^+$ state arises from an atomic orbital which is slightly diffuse, and that as a result the $\tilde{D}^2\Sigma^+$ state will have the shortest Ca-O separation. These suggestions are consistent with our assignment of predominantly 5$s\sigma$ atomic orbital character for the $\tilde{D}^2\Sigma^+$ state.

The spectroscopic parameters observed for the $\tilde{D}^2\Sigma^+$ state of CaOH are also consistent with the previous work on the $\tilde{D}^2\Sigma^+$ state of CaF [29]. First, the spin-rotation constants of the $\tilde{D}^2\Sigma^+$ states of these two molecules (γ (CaOH) = 8.47 x 10^{-4} cm^{-1}, γ

(CaF) = 3 x 10^{-4} cm^{-1}) are similar in magnitude and sign. Second, as for CaOH, the $\tilde{D}^2\Sigma^+$ state of CaF was found to have the shortest Ca-ligand separation (r_0 (Ca-F) = 1.893 Å) of the ground and first four excited electronic states. The similarity between the molecular parameters for the $\tilde{D}^2\Sigma^+$ state of each molecule suggests that the atomic orbital character of this state does not chane significantly as the ligand varies. For each molecule, the dominant orbital character of the $\tilde{D}^2\Sigma^+$ state is 5*sσ*.

While the orbital character of the observed electronic states of CaF and CaOH generally appears invariant, the electronic energy state ordering does not. Figure 8.3 shows a comparison of the observed electronic states of CaOH with CaF. This diagram illustrates that the electronic states have reordered slightly from halide to hydroxide ligand. With the exception of the $^2\Delta$ state, the electronic states have shifted to slightly lower energies in CaOH as compared to CaF. In addition, the $^2\Sigma^+$ states seem to have been the most affected by the change in ligand. Specifically, the $\tilde{D}^2\Sigma^+$ state has moved such that it is more isolated in CaOH. This increased isolation, which does not affect the molecular parameters of CaOH as compared to CaF, is further evidence that the $\tilde{D}^2\Sigma^+$ arises from an atomic orbital which does not interact with neighboring electronic states (5*sσ*). For example, as previously mentioned, there is no significant change in the observed spin rotation constants of CaOH and CaF, despite the neighboring $^2\Pi$ states being closer in energy to the $\tilde{D}^2\Sigma^+$ state of CaF. Further high resolution investigations of the other higher lying states of CaOH are needed to see if the apparent invariance of atomic orbital character with ligand change holds as the energies of the states increase.

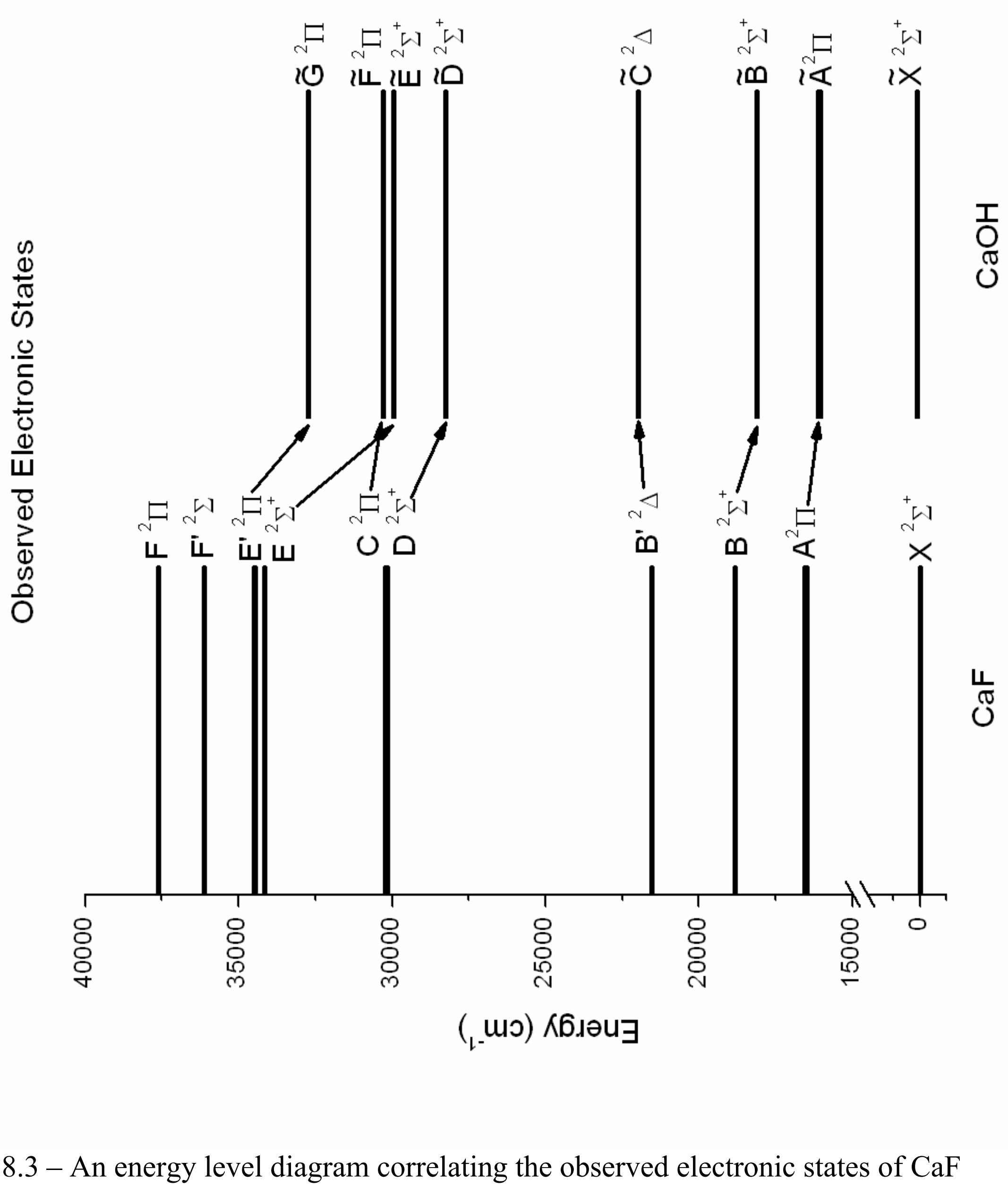

Figure 8.3 – An energy level diagram correlating the observed electronic states of CaF with those of CaOH.

References

[1] J.-G. Wang, P. M. Sheridan, M. J. Dick and P. F. Bernath, J. Mol. Spectrosc. **236**, 21 (2006).

[2] S. Yu, J.-G. Wang, P. M. Sheridan, M. J. Dick and P. F. Bernath, J. Mol. Spectrosc. **240** 14 (2006).

[3] J. M. Berg, J. E. Murphy, N. A. Harris and R. W. Field, Phys. Rev. A. **48**, 3012 (1993).

[4] R. C. Hilborn, Z. Qingshi and D. O. Harris, J. Mol. Spectrosc. **97**, 73 (1983).

[5] P. F. Bernath and C. R. Brazier, Astrophys J. **288**, 373 (1985).

[6] J. A. Coxon, M. Li and P. L. Presunka, J. Mol. Spectrosc. **150**, 33 (1991).

[7] J. A. Coxon, M. Li and P. L. Presunka, Mol. Phys. **76**, 1463 (1992).

[8] M. Li and J. A. Coxon, J. Chem. Phys. **97**, 8961 (1992).

[9] J. A. Coxon, M. Li and P. L. Presunka, J. Mol. Spectrosc. **164**, 118 (1994).

[10] M. Li and J. A. Coxon, J. Chem. Phys. **102**, 2663 (1995).

[11] M. Li and J. A. Coxon, J. Chem. Phys. **104**, 4961 (1996).

[12] M. Li and J. A. Coxon, Can. J. Phys. **72**, 1200 (1994).

[13] R. F. Wormsbecher, M. Trkula, C. Martner, R. E. Penn and D. O. Harris, J. Mol. Spectrosc. **97**, 29 (1993).

[14] P. F. Bernath and S. Kinsey-Nielsen, Chem. Phys. Lett. **105**, 663 (1984).

[15] C. N. Jarman and P. F. Bernath, J. Chem. Phys. **97**, 1711 (1992).

[16] Z. J. Jakubek and R. W. Field, J. Chem. Phys. **98**, 6574 (1993).

[17] L. M. Ziurys, W. L. Barclay Jr. and M. A. Anderson, Astrophys J. **384**, L63-L66 (1992).

[18] D. A. Fletcher, M. A. Anderson, W. L. Barclay Jr. and L. M. Ziurys, J. Chem. Phys. **102**, 4334 (1995).

[19] B. P. Nuccio, A. J. Apponi and L. M. Ziurys, J. Chem. Phys. **103**, 9193 (1995).

[20] L. M. Ziurys, D. A. Fletcher, M. A. Anderson and W. L. Barclay Jr., Astrophys J. Suppl. Ser. **102**, 425 (1996).

[21] C. T. Scurlock, D. A. Fletcher and T. C. Steimle, J. Mol. Spectrosc. **159**, 350 (1993).

[22] T. C. Steimle, D. A. Fletcher, K. Y. Jung and C. T. Scurlock, J. Chem. Phys. **96**, 2556 (1992).

[23] R. Pereira and D. H. Levy, J. Chem. Phys. **105**, 9733 (1996).

[24] R. A. Hailey, C. Jarman and P. F. Bernath, J. Chem. Phys. 107, 669 (1997).

[25] S. Gerstenkorn, J. Verges and J. Chevillard, *Atlas du Spectre d'Absorption de la Molecule d'Iode* Laboratoire Aimé-Cotton, CNRS II 91405, Orsay, 1982.

[26] J. M. Brown, E. A. Colbourn, J. K. G. Watson and F. D. Wayne, J. Mol. Spectrosc. **74**, 294 (1979).

[27] H. Lefebvre-Brion and R. W. Field, *The Spectra and Dynamics of Diatomic Molecules,* Elsevier, Amsterdam, 2004.

[28] C. M. Taylor, R. K. Chaudhuri and K. F. Freed, J. Chem. Phys. **122**, 044317 (2005).

[29] C. M. Gittins, N. A. Harris, R. W. Field, J. Vergès, C. Effantin, A. Bernard, J. D'Incan, W. E. Ernst, P. Bundgen and B. Engels, J. Mol. Spectrosc. **161**, 303 (1993).

Chapter 9 – Conclusions and Future Work

The work presented in this thesis has entailed an investigation into the spectroscopy of calcium and strontium-containing polyatomic molecules. Spectra for seven electronic transitions from six different molecules were presented. For each electronic transition studied, this work marked the first time the transition had been observed using high-resolution spectroscopic techniques. The analysis of the resulting spectra has led to a better understanding of the geometric structure and electronic configuration of the states observed. In addition, from the molecular parameters determined, a greater understanding of the coupling between the various angular momenta and the interactions between the excited electronic states of small alkali earth containing polyatomic molecules has been gained.

The rotational analysis of the $\tilde{A}\,^2\Pi$ - $\tilde{X}\,^2\Sigma^+$ system of SrCCH has yielded rotational and fine structure parameters for both states, as well as confirmed a linear geometry for the $\tilde{A}\,^2\Pi$ excited state. Using the rotational constant of the $\tilde{A}\,^2\Pi$ state the Sr-C bond length was determined. This bond length was found to be shorter than that in the ground state, and this reduction was attributed to a polarization of the unpaired electron on the strontium atom away from the ligand. Λ-doubling parameters have also been determined for the $\tilde{A}$ state. A comparison of the *p* constant with those of the other alkaline earth acetylides suggested that SrCCH and CaCCH follow the pure precession and unique perturber relationships, unlike MgCCH. Finally, a search for the $\tilde{B}\,^2\Sigma^+$ - $\tilde{X}\,^2\Sigma^+$ transition was not successful, as with CaCCH, suggesting that the $\tilde{B}$ state may be predissociative. Future work might include an investigation of the $\tilde{B}\,^2\Sigma^+$ - $\tilde{X}\,^2\Sigma^+$ transition of SrCCH using an absorption experiment, such as cavity ringdown spectroscopy. A similar investigation has already been successful in finding the $\tilde{B}\,^2\Sigma^+$ - $\tilde{X}\,^2\Sigma^+$ transition of CaCCH [1].

The $\tilde{B}\,^2A_1$- $\tilde{X}\,^2A_1$ transitions of $CaCH_3$ and $SrCH_3$ have been rotationally analyzed, allowing rotational and fine structure parameters to be determined for the $\tilde{B}\,^2A_1$ states of each molecule. From the rotational constants, structures have been estimated for the $\tilde{B}\,^2A_1$ states of $CaCH_3$ and $SrCH_3$. The spin-rotation parameters calculated for the $\tilde{B}\,^2A_1$ states using the pure precession and unique perturber approximations are in relatively good agreement with the experimentally determined values. Finally, the $K' = 1$ energy levels of the $\tilde{B}\,^2A_1$ state of $CaCH_3$ appear to be perturbed, possibly by an excited vibrational state of the $\tilde{A}\,^2E$ state. Further investigation of this perturbation is warranted. In particular, an investigation of the $CaCD_3$ isotopologue is of interest to see if the perturbation changes as both the location of the electronic states and vibrational frequencies shift.

A high-resolution spectrum of the $\tilde{A}\,^2E$ - $\tilde{X}\,^2A_1$ electronic transition of $SrCH_3$ has been recorded. The analysis of this spectrum has allowed the $\tilde{A}\,^2E$ state to be fully characterized. Rotational and fine structure parameters for the $\tilde{A}\,^2E$ state were determined in a rotational analysis of the data. The Jahn-Teller effect was found to be small in the lowest vibrational level of the $\tilde{A}\,^2E$ state. Estimates of the spin-rotation parameters from pure precession expressions are in relatively good agreement with the experimentally determined values, and any discrepancy from the experimental values indicates that the $\tilde{A}\,^2E$ state is not entirely composed of *p* atomic orbital character. From the rotational constants, the structure of $SrCH_3$ in the $\tilde{A}\,^2E$ state has been estimated. The metal-ligand bond length was found to decrease slightly in the $\tilde{A}\,^2E$ state from the $\tilde{X}\,^2A_1$ state, similar to, but less than, other strontium containing radicals. Future work might include an investigation of the virbrational structure of the $\tilde{A}\,^2E$ state of $SrCH_3$. It would be interesting to determine whether the Jahn-Teller interaction is still negligible in the excited vibrational levels of the $\tilde{A}\,^2E$ state of $SrCH_3$.

For $CaBH_4$ and $SrBH_4$, the $\tilde{B}^2E - \tilde{X}^2A_1$ electronic transitions have been recorded and analyzed, yielding rotational and fine structure parameters for each observed state for the first time. No evidence for Jahn-Teller coupling or internal rotation of the BH_4 ligand was found for either molecule. From the rotational constants, a tridentate structure has been confirmed for the $\tilde{X}^2A_1$ and $\tilde{B}^2E$ states of each borohydride. A comparison of the molecular parameters of $CaBH_4$ and $SrBH_4$ with those of their monomethyl counterparts shows a large reduction in the spin-orbit splitting and the metal ligand separation. These reductions indicate an increased amount of *d*-orbital character in the first excited ^2E state of the borohydrides, as compared to the monomethyls of both strontium and calcium. This observation is consistent with theoretical calculations [2]. A reordering of the first excited ^2E and $^2A_1$ states has also been confirmed for $CaBH_4$ and $SrBH_4$, as compared to $CaCH_3$ and $SrCH_3$. Unfortunately, the $\tilde{A}^2A_1$ - $\tilde{X}^2A_1$ transitions were too weak to be studied at high-resolution. Future work might include another attempt to record the high-resolution spectra of these transitions. The $\tilde{A}^2A_1$ states are of interest due to their potential roles as unique perturber pairs with the $\tilde{B}^2E$ states of each borohydride.

Using the technique of optical-optical double resonance spectroscopy, a high resolution spectrum of the $\tilde{D}^2\Sigma^+$ - $\tilde{A}^2\Pi$ transition of CaOH was recorded. Rotational and fine structure parameters were determined for the $\tilde{D}^2\Sigma^+$ state from a rotational analysis of the data. Small values for the Ca-O separation and the spin rotation constant in the $\tilde{D}^2\Sigma^+$ state are consistent with predominant 5*sσ* orbital character for the $\tilde{D}^2\Sigma^+$ state of CaOH. This atomic orbital assignment is in agreement with previous work on CaF [3] and recent theoretical calculations on CaOH [4].

Finally, a comparison of the electronic state energy ordering of CaOH and CaF shows that the substitution of OH^- for F^- causes the electronic states to shift to lower energy but does not significantly affect the atomic orbital character of the $\tilde{D}^2\Sigma^+$ state. Further optical-optical double resonance spectra of the higher lying states of CaOH are warranted. In particular, investigations of the excited states for which non-linear geometries have been suggested are of interest.

In addition, to the specific recommendations for future work outlined above, two general suggestions for future projects may be made. First, high-resolution spectra should be recorded for the various isotopologues of each molecule studied in this thesis. This would allow the molecular structures determined for each observed electronic state to be refined. As it stands now, the structures outlined in this thesis are only preliminary as many assumptions had to be made in order to derive them. Secondly, an investigation of the higher-lying states of each molecule studied (not just CaOH) is warranted. To date there has been very little experimental work completed on the higher-lying states of the calcium and strontium containing polyatomic molecules. The optical-optical resonance technique used to study the $\tilde{D}^2\Sigma^+$ state of CaOH, could be applied to each of the molecules investigated in this thesis. Again, these higher-lying states are of interest due to their potential to adopt unique structures and different atomic orbital configurations as the energy of the state increases.

References

[1] D. W. Tokaryk, A. G. Adam and M. E. Slaney, Chem. Phys. Lett. **433**, 264 (2007).

[2] J. V. Ortiz, J. Am. Chem. Soc. **113**, 1102 (1991).

[3] C. M. Gittins, N. A. Harris, R. W. Field, J. Vergès, C. Effantin, A. Bernard, J. D'Incan, W. E. Ernst, P. Bundgen and B. Engels, J. Mol. Spectrosc. **161**, 303 (1993).

[4] C. M. Taylor, R. K. Chaudhuri and K. F. Freed, J. Chem. Phys. **122**, 044317 (2005).

Appendix A1: Measured Lines (in cm^{-1}) for the $\tilde{B}^2A_1 - \tilde{X}^2A_1$ Transition of $SrCH_3$

N'	K'	J'	N"	K"	J"	ν_{obs}	$\nu_{obs-calc}$
$^{R}R_{11}$[a]							
1	0	1.5	0	0	0.5	14787.8938	-0.0004
2	0	2.5	1	0	1.5	14788.2044	-0.0001
3	0	3.5	2	0	2.5	14788.5155	0.0012
4	0	4.5	3	0	3.5	14788.8227	-0.0010
5	0	5.5	4	0	4.5	14789.1329	0.0002
6	0	6.5	5	0	5.5	14789.4406	-0.0006
7	0	7.5	6	0	6.5	14789.7512	0.0018
8	0	8.5	7	0	7.5	14790.0505	-0.0067
9	0	9.5	8	0	8.5	14790.3611	-0.0036
10	0	10.5	9	0	9.5	14790.6811	0.0091
$^{R}R_{22}$							
2	0	1.5	1	0	0.5	14788.5767	-0.0059
3	0	2.5	2	0	1.5	14789.0433	-0.0020
4	0	3.5	3	0	2.5	14789.5077	0.0001
5	0	4.5	4	0	3.5	14789.9727	0.0032
6	0	5.5	5	0	4.5	14790.4388	0.0078
7	0	6.5	6	0	5.5	14790.8927	0.0006
8	0	7.5	7	0	6.5	14791.3498	-0.0030
9	0	8.5	8	0	7.5	14791.8155	0.0023
10	0	9.5	9	0	8.5	14792.2771	0.0037
11	0	10.5	10	0	9.5	14792.7277	-0.0056
$^{P}P_{11}$							
0	0	0.5	1	0	1.5	14787.1972	0.0056
1	0	1.5	2	0	2.5	14786.7277	0.0007
2	0	2.5	3	0	3.5	14786.2633	0.0013
3	0	3.5	4	0	4.5	14785.7932	-0.0034
4	0	4.5	5	0	5.5	14785.3259	-0.0048
5	0	5.5	6	0	6.5	14784.8619	-0.0026
6	0	6.5	7	0	7.5	14784.3973	-0.0006
7	0	7.5	8	0	8.5	14783.9305	-0.0005
$^{P}P_{22}$							
1	0	0.5	2	0	1.5	14786.9628	0.0023
2	0	1.5	3	0	2.5	14786.6522	0.0038
3	0	2.5	4	0	3.5	14786.3360	0.0001
4	0	3.5	5	0	4.5	14786.0198	-0.0031
5	0	4.5	6	0	5.5	14785.7064	-0.0032
6	0	5.5	7	0	6.5	14785.3930	-0.0029
7	0	6.5	8	0	7.5	14785.0760	-0.0059
8	0	7.5	9	0	8.5	14784.7723	0.0046
$^{R}Q_{21}$							
1	0	0.5	0	0	0.5	14788.1120	-0.0053
2	0	1.5	1	0	1.5	14788.5767	0.0003
3	0	2.5	2	0	2.5	14789.0433	0.0083

N'	K'	J'	N"	K"	J"	ν_{obs}	$\nu_{obs-calc}$
$^{P}Q_{12}$							
0	0	0.5	1	0	0.5	14787.1972	-0.0006
1	0	1.5	2	0	1.5	14786.7389	0.0015
2	0	2.5	3	0	2.5	14786.2743	-0.0022
3	0	3.5	4	0	3.5	14785.8155	0.0003
4	0	4.5	5	0	4.5	14785.3589	0.0055
$^{R}R_{11}$							
2	1	2.5	1	1	1.5	14788.1044	-0.0007
3	1	3.5	2	1	2.5	14788.4172	-0.0018
4	1	4.5	3	1	3.5	14788.7331	0.0024
5	1	5.5	4	1	4.5	14789.0433	0.0023
6	1	6.5	5	1	5.5	14789.3482	-0.0022
7	1	7.5	6	1	6.5	14789.6588	-0.0002
8	1	8.5	7	1	7.5	14789.9720	0.0050
9	1	9.5	8	1	8.5	14790.2715	-0.0029
10	1	10.5	9	1	9.5	14790.5793	-0.0020
11	1	11.5	10	1	10.5	14790.8927	0.0048
$^{R}R_{22}$							
2	1	1.5	1	1	0.5	14788.5262	-0.0009
3	1	2.5	2	1	1.5	14788.9823	0.0009
4	1	3.5	3	1	2.5	14789.4406	0.0015
5	1	4.5	4	1	3.5	14789.8995	0.0016
6	1	5.5	5	1	4.5	14790.3611	0.0040
7	1	6.5	6	1	5.5	14790.8199	0.0036
8	1	7.5	7	1	6.5	14791.2755	0.0000
9	1	8.5	8	1	7.5	14791.7315	-0.0029
10	1	9.5	9	1	8.5	14792.1906	-0.0026
$^{P}P_{11}$							
1	1	1.5	2	1	2.5	14786.6215	0.0028
2	1	2.5	3	1	3.5	14786.1652	0.0028
3	1	3.5	4	1	4.5	14785.7064	0.0051
4	1	4.5	5	1	5.5	14785.2335	-0.0044
5	1	5.5	6	1	6.5	14784.7723	-0.0008
6	1	6.5	7	1	7.5	14784.3053	-0.0021
7	1	7.5	8	1	8.5	14783.8408	-0.0002
$^{P}P_{22}$							
1	1	0.5	2	1	1.5	14786.9262	-0.0040
2	1	1.5	3	1	2.5	14786.5961	0.0020
3	1	2.5	4	1	3.5	14786.2743	0.0017
4	1	3.5	5	1	4.5	14785.9527	-0.0022
5	1	4.5	6	1	5.5	14785.6365	-0.0020
6	1	5.5	7	1	6.5	14785.3259	0.0034
7	1	6.5	8	1	7.5	14785.0089	0.0022
8	1	7.5	9	1	8.5	14784.6886	-0.0023

N'	K'	J'	N"	K"	J"	ν_{obs}	$\nu_{obs-calc}$
${}^{P}P_{22}$							
9	1	8.5	10	1	9.5	14784.3724	-0.0026
${}^{Q}Q_{11}$							
1	1	1.5	1	1	1.5	14787.3970	0.0007
2	1	2.5	2	1	2.5	14787.3231	-0.0044
3	1	3.5	3	1	3.5	14787.2588	0.0049
4	1	4.5	4	1	4.5	14787.1777	-0.0004
5	1	5.5	5	1	5.5	14787.1027	0.0018
6	1	6.5	6	1	6.5	14787.0192	-0.0035
${}^{Q}Q_{22}$							
1	1	0.5	1	1	0.5	14787.7008	-0.0018
2	1	1.5	2	1	1.5	14787.7540	-0.0007
3	1	2.5	3	1	2.5	14787.8155	-0.0054
4	1	3.5	4	1	3.5	14787.8938	0.0030
5	1	4.5	5	1	4.5	14787.9603	-0.0017
6	1	5.5	6	1	5.5	14788.0314	-0.0022
${}^{P}Q_{12}$							
1	1	1.5	2	1	1.5	14786.6215	-0.0062
2	1	2.5	3	1	2.5	14786.1793	0.0034
3	1	3.5	4	1	3.5	14785.7185	-0.0006
4	1	4.5	5	1	4.5	14785.2575	-0.0025
${}^{R}Q_{21}$							
2	1	1.5	1	1	1.5	14788.5206	-0.0027
3	1	2.5	2	1	2.5	14788.9720	-0.0005
4	1	3.5	3	1	3.5	14789.4253	-0.0003
5	1	4.5	4	1	4.5	14789.8867	0.0067
6	1	5.5	5	1	5.5	14790.3333	-0.0017
${}^{Q}R_{12}$							
1	1	1.5	1	1	0.5	14787.3970	-0.0030
2	1	2.5	2	1	1.5	14787.3341	-0.0023
3	1	3.5	3	1	2.5	14787.2672	-0.0002
4	1	4.5	4	1	3.5	14787.1977	0.0018
5	1	5.5	5	1	4.5	14787.1230	0.0000
${}^{Q}P_{21}$							
1	1	0.5	1	1	1.5	14787.7008	0.0020
2	1	1.5	2	1	2.5	14787.7436	-0.0021
3	1	2.5	3	1	3.5	14787.8155	0.0081

Appendix A2: Measured Lines (in cm^{-1}) for the $\tilde{B}^2A_1$ – $\tilde{X}^2A_1$ Transition of $CaCH_3$

N'	K'	J'	N"	K"	J"	ν_{obs}	$\nu_{obs-calc}$
$^{R}R_{11}$[a]							
1	0	1.5	0	0	0.5	16010.6832	-0.0007
2	0	2.5	1	0	1.5	16011.1730	-0.0003
3	0	3.5	2	0	2.5	16011.6632	-0.0013
4	0	4.5	3	0	3.5	16012.1552	-0.0022
5	0	5.5	4	0	4.5	16012.6506	-0.0016
6	0	6.5	5	0	5.5	16013.1486	-0.0002
7	0	7.5	6	0	6.5	16013.6520	0.0048
8	0	8.5	7	0	7.5	16014.1496	0.0021
9	0	9.5	8	0	8.5	16014.6506	0.0007
10	0	10.5	9	0	9.5	16015.1568	0.0026
11	0	11.5	10	0	10.5	16015.6576	-0.0032
12	0	12.5	11	0	11.5	16016.1678	-0.0017
$^{R}R_{22}$							
2	0	1.5	1	0	0.5	16011.2661	0.0006
3	0	2.5	2	0	1.5	16011.7920	-0.0023
4	0	3.5	3	0	2.5	16012.3203	-0.0046
5	0	4.5	4	0	3.5	16012.8575	0.0002
6	0	5.5	5	0	4.5	16013.3862	-0.0053
7	0	6.5	6	0	5.5	16013.9290	0.0015
8	0	7.5	7	0	6.5	16014.4668	0.0013
9	0	8.5	8	0	7.5	16015.0029	-0.0026
10	0	9.5	9	0	8.5	16015.5513	0.0038
11	0	10.5	10	0	9.5	16016.0901	-0.0015
12	0	11.5	11	0	10.5	16016.6366	-0.0013
$^{P}P_{11}$							
0	0	0.5	1	0	1.5	16009.6876	-0.0020
1	0	1.5	2	0	2.5	16009.1681	0.0004
2	0	2.5	3	0	3.5	16008.6478	0.0001
3	0	3.5	4	0	4.5	16008.1300	0.0006
4	0	4.5	5	0	5.5	16007.6158	0.0029
5	0	5.5	6	0	6.5	16007.0981	-0.0003
6	0	6.5	7	0	7.5	16006.5833	-0.0024
7	0	7.5	8	0	8.5	16006.0768	0.0018
8	0	8.5	9	0	9.5	16005.5682	0.0018
9	0	9.5	10	0	10.5	16005.0562	-0.0036
$^{P}P_{22}$							
1	0	0.5	2	0	1.5	16009.2241	-0.0019
2	0	1.5	3	0	2.5	16008.7428	-0.0008
3	0	2.5	4	0	3.5	16008.2617	-0.0012
4	0	3.5	5	0	4.5	16007.7864	0.0023
5	0	4.5	6	0	5.5	16007.3079	0.0008
6	0	5.5	7	0	6.5	16006.8352	0.0031
7	0	6.5	8	0	7.5	16006.3567	-0.0023

N'	K'	J'	N"	K"	J"	ν_{obs}	$\nu_{obs-calc}$
${}^{P}P_{22}$							
8	0	7.5	9	0	8.5	16005.8870	-0.0010
9	0	8.5	10	0	9.5	16005.4228	0.0037
${}^{R}Q_{21}$							
1	0	0.5	0	0	0.5	16010.7345	-0.0030
2	0	1.5	1	0	1.5	16011.2661	0.0034
3	0	2.5	2	0	2.5	16011.7920	0.0023
4	0	3.5	3	0	3.5	16012.3203	0.0019
5	0	4.5	4	0	4.5	16012.8484	-0.0005
6	0	5.5	5	0	5.5	16013.3821	0.0008
7	0	6.5	6	0	6.5	16013.9184	0.0029
8	0	7.5	7	0	7.5	16014.4508	-0.0008
9	0	8.5	8	0	8.5	16014.9893	-0.0004
${}^{P}Q_{12}$							
2	0	2.5	3	0	2.5	16008.6532	-0.0009
3	0	3.5	4	0	3.5	16008.1385	0.0008
4	0	4.5	5	0	4.5	16007.6248	0.0017
5	0	5.5	6	0	5.5	16007.1108	0.0004
6	0	6.5	7	0	6.5	16006.5980	-0.0016
7	0	7.5	8	0	7.5	16006.0962	0.0055
8	0	8.5	9	0	8.5	16005.5809	-0.0031
${}^{R}R_{11}$							
2	1	2.5	1	1	1.5	16010.7568	
3	1	3.5	2	1	2.5	16011.2661	
4	1	4.5	3	1	3.5	16011.7690	
5	1	5.5	4	1	4.5	16012.2727	
6	1	6.5	5	1	5.5	16012.7820	
7	1	7.5	6	1	6.5	16013.2884	
8	1	8.5	7	1	7.5	16013.7957	
9	1	9.5	8	1	8.5	16014.3119	
10	1	10.5	9	1	9.5	16014.8127	
11	1	11.5	10	1	10.5	16015.3332	
12	1	12.5	11	1	11.5	16015.8453	
${}^{R}R_{22}$							
2	1	1.5	1	1	0.5	16010.6058	
3	1	2.5	2	1	1.5	16011.0640	
4	1	3.5	3	1	2.5	16011.5009	
5	1	4.5	4	1	3.5	16011.9067	
6	1	5.5	5	1	4.5	16012.2727	
${}^{P}P_{11}$							
1	1	1.5	2	1	2.5	16008.7365	
2	1	2.5	3	1	3.5	16008.2307	
3	1	3.5	4	1	4.5	16007.7277	
4	1	4.5	5	1	5.5	16007.2237	

N'	K'	J'	N"	K"	J"	ν_{obs}	$\nu_{obs-calc}$
${}^{P}P_{11}$							
5	1	5.5	6	1	6.5	16006.7205	
6	1	6.5	7	1	7.5	16006.2169	
7	1	7.5	8	1	8.5	16005.7137	
8	1	8.5	9	1	9.5	16005.2107	
${}^{P}P_{22}$							
1	1	0.5	2	1	1.5	16008.7365	
2	1	1.5	3	1	2.5	16008.0825	
3	1	2.5	4	1	3.5	16007.5375	
4	1	3.5	5	1	4.5	16006.9609	
5	1	4.5	6	1	5.5	16006.3567	
6	1	5.5	7	1	6.5	16005.7137	
${}^{Q}Q_{11}$							
1	1	1.5	1	1	1.5	16009.7448	
2	1	2.5	2	1	2.5	16009.7448	
3	1	3.5	3	1	3.5	16009.7448	
4	1	4.5	4	1	4.5	16009.7448	
5	1	5.5	5	1	5.5	16009.7448	
6	1	6.5	6	1	6.5	16009.7526	
7	1	7.5	7	1	7.5	16009.7541	
8	1	8.5	8	1	8.5	16009.7599	
9	1	9.5	9	1	9.5	16009.7662	
${}^{Q}Q_{22}$							
1	1	0.5	1	1	0.5	16009.7472	
2	1	1.5	2	1	1.5	16009.5933	
3	1	2.5	3	1	2.5	16009.5513	
4	1	3.5	4	1	3.5	16009.4786	
${}^{P}Q_{12}$							
1	1	1.5	2	1	1.5	16008.7365	
2	1	2.5	3	1	2.5	16008.2307	
3	1	3.5	4	1	3.5	16007.7277	
4	1	4.5	5	1	4.5	16007.2304	
5	1	5.5	6	1	5.5	16006.7296	
6	1	6.5	7	1	6.5	16006.2300	
7	1	7.5	8	1	7.5	16005.7321	
8	1	8.5	9	1	8.5	16005.2192	
${}^{R}Q_{21}$							
2	1	1.5	1	1	1.5	16010.6058	
3	1	2.5	2	1	2.5	16011.0640	
4	1	3.5	3	1	3.5	16011.5009	
5	1	4.5	4	1	4.5	16011.9067	
6	1	5.5	5	1	5.5	16012.2727	
7	1	6.5	6	1	6.5	16012.6506	

N'	K'	J'	N"	K"	J"	ν_{obs}	$\nu_{obs-calc}$
$^{Q}R_{12}$							
1	1	1.5	1	1	0.5	16009.7448	
2	1	2.5	2	1	1.5	16009.7448	
3	1	3.5	3	1	2.5	16009.7526	
4	1	4.5	4	1	3.5	16009.7526	
5	1	5.5	5	1	4.5	16009.7541	
6	1	6.5	6	1	5.5	16009.7599	
7	1	7.5	7	1	6.5	16009.7662	
$^{Q}P_{21}$							
1	1	0.5	1	1	1.5	16009.7472	
2	1	1.5	2	1	2.5	16009.5933	
3	1	2.5	3	1	3.5	16009.5513	
4	1	3.5	4	1	4.5	16009.4786	
$^{S}R_{21}$							
3	1	2.5	1	1	1.5	16012.0714	
4	1	3.5	2	1	2.5	16013.0057	
5	1	4.5	3	1	3.5	16013.9184	
$^{O}P_{12}$							
1	1	1.5	3	1	2.5	16007.2237	
2	1	2.5	4	1	3.5	16006.2169	
3	1	3.5	5	1	4.5	16005.2107	

Appendix A3: Measured Lines (in cm^{-1}) for the $\widetilde{A}\,^2E-\widetilde{X}\,^2A_1$ Transition of $SrCH_3$

J'	Parity	J"	Parity	ν_{obs}	$\nu_{obs-calc}$
$^{r}Q_{11}(0)$					
0.5	f	0.5	e	13655.5708	0.0078
1.5	f	1.5	e	13655.6704	0.0064
2.5	f	2.5	e	13655.7724	0.0053
3.5	f	3.5	e	13655.8785	0.0061
4.5	f	4.5	e	13655.9857	0.0057
5.5	f	5.5	e	13656.0940	0.0042
6.5	f	6.5	e	13656.2038	0.0019
$^{r}P_{11}(0)$					
0.5	e	1.5	e	13655.3653	0.0037
1.5	e	2.5	e	13655.2699	0.0067
2.5	e	3.5	e	13655.1675	0.0006
3.5	e	4.5	e	13655.0665	-0.0064
4.5	e	5.5	e	13654.9778	-0.0034
5.5	e	6.5	e	13654.8865	-0.0052
$^{r}R_{11}(0)$					
1.5	e	0.5	e	13656.4304	0.0001
2.5	e	1.5	e	13657.1099	0.0005
3.5	e	2.5	e	13657.7907	0.0001
4.5	e	3.5	e	13658.4702	-0.0039
5.5	e	4.5	e	13659.1591	-0.0007
6.5	e	5.5	e	13659.8456	-0.0022
7.5	e	6.5	e	13660.5417	0.0037
8.5	e	7.5	e	13661.2352	0.0046
$^{r}Q_{12}(0)$					
0.5	e	0.5	f	13655.3653	-0.0025
1.5	e	1.5	f	13655.2766	0.0031
2.5	e	2.5	f	13655.1788	-0.0026
3.5	e	3.5	f	13655.0844	-0.0071
4.5	e	4.5	f	13654.9979	-0.0060
5.5	e	5.5	f	13654.9124	-0.0061
$^{r}P_{12}(0)$					
0.5	f	1.5	f	13654.4056	-0.0006
1.5	f	2.5	f	13653.7333	-0.0027
2.5	f	3.5	f	13653.0666	-0.0013
3.5	f	4.5	f	13652.3988	-0.0033
4.5	f	5.5	f	13651.736	-0.0026
5.5	f	6.5	f	13651.0763	-0.0011
6.5	f	7.5	f	13650.4164	-0.0022
7.5	f	8.5	f	13649.7593	-0.0028
8.5	f	9.5	f	13649.1089	0.0009

J'	Parity	J"	Parity	ν_{obs}	$\nu_{obs-calc}$
$^{r}R_{12}(0)$					
1.5	f	0.5	f	13655.6704	0.0003
2.5	f	1.5	f	13655.7724	-0.0050
3.5	f	2.5	f	13655.8906	0.0038
4.5	f	3.5	f	13656.0033	0.0048
5.5	f	4.5	f	13656.1156	0.0031
6.5	f	5.5	f	13656.2230	-0.0057
$^{r}Q_{22}(0)$					
1.5	e	1.5	f	13934.2001	-0.0004
2.5	e	2.5	f	13934.0163	0.0007
3.5	e	3.5	f	13933.8355	0.0020
4.5	e	4.5	f	13933.6583	0.0041
5.5	e	5.5	f	13933.4875	0.0098
6.5	e	6.5	f	13933.3024	-0.0016
$^{r}P_{22}(0)$					
1.5	f	2.5	f	13933.0350	-0.0046
2.5	f	3.5	f	13932.4642	-0.0028
$^{r}R_{22}(0)$					
1.5	f	0.5	f	13934.9670	-0.0067
2.5	f	1.5	f	13935.1699	-0.0066
3.5	f	2.5	f	13935.3811	-0.0009
4.5	f	3.5	f	13935.5913	0.0010
5.5	f	4.5	f	13935.7979	-0.0035
$^{r}Q_{21}(0)$					
1.5	f	1.5	e	13934.9670	-0.0006
2.5	f	2.5	e	13935.1614	-0.0048
3.5	f	3.5	e	13935.3682	0.0006
4.5	f	4.5	e	13935.5691	-0.0026
5.5	f	5.5	e	13935.7807	0.0020
6.5	f	6.5	e	13935.9873	-0.0012
$^{r}P_{21}(0)$					
1.5	e	2.5	e	13934.1920	0.0018
2.5	e	3.5	e	13934.0039	0.0028
3.5	e	4.5	e	13933.8170	0.0021
4.5	e	5.5	e	13933.6264	-0.0051
5.5	e	6.5	e	13933.4457	-0.0051
6.5	e	7.5	e	13933.2801	0.0071

J'	Parity	J"	Parity	ν_{obs}	$\nu_{obs-calc}$
$^{r}R_{21}(0)$					
1.5	e	0.5	e	13935.3571	-0.0002
2.5	e	1.5	e	13935.9443	0.0007
3.5	e	2.5	e	13936.5380	0.0054
4.5	e	3.5	e	13937.1306	0.0062
5.5	e	4.5	e	13937.7212	0.0022
6.5	e	5.5	e	13938.3166	0.0002
7.5	e	6.5	e	13938.9144	-0.0022
$^{p}R_{11}(1)$					
2.5	e	1.5	e	13657.1099	0.0040
3.5	e	2.5	e	13657.7780	-0.0005
4.5	e	3.5	e	13658.4531	-0.0034
5.5	e	4.5	e	13659.1424	0.0038
6.5	e	5.5	e	13659.8195	-0.0045
7.5	e	6.5	e	13660.5127	0.0004
$^{p}Q_{11}(1)$					
1.5	f	1.5	e	13656.0492	-0.0029
2.5	f	2.5	e	13656.3262	-0.0021
3.5	f	3.5	e	13656.6128	-0.0006
$^{p}P_{11}(1)$					
0.5	e	1.5	e	13655.4101	0.0066
1.5	e	2.5	e	13655.2766	0.0021
2.5	e	3.5	e	13655.1675	0.0043
3.5	e	4.5	e	13655.0708	0.0100
4.5	e	5.5	e	13654.9797	0.0160
5.5	e	6.5	e	13654.8608	-0.0099
6.5	e	7.5	e	13654.7979	0.0169
$^{p}Q_{12}(1)$					
0.5	e	0.5	f	13655.4101	0.0029
1.5	e	1.5	f	13655.2766	-0.0069
2.5	e	2.5	f	13655.1788	0.0021
3.5	e	3.5	f	13655.0868	0.0082
4.5	e	4.5	f	13655.0007	0.0149
5.5	e	5.5	f	13654.8869	-0.0101
$^{p}P_{12}(1)$					
0.5	f	1.5	f	13654.6288	-0.0061
1.5	f	2.5	f	13654.1181	-0.0048
2.5	f	3.5	f	13653.6204	-0.0081
3.5	f	4.5	f	13653.1327	-0.0100
$^{p}R_{12}(1)$					
1.5	f	0.5	f	13656.0492	-0.0066
2.5	f	1.5	f	13656.3325	-0.0048
3.5	f	2.5	f	13656.6245	-0.0024

J'	Parity	J"	Parity	ν_{obs}	$\nu_{obs-calc}$
$^{p}Q_{22}(1)$					
0.5	e	0.5	f	13934.5691	-0.0035
1.5	e	1.5	f	13934.3809	-0.0049
2.5	e	2.5	f	13934.2001	-0.0012
3.5	e	3.5	f	13934.0163	-0.0032
4.5	e	4.5	f	13933.8355	-0.0049
5.5	e	5.5	f	13933.6583	-0.0058
$^{p}P_{22}(1)$					
0.5	f	1.5	f	13933.7988	-0.0014
1.5	f	2.5	f	13933.2198	-0.0055
2.5	f	3.5	f	13932.6512	-0.0018
$^{p}R_{22}(1)$					
1.5	f	0.5	f	13935.1614	0.0032
2.5	f	1.5	f	13935.3571	-0.0048
3.5	f	2.5	f	13935.5691	0.0014
4.5	f	3.5	f	13935.7807	0.0044
5.5	f	4.5	f	13935.9873	-0.0003
6.5	f	5.5	f	13936.2011	-0.0007
$^{p}Q_{21}(1)$					
1.5	f	1.5	e	13935.1614	0.0069
2.5	f	2.5	e	13935.3571	0.0042
3.5	f	3.5	e	13935.5691	0.0149
4.5	f	4.5	e	13935.7598	0.0013
5.5	f	5.5	e	13935.9640	-0.0015
$^{p}P_{21}(1)$					
0.5	e	1.5	e	13934.5691	0.0002
1.5	e	2.5	e	13934.3809	0.0040
2.5	e	3.5	e	13934.1920	0.0042
3.5	e	4.5	e	13934.0039	0.0023
4.5	e	5.5	e	13933.8170	-0.0013
5.5	e	6.5	e	13933.6264	-0.0114
$^{p}R_{21}(1)$					
2.5	e	1.5	e	13936.1301	-0.0004
3.5	e	2.5	e	13936.7201	0.0008
4.5	e	3.5	e	13937.3128	0.0017
5.5	e	4.5	e	13937.9009	-0.0048
6.5	e	5.5	e	13938.5110	0.0078
$^{r}Q_{11}(1)$					
1.5	f	1.5	e	13655.5708	-0.0007
2.5	f	2.5	e	13655.6955	0.0061
3.5	f	3.5	e	13655.8063	0.0031
4.5	f	4.5	e	13655.9258	0.0096

J'	Parity	J"	Parity	ν_{obs}	$\nu_{obs-calc}$
$^{r}P_{11}(1)$					
1.5	e	2.5	e	13654.7979	0.0040
2.5	e	3.5	e	13654.5254	0.0011
3.5	e	4.5	e	13654.2530	0.0025
4.5	e	5.5	e	13653.9762	0.0002
$^{r}R_{11}(1)$					
2.5	e	1.5	e	13656.4704	0.0034
3.5	e	2.5	e	13656.9724	0.0041
4.5	e	3.5	e	13657.4688	<0.0000
5.5	e	4.5	e	13657.9703	0.0003
6.5	e	5.5	e	13658.4702	-0.0023
$^{r}Q_{12}(1)$					
1.5	e	1.5	f	13654.7979	-0.0050
2.5	e	2.5	f	13654.5392	0.0014
3.5	e	3.5	f	13654.2692	0.0008
4.5	e	4.5	f	13653.9967	-0.0014
5.5	e	5.5	f	13653.7333	0.0049
$^{r}P_{12}(1)$					
1.5	f	2.5	f	13653.6383	-0.0040
2.5	f	3.5	f	13652.9892	-0.0003
3.5	f	4.5	f	13652.3281	-0.0044
4.5	f	5.5	f	13651.6733	-0.0013
5.5	f	6.5	f	13651.0112	-0.0062
6.5	f	7.5	f	13650.3554	-0.0061
7.5	f	8.5	f	13649.7091	0.0017
8.5	f	9.5	f	13649.0474	-0.0079
$^{r}R_{12}(1)$					
1.5	f	0.5	f	13655.5708	-0.0044
2.5	f	1.5	f	13655.6955	-0.0028
3.5	f	2.5	f	13655.8131	-0.0036
4.5	f	3.5	f	13655.9353	0.0013
5.5	f	4.5	f	13656.0492	-0.0027
$^{r}Q_{22}(1)$					
2.5	e	2.5	f	13933.6829	-0.0037
4.5	e	4.5	f	13933.3200	-0.0057
5.5	e	5.5	f	13933.1455	-0.0039
6.5	e	6.5	f	13932.9735	-0.0026
$^{r}R_{22}(1)$					
2.5	f	1.5	f	13934.8430	-0.0042
3.5	f	2.5	f	13935.0506	-0.0025
4.5	f	3.5	f	13935.2576	-0.0040
5.5	f	4.5	f	13935.4756	0.0027

J'	Parity	J"	Parity	ν_{obs}	$\nu_{obs\text{-}calc}$
${}^{r}Q_{21}(1)$					
2.5	f	2.5	e	13934.8430	0.0048
3.5	f	3.5	e	13935.0407	0.0011
4.5	f	4.5	e	13935.2377	-0.0061
5.5	f	5.5	e	13935.4568	0.0060
${}^{r}P_{21}(1)$					
2.5	e	3.5	e	13933.6829	0.0098
3.5	e	4.5	e	13933.4875	0.0006
5.5	e	6.5	e	13933.1235	0.0004
${}^{r}R_{21}(1)$					
2.5	e	1.5	e	13935.6171	0.0013
3.5	e	2.5	e	13936.2011	-0.0035
4.5	e	3.5	e	13936.7939	-0.0025
5.5	e	4.5	e	13937.3916	0.0006
6.5	e	5.5	e	13937.9991	0.0106
7.5	e	6.5	e	13938.5898	0.0010

Appendix A4: Measured Lines (in cm^{-1}) for the $\tilde{B}\,^2E - \tilde{X}\,^2A_1$ Transition of $SrBH_4$

J'	Parity	J"	Parity	ν_{obs}	$\nu_{obs-calc}$
$^{r}Q_{22}(0)$					
1.5	e	1.5	f	14517.244	-0.001
2.5	e	2.5	f	14517.0891	0.0005
3.5	e	3.5	f	14516.9415	-0.002
4.5	e	4.5	f	14516.8112	-2E-04
5.5	e	5.5	f	14516.6906	-3E-04
$^{r}R_{22}(0)$					
1.5	f	0.5	f	14517.9991	0.0015
2.5	f	1.5	f	14518.2158	-0.002
3.5	f	2.5	f	14518.4491	-4E-04
4.5	f	3.5	f	14518.6927	-9E-04
5.5	f	4.5	f	14518.9495	-3E-04
6.5	f	5.5	f	14519.2192	0.001
$^{r}P_{21}(0)$					
1.5	e	2.5	e	14517.2398	0.0005
2.5	e	3.5	e	14517.0811	0.001
3.5	e	4.5	e	14516.9323	-7E-04
4.5	e	5.5	e	14516.7968	-0.001
5.5	e	6.5	e	14516.6758	0.0007
$^{r}P_{22}(0)$					
1.5	f	2.5	f	14516.1173	0.0007
2.5	f	3.5	f	14515.5834	0.0003
3.5	f	4.5	f	14515.067	0.0053
4.5	f	5.5	f	14514.5504	-0.002
5.5	f	6.5	f	14514.0584	0.003
6.5	f	7.5	f	14513.5713	0.0009
$^{r}R_{21}(0)$					
1.5	e	0.5	e	14518.3733	0.0015
2.5	e	1.5	e	14518.9671	0.0012
3.5	e	2.5	e	14519.5736	0.0014
4.5	e	3.5	e	14520.1911	0.0005
5.5	e	4.5	e	14520.818	-0.003
6.5	e	5.5	e	14521.4667	0.003
7.5	e	6.5	e	14522.1173	-0.001
8.5	e	7.5	e	14522.7815	-0.004
9.5	e	8.5	e	14523.4604	-0.004
$^{r}Q_{21}(0)$					
1.5	f	1.5	e	14517.9972	0.0033
2.5	f	2.5	e	14518.2097	-0.002
3.5	f	3.5	e	14518.4409	-3E-05
4.5	f	4.5	e	14518.6821	-5E-04
5.5	f	5.5	e	14518.9362	-3E-04
6.5	f	6.5	e	14519.2019	-5E-04

J'	Parity	J"	Parity	ν_{obs}	$\nu_{obs-calc}$
${}^{r}R_{11}(0)$					
1.5	e	0.5	e	14319.8357	-0.005
2.5	e	1.5	e	14320.2573	0.0089
3.5	e	2.5	e	14320.6632	-0.005
4.5	e	3.5	e	14321.1042	0.0037
5.5	e	4.5	e	14321.5478	0.0035
6.5	e	5.5	e	14322.0079	0.0079
7.5	e	6.5	e	14322.468	0.0004
${}^{r}Q_{12}(0)$					
0.5	e	0.5	f	14319.0635	-0.005
1.5	e	1.5	f	14318.7091	-0.005
2.5	e	2.5	f	14318.3708	-3E-04
3.5	e	3.5	f	14318.0351	-0.005
4.5	e	4.5	f	14317.7159	-0.005
5.5	e	5.5	f	14317.4126	-0.002
6.5	e	6.5	f	14317.1149	-0.004
${}^{r}P_{11}(0)$					
0.5	e	1.5	e	14319.0584	-0.006
1.5	e	2.5	e	14318.7091	0.0014
2.5	e	3.5	e	14318.3697	0.0071
3.5	e	4.5	e	14318.026	-0.003
4.5	e	5.5	e	14317.7076	-3E-04
${}^{r}R_{12}(0)$					
1.5	f	0.5	f	14320.2074	0.0004
2.5	f	1.5	f	14320.6148	0.0032
3.5	f	2.5	f	14321.0338	0.0058
4.5	f	3.5	f	14321.4619	0.0057
${}^{r}P_{12}(0)$					
0.5	f	1.5	f	14318.6844	-0.002
1.5	f	2.5	f	14318.3303	0.0042
2.5	f	3.5	f	14317.971	-0.006
3.5	f	4.5	f	14317.6336	-0.007
${}^{r}Q_{11}(0)$					
0.5	f	0.5	e	14319.816	0.0028
1.5	f	1.5	e	14320.2074	0.004
2.5	f	2.5	e	14320.6102	0.0047
3.5	f	3.5	e	14321.0165	-0.003
${}^{p}P_{11}(1)$					
0.5	e	1.5	e	14319.1026	0.0012
1.5	e	2.5	e	14318.7081	-1E-03
2.5	e	3.5	e	14318.3523	-0.002
3.5	e	4.5	e	14318.0167	-2E-05
${}^{p}R_{11}(1)$					
2.5	e	1.5	e	14320.2418	0.0011
3.5	e	2.5	e	14320.6518	-0.004

J'	Parity	J"	Parity	ν_{obs}	$\nu_{obs-calc}$
4.5	e	3.5	e	14321.0948	0.0094
${}^{p}R_{12}(1)$					
1.5	f	0.5	f	14319.4519	-0.014
2.5	f	1.5	f	14319.491	4E-05
3.5	f	2.5	f	14319.5307	-0.002
4.5	f	3.5	f	14319.5792	-0.009
${}^{p}Q_{11}(1)$					
1.5	f	1.5	e	14319.4519	-0.012
2.5	f	2.5	e	14319.491	0.0051
3.5	f	3.5	e	14319.5195	-0.005
4.5	f	4.5	e	14319.5792	0.0019
${}^{p}Q_{12}(1)$					
0.5	e	0.5	f	14319.1026	-7E-04
1.5	e	1.5	f	14318.71	-0.004
2.5	e	2.5	f	14318.3697	0.0074
3.5	e	3.5	f	14318.026	-0.001
4.5	e	4.5	f	14317.7076	0.002
${}^{p}Q_{22}(1)$					
0.5	e	0.5	f	14517.5986	-0.003
2.5	e	2.5	f	14517.2761	-0.001
3.5	e	3.5	f	14517.1358	0.0032
4.5	e	4.5	f	14517.0067	0.0066
5.5	e	5.5	f	14516.8809	0.0012
${}^{p}R_{22}(1)$					
1.5	f	0.5	f	14518.1832	-0.002
2.5	f	1.5	f	14518.4052	-6E-04
3.5	f	2.5	f	14518.6368	-0.001
4.5	f	3.5	f	14518.88	-0.002
5.5	f	4.5	f	14519.1386	5E-05
6.5	f	5.5	f	14519.4087	0.0017
${}^{p}P_{22}(1)$					
0.5	f	1.5	f	14516.8503	-2E-04
1.5	f	2.5	f	14516.3069	0.0018
2.5	f	3.5	f	14515.7704	-0.001
3.5	f	4.5	f	14515.249	-0.001
4.5	f	5.5	f	14514.7471	0.0059
5.5	f	6.5	f	14514.2477	0.0036
6.5	f	7.5	f	14513.755	-0.004
${}^{p}R_{21}(1)$					
2.5	e	1.5	e	14519.1529	-0.003
3.5	e	2.5	e	14519.763	0.0014
4.5	e	3.5	e	14520.3807	0.0008
5.5	e	4.5	e	14521.007	-0.003
7.5	e	6.5	e	14522.3093	0.0017
8.5	e	7.5	e	14522.9759	0.0014

J'	Parity	J"	Parity	ν_{obs}	$\nu_{obs-calc}$
9.5	e	8.5	e	14523.6474	-0.006
$^pP_{21}(1)$					
0.5	e	1.5	e	14517.5986	-0.002
1.5	e	2.5	e	14517.4334	0.0047
2.5	e	3.5	e	14517.2741	0.0048
3.5	e	4.5	e	14517.1235	0.0013
4.5	e	5.5	e	14516.9869	-2E-04
5.5	e	6.5	e	14516.8617	-0.003
$^pQ_{21}(1)$					
1.5	f	1.5	e	14518.181	-0.002
2.5	f	2.5	e	14518.3996	-0.001
3.5	f	3.5	e	14518.6279	-0.002
4.5	f	4.5	e	14518.8695	-0.002
5.5	f	5.5	e	14519.1291	0.0035
6.5	f	6.5	e	14519.3903	-0.001
$^rQ_{21}(1)$					
2.5	f	2.5	e	14517.9033	-0.002
3.5	f	3.5	e	14518.1346	-5E-05
4.5	f	4.5	e	14518.3761	-2E-04
5.5	f	5.5	e	14518.6368	0.0067
6.5	f	6.5	e	14518.8943	-0.002
7.5	f	7.5	e	14519.1796	0.0056
$^rQ_{22}(1)$					
2.5	e	2.5	f	14516.7815	-1E-04
3.5	e	3.5	f	14516.6338	-0.003
4.5	e	4.5	f	14516.511	0.0065
$^rR_{22}(1)$					
2.5	e	1.5	e	14518.6586	-0.001
3.5	e	2.5	e	14519.2661	7E-05
4.5	e	3.5	e	14519.8859	0.0016
5.5	e	4.5	e	14520.516	0.0012
6.5	e	5.5	e	14521.1529	-0.004
7.5	e	6.5	e	14521.8096	-0.002
8.5	e	7.5	e	14522.4766	-0.002
$^rP_{21}(1)$					
2.5	e	3.5	e	14516.7765	0.0027
3.5	e	4.5	e	14516.618	-0.009
4.5	e	5.5	e	14516.4937	0.0021
$^rR_{22}(1)$					
2.5	f	1.5	f	14517.9033	-0.007
3.5	f	2.5	f	14518.1426	0.0001
4.5	f	3.5	f	14518.3855	-0.001
5.5	f	4.5	f	14518.6463	0.0033
6.5	f	5.5	f	14518.9149	0.0035
7.5	f	6.5	f	14519.2016	0.0096

J'	Parity	J"	Parity	ν_{obs}	$\nu_{obs-calc}$
$^{r}P_{22}(1)$					
2.5	f	3.5	f	14515.2712	-0.005
3.5	f	4.5	f	14514.7471	-0.008
4.5	f	5.5	f	14514.2452	-5E-04
5.5	f	6.5	f	14513.7533	0.0047
$^{r}R_{12}(1)$					
1.5	f	0.5	f	14320.1457	-0.008
2.5	f	1.5	f	14320.5766	0.0089
3.5	f	2.5	f	14320.9897	0.001
4.5	f	3.5	f	14321.4152	-0.005
5.5	f	4.5	f	14321.8578	-0.004
6.5	f	5.5	f	14322.3093	-0.006
7.5	f	6.5	f	14322.7732	-0.007
$^{r}P_{11}(1)$					
1.5	e	2.5	e	14319.3929	-0.004
2.5	e	3.5	e	14319.4225	-0.009
3.5	e	4.5	e	14319.4519	-0.021
4.5	e	5.5	e	14319.5195	-0.005
$^{r}R_{11}(1)$					
2.5	e	1.5	e	14321.3257	0.0083
$^{r}P_{12}(1)$					
1.5	f	2.5	f	14318.2639	-0.009
2.5	f	3.5	f	14317.9342	0.0006
3.5	f	4.5	f	14317.6081	0.0069
4.5	f	5.5	f	14317.2846	0.0059
$^{r}Q_{11}(1)$					
1.5	f	1.5	e	14320.1457	-0.006
2.5	f	2.5	e	14320.574	0.0114
3.5	f	3.5	e	14320.9844	0.0035
4.5	f	4.5	e	14321.4108	0.0015
5.5	f	5.5	e	14321.8547	0.006
6.5	f	6.5	e	14322.2985	-0.001
$^{r}Q_{12}(1)$					
1.5	f	1.5	f	14319.3993	-0.002
2.5	f	2.5	f	14319.4443	0.0052
3.5	f	3.5	f	14319.491	0.0077
4.5	f	4.5	f	14319.5307	-0.007

Appendix A5: Measured Lines (in cm^{-1}) for the $\tilde{B}\,^2E - \tilde{X}\,^2A_1$ Transition of $CaBH_4$

J'	Parity	J"	Parity	ν_{obs}	$\nu_{obs-calc}$
$^{r}Q_{11}(0)$					
0.5	f	0.5	e	15403.2096	0.00199
1.5	f	1.5	e	15403.5613	0.00019
2.5	f	2.5	e	15403.9303	0.00226
3.5	f	3.5	e	15404.3093	0.00091
4.5	f	4.5	e	15404.7036	0.00145
5.5	f	5.5	e	15405.1061	-0.0032
6.5	f	6.5	e	15405.5344	0.00453
7.5	f	7.5	e	15405.9623	-0.0015
$^{r}P_{11}(0)$					
0.5	e	1.5	e	15402.538	-0.0029
1.5	e	2.5	e	15402.2258	-0.0019
2.5	e	3.5	e	15401.9297	0.00167
3.5	e	4.5	e	15401.6401	-0.0017
4.5	e	5.5	e	15401.3646	-0.0044
$^{r}R_{11}(0)$					
1.5	e	0.5	e	15403.7158	0.00401
2.5	e	1.5	e	15404.4052	0.00375
3.5	e	2.5	e	15405.1061	0.00153
4.5	e	3.5	e	15405.8221	0.00092
5.5	e	4.5	e	15406.5478	-0.0035
6.5	e	5.5	e	15407.2981	0.00322
7.5	e	6.5	e	15408.0512	-0.0008
8.5	e	7.5	e	15408.8171	-0.0055
$^{r}Q_{12}(0)$					
0.5	e	0.5	f	15402.538	-0.0029
1.5	e	1.5	f	15402.2258	-0.0019
2.5	e	2.5	f	15401.9297	0.00167
3.5	e	3.5	f	15401.6401	-0.0017
4.5	e	4.5	f	15401.3646	-0.0044
$^{r}P_{12}(0)$					
0.5	f	1.5	f	15401.7262	0.00265
1.5	f	2.5	f	15401.0882	0.00051
2.5	f	3.5	f	15400.4691	0.00385
3.5	f	4.5	f	15399.856	-0.0002
4.5	f	5.5	f	15399.2587	-0.0019
$^{r}R_{12}(0)$					
1.5	f	0.5	f	15403.5613	0.00019
2.5	f	1.5	f	15403.9303	0.00226
3.5	f	2.5	f	15404.3093	0.00091
4.5	f	3.5	f	15404.7036	0.00145
5.5	f	4.5	f	15405.1061	-0.0032
6.5	f	5.5	f	15405.5344	0.00453
7.5	f	6.5	f	15405.9623	-0.0015

J'	Parity	J"	Parity	ν_{obs}	$\nu_{obs-calc}$
$^{r}Q_{22}(0)$					
1.5	e	1.5	f	15464.8147	0.00129
2.5	e	2.5	f	15464.6081	-0.002
3.5	e	3.5	f	15464.4237	-0.0006
4.5	e	4.5	f	15464.2538	-0.0024
5.5	e	5.5	f	15464.1064	0.00084
$^{r}P_{22}(0)$					
1.5	f	2.5	f	15463.3266	-0.0028
2.5	f	3.5	f	15462.6377	0.00629
3.5	f	4.5	f	15461.9488	-0.0023
$^{r}R_{22}(0)$					
1.5	f	0.5	f	15465.8012	-0.0016
2.5	f	1.5	f	15466.094	-0.0002
3.5	f	2.5	f	15466.4014	-0.0018
4.5	f	3.5	f	15466.7286	-0.0013
5.5	f	4.5	f	15467.0781	0.00383
$^{r}Q_{21}(0)$					
1.5	f	1.5	e	15465.8012	-0.0016
2.5	f	2.5	e	15466.094	-0.0002
3.5	f	3.5	e	15466.4014	-0.0018
4.5	f	4.5	e	15466.7286	-0.0013
5.5	f	5.5	e	15467.0781	0.00383
$^{r}P_{21}(0)$					
1.5	e	2.5	e	15464.8147	0.00129
2.5	e	3.5	e	15464.6081	-0.002
3.5	e	4.5	e	15464.4237	-0.0006
4.5	e	5.5	e	15464.2538	-0.0024
5.5	e	6.5	e	15464.1064	0.00084
$^{r}R_{21}(0)$					
1.5	e	0.5	e	15466.2957	-0.0018
2.5	e	1.5	e	15467.0781	-0.0054
3.5	e	2.5	e	15467.8873	0.00018
4.5	e	3.5	e	15468.7113	0.00298
5.5	e	4.5	e	15469.5504	0.00332
$^{p}Q_{22}(1)$					
0.5	e	0.5	f	15465.6536	-0.0014
1.5	e	1.5	f	15465.4322	-0.0019
2.5	e	2.5	f	15465.2331	0.00238
3.5	e	3.5	f	15465.0435	-0.0015
4.5	e	4.5	f	15464.8812	0.00441
5.5	e	5.5	f	15464.7268	0.00058
$^{p}P_{11}(1)$					
0.5	e	1.5	e	15402.688	0.00067
1.5	e	2.5	e	15402.538	0.0029
2.5	e	3.5	e	15402.4052	0.00215

J'	Parity	J"	Parity	ν_{obs}	$\nu_{obs-calc}$
3.5	e	4.5	e	15402.2846	-0.0019
$^{p}Q_{12}(1)$					
0.5	e	0.5	f	15402.688	0.00067
1.5	e	1.5	f	15402.538	0.0029
2.5	e	2.5	f	15402.4052	0.00215
3.5	e	3.5	f	15402.2846	-0.0019
$^{p}P_{12}(1)$					
0.5	f	1.5	f	15401.6986	0.00063
1.5	f	2.5	f	15401.0521	0.00105
2.5	f	3.5	f	15400.4274	0.00309
3.5	f	4.5	f	15399.8121	-0.001
4.5	f	5.5	f	15399.2146	-0.0015
$^{p}R_{12}(1)$					
1.5	f	0.5	f	15403.5245	2.9E-05
2.5	f	1.5	f	15403.8836	-0.0035
3.5	f	2.5	f	15404.2628	-0.0024
4.5	f	3.5	f	15404.6586	0.00098
5.5	f	4.5	f	15405.0591	-0.0048
6.5	f	5.5	f	15405.4825	-0.0013
7.5	f	6.5	f	15405.9156	-0.0017
$^{p}Q_{22}(1)$					
0.5	e	0.5	f	15465.6536	-0.0014
1.5	e	1.5	f	15465.4322	-0.0019
2.5	e	2.5	f	15465.2331	0.0024
3.5	e	3.5	f	15465.0435	-.0.0015
4.5	e	4.5	f	15464.8812	0.0044
5.5	e	5.5	f	15464.7268	0.0006
$^{p}P_{22}(1)$					
0.5	f	1.5	f	15464.6648	-0.0008
1.5	f	2.5	f	15463.9488	-0.0012
2.5	f	3.5	f	15463.2502	-0.0018
3.5	f	4.5	f	15462.5736	0.00206
4.5	f	5.5	f	15461.9094	0.00071
$^{p}R_{22}(1)$					
1.5	f	0.5	f	15466.4181	-0.0053
2.5	f	1.5	f	15466.712	-0.0028
3.5	f	2.5	f	15467.0264	0.00271
4.5	f	3.5	f	15467.351	0.00079
5.5	f	4.5	f	15467.7004	0.00608
$^{p}Q_{21}(1)$					
1.5	f	1.5	e	15466.4181	-0.0053
2.5	f	2.5	e	15466.712	-0.0028
3.5	f	3.5	e	15467.0264	0.00271
4.5	f	4.5	e	15467.351	0.00079
5.5	f	5.5	e	15467.7004	0.00608

J'	Parity	J"	Parity	ν_{obs}	$\nu_{obs-calc}$
${}^{p}P_{21}(1)$					
0.5	e	1.5	e	15465.6536	-0.0014
1.5	e	2.5	e	15465.4322	-0.0019
2.5	e	3.5	e	15465.2331	0.00238
3.5	e	4.5	e	15465.0435	-0.0015
4.5	e	5.5	e	15464.8812	0.00441
5.5	e	6.5	e	15464.7268	0.00058
${}^{p}R_{21}(1)$					
2.5	e	1.5	e	15467.7004	-0.0037
3.5	e	2.5	e	15468.5072	-0.0005
4.5	e	3.5	e	15469.3313	0.00235
${}^{r}Q_{11}(1)$					
1.5	f	1.5	e	15403.1555	0.00212
2.5	f	2.5	e	15403.3522	-0.0004
3.5	f	3.5	e	15403.5613	-0.002
4.5	f	4.5	e	15403.7877	0.0011
5.5	f	5.5	e	15404.0288	0.00588
${}^{r}P_{11}(1)$					
1.5	e	2.5	e	15402.1617	-0.0023
2.5	e	3.5	e	15401.8688	0.0002
3.5	e	4.5	e	15401.5834	-0.0012
4.5	e	5.5	e	15401.3128	-0.0004
${}^{r}R_{11}(1)$					
2.5	e	1.5	e	15404.3408	-0.0012
3.5	e	2.5	e	15405.0497	0.00233
4.5	e	3.5	e	15405.768	0.00267
5.5	e	4.5	e	15406.4986	0.00226
6.5	e	5.5	e	15407.239	-0.0016
7.5	e	6.5	e	15408.0005	0.00233
8.5	e	7.5	e	15408.763	-0.0062
${}^{r}Q_{12}(1)$					
1.5	e	1.5	f	15402.1617	-0.0023
2.5	e	2.5	f	15401.8688	0.0002
3.5	e	3.5	f	15401.5834	-0.0012
4.5	e	4.5	f	15401.3128	-0.0004
${}^{r}R_{12}(1)$					
1.5	f	0.5	f	15403.1555	0.00212
2.5	f	1.5	f	15403.3522	-0.0004
3.5	f	2.5	f	15403.5613	-0.002
4.5	f	3.5	f	15403.7877	0.0011
5.5	f	4.5	f	15404.0288	0.00588
${}^{r}Q_{22}(1)$					
2.5	e	2.5	f	15463.885	0.00011
3.5	e	3.5	f	15463.7004	0.00113
4.5	e	4.5	f	15463.5307	-0.0006

J'	Parity	J"	Parity	ν_{obs}	$\nu_{obs-calc}$
5.5	e	5.5	f	15463.3811	0.0002
$^{r}R_{22}(1)$					
2.5	f	1.5	f	15465.3684	-0.0005
3.5	f	2.5	f	15465.6757	-0.0023
4.5	f	3.5	f	15466.0029	-0.0018
5.5	f	4.5	f	15466.3522	0.0032
$^{r}Q_{21}(1)$					
2.5	f	2.5	e	15465.3684	-0.0005
3.5	f	3.5	e	15465.6757	-0.0023
4.5	f	4.5	e	15466.0029	-0.0018
5.5	f	5.5	e	15466.3522	0.0032
$^{r}P_{21}(1)$					
2.5	e	3.5	e	15463.885	0.00011
3.5	e	4.5	e	15463.7004	0.00113
4.5	e	5.5	e	15463.5307	-0.0006
5.5	e	6.5	e	15463.3811	0.0002
$^{r}R_{21}(1)$					
2.5	e	1.5	e	15466.3522	-0.0061
3.5	e	2.5	e	15467.1617	-0.0004
4.5	e	3.5	e	15467.9868	0.00337
5.5	e	4.5	e	15468.8217	-0.0007
6.5	e	5.5	e	15469.6838	0.00475
$^{r}P_{22}(1)$					
2.5	f	3.5	f	15461.9094	0.00324

Appendix A6: Measured Lines (in cm^{-1}) for the $\tilde{D}\,^2\Sigma^+ - \tilde{A}\,^2\Pi$ Transition of CaOH

J'	Parity	J"	Parity	ν_{obs}	$\nu_{obs-calc}$
P_{12}					
4.5	e	5.5	e	12120.1945	-0.00278
5.5	e	6.5	e	12119.3212	-0.00893
6.5	e	7.5	e	12118.4963	0.00106
7.5	e	8.5	e	12117.685	-0.0076
8.5	e	9.5	e	12116.9254	0.00319
9.5	e	10.5	e	12116.1841	0
10.5	e	11.5	e	12115.4778	-0.00048
11.5	e	12.5	e	12114.811	0.00626
12.5	e	13.5	e	12114.1665	0.00299
13.5	e	14.5	e	12113.5523	-0.0023
14.5	e	15.5	e	12112.9778	-0.00023
15.5	e	16.5	e	12112.4385	0.00469
16.5	e	17.5	e	12111.9325	0.01055
17.5	e	18.5	e	12111.4501	0.00762
19.5	e	20.5	e	12110.5917	0.01094
20.5	e	21.5	e	12110.2108	0.01224
21.5	e	22.5	e	12109.8537	0.00488
22.5	e	23.5	e	12109.5387	0.00714
23.5	e	24.5	e	12109.2509	0.00408
24.5	e	25.5	e	12108.9934	-0.00121
25.5	e	26.5	e	12108.7835	0.00854
26.5	e	27.5	e	12108.5995	0.01161
27.5	e	28.5	e	12108.4393	0.00588
28.5	e	29.5	e	12108.3119	0.0003
29.5	e	30.5	e	12108.2189	-0.00354
30.5	e	31.5	e	12108.1655	-0.00047
31.5	e	32.5	e	12108.1425	0.00029
41.5	e	42.5	e	12109.7175	0.0065
42.5	e	43.5	e	12110.0534	0.0042
43.5	e	44.5	e	12110.4247	0.00419
44.5	e	45.5	e	12110.8219	-0.00305
45.5	e	46.5	e	12111.2519	-0.01066
R_{12}					
6.5	e	5.5	e	12128.086	-0.00994
7.5	e	6.5	e	12128.6543	-0.01021
8.5	e	7.5	e	12129.2561	-0.00911
9.5	e	8.5	e	12129.8957	-0.00232
10.5	e	9.5	e	12130.5516	-0.01132
11.5	e	10.5	e	12131.2603	0.00038
12.5	e	11.5	e	12131.9865	-0.00249

J'	Parity	J"	Parity	ν_{obs}	$\nu_{obs-calc}$
13.5	e	12.5	e	12132.7526	0.00246
14.5	e	13.5	e	12133.5459	0.00255
15.5	e	14.5	e	12134.3758	0.00718
16.5	e	15.5	e	12135.2338	0.00784
17.5	e	16.5	e	12136.1201	0.00476
18.5	e	17.5	e	12137.032	-0.00478
19.5	e	18.5	e	12137.989	-0.00126
20.5	e	19.5	e	12138.9726	-0.00319
21.5	e	20.5	e	12139.9942	0.00083
22.5	e	21.5	e	12141.0395	-0.0035
23.5	e	22.5	e	12142.1216	-0.00309
24.5	e	23.5	e	12143.2406	0.00218
25.5	e	24.5	e	12144.3834	-0.00082
26.5	e	25.5	e	12145.565	0.00292
27.5	e	26.5	e	12146.7716	-0.00041
28.5	e	27.5	e	12148.0139	-0.00011
29.5	e	28.5	e	12149.2868	-0.0013
30.5	e	29.5	e	12150.5943	0.00003
31.5	e	30.5	e	12151.922	-0.01054
32.5	e	31.5	e	12153.2962	-0.00672
33.5	e	32.5	e	12154.7046	-0.00082
34.5	e	33.5	e	12156.1326	-0.00744
13.5	e	12.5	e	12132.7526	0.00246
14.5	e	13.5	e	12133.5459	0.00255
15.5	e	14.5	e	12134.3758	0.00718
16.5	e	15.5	e	12135.2338	0.00784
17.5	e	16.5	e	12136.1201	0.00476
18.5	e	17.5	e	12137.032	-0.00478
19.5	e	18.5	e	12137.989	-0.00126
20.5	e	19.5	e	12138.9726	-0.00319
21.5	e	20.5	e	12139.9942	0.00083
22.5	e	21.5	e	12141.0395	-0.0035
23.5	e	22.5	e	12142.1216	-0.00309
24.5	e	23.5	e	12143.2406	0.00218
25.5	e	24.5	e	12144.3834	-0.00082
26.5	e	25.5	e	12145.565	0.00292
27.5	e	26.5	e	12146.7716	-0.00041

J'	Parity	J"	Parity	ν_{obs}	$\nu_{obs-calc}$
R_{22}					
4.5	f	3.5	f	12130.6357	-0.00551
5.5	f	4.5	f	12131.8543	-0.00853
6.5	f	5.5	f	12133.1097	-0.00698
7.5	f	6.5	f	12134.4007	-0.00207
8.5	f	7.5	f	12135.7217	0.00061
10.5	f	9.5	f	12138.4564	0.00191
11.5	f	10.5	f	12139.8708	0.00122
12.5	f	11.5	f	12141.3135	-0.00343
Q12					
1.5	e	1.5	f	12124.6988	-0.00786
2.5	e	2.5	f	12124.4319	0.0032
3.5	e	3.5	f	12124.1854	0.00237
4.5	e	4.5	f	12123.9697	0.00003
5.5	e	5.5	f	12123.7846	-0.00405
6.5	e	6.5	f	12123.6357	-0.00429
7.5	e	7.5	f	12123.5176	-0.00611
8.5	e	8.5	f	12123.4304	-0.00945
9.5	e	9.5	f	12123.3887	0.00028
10.5	e	10.5	f	12123.3738	0.00435
11.5	e	11.5	f	12123.3738	-0.00917
12.5	e	12.5	f	12123.4181	-0.01091
13.5	e	13.5	f	12123.4972	-0.0104
14.5	e	14.5	f	12123.6048	-0.01396
15.5	e	15.5	f	12123.7487	-0.01383
16.5	e	16.5	f	12123.9277	-0.01124
17.5	e	17.5	f	12124.142	-0.00602
18.5	e	18.5	f	12124.3829	-0.0069
19.5	e	19.5	f	12124.6507	-0.01362
20.5	e	20.5	f	12124.9687	-0.00289
P_{22}					
0.5	f	1.5	f	12124.6988	-0.00659
1.5	f	2.5	f	12124.4319	0.00532
2.5	f	3.5	f	12124.1854	0.00533
3.5	f	4.5	f	12123.9697	0.00384
4.5	f	5.5	f	12123.7846	0.0006
5.5	f	6.5	f	12123.6357	0.00121
6.5	f	7.5	f	12123.5176	0.00023
7.5	f	8.5	f	12123.4304	-0.00225
8.5	f	9.5	f	12123.3887	0.00833
9.5	f	10.5	f	12123.3738	0.01324
10.5	f	11.5	f	12123.3738	0.00057
11.5	f	12.5	f	12123.4181	-0.00033

J'	Parity	J"	Parity	ν_{obs}	$\nu_{obs-calc}$
12.5	f	13.5	f	12123.4972	0.00103
13.5	f	14.5	f	12123.6048	-0.00169
14.5	f	15.5	f	12123.7487	-0.00071
15.5	f	16.5	f	12123.9277	0.00273
16.5	f	17.5	f	12124.142	0.00879
17.5	f	18.5	f	12124.3829	0.00876
18.5	f	19.5	f	12124.6507	0.00289
19.5	f	20.5	f	12124.9687	0.01446
Q_{22}					
5.5	f	5.5	e	12128.086	-0.00444
6.5	f	6.5	e	12128.6543	-0.00386
7.5	f	7.5	e	12129.2561	-0.00192
8.5	f	8.5	e	12129.8957	0.00573
9.5	f	9.5	e	12130.5516	-0.00243
10.5	f	10.5	e	12131.2603	0.01012
11.5	f	11.5	e	12131.9865	0.00809
12.5	f	12.5	e	12132.7526	0.01389
13.5	f	13.5	e	12133.5459	0.01483
14.5	f	14.5	e	12134.3758	0.0203
15.5	f	15.5	e	12135.2338	0.02181
16.5	f	16.5	e	12136.1201	0.01958
17.5	f	17.5	e	12137.032	0.01089
18.5	f	18.5	e	12137.989	0.01525
19.5	f	19.5	e	12138.9726	0.01416
20.5	f	20.5	e	12139.9942	0.01903
21.5	f	21.5	e	12141.0395	0.01555
22.5	f	22.5	e	12142.1216	0.01681
23.5	f	23.5	e	12143.2406	0.02292
24.5	f	24.5	e	12144.3834	0.02077
25.5	f	25.5	e	12145.565	0.02536
26.5	f	26.5	e	12146.7716	0.02287
27.5	f	27.5	e	12148.0139	0.02402
28.5	f	28.5	e	12149.2634	0.00028
29.5	f	29.5	e	12150.5683	-0.00015
30.5	f	30.5	e	12151.9042	-0.00167
31.5	f	31.5	e	12153.2749	-0.00051
32.5	f	32.5	e	12154.6842	0.00715
33.5	f	33.5	e	12156.1105	-0.00033
P_{11}					
12.5	e	13.5	e	12180.6554	0.00394
13.5	e	14.5	e	12180.1186	-0.00093
14.5	e	15.5	e	12179.6309	0.00412

J'	Parity	J"	Parity	ν_{obs}	$\nu_{obs-calc}$
16.5	e	17.5	e	12178.7621	0.00326
17.5	e	18.5	e	12178.3861	0.00244
18.5	e	19.5	e	12178.0414	-0.00628
19.5	e	20.5	e	12177.7454	-0.00549
20.5	e	21.5	e	12177.4927	-0.0006
21.5	e	22.5	e	12177.2669	-0.00799
22.5	e	23.5	e	12177.0896	-0.00608
23.5	e	24.5	e	12176.9538	-0.00184
24.5	e	25.5	e	12176.8496	-0.00519
25.5	e	26.5	e	12176.7912	-0.0019
26.5	e	27.5	e	12176.7718	0.00124
32.5	e	33.5	e	12177.4587	0.00165
33.5	e	34.5	e	12177.7138	0.00553
34.5	e	35.5	e	12177.9954	-0.00315
35.5	e	36.5	e	12178.3327	0.00486
36.5	e	37.5	e	12178.7004	0.00425
37.5	e	38.5	e	12179.1077	0.00427
38.5	e	39.5	e	12179.5552	0.00551
39.5	e	40.5	e	12180.0459	0.01102
40.5	e	41.5	e	12180.5612	0.00221
41.5	e	42.5	e	12181.132	0.01
42.5	e	43.5	e	12181.7218	-0.00208
43.5	e	44.5	e	12182.3624	-0.0022
R_{11}					
13.5	e	12.5	e	12199.1636	-0.00437
14.5	e	13.5	e	12200.0369	0.0056
15.5	e	14.5	e	12200.934	0.00045
17.5	e	16.5	e	12202.8444	-0.01035
18.5	e	17.5	e	12203.8604	-0.01327
19.5	e	18.5	e	12204.9206	-0.01085
20.5	e	19.5	e	12206.0146	-0.01346
21.5	e	20.5	e	12207.157	-0.0065
23.5	e	22.5	e	12209.5438	-0.00696
24.5	e	23.5	e	12210.7905	-0.01204
25.5	e	24.5	e	12212.0908	-0.00224
26.5	e	25.5	e	12213.417	-0.00526
27.5	e	26.5	e	12214.7899	-0.00025
28.5	e	27.5	e	12216.1955	-0.00119
29.5	e	28.5	e	12217.6371	-0.00475
30.5	e	29.5	e	12219.1182	-0.00741
31.5	e	30.5	e	12220.6461	-0.00182
32.5	e	31.5	e	12222.2042	-0.00456

J'	Parity	J"	Parity	ν_{obs}	$\nu_{obs-calc}$
33.5	e	32.5	e	12223.7972	-0.01089
34.5	e	33.5	e	12225.4433	-0.00257
35.5	e	34.5	e	12227.1145	-0.00758
36.5	e	35.5	e	12228.8327	-0.00397
37.5	e	36.5	e	12230.5834	-0.0062
38.5	e	37.5	e	12232.3862	0.00536
Q_{21}					
12.5	f	12.5	e	12199.1636	0.00706
13.5	f	13.5	e	12200.0369	0.01787
14.5	f	14.5	e	12200.934	0.01357
16.5	f	16.5	e	12202.8444	0.00447
17.5	f	17.5	e	12203.8604	0.00239
18.5	f	18.5	e	12204.9206	0.00566
19.5	f	19.5	e	12206.0146	0.00389
20.5	f	20.5	e	12207.157	0.0117
22.5	f	22.5	e	12209.5438	0.01293
23.5	f	23.5	e	12210.7905	0.00871
24.5	f	24.5	e	12212.0686	-0.00285
25.5	f	25.5	e	12213.4027	0.00288
26.5	f	26.5	e	12214.7648	-0.00207
27.5	f	27.5	e	12216.1703	-0.00226
28.5	f	28.5	e	12217.615	-0.00188
29.5	f	29.5	e	12219.0945	-0.00528
30.5	f	30.5	e	12220.6159	-0.00535